

DETERMINATION OF THREE-DIMENSIONAL TEMPERATURE FIELDS  
BY HOLOGRAPHIC INTERFEROMETRY AND NUMERICAL TECHNIQUES

BY

K.H. YEE

A THESIS SUBMITTED TO  
THE UNIVERSITY OF LEICESTER  
FOR THE DEGREE OF  
DOCTOR OF PHILOSOPHY  
AUGUST, 1982

UMI Number: U333328

All rights reserved

INFORMATION TO ALL USERS

The quality of this reproduction is dependent upon the quality of the copy submitted.

In the unlikely event that the author did not send a complete manuscript and there are missing pages, these will be noted. Also, if material had to be removed, a note will indicate the deletion.



UMI U333328

Published by ProQuest LLC 2015. Copyright in the Dissertation held by the Author.  
Microform Edition © ProQuest LLC.

All rights reserved. This work is protected against  
unauthorized copying under Title 17, United States Code.



ProQuest LLC  
789 East Eisenhower Parkway  
P.O. Box 1346  
Ann Arbor, MI 48106-1346



THESIS  
666505  
25.7.83

x752920943

DETERMINATION OF THREE-DIMENSIONAL TEMPERATURE FIELDS BY HOLOGRAPHIC INTERFEROMETRY AND NUMERICAL TECHNIQUES

By K.H. Yee

ABSTRACT

The object of this work is primarily to evaluate three-dimensional temperature field reconstruction by numerical techniques using experimental projection data from holographic interferograms with no degree of symmetry taken in reconstructing the test fields. The interferograms are produced using a pulsed laser, and are recorded by means of a photographic system for digitisation. The 3-D test fields are of two types: (i) the smoothly varying plume from a heated block, and (ii) the convective current set up by a localised heated spot on the floor inside an enclosure having walls, ceiling and floor all kept at a constant temperature.

A number of numerical techniques is investigated. Using either the Grid element or Finite element mathematical model, overdetermined but inexact sets of equations are obtained, and then inverted using known iterative algorithms of the ART type, and also a new Least Squares of Residuals Technique (LSRT) which was developed by the author. To test the numerical techniques, particularly as only a limited range of viewing angles is obtainable, a preliminary experiment was performed on the plume, providing a thermocouple traverse and projection data. Simulated projection data computed from thermocouple readings compared favourably with the holographic projection data particularly at high fringe numbers. The numerical techniques were tested using both simulated and real projection data. Using ART inversion, the Grid element model produced better approximation to the thermocouple temperature field than the Finite element model.

However, when solving the reconstruction equations using digitised projection data from the enclosure model severe instability was encountered with ART because the temperature field structure is now more complicated. Even with increased resolution the problem still persisted. LSRT was subsequently developed to overcome this. In reconstruction with LSRT, the temperature on each pixel is determined by the sum of the squares of each of the residuals and thus does not involve using the projection data directly. Although this technique has given much more stable reconstructions, the restricted viewing angle range from the data still presents a problem in that when a comparison is made with the physics of the enclosure model even the best reconstructions available do not show good results. A form of directional bias appears in all of them. Also on a few, some random errors can be seen. These reconstructions therefore suggest that in practise data from the missing views are required when seeking to reconstruct satisfactorily the numerical values and shape of complicated 3-D temperature fields.

## ACKNOWLEDGEMENTS

The author is grateful to his supervisor Dr. G.L. Booth for his support, encouragement and concern throughout the course of this research.

The author thanks members of the workshop staff who made some of the optical mounts for the holographic interferometers, in particular Messrs. P. Ingham, J. Donisthorpe, A. Wale, and R. Haynes. The author would also like to thank the photographer, Paul Smith, for producing the photographs for this thesis. Assistance obtained from Patricia Baglin, and also Doug Pratt, is greatly appreciated.

Finally, the author would like to express his gratitude to Professor G.D.S. MacLellan, the Head of Engineering Department, for allocating a SERC award to the author and making available the facilities in the Department for this research.

DETERMINATION OF THREE-DIMENSIONAL TEMPERATURE FIELDS  
BY HOLOGRAPHIC INTERFEROMETRY AND NUMERICAL TECHNIQUES

CONTENTS

	Page
ACKNOWLEDGEMENTS	i
CONTENTS	ii
NOMENCLATURE	v
CHAPTER 1 INTRODUCTION	1 - 9
1.1 Determination of Temperature Fields in Natural Convection Processes	2
1.1.1 Three-Dimensional Temperature Fields - The Tomographic Problem	4
1.2 The Experimental Approach	6
1.3 Problem Statement	8
CHAPTER 2 HOLOGRAPHIC TECHNIQUES	10 - 30
2.1 Holography	11
2.2 Double Exposure Holography	13
2.2.1 Localisation of Interferometric Fringes	14
2.3 Practical Advantages of Various Types of Double Exposure Holograms	17
2.3.1 Transmitted Light Reflection Holograms	18
2.3.2 Diffusely Transmitted-Light Transmission Hologram	19
2.4 The Light Diffusing Screen	20
2.5 Method of Processing Holographic Plates	22
2.6 Method of Recording the Interferometric Projection Data	24

2.6.1	Digitisation of Projection Data	25
CHAPTER 3	NUMERICAL TECHNIQUES FOR ANALYSING INTERFEROGRAMS	31 - 57
3.1	Basic Principles and Some Instability Problems	32
3.2	Choice of Mathematical Models	35
3.2.1	The Grid Element	36
3.2.2	The Finite Element	38
3.3	Choice of Inversion Techniques	43
3.3.1	ART (Algorithm Reconstruction Technique)	44
3.3.2	SIRT (Simultaneous Iterative Reconstruction Technique)	46
3.3.3	LSRT (Least Squares of Residuals Technique)	49
3.4	Numerical Processing	52
CHAPTER 4	PRELIMINARY LABORATORY TEST EXPERIMENT	58 - 98
4.1	Preliminary Test Section	59
4.1.1	Convective and Radiative Power Considerations	60
4.1.2	The Biot and Fourier Moduli	62
4.2	The Thermocouple Traverse	64
4.3	Relationship between Fringe Number and Temperature	66
4.4	Practical Limitations of Holographic Interferometry	68
4.5	Method of Digitisation of Interferograms	69
4.6	Results from Digitisation	71
4.6.1	Errors in Digitised Data	72A
4.7	Results from Computer Reconstructions	73
4.7.1	A Direct Inversion Technique	74
4.7.2	Iterative Inversion Techniques	77

CHAPTER 5	FABRICATION OF MODEL OF LOCALISED HEATING IN AN ENCLOSURE	99 - 120
5.1	Introduction	100
5.2	The Test Enclosure	102
5.2.1	The Test Tank	104
5.2.2	The Cooling System	105
5.2.3	The Heaters	106
5.3	The Holographic Interferometer	106
5.4	Collection of Fringe Data from Interferograms	109
5.5	Relationship between Refractive Index of Water and Temperature	110
CHAPTER 6	ANALYSIS OF RESULTS FROM THE CONSTANT TEMPERATURE ENCLOSURE	121 - 146
6.1	Experimental Results	122
6.2	Reconstructions	124
6.3	Flow Visualisation Results	125D
CHAPTER 7	CONCLUSIONS	147 - 156
7.1	3-D Temperature Measurement by Pulsed Laser Holographic Interferometry	148
7.2	The Method of Holographic Interferometry and Data Digitisation	150
7.3	A Comparision of the Holographic Data	152
7.4	The Techniques for Reconstructing 3-D Temperature Fields	153
APPENDIX 1	COMPUTER PROGRAM LISTING	157
REFERENCES		206

## NOMENCLATURE

Symbols denote the following quantities, or as defined otherwise in the text.

$[A_{ij}]$	projection matrix where $i$ and $j$ are the number of rays in rows and the number of pixels/nodes in columns respectively
$A_{mn}(\theta, \rho)$	coefficients of matrix $[A_{ij}]$ for the ray at $(\theta, \rho)$
$Bi$	Biot number
$C_j$	weight factor for the $j^{\text{th}}$ pixel used in the LSRT technique
$e_i$	error in the $i^{\text{th}}$ ray
$e_j$	error in the $j^{\text{th}}$ pixel
$Fo$	Fourier number
$f$	spatial frequency of interference fringes
$Gr$	Grashof number
$h$	heat transfer coefficient, $W m^{-2} K^{-1}$
$I$	Intensity of illumination as defined by eqn. (2.1)*
$i$	ray number, corresponds to values of $(\theta, \rho)$ in a sequence
$j$	pixel number
$k$	integer number; in postscript form denoting iteration cycle number
$M, N$	number of pixels on the reconstruction grid representing the refractive index field relative to the ambient in the $x$ and $y$ directions respectively
$N$	fringe number
$Nu$	Nusselt number

\* Having units  $W m^{-2}$ , when multiplied by  $\frac{1}{2}\epsilon c$  where  $\epsilon$ =dielectric constant for air,  $c$ =velocity of light in air, provided electric field component wave is in  $V_{rms} m^{-1}$ .

$n$	refractive index
$n_0$	ambient refractive index
$n_j$	refractive index relative to ambient for the $j^{\text{th}}$ pixel
$Pr$	Prandtl number
$Q$	heat transfer, W
$r_1, r_2$	integration limits defined by eqn. (3.25)
$S$	total pathlength of test section, $m^*$
$T$	temperature, $^{\circ}C$
$w_{\theta}$	sampled width of ray at angle of $\theta$ as defined by eqn. (3.30), $m^*$
$x, y$	spatial cartesian coordinates, $m^*$
$x_j$	value of the $j^{\text{th}}$ pixel
$\beta$	y intercept in the shifted coordinate system, according to eqn. (3.8(b))
$\gamma$	x intercept in the shifted coordinate system, according to eqn. (3.8(b))
$\Delta$	a small change in a quantity, or an angle.
$\Delta n$	refractive index relative to ambient ( $n - n_0$ )
$\Delta n_j$	fractional value of refractive index relative to ambient for the $j^{\text{th}}$ pixel
$\Delta x, \Delta y$	widths of the grid elements in the x and y directions respectively as shown in fig. 3.1
$\delta$	a measure of closeness to the original picture as defined by eqn. (3.34)
$\theta$	angular orientation of ray as shown in fig. 3.1

\* Or as stated otherwise  
vi

$\lambda$	wavelength
$v(k)$	variance after iteration cycle number $k$
$\rho$	radial position of ray as shown in fig. 3.1
$\Sigma$	summation
$\phi_i$	optical pathlength difference as defined by eqn. (3.1) for the $i^{\text{th}}$ ray
$\phi(\theta, \rho)$	optical pathlength difference as defined by eqn. (3.4) for the ray at $(\theta, \rho)$
$\psi(x, y)$	phase angle of wavefront

DETERMINATION OF THREE-DIMENSIONAL TEMPERATURE FIELDSBY HOLOGRAPHIC INTERFEROMETRY AND NUMERICAL TECHNIQUESSYNOPSISCHAPTER 1INTRODUCTION

Techniques for the measurement of three-dimensional temperature fields in natural convection situations are assessed. Holographic interferometry is introduced as a means of gathering projection data which are used for subsequent numerical analysis to extract temperatures. A review is made of existing tomographic techniques, particularly in the reconstruction of temperature fields with experimental holographic data, which are restricted in the range of viewing angles and also noisy.

The natural convection situation of interest is then described, together with an outline of a preliminary laboratory experiment used to validate the techniques of temperature field reconstruction.

## CHAPTER 1

### INTRODUCTION

#### 1.1 DETERMINATION OF TEMPERATURE FIELDS IN NATURAL CONVECTION PROCESSES

Of interest is the natural convection process within an enclosure having constant temperature walls, resulting from a localised heated area on the floor of the chamber. Examples are a localised fire in a room or a spent nuclear fuel element in a cooling pond. An attempt to model this situation theoretically would lead to the steady state\* temperature distribution and the fluid velocity distribution throughout the chamber. In general these distributions will be three-dimensional although for a centrally placed hot spot there could be some degree of symmetry. In evaluating theoretical predictions it is necessary to determine these three dimensional fields experimentally for comparison.

One method of measuring the temperature field would be to place a large number of thermocouples throughout the chamber volume. However the leads coming out of the chamber from the thermocouple junctions would have a marked effect on the natural convection flow. The temperature of the thermocouple junction is not necessarily that of the fluid immediately surrounding it. It results from a balance between heat transfer from the fluid to the junction and the heat leak along the lead wires resulting from the temperature gradient through which they pass. Although this effect can be minimised by suitable orientation of the lead wires this presents practical problems particularly as the temperature field is not known ab initio.

Non-invasive optical techniques using instruments such as the Mach-Zehnder or Michelson interferometer have found wide use in

\* Heat sinks are provided by heat losses through surface of enclosure, and also in the case of the cooling pond by the breeze over the water surface.

experimental natural convection research; A. Dowd (1981), Kuehn and Goldstein (1978), Yousef and Tarasuk (1981), and Meyer, Mitchell and El-Wakil (1979). These methods are attractive in that they do not influence the temperature and flow field in the way insertions of thermocouples do. Such instruments measure two-dimensional temperature fields. Essentially a light beam is split into two. One beam, the object beam passes through the test section whilst the second, the reference beam, passes through a similar geometry pathlength. When transparent windows are used in the defining walls of the test section, identical walls must be incorporated in the reference beam. On viewing the two beams recombined an interference pattern is seen. Dark fringes occur when the optical pathlength difference between the two beams is an odd number of half wavelengths

$$\int_S (n - n_0) \cdot dS = (2k + 1) \cdot \frac{\lambda}{2} \quad (1.1)$$

Here  $n$  and  $n_0$  are the refractive indices of the medium in the object and reference beam respectively,  $S$  is the depth of the test section along the beam path and  $\lambda$  the wavelength of the illuminating radiation. Going from one dark (or light) fringe to the next the optical pathlength changes by  $\lambda$ . Refractive index can be related to temperature. If the test section has a two-dimensional temperature distribution, with temperature varying in a plane normal to the beam path but not along it, that temperature distribution can be deduced from the fringe spacing. Eqn. (1.1) then can be written

$$(n - n_0) \cdot S = (2k + 1) \cdot \frac{\lambda}{2} \quad (1.2)$$

and by counting fringes out from a point at which the temperature is known and using eqn. (1.2), the refractive index (and hence temperature)

throughout the viewing field is uniquely determined. However, if there are significant changes in  $n$  along the beam path, as occur in a three-dimensional situation, a single view obtained as described above does not allow the distribution of  $n$  to be determined.

### 1.1.1 THREE-DIMENSIONAL TEMPERATURE FIELDS - THE TOMOGRAPHIC PROBLEM

If in the Mach-Zehnder interferometer the refractive index in the test section varies along the direction of the beam, the fringe pattern is related to the integrated optical pathlength difference,  $\int (n - n_0) \cdot dS$ , along the beam. By counting fringes along a line drawn across the field of view information about the plane, parallel to the object beam direction and behind that line, is obtained and is called projection data. This is shown in fig. 1.1 which represents a two-dimensional slice through the test object. Projection data can be obtained for many values of  $\theta$ , the viewing direction. Every set of projection data has locked into it information about every point in this cutting plane through the object. The tomographic problem is to unscramble from the many sets of projection data the point to point variation of refractive index across this slice of the object. Considerable work has been done on this problem both for the case where projection data from views over  $180^\circ$  are available, and for the case where the range of viewing angle is restricted to a lower value. The book by Gabor T. Herman (1980) is a good introduction to the problem. In the field of holographic interferometry, Sweeney (1972) made an advance by demonstrating some numerical methods which are capable of reconstructing three-dimensional temperature fields from simulated projection data collected over a viewing angle range of  $90^\circ$  or less. These computer algorithmic methods were called GRID, SINC, and ART. There are however instability problems with GRID and SINC as pointed out by Walklate (1977) in attempting to obtain interferometric tomographs which required only a modest increase

in resolution. Implied in these methods are assumptions that the data to be fed in are almost noiseless and that the approximate mathematical model forming the point to point value equation set to be solved does not produce appreciable errors. The data are then inverted directly by a back substitution procedure for which it is notoriously difficult to achieve a stable solution in the presence of errors.

However should experimental as opposed to simulated interferometric data be used the possibility of solution with the iterative inversion procedure, ART, is more hopeful. It allows the use of relaxation parameters normally ranging from 0.025 to 0.25 which should have some stabilising effect permitting the picture to be built up much more gradually. In the iteration process this procedure can also be constrained to produce positive values of density only since it is known that negative densities cannot physically exist. Over the years there were two major modifications to this technique of solution:

(i) the iteration process should be stopped when all the residuals were within certain specified tolerances based on knowledge of expected errors so that the technique could not over-reconstruct and produce an erroneous solution, Herman (1975),

(ii) the constant point values or pixels should be replaced with bilinear functions\* in order to reduce inconsistencies arising from the approximate mathematical model governing the equation set to be solved, Herman and Lent (1976).

Unfortunately though, these modifications were not applied to experimental data from holographic interferometry where the reconstructed point to point variation values of  $n$  have to be much more exact than those from a conventional density variation tomograph.

So by solving the tomographic problem for each of a set of parallel

\* Linear functions of the variables  $x$  and  $y$ .

slices through the test object, the solution can be stacked up to give the three-dimensional picture that is required.

## 1.2 EXPERIMENTAL APPROACH

In principle the Mach-Zehnder could be used to collect sets of projection data. An interferogram at one viewing angle could be obtained, then the test object rotated through a small angle and a second interferogram taken, and so on. However this poses major problems. Since a dummy test section has to be incorporated in the reference beam of the interferometer, that too has to be rotated and creates problems of exact alignment. More seriously the process would be time consuming. It would be very difficult in the natural convection situation to ensure that the test region remained absolutely steady throughout the collection of the required interferograms.

The method of interferometric holography, see for instance Vest (1979) or Ostrovsky, Butusov and Ostrovskaya (1980), offers a way of overcoming these difficulties. Holography is a technique by which three-dimensional information about an object can be recorded on a suitable holographic plate. Subsequent viewing of the developed plate, illuminated by light from the recording laser shows the test object. By viewing the plate from different angles it is as though the object were being looked at from these different angles. By taking a double exposure of the photographic plate,

- (a) of the test section in the quiescent state (localised heated spot not operating)
- (b) of the test section in the operating condition with the natural convection flow established

two holograms are effectively taken, superimposed on each other. In the

Mach-Zehnder context (a) is the reference beam and (b) is the object beam. On reconstruction of the developed plate a fringe pattern is obtained which is related to the changes in refractive index ( and hence temperature ) between the first and second exposure.

The double exposure overcome the problem of the dummy section. Using a pulsed laser in which the laser energy is given out in a single pulse 25 nanoseconds long in conjunction with the dimensionality of the hologram sets of projection data are obtained all at one instant in time.

There is an added advantage accruing from the use of a pulsed laser. The quality of a hologram obtained using continuous wave lasers is sharply dependent on vibration levels in the building and special anti-vibration tables are needed to get good holograms. In the 25 nanosecond exposure time given by the pulsed laser the object has no time to move so experiments can be carried out on a normal laboratory bench.

In solution of the tomographic problem it is best if projection data over  $180^\circ$  range of viewing angles is available. Solutions can be obtained from a smaller range but they are likely to be less than perfect. Noise in the experimental data also degrades the solution. Generally it is only practical to build a holographic rig with a viewing angle of  $70^\circ$  to  $120^\circ$ . Sweeney (1972) studied several numerically simulated three-dimensional temperature fields reconstructable with data collection over a viewing angle of less than  $90^\circ$ . Using three pairs of reference/object beams Matulka and Collins (1971) were able to build a holographic interferometer with a viewing angle of  $90^\circ$  around a small supersonic jet nozzle, but the range was not continuous and the interferometer was made rotatable for obtaining the missing views at a later time. Sweeney and Vest (1974) in experiments with a tank of water produced a  $30^\circ$  field of

view using a single but wide pair of reference/object beams.

### 1.3 PROBLEM STATEMENT

The problem tackled in the work reported in this thesis was to assess measurement of three-dimensional temperature fields in natural convection situations by using a holographic interferometer to obtain projection data and subsequent numerical analysis to extract temperatures from that data, and to review existing solutions of the tomographic problem and test their efficacy when applied to the natural convection problem; particularly considering the effect of restriction on the range of viewing angles and noise on the projection data.

The particular natural convection situation is a rectangular box, filled with water, having a small electrically heated element which can be placed at various positions on the floor of the box. The sides and top of the box are held at constant temperature.

However before studying the natural convection process in an enclosed chamber it seemed appropriate to investigate the thermal plume above a heated copper block in free air. Here it is possible to take thermocouple readings without affecting the natural convection flow. Such readings can be compared with those obtained from projection data with subsequent numerical analysis. This comparison is used to build confidence in the general approach adopted.

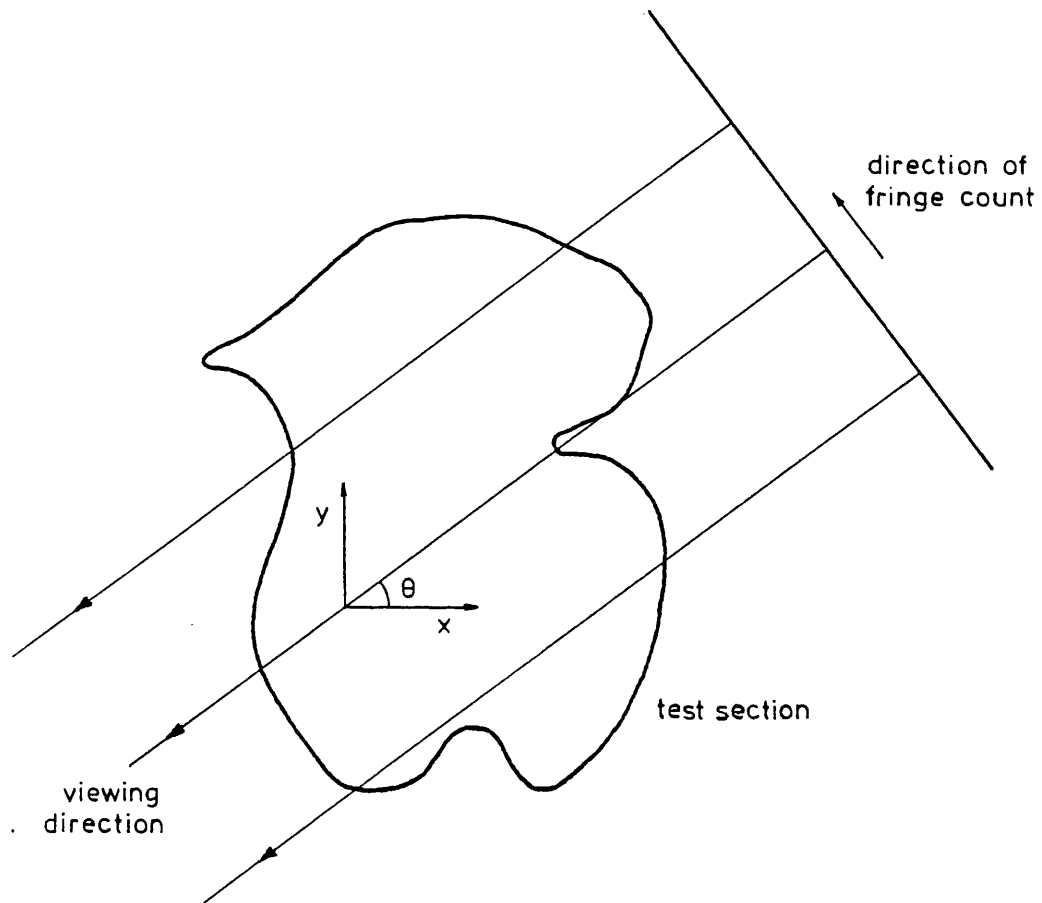


FIG. 1.1 TWO-DIMENSIONAL SLICE THROUGH A TEST OBJECT

SYNOPSISCHAPTER 2HOLOGRAPHIC TECHNIQUES

The theory of formation of holographic images is outlined briefly. There are many different types of holograms, made with a single wavelength laser, suitable for interferometric measurements. Initial trial experiments have been conducted to investigate the practical limitations of each type. For a proper reconstruction of a 3-D temperature field, a large range of viewing angles and good sharp holographic reconstruction with minimal image distortion are needed. The practical advantages of a diffusively illuminated transmitted-light, off-axis set-up are discussed.

The method of chemical processing of the holographic plates and the technique used for recording and digitising the fringes from the holographic interferograms are described.

CHAPTER 2HOLOGRAPHIC TECHNIQUES2.1 HOLOGRAPHY

The principle of holography was established by Gabor (1948) but it was only with the development of the laser towards the end of 1961 that a sufficiently coherent and intense light source became available to make the principle a practical possibility. Holograms can be made of solid non-transparent objects and of transparent objects, reflected-light and transmitted-light holograms respectively. Since the test region in this research is transparent discussion is confined to transmitted-light holograms.

The basic process consists of illuminating a photographic plate with two beams from a single laser source. One beam, the object beam, passes through the region of interest containing a transparent object, and then falls onto a special photographic plate. At the same time the second beam, the reference beam, falls directly onto the plate, see fig. 2.1. After exposure and development, the plates is found to have a microscopically small interference pattern. Upon re-illumination with the reference beam, fig. 2.2(a), the interference pattern acts as a complex diffraction grating and diffracts three main beams, the zero order, the positive and the negative first order, one of which is an exact re-creation of the original object beam.

This phenomenon may be described mathematically by the superposition of coherent waves. Fig. 2.1 shows the co-ordinate system used. Let the scalar waves be described as follows:

$\underline{A}(x) = A \cdot e^{-i2\pi fx}$ , is the distinct holographic reference beam where  
 $f = \frac{\sin \theta}{\lambda}$  is the spatial frequency,  
 $\underline{a}(x,y) = a(x,y) \cdot e^{-i\psi(x,y)}$  is the object beam.

Use of scalar operators assumes the polarisations of both beams are parallel.

The combination of both beams can be represented as:

$$\underline{Z} = A \cdot e^{-i2\pi fx} + \underline{a}(x,y)$$

Only intensity which is given by the square of the amplitude,  $\underline{Z} \cdot \underline{Z}^*$ , can be recorded on the photographic plate, where \* denotes the complex conjugate.

Its distribution is

$$\begin{aligned} I(x,y) &= A^2 + a^2(x,y) + A \cdot e^{i2\pi fx} \underline{a}(x,y) + A \cdot e^{-i2\pi fx} \underline{a}^*(x,y) \\ &= A^2 + a^2(x,y) + 2A \cdot a(x,y) \cdot \cos(2\pi fx - \psi(x,y)) \end{aligned} \quad (2.1)$$

The last term in eqn. (2.1) represents a recording of the object beam by a process of modulation. Assuming the transmittance\* of the plate to be proportional to exposure,  $I \cdot t$  where  $t$  is exposure time, the transmittance for the plate may therefore be written as:

$$T(x,y) = \left\{ tA^2 + t[ a^2(x,y) + A \cdot e^{i2\pi fx} \underline{a}(x,y) + A \cdot e^{-i2\pi fx} \underline{a}^*(x,y) ] \right\} \beta'$$

where  $\beta'$  is a constant dependent on the sensitivity of the emulsion.

Upon reconstruction with the reference beam the transmitted waves are as

follows:

$$\begin{aligned} C &= A e^{-i2\pi fx} T(x,y) \\ &= [t\beta'(A^2 + a^2(x,y))] A e^{-i2\pi fx} + [t\beta'A^2] \underline{a}(x,y) + (t\beta'A^2(x)) \underline{a}^*(x,y) \\ &\quad \dots\dots(2.2) \end{aligned}$$

where the square brackets represent attenuation.

The first term represents the direct transmission of the re-illuminated reference beam, the second term represents the production of the object

\* Transmittance is defined as the ratio between the amplitudes of the light waves after and before passing through the developed photographic emulsion.

wavefront at an angle of  $\theta$ , and the third term is a modified reconstruction of the complex conjugate of the object beam at an angle of  $-\theta$ .

The complex conjugate is normally suppressed by diffraction effects in the usually thin emulsions used, (7 - 17 $\mu$ m), except when  $\theta$  is very small. However, a reversal in the direction of the reilluminating reference beam ray paths through replacing  $Ae^{-2\pi fxi}$  by  $Ae^{+2\pi fxi}$ , causes the  $(t\beta'A^2(x))$  component in eqn. (2.2) to attenuate only as  $(t\beta'A^2)$ , and projects a real undistorted image of  $\underline{a}^*(x,y)$  as in fig. 2.2(b).

Similar results follow when a description is made of the process using a diffusing screen. With the phase and direction now being randomised spatially, the object beam is described by a complex vector in three-dimensional space, see DeVelis & Reynolds\*.

## 2.2 DOUBLE EXPOSURE HOLOGRAPHY

In double exposure holography, the holographic plate is first exposed to scattered light from a diffusing screen that has passed through the object of interest in its quiescent state. A second exposure is then made on the same plate to scattered light that has passed through the object in a disturbed state. (In this research the quiescent state is the object of interest all at uniform temperature. The disturbed state is when the temperature distribution that is to be determined has been established.) On viewing, when reilluminated by the reference beam alone, the two object wavefronts are superimposed. Due to phase differences between the two wavefronts a pattern of light and dark fringes is seen.

The amplitudes of the first and second exposure can now be described as:

$$\underline{Z}_1 = A \cdot e^{-2\pi fxi} + a(x,y) \cdot e^{-i\psi} \quad (2.3)$$

$$\underline{Z}_2 = A \cdot e^{-2\pi fxi} + a(x,y) \cdot e^{-i(\psi+\Delta)} \quad (2.4)$$

---

\* In this chapter and others following, a reference without a date following is for a book whereas reference with date is invariably for a paper.

The combined intensities of  $\underline{Z}_1$  and  $\underline{Z}_2$  on the photographic plate becomes:

$$\begin{aligned}
 & I_1 + I_2 \\
 = & 2A^2 + 2a^2(x,y) + A \cdot a(x,y) \cdot e^{-i(\psi-\beta)} + A \cdot a(x,y) \cdot e^{i(\psi-\beta)} + A \cdot a(x,y) \cdot e^{-(\psi+\Delta-\beta)} \\
 & + A \cdot a(x,y) \cdot e^{+i(\psi+\Delta-\beta)} \quad \dots\dots(2.5)
 \end{aligned}$$

where  $\beta = 2\pi fx$ , phase angle of reference beam.

Upon reconstruction with the reference beam the intensity of the virtual image is:

$$\begin{aligned}
 I_v &= [A \cdot a(x,y) \cdot e^{-i\psi} + A \cdot a(x,y) \cdot e^{-i(\psi+\Delta)}] [A \cdot a(x,y) \cdot e^{i\psi} + A \cdot a(x,y) \cdot e^{i(\psi+\Delta)}] \\
 &= 2A^2 \cdot a^2(x,y) \cdot [1 + \cos \Delta] \quad (2.6)
 \end{aligned}$$

The magnitude of  $\cos \Delta$  is a maximum whenever  $\Delta = n\pi$ , where  $n$  is an integer. Constructive interference occurs when  $n$  is even, and bright fringes are seen. Dark fringes are produced when  $n$  is odd. The factor of 2, which can cause non-linear reproduction, is reduced to unity by making two half exposures so that the total energy from the two exposures is still confined to the linear region of the characteristic response curve of the emulsion.

### 2.2.1 LOCALISATION OF FRINGES

When a diffusing screen is used to create a three-dimensional interferogram fringes appear to be localised in space much more than with a single plane wavefront. This is because an observing instrument such as the eye collects light rays over a finite range of viewing angle. Maximum contrast or visibility occurs at a point in space where the difference in phase between any ray chosen passing through that point and another also passing through that point, but from a slightly different angle, is either zero or almost zero. A collection of such points in space

forms the surface of localisation.

A mathematical description based on this model for a symmetrical phase object is given by Vest and Sweeney (1970), and was further developed by Vest in 1979 for an asymmetric phase object using the cartesian co-ordinate system. Ostrovsky, Butusov and Ostrovskaya suggested ways by which the surface on which fringes are distinct may be shifted to coincide with the plane of the phase object by placing thin glass wedges in the test region during one of the two exposures.

The surface of localisation may be predicted as follows:

From fig. 2.3, the optical pathlength difference due to changes of refractive index between the two exposure is given by

$$\Delta\phi = \int_{-L/2}^{L/2} \Delta n(x,y) \cdot \sec\alpha \, dy \quad (2.7)$$

where  $x = f(y) = [X - (Y-y) \cdot \tan\alpha]$ . At an angle of  $\alpha$ , and about the optical axis, fringes appear distinct or in focus only when relative phase changes are zero, viz:

$$\frac{d\phi}{d\alpha} = 0 \quad (2.8)$$

Eqn. (2.7) can thus be utilised to obtain

$$\frac{d\phi}{d\alpha} = \int_{-L/2}^{L/2} \left[ \Delta n(x,y) \cdot \frac{\sin\alpha}{\cos^2\alpha} + \frac{\partial \Delta n}{\partial x} \cdot \frac{dx}{d\alpha} \sec\alpha \right] \cdot dy \quad (2.9)$$

If  $\alpha=0$  and  $\partial\Delta n/\partial x$  is independent of  $y$ , eqns. (2.9) and (2.8) become

$$\begin{aligned} \frac{d\phi}{d\alpha} &= \frac{\partial \Delta n}{\partial x} \int_{-L/2}^{L/2} [Yy - y^2/2] \, dy \\ &= YL = 0 \end{aligned} \quad (2.10)$$

Provided  $\Delta n$  is homogeneous in the  $y$  direction, fringes are localised

in a plane intersecting the y axis at  $Y=0$ , at the centre of the test section.

If  $\alpha$  is defined arbitrary and  $\Delta n$  varies in the x direction only according to  $\Delta n = n_0 + \epsilon x$ , the optical pathlength difference is

$$= [ n_0 + \epsilon (X - Y \tan \alpha) ] L \sec \alpha \quad (2.11)$$

giving a condition for localisation

$$\frac{d \phi}{d \alpha} = \frac{L}{\cos^2 \alpha} [ (n_0 + \epsilon X) \sin \alpha - Y \left( \frac{1 + \sin^2 \alpha}{\cos \alpha} \right) ] = 0$$

..... (2.12)

$$[ \epsilon \sin \alpha ] \cdot x - [ \epsilon \left( \frac{1 + \sin^2 \alpha}{\cos \alpha} \right) ] y = -n_0 \cdot \sin \alpha \quad (2.13)$$

where x and y describe the locus representing the plane surface on which fringes appear to be in sharp focus.

$\epsilon$  is the quantity that experiments are carried out to determine and thus is an unknown during the data collection stage. Experimentally, the surface of fringe localisation, which can become quite complicated for an asymmetric index field, can be determined either by eye or by an observing instrument with a variable focal length lens such as a camera.

In digitisation fringes need to be measured accurately from a known reference point which could well lie within the test section. However, in practice in viewing an interferogram absolutely parallel rays from a particular direction could not always be obtained easily and so a plane of localisation appears which could lie outside the test section. Optical elements can thus be used to shift this plane of localisation if necessary to within the test section.

### 2.3 PRACTICAL ADVANTAGES OF VARIES TYPES OF DOUBLE EXPOSURE HOLOGRAMS

The study of variations in refractive index to deduce temperature and pressure requires a beam of coherent light to be transmitted through the test section, and a double exposure hologram or interferogram thus produced is of the transmitted light type. Experimentally, this type of interferogram can be made in a number of ways displaying interference fringes in accordance with the mathematical description outlined in the previous sections.

If the phase field is predominantly two-dimensional, such as flow in a turbine cascade, a collimated beam of coherent light is allowed to pass through the test section and fall onto a holographic plate with the reference beam on the same side. Because of the deep zone of localisation associated with non-diffused illumination the fringes appear in the plane of the hologram, and may be viewed either with a laser or white light. An undesirable diffraction pattern normally exists near the edges of the cascade block on the interferogram and Brandt et. al. (1976) and Bryanston-Cross et. al. (1980) used an ordinary optical lens to image the cascade onto the holographic plate, and suppressed such disturbances successfully. On reconstruction of the wavefronts forming the projected real image, the lens of the copying camera is placed where the wavefronts come to a focal point, and the camera is focussed on the interferogram. Information is available in two dimensions only from an image plane transmitted light interferogram.

If the variation of the test field is in three dimensions the test region must be illuminated with diffused light. Some explorative experiments were conducted to establish

- (i) the practical aspects of two types of holographic interferograms

(ii) the resolution and range of viewing angles one may obtain from diffusing screens.

### 2.3.1 TRANSMITTED LIGHT REFLECTION HOLOGRAMS

First used by Denisyuk (1962), this type of hologram is made with the reference beam on the opposite side of the plate. Stationary waves are being created with antinodes exposing the silver halide grains at intervals of  $\lambda/2$  throughout the thickness of the emulsion. The possibility of reconstruction with white reference beam becomes evident as the imprinted object wavefront at the antinodes acts like a half silvered mirror, and successive reinforcements from successive antinodal planes form the image strongly.

From an experimental point of view, this set-up has considerable advantages;

(i) closer examination and at a wider range of angles is possible by moving the plate closer to the test section,

(ii) noise or undesirable disturbance due to finite fringes is reduced as the reference beam is moved well away from the test section.

However in practice the efficiency of reflection holograms, especially interferograms, is still quite low. Using Agfa-Gaveart 8E75HD (high definition) holographic plates, reflection interferograms were produced of amongst other things a plume of hot air from a small electrically-heated vertical plate, and the cell structure shock wave from the nozzle. On reconstruction using the slightly divergent light beam of an overhead projector, the fringes and images do not appear to be distinct, fringes can only be resolved where their frequency is at 1/mm or less, and also

there are signs of severe image distortion when viewed from the maximum angle range at approximately  $23^\circ$  on either side.

Later a diluted swelling agent, triethanolamine, was used to re-swell the holographic emulsion to its original thickness and to determine whether better results could be obtained by reconstruction in laser light. Although the image appears sharper, its quality still remains poor, and image distortion is evident probably due to removal of more silver around the edges, where exposure was less, during the fixing process.

### 2.3.2 DIFFUSELY TRANSMITTED-LIGHT TRANSMISSION HOLOGRAM

This type of hologram is made with the reference and object beam both on the same side of the holographic plate employing an optical set-up as in fig. 2.1 similar to that discovered by Leith and Upatnieks (1962, 1964). The reference and object beams are obtained by dividing the laser beam with a beamsplitter. The reference beam is then diverted away from the area of interest and recombined afterwards with the object beam at the holographic plate. The light diffusing screen is normally placed in the object beam just behind the test region.

Good three-dimensional interferograms of this type resulted from the experiment using Agfa-Gaveart 8E75HD plates, provided certain conditions discovered from earlier explorative experimental work on the holographic technique are met, such as object to reference beam angle less than  $60^\circ$ , matching pathlengths of object and reference beams to less than 5 cm, controlling exposure and development to obtain a dark grey density on the plate, and either making holograms with a pulsed laser or, if a continuous laser is being used, in the evenings when the laboratory stabilises.

This method of producing interferograms to obtain quantitative data was chosen on the basis of good sharp reconstruction with a useful

viewing angle range of  $80^\circ - 85^\circ$  from a single object beam.

The disadvantages are:

- (i) space has to be created around the area of interest for the reference beam to pass through undisturbed,
- (ii) the holographic plate cannot be placed close to the area of interest for a wide viewing angle, and
- (iii) a laser is needed for reconstruction.

#### 2.4 THE LIGHT DIFFUSING SCREEN

A good diffuser must be able to scatter light evenly over a wide range of angles, in the horizontal directions preferably, and have a smooth surface to minimise speckle so that fine fringes can be resolved. Published literature indicates that a variety of diffusing screens has been used, and that there is not one that is ideal for use in holographic interferometry.

The phase grating of Vest and Sweeney (1970) can be used if interferograms are produced having fringes with a frequency greater than 5/mm. However the angle of view is discrete and the number of viewing angles is limited as the intensity of the fourth and higher diffracted orders falls to quite low levels. Gates (1968), and Fraser and Kinloch (1974) produced scatter plates which act as diffuser and beam splitter simultaneously. Because gaps are not required to allow the reference beam in, theoretically a  $180^\circ$  range of viewing angles is possible (Fraser and Kinloch 1974), but the holographic system has to be complex requiring several of these scatter plates of smoked glass, and hence several beams around the test region. Basically part of the beam falling on the smoked glass screen passes through and acts as the reference beam. The other part is scattered and acts as the diffused object beam. To allow the reference beam through without

disturbance, the test region must be at a distance away from each scatter plate, and as a result of this the system would work well only if a high power laser is available to expose the plates.

In the investigations reported herein, the fringe frequency was anticipated not to exceed 5/mm. Therefore several types of commercially available glass were tried with the objective of achieving a wide range of viewing angles as well as good resolution on reconstruction.

With Pacific, and diffused glass, light tends to diffract more than diffuse and the fringe resolution is poor at worse than 1 fringe per mm.

At the other extreme, with flashed opal glass, fringe resolution is good and light does appear to diffuse over a large angle approximately over  $150^\circ$ , but on reconstruction the object wavefronts appeared very weak due to the low intensity of the object beam reaching the plate during exposure.

Commercial ground glass gave quite good results, but the coarse grain produced sharp pinpricks of light, which produce speckles, impairing fringe resolution as noted by Bryanston-Cross (1977).

Acid ground glass was finally chosen as on reconstruction wavefronts over a wide viewing angle range of  $80^\circ - 85^\circ$  had been achieved from just a single object beam, and the fringe resolution was better than that with commercial ground glass because of the finer grain. A  $120^\circ$  field of view was obtainable from the same screen by use of two object beams shone on the screen at an angle.

## 2.5 METHOD OF PROCESSING HOLOGRAPHIC PLATES

The exposed plates are developed for six to ten minutes within which time a dark grey density level is sought, and within twenty minutes after exposure to prevent any loss in quality. A dark green Kodak 03 safety light is used after two minutes of development to check density if required. Concentrated Neofin Blau is used available in 500ml, and mixed with 0.3 g benzotriazole, an antifoggant, and 60 g of sodium metaborate for increased contrast. Without these chemicals added, a bright haze appears all over the image, but development time is much faster at three minutes.

After a wash in fresh water for 1 minute, the plates are fixed for 4 minutes using Agfa-Gaveart G334, diluted 1 part to 4 parts water.

After a further wash for 3 minutes, in the normally lit laboratory, the holographic interferograms are bleached until one minute after they become clear. This is to increase their efficiency in reconstruction from around 5% to around 30%, by converting the silver image into a transparent diffracting screen consisting mainly of silver bromide. The ingredients of the bleach are; 20g glycerol, 500ml deionised water, 500ml isopropyl alcohol, 300mg phenosafranine, 150g ferric nitrate, and 33g potassium bromide. This is diluted 1 part with 4 parts distilled water for use.

They are then given a final wash for 10 - 15 minutes, and are dried in warm flowing air from an electric fan heater.

The precipitated silver image from development of the exposed silver grains is not dissolved away by the bleaching agent ferric nitrate. Instead it gets mostly converted into silver bromide by the correctly constituted concentration of potassium bromide. Since a desensitizing

agent, phenosafranine, is already added in the bleach, a post bleach process was found unnecessary to prevent printout (post bleach blackening).

These chemical are formulated by Phillips and Porter (1976) for use on European holographic materials made by Agfa-Gaveart. Much of the reported American research work in this field, e.g. Pennington and Harper (1970), and Graube (1974), made use of Kodak emulsions, which are not generally available in this country. Phillips and Porter could not reproduce the results claimed using any of the reported processes on Agfa-Gaveart materials.

The reflection holograms were processed in four stages - development, fixing, bleaching, and fixing. Similar chemicals are used except for the bleach. The ingredients are; 20g potassium bromide (anhydrous), 20g mercuric chloride, and 1 litre water. Because mercuric chloride is poisonous and caustic, impervious rubber gloves were worn.

After the first fix, the plates were rinsed in water for 15 seconds. Mercuric bleaching followed until the plates appeared clear (1 - 2 minutes) and a further rinse of 15 seconds was given. The plates were now ready for final fixing, in a tray separated from the first to prevent the first tray of fixer being contaminated, until they turned brown (2 - 5 minutes). Finally, the holograms were washed for 5 minutes in fresh flowing water and dried in warm still air.

The use of mercuric chloride bleach was suggested by Jeong and Lodge (1978).

## 2.6 METHOD OF RECORDING THE INTERFEROMETRIC PROJECTION DATA

A particularly accurate technique of collecting holographic data from any specific angle is to place a large distortion free ray collecting lens in front of the interferogram, and use a pinhole filter\* to let out light rays from certain directions only as shown in fig. 2.4. By sliding the filter across, rays from different directions are projected onto the screen. The interferograms produced are similar in type to those obtainable from a Mach-Zehnder interferometer.

In practice, this technique produced images of very low intensity from interferograms made with a highly diffused object beam, and reilluminated using only a modest power, 15 mW, He-Ne laser.

The technique employed in this investigation was an approximation to this filtering technique by the use of a Nikon 200mm f4 telephoto lens placed at a distance away, fig. 2.5. With an extension tube, 27.5 mm, for image magnification, this lens was fixed onto a 35mm Nikon FM camera body, and was placed at least 1.4 metres away from the interferogram. At a given projection angle, traversing the camera across proved unnecessary as calculations indicated negligible angular deviations, i.e. though the rays collected by the lens are over a small angular cone converging towards the lens a small error could occur on the edges of the image where in imaging a point there from a 25.4 mm diameter object, say, with the camera lens 1.4 metres away maximum angular deviation of some the imaging rays from parallel could only be  $\pm 2.0^\circ$  approximately.

But because the camera lens has a finite aperture which collects a small cone of rays from a point on the object this error is likely to be less, but displaying a fringe pattern not as sharp as that say from plane wave illumination of the object such as with a Mach-Zehnder interferometer.

\* Placed in the focal plane of the lens.

Fine grain Ilford FP4 film was used to record the images at mostly  $10^\circ$  intervals. Three shot with varying exposure times were taken from each projection angle so the best print with the sharpest fringe pattern could be taken for digitisation.

#### 2.6.1 DIGITISATION OF PROJECTION DATA

In this manual process 17.5 cm x 12.5 cm prints were made of each image from a projection angle. Using a sharp compass needle, a line representing a horizontal plane of interest was scratched on each print. The fringes and any reference guides were mapped onto a piece of paper an edge of which was held against this scratched line.

When the magnification factor of each print representing the fringe pattern from each projection angle was calculated, fringe number - true distance co-ordinates were obtained.

Using the same set of prints this digitisation process was repeated for different horizontal planes of interest.

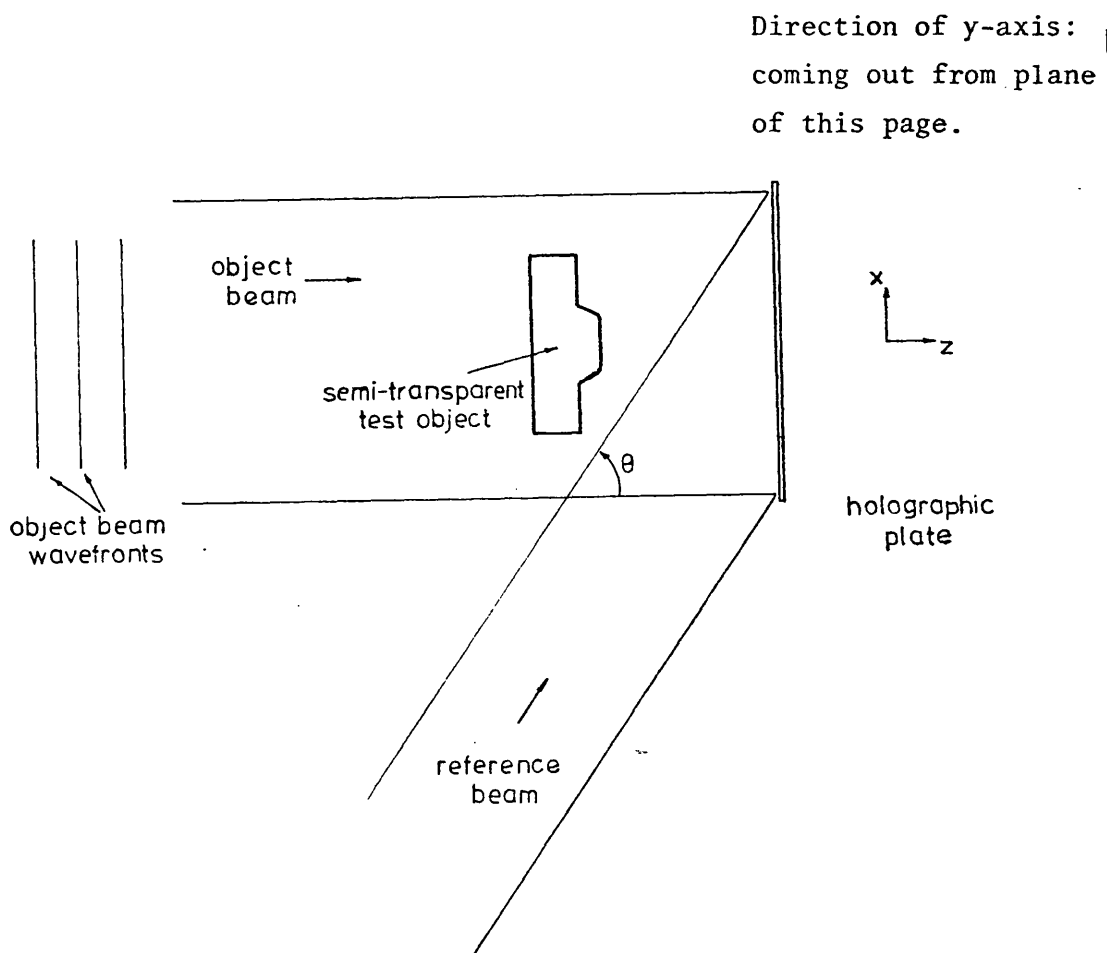


FIG. 2.1 ARRANGEMENT FOR PRODUCING A HOLOGRAM

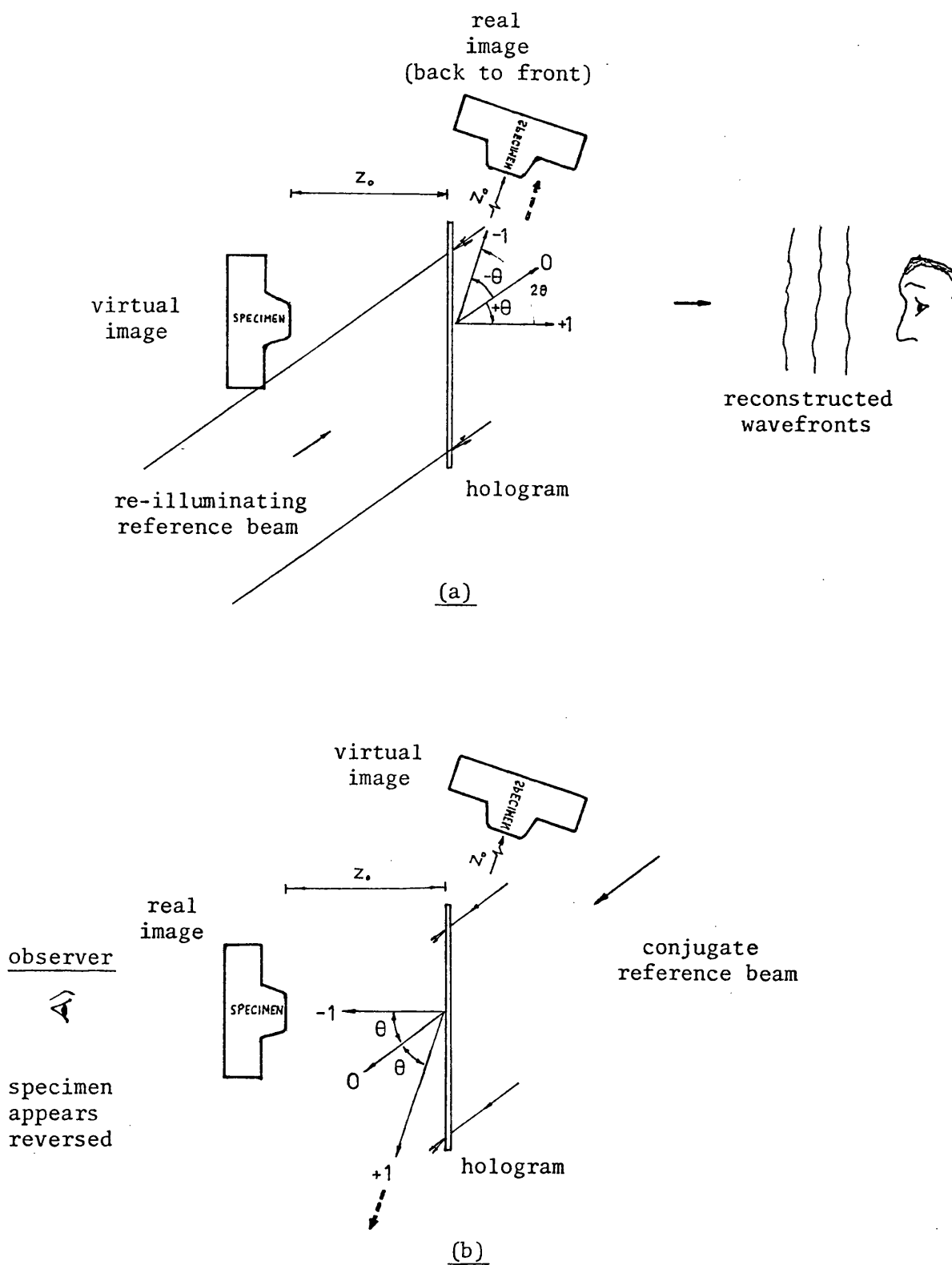


FIG. 2.2 IMAGES OBTAINABLE FROM A HOLOGRAM - (a) VIRTUAL, (b) REAL

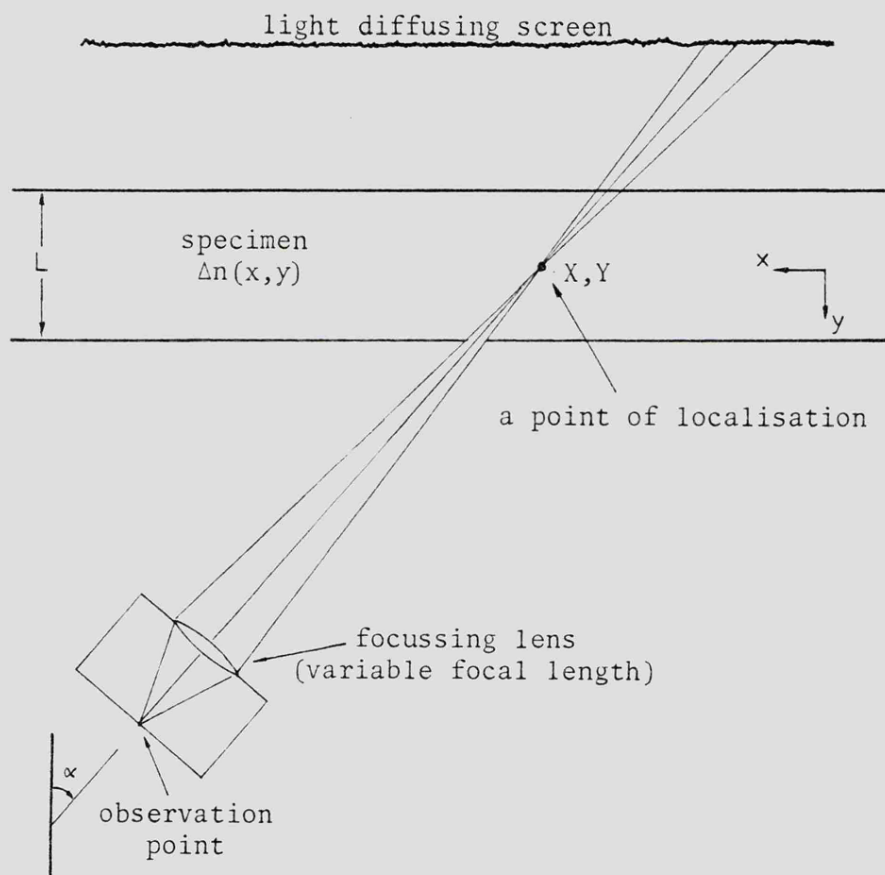


FIG. 2.3 LOCALISATION OF FRINGES

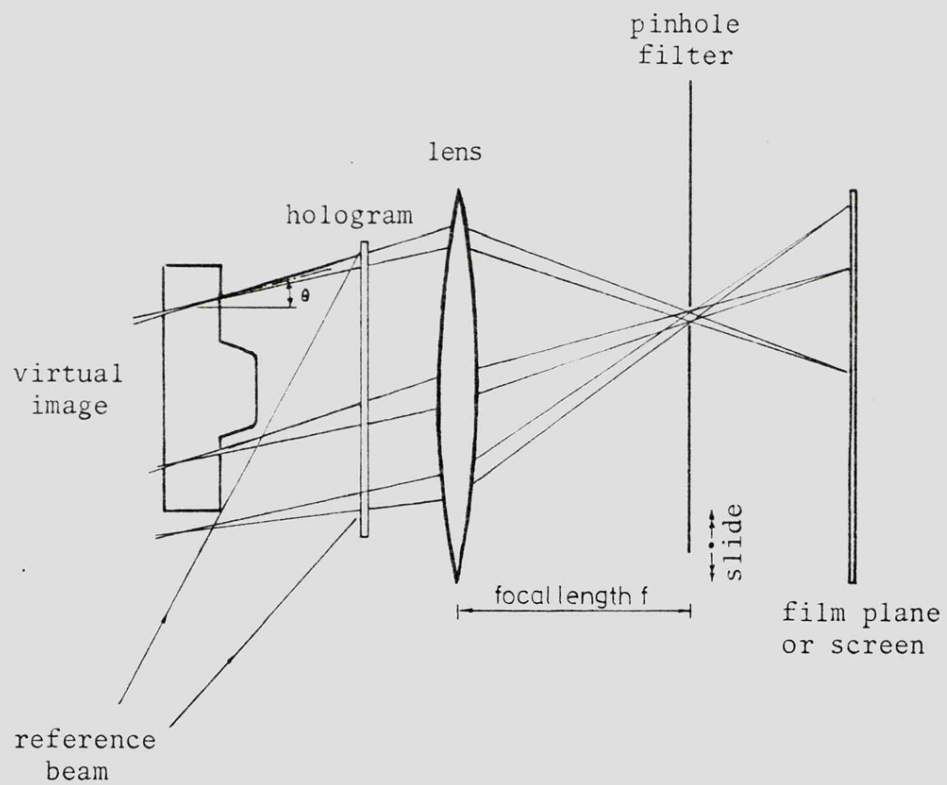


FIG. 2.4 SPATIAL FILTERING TECHNIQUE FOR IMAGING FROM PARALLEL  
OR QUASI-PARALLEL LIGHT RAYS

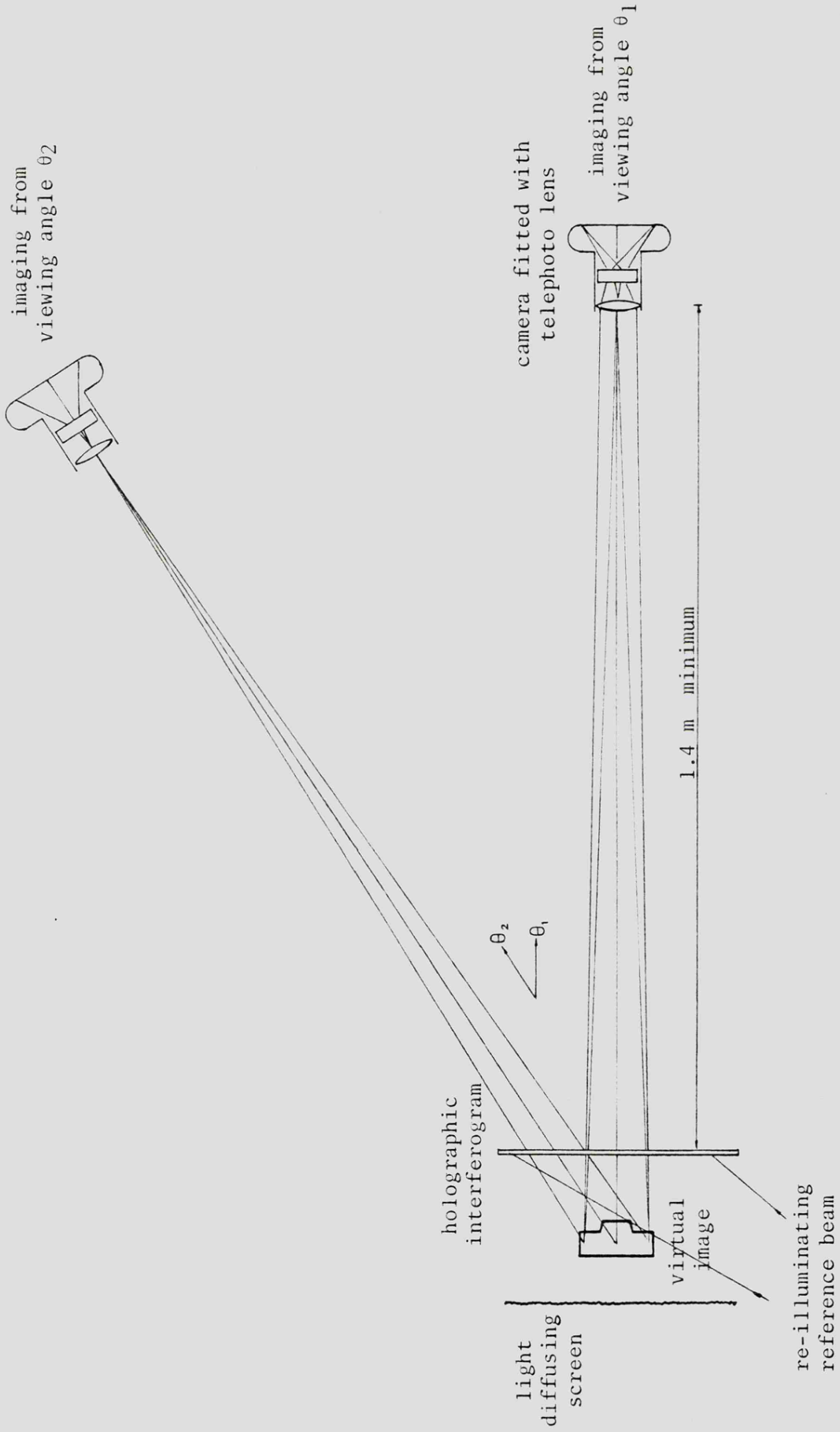


FIG. 2.5 TELEPHOTO LENS TECHNIQUE FOR IMAGING FROM QUASI-PARALLEL LIGHT RAYS

SYNOPSISCHAPTER 3NUMERICAL TECHNIQUES FOR ANALYSING INTERFEROGRAMS

The numerical techniques for reconstructing the digitised holographic projection data are described. A two-dimensional mathematical model is used to represent the numerically reconstructed temperature field. The three-dimensional temperature field is therefore obtained by stacking up a number of these two-dimensional reconstructed fields on top of one another.

It is found that the projection equations to be solved will be inconsistent with the holographic projection data because of (i) measurement errors, (ii) errors in the approximation of the mathematical model representing the temperature field, and (iii) computation errors caused by inversion of equations using an incomplete set of projection data from a restricted range of viewing angles.

The actual form of the equations to be solved is given, and two mathematical models are proposed; and numerical techniques likely to be able to produce solutions to these equations are presented.

CHAPTER 3

NUMERICAL TECHNIQUES FOR ANALYSING INTERFEROGRAMS

3.1 BASIC PRINCIPLES AND SOME INSTABILITY PROBLEMS

Each data point represents an optical pathlength difference, or the number of fringe shifts, taken from an interferogram, and corresponds to a ray of light having passed all the way through a volume containing the refractive index field of interest. It is assumed that the ray travels in a straight line and that any bending caused by variation of refractive index gradients within the three-dimensional field created is considered insignificant. This assumption is valid for most interferometric problems. Mathematically, in the refractionless limit, the optical pathlength difference is expressed as

$$\phi_i = \int_{S_i} [n(x,y,z) - n_o] \cdot dS_i \quad (3.1)$$

where

- $n(x,y,z)$  = the 3-D refractive index field,
- $n_o$  = the reference refractive index field considered homogeneous throughout,
- $S_i$  = the optical pathlength taken by ray  $i$ ,  $i=1, 2, \dots, m$ ,  $m$  being the total number of data points.

By taking planes  $z = \text{constant}$ , one at a time, this problem reduces to a series of two-dimensional ones to determine  $n(x,y)$  in each plane. The plane is divided into a series of pixels (picture elements), fig. 3.1. Within each pixel the refractive index may either be considered constant, or varying continuously fitting some polynomial function. In each pixel the

geometric ray paths  $dS_i$  can be evaluated.

A set of linear algebraic equations may be set up incorporating all the data points having the form:

$$[A] \cdot [n] = [\phi] \quad (3.2)$$

There are three sources of error making stable inversion of these equations by standard matrix inversion techniques extremely difficult:

- i) use of real experimental data which are invariably noisy,
- ii) approximation of a continuously varying 2-D function by a discrete number of pixels or n's.
- iii) lack of constraints in the equations on some of pixel n's as a result of a restricted range of viewing angles available from a holographic interferogram.

Thus the equations to be solved have the form:

$$[A_{ij}] \cdot [n_j] = [\phi_i] + [e_i] \quad (3.3)$$

where  $[A_{ij}]$  = the coefficient matrix,  
 $[n_j]$  = the solution or image vector,  
 $[\phi_i]$  = the error-free projection data vector,  
 $[e_i]$  = error vector to account for measurement and modelling errors, and  
 $j$  = pixel number.

Instability in the process of inversion caused by (iii) alone, where values of pixels are to be evaluated from an incomplete or restricted set of

projection data, can be overcome to an extent if the number of data points is greater than the number of pixels. This use of redundant data allows values of  $n$  to be determined much more accurately by averaging the over-determined set of data in the least squares sense so that each of the pixels approximately modelling the reconstructed field may have a sensible value of refractive index assigned to it. This however is not the complete answer. Walklate (1977) showed, using the sinc function\* from Sweeney's work, that, even with redundant data, instability still occurs when the number of pixels is increased from a 3x5 to a 5x5 resolution. This test was carried out using simulated data spread over an angle of  $45^\circ$ , and the inversion was performed following a procedure developed by Golub (1965). This is a back-substitution procedure, and is available from a computer package in the NAG library. However, its use in this field is rather limited because reconstructed values of temperatures could be negative which are known to be incorrect from a knowledge of the experimental condition but this procedure could not be constrained to produce only positive values,\*\* preferably at or above that of the environment around the test section.

For projection data over  $180^\circ$ , Crowther and Klug (1974) suggested the use of an extended field, which is larger than the field to be reconstructed, implying the use of a large A matrix to 'dump' artifacts\*\*\* caused by errors similar to those of type (i) and (ii) above. However this is unlikely to be successful with digitised projection data from double exposure holograms because of the restricted angles of view. The reconstruction would tend to be biased in the directions according to the viewing angles from which the projection data were collected.

The development of a reconstruction technique that would invert stably based on certain measuring criteria and give a sensible picture

\*  $\text{sinc}(x) = \sin(\pi x)/\pi x$ . \*\* If physically known artificial weights are introduced into the equations to prevent negative values occurring, the reconstruction would become unstable as shown by Walklate (1977).

\*\*\* These are random errors, and dumping implies the creation of buffer stores around the main reconstruction grid to reduce such errors within.

is thus seen as essential in solving eqn. (3.3) using noisy data of restricted viewing angle from experimental interferometric measurements.

### 3.2 CHOICE OF MATHEMATICAL MODELS

The reconstructed temperature field may be represented by a surface made up from one of two types of pixels. A uniformly flat surface element with a constant value of temperature assigned to it is the first type. The second type has a surface which may curve according to the temperature distribution. Plane by plane reconstruction using pixels enables eqn. (3.1) to be reduced to

$$\int_{-\infty}^{+\infty} f(x,y) \cdot dS = \phi(\theta, \rho) \quad (3.4)$$

where  $f(x,y) = n(x,y) - n_0$

$\rho = 1, 2, 3, \dots$  etc. the ray number from viewing angle of  $\theta$ .

It is mathematically convenient to express an approximate  $\bar{f}(x,y)$  to the true refractive index field  $f(x,y)$  as a sum over all pixel

$$\bar{f}(x,y) = \sum_{m=1}^M \sum_{n=1}^N f(m,n) \cdot H_{mn}(x,y) \quad (3.5)$$

where  $f(m,n)$  is a representation of the refractive index of the  $(m,n)^{\text{th}}$  pixel and  $H_{mn}$  is a suitable weighting function. The form taken by  $H$  is dependent on the description of the pixel. When  $f(x,y)$  in eqn. (3.4) is replaced by  $\bar{f}(x,y)$  for many of the pixels  $H$  will have the value zero.

Thus, if  $f(x,y) = \bar{f}(x,y)$ , a condition normally difficult to satisfy

due to the limited number of  $f(m,n)$ , then eqn. (3.4) becomes

$$\sum_{m=1}^M \sum_{n=1}^N \int_{-\infty}^{+\infty} f(m,n) \cdot H_{mn}(x,y) \, dS = \phi(\theta,\rho) \quad (3.6)$$

In setting up the system of linear equations a function is chosen for  $H_{mn}(x,y)$  which is integrable so that coefficients for matrix A in eqn. (3.2) or (3.3) may be evaluated.

### 3.2.1 THE GRID ELEMENT

Each pixel or element as shown in fig. 3.1 is considered to have a constant value of refractive index over it. In this case, the function

$H_{mn}(x,y)$  is

$$H_{mn}(x,y) = \text{rect} \left[ \frac{1}{\Delta x} (x - \Delta x \cdot m) \right] \cdot \text{rect} \left[ \frac{1}{\Delta y} (y - \Delta y \cdot n) \right]$$

where

$$\text{rect}(x) = \begin{cases} 1, & \text{if } |x| \leq \frac{1}{2} \\ 0, & \text{if } |x| > \frac{1}{2} \end{cases}$$

The fringe number integral, eqn. (3.6), now becomes

$$\sum_{m=1}^M \sum_{n=1}^N f(m,n) \left[ \int_{-\infty}^{+\infty} \text{rect} \left( \frac{x}{\Delta x} \right) \cdot \text{rect} \left( \frac{\alpha_j x' + \beta_{ij}}{\Delta y} \right) \cdot \sqrt{1 + \alpha_j^2} \, dx' \right] = \phi(\theta,\rho) \quad (3.7)$$

where  $\alpha_j = \tan \theta$  at  $j^{\text{th}}$  projection angle,  
 $x' = x - \Delta x \cdot m$ , and  $y' = y - \Delta y \cdot n$  are values of  $x$  and  $y$   
relative to the centre of the pixel under consideration,  
 $\beta =$  intercept, as shown in fig. 3.1.

The integral in square brackets gives the elemental pathlengths or coefficients of matrix A for a ray path at  $(\theta, \rho)$ , and thus eqn. (3.7)

becomes

$$\sum_{m=1}^M \sum_{n=1}^N A_{mn}(\theta, \rho) \cdot f(\Delta x.m, \Delta y.n) = \phi(\theta, \rho) \quad (3.8)$$

Evaluating geometrically gives the value of a coefficient as

$$A_{mn}(\theta, \rho) = \begin{cases} [1 + \tan^2 \theta]^{\frac{1}{2}} \cdot \Delta x, & \text{if } |\beta| \leq (\Delta y - \Delta x \cdot |\tan \theta|) / 2 \quad \& \quad |\tan \theta| \leq \Delta y / \Delta x \\ [1 + \tan^2 \theta]^{\frac{1}{2}} \cdot \Delta y / |\tan \theta|, & \text{if } |\beta| \leq (\Delta x |\tan \theta| - \Delta y) / 2 \quad \& \quad |\tan \theta| \geq \Delta y / \Delta x \\ [1 + \tan^2 \theta]^{\frac{1}{2}} \cdot [(\Delta x \cdot |\tan \theta| + \Delta y) / 2 - |\beta|] / |\tan \theta|, & \text{if } |\Delta y - \Delta x \cdot |\tan \theta|| / 2 < |\beta| \leq |\Delta y + \Delta x \cdot |\tan \theta|| / 2 \\ \Delta y, & \text{if } |\gamma| < \Delta x / 2 \quad \& \quad |\tan \theta| = \infty \\ 0, & \text{if } |\beta| > (\Delta x \cdot |\tan \theta| + \Delta y) / 2 \end{cases} \quad (3.8(a))$$

where

$$\begin{aligned} \beta &= \rho \cdot \sec(\theta) + (m-1) \cdot \Delta x \cdot \tan(\theta) - (n-1) \cdot \Delta y \\ \gamma &= \rho + \Delta x \cdot (m-1) \end{aligned} \quad (3.8(b))$$

Although a simple element, obtaining solutions by directly inverting the simultaneous linear equations thus formed even in the least squares sense by use of redundant projection data is a problem as discovered by researchers, Alwang, Cavanaugh, Burr and Hauer (1970), and Sweeney (1972). The reconstructions were found to be sensitive to grid size. However, the inversion of eqn. (3.8) is more likely to be successful with an iterative procedure because coefficients of matrix A are not directly used in inverting for the refractive index field and reconstructions are obtained by gradually building up the reconstructed field iteratively using a small value relaxation

parameter and a temperature field measuring criteria without having to satisfy the projection equations exactly. As iterative techniques can adopt relaxation parameters it is therefore possible to obtain good solutions even when the projection data is noisy or inconsistent.

### 3.2.2 THE FINITE ELEMENT

A closer match between the reconstructed and actual temperature field, particularly at the pixel edges surrounded by adjacent pixels where these edges should be nicely blended to one another, can be achieved by finite element methods. The principle objective of adopting such a method is to reduce the modelling errors in setting up the system of simultaneous equations by specifying elements which have smoothly varying surfaces for a smoother reconstructed picture. A square element has been chosen for the pixel as trial reconstructions using a rectangular element proved less satisfactory. With a square element the extreme lengths in the x and y directions on the element surface are similar, and so the surface of the refractive index field can be described by a given polynomial with greater precision.

The change of refractive index within each element is described by a second degree polynomial

$$\Delta n(x,y) = a + bx + cy + dxy + ex^2 + fy^2 + gxy^2 + hx^2y \quad (3.9)$$

where x and y can be conveniently taken from the centre of a square pixel as shown in fig. 3.2. The form of this polynomial was suggested by Walklate (1980). The use of a higher degree polynomial would require much more computer core storage and time. The coefficient a, b, c,.... h are expressed in terms of nodal points on the boundaries or edges of the

element. In terms of these coefficients, the refractive index changes at the nodal points are as follows:

Location	$\Delta n(x,y)$ at node	a	bx	cy	dxy	$ex^2$	$fy^2$	$gxy^2$	$hx^2y$	eqn. number
$x=-\frac{1}{2}, y=-\frac{1}{2}$	$\Delta n(m-\frac{1}{2}, n-\frac{1}{2})$	a	$-b/2$	$-c/2$	$d/4$	$e/4$	$f/4$	$-g/8$	$-h/8$	(3.10)
$x=-\frac{1}{2}, y=0$	$\Delta n(m-\frac{1}{2}, n)$	a	$-b/2$	0	0	$e/4$	0	0	0	(3.11)
$x=-\frac{1}{2}, y=\frac{1}{2}$	$\Delta n(m-\frac{1}{2}, n+\frac{1}{2})$	a	$-b/2$	$c/2$	$-d/4$	$e/4$	$f/4$	$-g/8$	$h/8$	(3.12)
$x=0, y=-\frac{1}{2}$	$\Delta n(m, n-\frac{1}{2})$	a	0	$-c/2$	0	0	$f/4$	0	0	(3.13)
$x=0, y=\frac{1}{2}$	$\Delta n(m, n+\frac{1}{2})$	a	0	$c/2$	0	0	$f/4$	0	0	(3.14)
$x=\frac{1}{2}, y=-\frac{1}{2}$	$\Delta n(m+\frac{1}{2}, n-\frac{1}{2})$	a	$b/2$	$-c/2$	$-d/4$	$e/4$	$f/4$	$g/8$	$-h/8$	(3.15)
$x=\frac{1}{2}, y=0$	$\Delta n(m+\frac{1}{2}, n)$	a	$b/2$	0	0	$e/4$	0	0	0	(3.16)
$x=\frac{1}{2}, y=\frac{1}{2}$	$\Delta n(m+\frac{1}{2}, n+\frac{1}{2})$	a	$b/2$	$c/2$	$d/4$	$e/4$	$f/4$	$g/8$	$h/8$	(3.17)

For simplicity, let  $\Delta n(m-\frac{1}{2}, n-\frac{1}{2})$  in eqn. (3.10) be  $n_1$ ,  $\Delta n(m-\frac{1}{2}, n)$  in eqn. (3.11) be  $n_2$ , etc. Solving eqns. (3.10) to (3.17) to obtain a to h:

$$c = n_5 - n_4$$

$$b = n_7 - n_2$$

$$2 \cdot b + g/2 = -n_1 - n_3 + n_6 + n_8$$

$$2 \cdot b = 2n_7 - 2n_2$$

$$\therefore g = -2n_1 + 4n_2 - 2n_3 + 2n_6 - 4n_7 + 2n_8$$

$$-d/2 + f/2 = (n_3 - n_2) + (n_6 - n_7)$$

$$d/2 + f/2 = (n_1 - n_2) + (n_8 - n_7)$$

$$\therefore f = n_1 - 2n_2 + n_3 + n_6 - 2n_7 + n_8$$

and so on.

In matrix form, the coefficients are as follows:

$$\begin{vmatrix} -\frac{1}{4} & \frac{1}{2} & -\frac{1}{4} & \frac{1}{2} & \frac{1}{2} & -\frac{1}{4} & \frac{1}{2} & -\frac{1}{4} \\ 0 & -1 & 0 & 0 & 0 & 0 & 1 & 0 \\ 0 & 0 & 0 & -1 & 1 & 0 & 0 & 0 \\ 1 & 0 & -1 & 0 & 0 & -1 & 0 & 1 \\ 1 & 0 & 1 & -2 & -2 & 1 & 0 & 1 \\ 1 & -2 & 1 & 0 & 0 & 1 & -2 & 1 \\ -2 & 4 & -2 & 0 & 0 & 2 & -4 & 2 \\ -2 & 0 & 2 & 4 & -4 & -2 & 0 & 2 \end{vmatrix} \begin{vmatrix} n_1 \\ n_2 \\ n_3 \\ n_4 \\ n_5 \\ n_6 \\ n_7 \\ n_8 \end{vmatrix} = \begin{vmatrix} a \\ b \\ c \\ d \\ e \\ f \\ g \\ h \end{vmatrix} \quad (3.18)$$

Thus, for  $\theta \leq 45^\circ$  and replacing  $y$  by  $(\beta + x \cdot \tan \theta)$ , eqn.(3.4) becomes

$$\phi(\theta, \rho) = \sum_{m=1}^M \sum_{n=1}^N (1 + \tan \theta)^{\frac{1}{2}} \int_{-\frac{1}{2}}^{\frac{1}{2}} [a + bx + c(\beta + x \cdot \tan \theta) + d(\beta x + x^2 \cdot \tan \theta) + ex^2 + f(\beta + x \cdot \tan \theta)^2 + gx(\beta + x \cdot \tan \theta)^2 + hx^2(\beta + x \cdot \tan \theta)] dx \quad \dots\dots (3.19)$$

$$= \sum_{m=1}^M \sum_{n=1}^N (1 + \tan \theta)^{\frac{1}{2}} \left[ ax + \frac{bx^2}{2} + c(\beta x + \frac{x^2}{2} \cdot \tan \theta) + d(\beta \frac{x^2}{2} + \frac{x^3}{3} \tan \theta) + \frac{ex^3}{3} + f(\beta^2 x + \frac{x^3}{3} \tan^2 \theta + \beta x^2 \tan \theta) + g(\beta^2 \frac{x^2}{2} + \frac{x^4}{4} \tan^2 \theta + 2\beta x^3 \tan \theta) + h(\beta \frac{x^3}{3} + \frac{x^4}{4} \cdot \tan \theta) \right]_{x=-\frac{1}{2}}^{x=\frac{1}{2}}$$

Similar forms of expressions are derived for the case  $45^\circ < \theta < 90^\circ$  with  $x$  replaced by

$$x = \left( \frac{y - \beta}{\tan \theta} \right) \quad (3.20)$$

and measured from the centre of the element, and where  $y = y/\Delta y$ ,  $\Delta y$  being taken as unity for the square element.

The contribution by each element to the value of optical pathlength difference  $\phi_i$  for the ray  $i$  can thus be evaluated as follows:

Condition 1

$$(1 + \tan^2\theta)^{\frac{1}{2}} \cdot \left[ a + c\beta + d \cdot \frac{\tan\theta}{12} + \frac{e}{12} + f(\beta^2 + \frac{\tan^2\theta}{12}) + g(\beta \cdot \frac{\tan\theta}{6}) + h \cdot \frac{\beta}{12} \right]$$

if  $0^\circ \leq \theta \leq 45^\circ$ , and ray passes through opposite sides (3.21)

Condition 2

$$(1 + \frac{1}{\tan^2\theta})^{\frac{1}{2}} \cdot \left[ a + b(\frac{-\beta}{\tan\theta}) + \frac{d}{12 \cdot \tan\theta} + \frac{e}{\tan^2\theta} \frac{(1 + \beta^2)}{12} + \frac{f}{12} + g(\frac{-\beta}{12 \cdot \tan\theta}) + h(\frac{\beta}{6 \cdot \tan^2\theta}) \right]$$

if  $45^\circ < \theta < 90^\circ$ , and ray passes through opposite sides (3.22)

Condition 3

$$\left[ a + b\gamma + e\gamma^2 + \frac{f}{12} + g\gamma \right], \quad \text{if } \theta = 90^\circ \quad (3.23)$$

Condition 4

$$(1 + \tan^2\theta)^{\frac{1}{2}} \cdot \left[ ax + \frac{bx^2}{2} + c(\beta x + \frac{x^2}{2} \cdot \tan\theta) + d(\beta \cdot \frac{x^2}{2} + \frac{x^3}{3} \cdot \tan\theta) + e \cdot \frac{x^3}{3} + \right. \\ \left. f(\beta^2 \cdot x + \frac{x^3}{3} \cdot \tan^2\theta + \beta \cdot x^2 \cdot \tan\theta) + g(\beta \frac{x^2}{2} + \frac{x^4}{4} \cdot \tan^2\theta + \frac{2\beta x^3}{3} \cdot \tan\theta) + \right. \\ \left. h(\frac{\beta x^3}{3} + \frac{x^4}{4} \cdot \tan\theta) \right]_{r_1}^{r_2}, \quad (3.24)$$

if ray passes through adjacent sides of element, where

$$\left. \begin{array}{l} r_2 = (-\frac{1}{2} + s \cdot \cos\theta) \\ r_1 = -\frac{1}{2} \end{array} \right\} \quad \text{if } \beta > 0 \ \& \ \theta > 0^\circ, \text{ or } \beta < 0 \ \& \ \theta < 0^\circ \quad (3.25)$$

$$\left. \begin{array}{l} r_2 = \frac{1}{2} \\ r_1 = (\frac{1}{2} - s \cdot \cos\theta) \end{array} \right\} \quad \text{if } \beta < 0 \ \& \ \theta > 0^\circ, \text{ or } \beta > 0 \ \& \ \theta < 0^\circ$$

and  $s$  = physical pathlength through element.

For the single element, the coefficients may be put in a matrix A' in which each row represents a ray:

$$\begin{array}{c|c|c|c}
 \begin{array}{cccc}
 a'_{11} & a'_{12} & \dots & a'_{18} \\
 a'_{21} & a'_{22} & \dots & a'_{28} \\
 \vdots & & & \\
 \vdots & & & \\
 a'_{\theta\rho,1} & & & a'_{\theta\rho,8}
 \end{array} & & \begin{array}{c} a \\ b \\ c \\ d \\ e \\ f \\ g \\ h \end{array} & = & \begin{array}{c} \phi_{11} \\ \phi_{12} \\ \phi_{13} \\ \vdots \\ \phi_{21} \\ \phi_{22} \\ \vdots \\ \phi_{\theta\rho} \end{array} \\
 \end{array} \quad (3.26)$$

or in symbolic form,

$$[A'] [z] = [\phi_i] \quad (3.27)$$

A system of equations with the refractive index field may now be obtained by substituting the l.h.s. of eqn.(3.18) for the vector [z]:

$$\begin{array}{c|c|c|c|c|c}
 \begin{array}{ccc}
 a'_{11} & \dots & a'_{18} \\
 \vdots & & \\
 \vdots & & \\
 a'_{\theta\rho,1} & \dots & a'_{\theta\rho,8}
 \end{array} & & \begin{array}{cccccccc}
 -\frac{1}{4} & \frac{1}{2} & -\frac{1}{4} & \frac{1}{2} & \frac{1}{2} & -\frac{1}{4} & \frac{1}{2} & -\frac{1}{4} \\
 0 & -1 & 0 & 0 & 0 & 0 & 1 & 0 \\
 0 & 0 & 0 & -1 & 1 & 0 & 0 & 0 \\
 1 & 0 & -1 & 0 & 0 & -1 & 0 & 1 \\
 1 & 0 & 1 & -2 & -2 & 1 & 0 & 1 \\
 1 & -2 & 1 & 0 & 0 & 1 & -2 & 1 \\
 -2 & 4 & -2 & 0 & 0 & 2 & -4 & 2 \\
 -2 & 0 & 2 & 4 & -4 & -2 & 0 & 2
 \end{array} & & \begin{array}{c} n_1 \\ n_2 \\ n_3 \\ n_4 \\ n_5 \\ n_6 \\ n_7 \\ n_8 \end{array} & = & \begin{array}{c} \phi_{11} \\ \phi_{12} \\ \phi_{13} \\ \vdots \\ \phi_{21} \\ \phi_{22} \\ \vdots \\ \phi_{\theta\rho} \end{array} \\
 \end{array} \quad (3.28)$$

To model the temperature field adequately, a collection of such

elements is required and as such the matrices  $[A']$  and that on the l.h.s. of eqn.(3.18) need to be expanded considerably to include all the elemental coefficients, but neighbouring elements share some of the nodal points, as shown in fig. 3.3, the number of columns in the coefficient matrix on the l.h.s. of eqn.(3.18) can be reduced. Modelling with 4 x 4 elements, square and rectangular, each giving 65 nodal values, and with 6 x 3 square elements has been carried out using the University's Cyber 73 computer. It is apparent that much more calculations and core storage are required to set up the weighting projection matrix  $[A]$ , from the two matrices on the l.h.s. of eqn.(3.28), using this type of element than with the Grid element because of the greater number of terms required to define each element.

### 3.3 CHOICE OF INVERSION TECHNIQUES

Attention is given to the principles of only those few techniques likely to be capable of reconstructing properly from the set of simultaneous linear projection equations which have in them the three types of errors mentioned in section 3.1. They are found to be iterative in nature. As the ability to reconstruct the temperature field is the prime consideration the cost effectiveness of these techniques is regarded as a secondary factor; less emphasis is being placed on the actual processing time as space saving matrices are being developed with these techniques to store only those elements of matrices with non-zero coefficients to overcome core storage problems.

Other techniques exist for inverting simultaneous equations. The direct methods of solution by whatever criteria used can be ruled out as they invariably use a form of back-substitution which tends to produce instability from relatively high noise levels buried in data with small values of fringe number. Also it would not be worthwhile to consider any further Operational Research algorithms, in particular Simplex methods. Trial runs on Simplex methods have shown that the projection equations

were too inconsistent and thus produced meaningless answers. In the Simplex methods, the grid element model was chosen to represent the reconstructed field with digitised projection data supplied by holographic interferograms from the heated copper block experiment.

### 3.3.1 ART (ALGORITHM RECONSTRUCTION TECHNIQUE) 1970 (1937)

This technique was first proposed by Kaczmarz (1937). It was rediscovered by Gordon, Bender and Herman (1970) for the reconstruction of three-dimensional density fields and was called ART. The formula to be used is

$$n_j^{k+1} = n_j^k + \lambda \cdot \left[ \frac{\phi(\theta, \rho) - \phi^k(\theta, \rho)}{\ell(\theta, \rho)} \right] \quad (3.29)$$

where

$n_j$  represents the value of refractive index for the pixel number  $j$  in the  $M \times N$  field where  $j = 1, \dots, (M \times N)$

$k$  the previous iteration cycle number,

$n^{k+1}$  the new value of refractive index,

$\phi(\theta, \rho) - \phi^k(\theta, \rho)$  the residual between the original optical pathlength difference and the last iterated pathlength difference for a single ray at  $(\theta, \rho)$ ,

$\ell(\theta, \rho)$  the physical pathlength of the ray at  $(\theta, \rho)$  within the reconstructing field,

$\lambda$  a relaxation parameter.

All  $n_j$ 's can be initialised as zero. During each iteration each projection angle  $\theta$  is considered, and each ray that intersects pixels  $j$ ,  $j = 1, \dots, (M \times N)$ , within the reconstructing field is used to change those

values of refractive indices on the pixels according to eqn.(3.29). Each one of the rays from each projection angle is thus systematically worked through. This is the form of ART that will be applied to reconstructing the refractive index field. The accuracy of reconstruction should improve, according to Herman, Lent and Rowland (1973), by feeding in projection data sampled at regular intervals according to the sampling width:

$$w_{\theta} = \begin{cases} \Delta y \cdot |\cos\theta|, & \text{if } 0 \leq |\theta| \leq \pi/4 \\ \Delta x \cdot |\sin\theta|, & \text{if } \pi/4 < |\theta| \leq \pi/2, \end{cases} \quad (3.30)$$

because now each value of  $\phi(\theta, \rho)$  approximately changes an equal number of pixels as shown in fig. 3.4. For the square element,  $\Delta y$  can be interchanged with  $\Delta x$  in eqn.(3.30). Each pixel  $n_j$  is changed when its centre lies within the ray width  $w_{\theta}$ . The ray of each  $\phi(\theta, \rho)$  is taken to lie in the middle.

The relaxation parameter  $\lambda$  may either be a constant, or a variable fraction with iteration number - the best value of  $\lambda$  to be taken will be discussed in Chapter 4.

Herman, Lent and Rowland (1973) suggested that the iteration process ought to be stopped when the variance

$$v(k) = \frac{1}{(M \times N)} \sum_{j=1}^{(M \times N)} (n_j^k - \bar{n})^2 \quad (3.31)$$

changes by less than 1% in the next iteration:

$$|v(k+1) - v(k)| < \frac{1}{100} v(k) . \quad (3.32)$$

An alternative approach by Herman (1975) was to give a tolerance  $\pm \epsilon(\theta, \rho)$  to each  $\phi(\theta, \rho)$  such that the process of iteration is automatically stopped when all the tolerances are satisfied. In effect,  $\lambda$  is set to unity in all iterations except when either the magnitude of a residual is within

$2.\varepsilon(\theta,\rho)$ , when  $\lambda$  is made smaller, and then even smaller at the higher iteration numbers  $k$ , or when a residual is within  $\pm\varepsilon(\theta,\rho)$ , when  $\lambda$  is set to zero.

The accuracy of the reconstructed field, in particular local values on pixels, using such general measures is rather unsatisfactory because it is insensitive to artifacts on the reconstruction, even though an overall view of the reconstruction might just appear to be sensible qualitatively. The author used a different criteria for terminating the iteration. This method will be described in Chapter 4.

Also in the iteration with this technique, all  $n_j$ 's are chosen to be constrained such that the reconstructed temperature field produces no temperatures less than that at the ambient - known to be the minimum.

### 3.3.2 SIRT (SIMULTANEOUS ITERATIVE RECONSTRUCTION TECHNIQUE) 1972

In ART  $n_j$  changes whenever there is a single ray of  $\phi(\theta,\rho)$  or  $P$  which passes through a point corresponding to the centre of pixel  $j$ ,  $j = 1, (M \times N)$ . In the technique of SIRT proposed by P. Gilbert (1972) the refractive index  $n_j$  of a point on the reconstruction grid is changed using simultaneously all the data  $\phi(\theta,\rho)$  from projections which pass through a pixel. In symbolic form

$$n_j^{k+1} = \left[ n_j^k + \frac{\sum P_{\theta\rho}}{\sum L_{\theta\rho}} - \frac{\sum R_{\theta\rho}^k}{\sum N_{\theta\rho}} \right] \quad (3.33)$$

where  $\sum P_{\theta\rho}$  is a summation of all the true projected densities to which pixel  $j$  contributes or which have passed through pixel  $j$ ,  $j = 1, (M \times N)$ .  $L_{\theta\rho}$  is the pathlength of a ray at  $(\theta,\rho)$  within the reconstructing field.

$\sum R_{\theta\rho}^k$  is a summation of all the reconstructed projected densities which have a contribution from pixel  $j$ , from the reconstructed field after  $k$  cycles of iteration. The addition of all those  $\rho_j$ 's with their pixel centres lying within the ray of a predetermined width, mid-distance between adjacent rays similar to  $w_\theta$  in the previous section, or see Gilbert (1972), gives a value of the reconstructed projected density.

$N_{\theta\rho}$  is the number of pixel centres within a ray at  $(\theta, \rho)$

Projected density and density at a point  $\rho_j$  are analogous to fringe number and  $n_j$  respectively in the context of holographic interferometry. In handling true projected data  $P_{\theta\rho}$  as against pseudo projection data  $R_{\theta\rho}$ , generated artificially by summing up values at pixel centres only for each projection data point, Gilbert showed that using a model structure with five circular regions, SIRT produces better reconstructions than ART. Some of the results of Gilbert are shown in fig. 3.5 and 3.6. The measure of closeness to the original picture is

$$\delta = \left[ \frac{\sum (\rho_j - \rho_j^k)^2}{\sum (\rho_j - \bar{\rho}_j)^2} \right]^{\frac{1}{2}} \quad (3.34)$$

where

$\rho_j$  = density of the original at point  $j$ ,

$\rho_j^k$  = density of the reconstructing picture at the same point,

$\bar{\rho}_j$  = average density of the original.

Fig. 3.5 shows that with presumably a full  $180^\circ$  range of viewing angles SIRT produces a reconstruction that matches the original better than ART. and also that although SIRT does begin to diverge in reconstructing after approximately ten iteration it does so much more slowly than ART. It is this ability of using projection data simultaneously to find a good average value to change the value on a particular pixel that enables SIRT to handle

noisy projection data more effectively. However, the cost and storage requirement for SIRT reconstructions go up by a factor of two or more.

A version similar in principle to SIRT was adopted by the author in reconstructing the refractive index field:-

$$n_j^{k+1} = \left[ n_j^k + \lambda \cdot \left( \frac{\sum [\phi(\theta, \rho) - \phi^k(\theta, \rho)]}{\sum L_{\theta\rho}} \right) \right] \quad (3.35)$$

where

$\phi(\theta, \rho)$  = the optical pathlength difference in metres,

$\lambda$  = a relaxation parameter.

A value of  $\lambda = 0.33$  or less was found to reconstruct better with digitised projection data than with  $\lambda = 1.00$ .

No criteria was suggested by Gilbert for stopping the iteration even though on continued iteration, with the residuals from the projection data getting smaller, the reconstruction does get worse. Based on experience from the reconstructed model by Gilbert (1972) and the author 10 - 15 iterations should be sufficient.

For similar pictorial resolutions and error free data sets used to reconstruct the five circular disc model as shown in fig. 3.6(a), the SIRT algorithm produced smoother reconstructions, figs. 3.6(b) & 3.6(d). This is mainly because in each iteration cycle of SIRT the density value of each pixel on the reconstruction grid was changed once only, one by one, and each one by an average amount calculated using all the line integrals i.e. projection data intersecting that pixel. With ART reconstructions, as in figs. 3.6(c) & 3.6(e), in each iteration cycle each pixel changes its value several times, and each time by an amount calculated from a single line integral

point intersecting that pixel without considering any other projection data points that might also be intersecting that pixel. Because of this greater frequency of changes and with such changes being performed without the averaging affect from all the projection data as in SIRT, the ART algorithm needs to have good digitised projection data together with a much more closely matched mathematical model for reconstruction, otherwise random errors or artifacts would appear on the reconstruction grids. These errors, as noted from reconstructions made by the author, invariably grow worse rather than disappear with further iteration using this technique. Such effects may also be implied by the performance curves,  $\delta$  vs iteration number, as shown in fig. 3.5.

### 3.3.3 LSRT (LEAST SQUARES OF RESIDUALS TECHNIQUE) 1980

This is a technique developed by the author to reduce the cause of instability characterised by the appearance of random errors or artifacts on the surface of the reconstructed temperature field. Instability is a problem arising from the use of a set of simultaneous projection equations which are inconsistent with one another due to (i) measurement errors, and (ii) the approximating mathematical model representing the surface of the temperature field. As well as instability there is the problem of directional bias in the reconstruction. This is due to inversion from an incomplete set of projection data obtained from only a limited range of viewing angles. This technique can reduced this effect by introducing a small predetermined value of refractive index change to each pixel on the reconstruction grid during each cycle of iteration in the reconstruction process. Such a value can either be accepted or rejected in the inversion process by a criterion.

The reason for using the LSRT procedure is because ART and SIRT have

Following pages: 50, 50A, and then 51.

no measuring criterion on the reconstruction grid as such that determines whether or not a value of  $n_j$  is already being unduly biased. This is because each data projection point is an integrated value of several pixels within the temperature field which may have several peak values of temperature, and in reconstructing with projection data from a limited viewing angle range these peaks may not show up well in their proper places and hence the bias in values on certain pixels. In the process of reconstruction the projection equations are also degraded by measurement and modelling errors and the task of inverting the digitised projection data to produce a sensible or the true reconstruction thus becomes very difficult.

So rather than to use the digitised data to determine the refractive index at any point on the reconstruction grid directly, LSRT generates a small fractional value of refractive index,  $\Delta n$ , in each cycle of iteration.  $\Delta n$  is applied onto each of the pixels on the reconstruction grid, and its value becomes smaller as the number of cycles of iteration increases. Also,  $\Delta n$  is weighted according to its location on the reconstruction grid to become  $\Delta n_j$ ,  $j = 1, (M \times N)$  where  $j$  is the pixel number. Though weighting is not absolutely essential it has been found to produce better reconstructions. In the beginning all pixels are initialised with zero values. Now on adding  $\Delta n_j$  to a pixel the temporarily modified or changed value of  $n_j$  is compared with all the projection data intersecting that pixel using the sum of residuals as a measuring criteria in the least squares sense. If this sum is larger than with the unmodified value of  $n_j$  then that modified value of  $n_j$  is rejected, and the technique is then reset to consider the next pixel in a similar way until all the  $\Delta n_j$ 's are applied. The same adding process is then repeated but this time with all the values of  $\Delta n_j$  made negative. When this has been completed one complete cycle of iteration is performed. This algorithm will therefore be more stable in reconstructing than with either ART or SIRT.

This technique is included in the program listing in Appendix 1 which also contains a subroutine called KAISYM also developed by the author to produce a set of conservative weight factors,  $0.15 \leq C_j \leq 1.25$ , for the entire reconstructing grid, based on producing values of  $n_j$  such that when computed projection data were obtained they would not over-estimate any of the input digitised projection data. This is to ensure that the digitised data are not used to their full extent to reduce the possibility of producing any misleadingly over-optimistic or peaky factors, especially when experimental digitised data are used because they contain a level of noise which causes serious errors to occur and interferes with the subsequent iterative process of reconstruction. Such interference must be minimised with experimental digitised data for such data could by itself produce artifacts or random errors on the pixels of the reconstructed field easily. It has been found that invariably these artifacts would not subside but grow worse as iteration continues. The  $C_j$  values were evaluated with the digitised input data being sampled at regular intervals according to eqn.(3.20). To reduce the possibility of direction bias KAISYM was allowed to iterate not more than once in obtaining the values of  $C_j$ . Basically all projection data intersecting a particular pixel is considered and whichever one that has the lowest value of average change of refractive index,  $[\phi(\theta,\rho)/L(\theta,\rho)]$ , is taken for that pixel. Without calculating for any residuals a whole series of such values can thus be obtained. Dividing these values by the maximum on the grid gives the  $C_j$  factors. In trial tests it was found that a maximum weight factor of 1.25 is better than 1.0, and so all  $C_j$  values were multiplied by 1.25, and also the minimum is taken to be 0.15 for those  $C_j$  factors less than 0.15.

A small fractional value of refractive index,  $D^k$ , can now be generated. This is a fraction of the average change of refractive index defined as

$$\bar{n} = \frac{\sum \phi(\theta,\rho)}{\sum L(\theta,\rho)} \quad (3.36)$$

$D^k$  is also made to be dependent on the number of iterations  $k$  as trial tests showed better reconstruction when  $D^k$  is under-relaxed as follows:-

$$\begin{aligned}
 D^k &= \bar{n}/3.0 && \text{for } k=1, \quad 30 \\
 D^k &= \bar{n}/9.0 && \text{for } k=31, \quad 50 \\
 D^k &= \bar{n}/25.0 && \text{for } k=51, \quad 80 \\
 D^k &= \bar{n}/40.0 && \text{for } k=81, \quad 110 \\
 D^k &= \bar{n}/60.0 && \text{for } k=111, \quad 140 \\
 D^k &= \bar{n}/80.0 && \text{for } k=141, \quad 200.
 \end{aligned} \tag{3.37}$$

These variable relaxation parameters are obtained by a process of trial and error on applying the method to practical data\*.

Therefore, the quantity to add is

$$(\text{Sign} \cdot D^k \cdot C_j) \tag{3.38}$$

where  $\text{Sign} = \begin{cases} +1 & \text{when } k = \text{an odd number} \\ -1 & \text{when } k = \text{an even number} \end{cases}$

A full cycle of iteration for LSRT involves two rounds of iteration in which  $k$  changes from an odd to an even number. So the number of full cycles of iteration is strictly  $k/2$ . In each iteration pixels are considered one by one from  $j = 1$  to  $(M \times N)$  to determine whether the quantity to be added is needed based on the sum of the squares of each residual. The procedure is as follows:

$$\text{Determine } n_j^{k+1} = n_j^k + \lambda \cdot [\text{Sign} \cdot D^k \cdot C_j] \tag{3.39}$$

where  $\lambda=1$  initially, and if:-

$$\Sigma [\phi(\theta, \rho) - \phi(\theta, \rho)^{k+1}]^2 < \Sigma [\phi(\theta, \rho) - \phi(\theta, \rho)^k]^2 \quad \text{then take}$$

\* It is however possible that, in general, the denominator 3.0 in eqn.(3.37) may need to be increased to a slightly bigger value, to say 5.0, depending on the geometry and complexity of the test field. If this is the case denominator 9.0 may also need to be increased slightly, to say 11, Such alterations would merely result in a slower rate of convergence.

$$n^{k+1} = n^{k+1}, (\lambda=1),$$

$\Sigma[\phi(\theta,\rho) - \phi(\theta,\rho)^{k+1}]^2 \geq \Sigma[\phi(\theta,\rho) - \phi(\theta,\rho)^k]^2$  then take the old value

$$n^{k+1} = n^k, (\lambda=0).$$

Using the grid element pixel as the mathematical model this technique has been able to produce stable reconstructions even with the interferometric data from the second laboratory experiment in which the natural convection current from a heater located in a number of positions on the floor of the constant temperature enclosure sets up a 3-D temperature distribution. Chapter 6 gives these results. A graph of the sum of squares of residuals against iteration number  $k$  will show that the slope gets very small after a while at which point iteration should be terminated, see fig. 4.8, but in this project LSRT is allowed to run for  $k$  up to 200, or 100 complete cycles of iteration for testing purpose.

### 3.4 NUMERICAL PROCESSING

A listing of the LSRT algorithm appears in Appendix 1. This listing, the main computer program used in this project, also includes the ART algorithm which has produced some acceptable reconstruction results for the heated copper block experiment in Chapter 4. It also contains several subroutines for evaluating weight coefficients from either the GRID or Finite Element mathematical model. In the trial tests, codes had been written with the ability to reconstruct using a number of resolutions. In the present form it is set to reconstruct with a 9 x 5 Grid Element resolution using the LSRT technique.

Because of the large memory space required by these numerical

techniques the program in Appendix 1 contains two large matrices which are developed in a form to store non-zero elemental coefficients only to overcome the memory overflow problem on the University Cyber 73 computer.

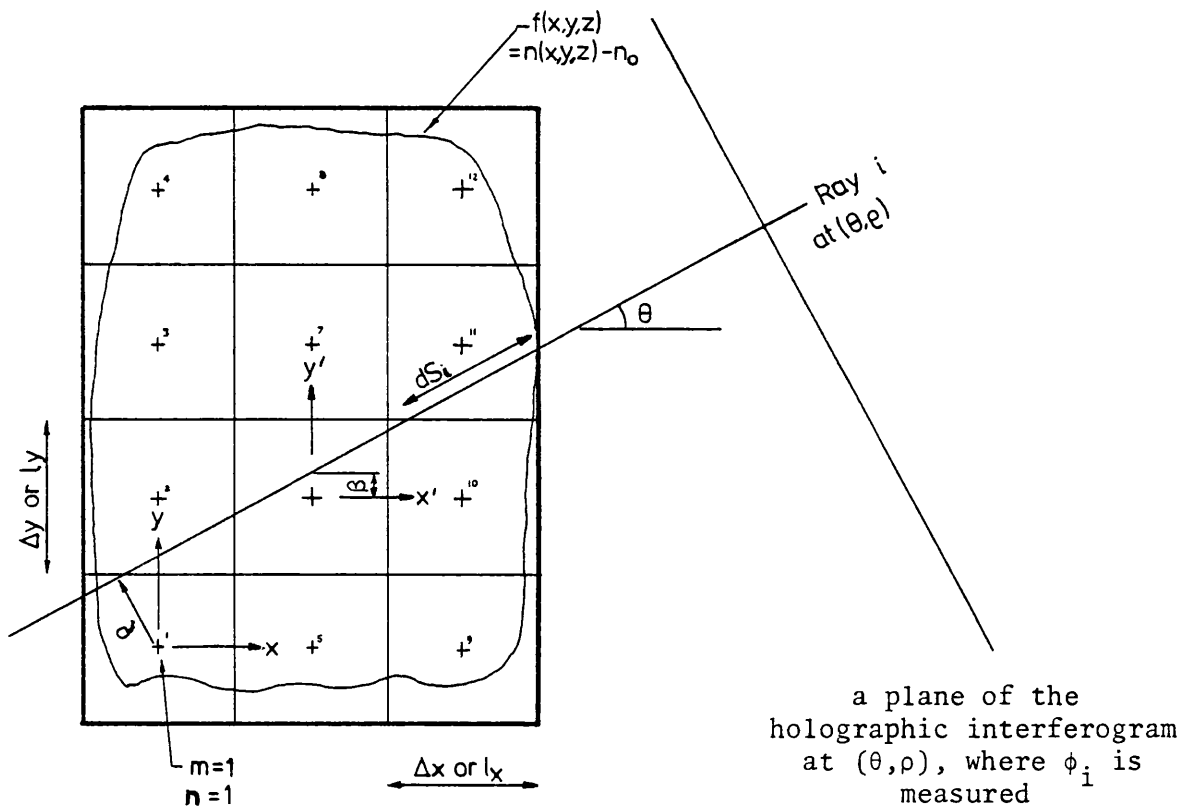


FIG. 3.1 NOTATION ON THE GRID ELEMENT MODEL

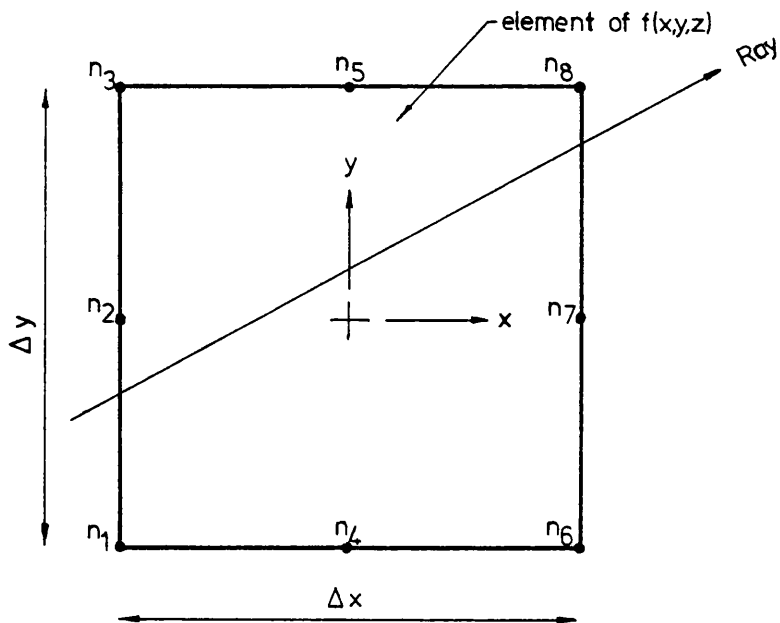


FIG. 3.2 THE FINITE ELEMENT

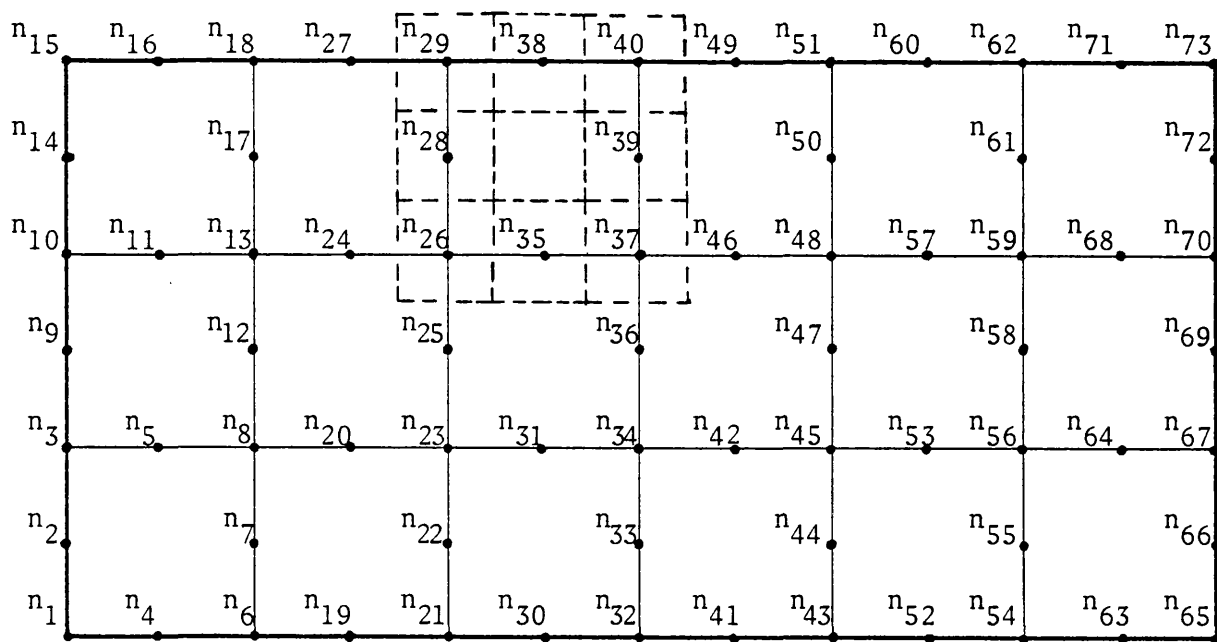


FIG. 3.3 A 6x3 FINITE ELEMENT MODEL

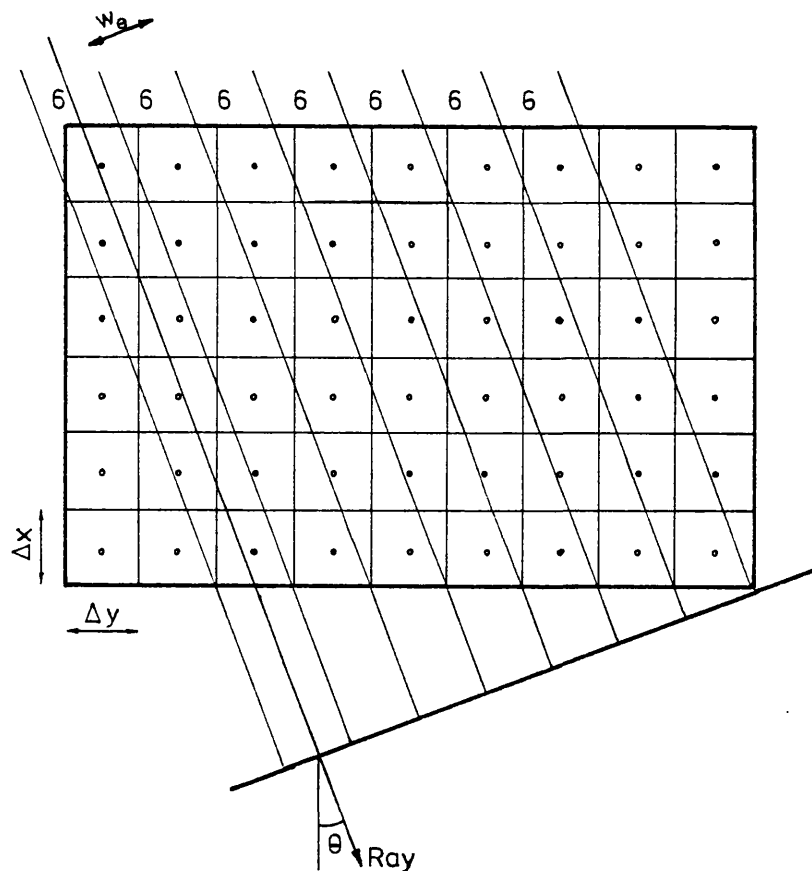


FIG. 3.4 CORRECTED RAY WIDTHS ACCORDING TO  $\Delta y \cdot \cos \theta$ , EACH CONTAINING AN EQUAL NUMBER OF PIXEL CENTRES

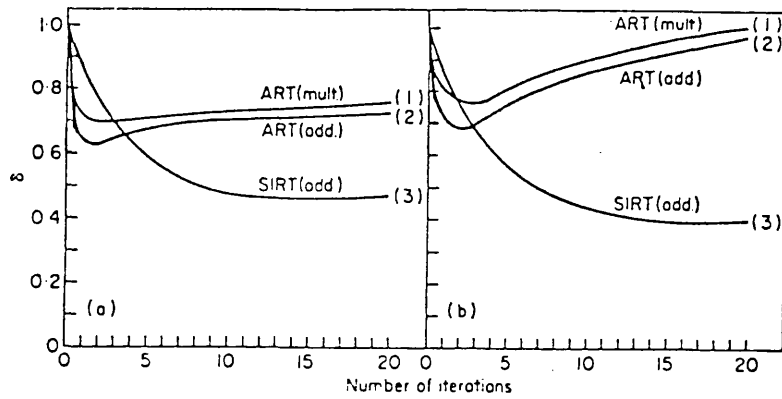
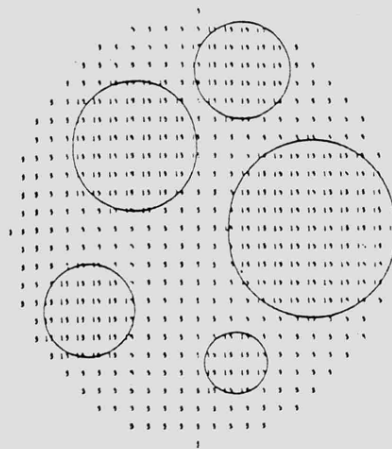
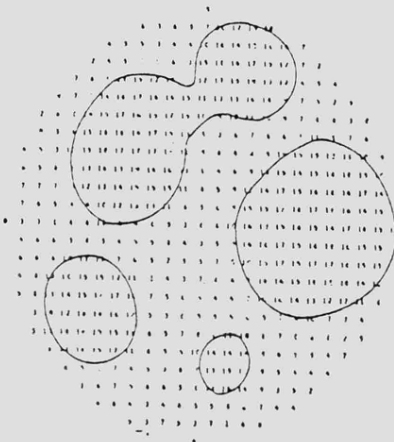


FIG. 3.5 (a) PERFORMANCE OF ART AND SIRT, CURVES (2) & (3), IN RECONSTRUCTING THE OBJECT SHOWN IN FIG. 3.6(a), USING 10 EQUALLY-SPACED PROJECTIONS

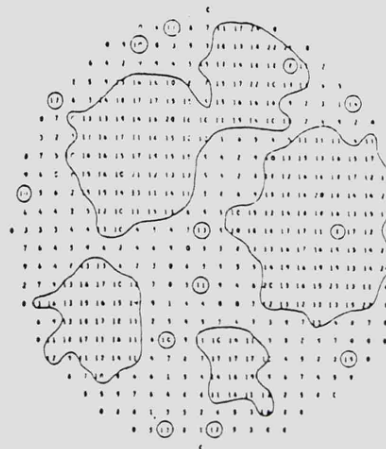
(b) AS FOR (a) EXCEPT RECONSTRUCTING USING 25 EQUALLY-SPACED PROJECTIONS



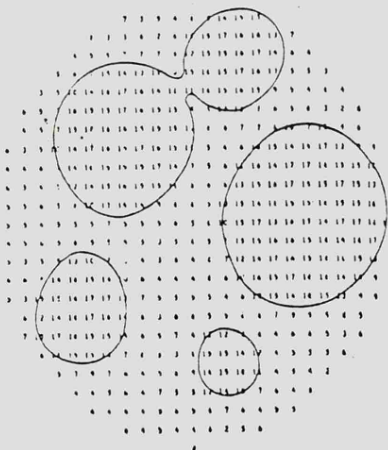
(a)



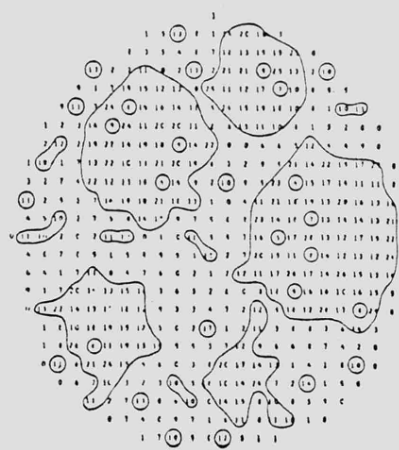
(b)



(d)



(c)



(e)

FIG. 3.6

- (a) THE MODEL OBJECT USED FOR THE RECONSTRUCTION, WITH DENSITY VALUES SHOWN AND CONTOURED AT THE DENSITY LEVEL OF 10, WHICH IS INTERMEDIATE BETWEEN THE BACKGROUND DENSITY AND THE CIRCULAR REGIONS OF HIGH DENSITY
- (b) & (c) A RECONSTRUCTION OF (a) USING 20 CYCLES OF SIRT WITH 10 EQUALLY-SPACED PROJECTIONS AND 25 EQUALLY-SPACED PROJECTIONS RESPECTIVELY
- (d) & (e) A RECONSTRUCTION OF (a) USING 20 CYCLES OF ART WITH 10 EQUALLY-SPACED PROJECTIONS AND 25 EQUALLY-SPACED PROJECTIONS RESPECTIVELY

SYNOPSISCHAPTER 4PRELIMINARY LABORATORY TEST EXPERIMENT

A preliminary laboratory experiment was set up from which holographic data were obtained from a flat horizontal plane and used to test for stability the inversion techniques described in Chapter 3, and to determine the accuracy obtainable.

The computer solutions are then compared with that from a thermocouple traverse over the same horizontal plane. Noise free computed data, obtained from the thermocouple traverse results, have also been used to test the computer algorithms, and the solutions obtained have also been compared with the thermocouple traverse results.

## CHAPTER 4    PRELIMINARY LABORATORY TEST EXPERIMENT

### 4.1    PRELIMINARY TEST SECTION

A simple three-dimensional temperature field which allows thermocouple probe measurement was generated as the natural convection plume from an electrically heated copper block. The block has dimensions of 2.54 cm (width), 3.49 cm (length), and 11.11 cm (height). Wigston Heating Elements Co., Leicester supplied the sheet element, size 5.0 x 11.3 cm, and rating 400W at 240V mains. This was split into two halves, and the copper block was made so as to sandwich these half elements. A 240V, 15A variac was used to control the input power to this block.

With the maximum size of optical lenses commercially available limited to a diameter of 14.5 cm, the cross-section of the heated surface, measuring 2.54 cm x 3.49 cm, was thought to be optimal for producing wide viewing from a single object beam holographic system, and yet not being too small for resolving the fringes created.

If the input power is too small and hence the temperature range across the plume, there would only be a few fringes, making the digitised results from each viewing angle unreliable as they are mostly approximations. Too large a power input would make the convection plume turbulent and also make this block glow red which would fog the holographic plate. The operating condition was finally determined from tests using a Mach-Zehnder interferometer having an aperture of 5.0 cm. A reasonably steady hot air plume with 16 to 20 fringes was seen at 164.5V, 1.15A, with the block at 380°C.

The holographic interferometer was built around this copper block test section as shown in Fig. 4.1 and Fig. 4.2.

Fig. 4.3 shows interferograms obtained with this holographic set-up. Four views about the image of the test object are shown.

#### 4.1.1 CONVECTIVE AND RADIATIVE POWER CONSIDERATIONS

At a room temperature of 20°C, thermocouple embedded in the block indicated a mean surface temperature of 380°C. The radiative power was therefore significant and was unduly warming up the optics of the holographic interferometer, and thus produced interferograms covered with unwanted background fringes at a frequency of approximately 5/cm. 7mm hardboard was used as a heat shield while the block was being heated up to its stable temperature which however took at least 15 mins and thus its use proved ineffective. However, a test on the Mach-Zehnder showed that the plume stabilised itself within six seconds after a gentle disturbance. It thus showed that the block could be brought into the test region after being heated up elsewhere.

At the surface temperature indicated above, the net radiative power using Stefan-Boltzmann law became

$$\begin{aligned}\phi &= \epsilon \sigma \{T_{\text{wall}}^4 - T_{\infty}^4\} \times \text{surface area} \\ &= 0.83 \times 5.67 \times 10^{-8} \times (653^4 - 293^4) \times (0.01517 \text{m}^2) \\ &= 124.6 \text{ Watts}\end{aligned}$$

where  $\epsilon$  was taken to be at 0.83,  $\epsilon=0.87$  for black oxidised copper from Ozisik. In use the surface became oxidised to a dark grey colour due to continuous heating and cooling.

Because pulsed laser holographic interferograms represent conditions at a particular instant in time it is desirable to have laminar flow so as to achieve a condition similar to that from the independent thermocouple traverse. For this particular heated copper block, the transition to turbulent flow should occur in the neighbourhood of  $\text{Gr.Pr} \approx 5 \times 10^8$ . Evaluation of the air properties at the arithmetic mean temperature of 200°C from  $(T_{\text{wall}} + T_{\infty})/2$  gave

$$\begin{aligned}\text{Gr} &= \frac{g\beta}{\nu^2} [T_{\text{wall}} - T_{\infty}] \cdot L^3 = 17.0 \times 10^6 \times 360 \times 0.111125^3 \\ &= 8.0077 \times 10^6, \quad \text{and Pr} = 0.6815.\end{aligned}$$

$$\therefore \text{Gr.Pr} = 5.457 \times 10^6$$

Although this calculation indicated laminar flow, a slight

unsteadiness was detectable over the top surface\*.

The heat transferred by natural convection was obtained by using the empirical Nusselt relations (Ede, and Eckert).

For the vertical surfaces:-

$$\begin{aligned} \text{Nu} &= 0.62 (\text{Gr.Pr})^{\frac{1}{4}} \\ &= \underline{33.4} \end{aligned}$$

and the heat transfer coefficient

$$\begin{aligned} h &= \frac{\text{Nu} \cdot k}{L_{\text{wall}}} = \frac{33.4 \times 0.039}{0.111125} \\ &= \underline{11.73 \text{ Wm}^{-2}\text{K}^{-1}} \end{aligned}$$

Therefore, the convective power from the vertical surfaces having a total area of  $0.0134\text{m}^2$  was

$$\begin{aligned} Q &= h.A.dT \\ &= 11.73 \times 0.0134 \times 360 \\ &= \underline{56.57 \text{ W}} \end{aligned}$$

For the top surface:-

$$\begin{aligned} \text{Gr} &= \frac{g\beta}{\nu^2} (T_w - T_\infty) L^3 \\ &= \underline{2.47 \times 10^5} \end{aligned}$$

where L is the arithmetic mean of the length of two dimensions -

$(0.0254 + 0.034925)/2$ , and

$$\begin{aligned} \text{Nu} &= 0.54 (\text{Gr.Pr})^{\frac{1}{4}} \\ &= \underline{9.81} \end{aligned}$$

Therefore,

$$\begin{aligned} Q_{\text{ts}} &= h.A.dT \\ &= 12.68 \times 0.000887 \times 360 \\ &= \underline{4.05 \text{ W}} \end{aligned}$$

For the bottom surface:-

$$\begin{aligned} \text{Nu} &= 0.27 (\text{Gr.Pr})^{\frac{1}{4}} \\ &= \underline{4.095} \end{aligned}$$

\* This is due to edge effects created by the rising hot air from the vertical side walls.

Therefore,

$$Q_{bs} = 0.5 \times Q_{\text{top surface}}$$

$$= \underline{2.0 \text{ W}}$$

Finally,

$$Q_{\text{convective}} = 56.57 + 4.05 + 2.0 = \underline{62.62 \text{ W}}$$

and

$$Q_{\text{total}} = 124.6 + 62.62 \text{ W} = \underline{187.22 \text{ W}^*}$$

Actual electrical power input =  $164.5 \text{ V} \times 1.15 \text{ A} = \underline{189.2 \text{ W}}$

The assumption made was that the block was made up of vertical walls and horizontal plates.

#### 4.1.2 THE BIOT AND FOURIER MODULI

It was determined that the copper block was required to operate at the surface temperature of  $380^\circ\text{C}$ . Consideration was given in the design as to the time required for the block to reach this temperature (maximum) at constant power input to determine the interval between the first and second exposure.

The block was assumed to be at a constant temperature throughout at any given time, and by the lumped parameter assumption (Welty) the energy equation becomes

$$\rho c V \frac{d\theta}{dt} = \dot{q} - h S \theta \quad (4.1)$$

where  $\theta = T - T_\infty$ , temperature relative to that of the environment at  $T_\infty$

$\dot{q}$  = power input,  $189.2 \text{ W}$

$V$  = volume,  $9.858 \times 10^{-5} \text{ m}^3$

$S$  = surface area,  $0.01517 \text{ m}^2$

$h$  = combined convective and radiative heat transfer coefficient,

$c$  = specific heat capacity, and

$t$  = time in seconds.

\* As a calculation in heat transfer,  $Q_{\text{total}}$  shows exceptionally good agreement with the input power, despite having to estimate a value for  $\epsilon$ .

Rearranging and integrating give

$$\ln \left[ 1 - \frac{hS\theta}{\dot{q}} \right] = -\frac{hS}{\rho Vc} \cdot t = -Bi.Fo \quad (4.2)$$

where Biot modulus  $Bi = \frac{hV}{kS} = \frac{(189.2/(360 \times 0.01517)) \cdot (9.858 \times 10^{-5})}{365 \times 0.01517}$

$$= 0.000616$$

$$\text{Fourier modulus } Fo = \left[ \frac{k \cdot t}{\rho \cdot c \cdot (V/S)^2} \right] = \left[ \frac{\alpha t}{(V/S)^2} \right]$$

The response of the system could now be described by the equation

$$\theta = \frac{\dot{q}}{h \cdot S} \left( 1 - e^{-L \cdot t} \right) \quad (4.3)$$

or

$$\theta = \theta_{\max} \left( 1 - e^{-L \cdot t} \right) \quad (4.4)$$

where  $L = \frac{h \cdot S}{\rho Vc} = 1.557 \times 10^{-3} \text{ s}^{-1}$ ,  $\rho$  and  $c$  were taken as  $8890 \text{ kg/m}^3$  and  $385 \text{ J/kg } ^\circ\text{K}$  respectively.

Since  $Bi \ll 0.1$ , this lumped parameter analysis would yield an error much less than 5% (Welty). The small value of  $L$  in eqn. (4.4) showed that the temperature drop as a result of fluctuation using a 50Hz alternating current was very small indeed. When the maximum surface temperature was reached, complete loss of heat generation for 0.01 second, such as an application of a 50Hz regular square pulse for the purpose of calculation, resulted in a temperature change of  $0.0056^\circ\text{C}$ , from  $(L \cdot \theta_{\max} \times 0.01\text{s})$  by rearranging eqn. (4.1), and so a dc source was not necessary.

With constant power input, the time required for the block to rise to 0.95 of its maximum temperature would be 32 minutes, and to 0.99: 49 minutes. The power input was 189.2 W.

## 4.2 THE THERMOCOUPLE TRAVERSE

The temperature distribution in the horizontal plane from which interferometric projection data were obtained was also measured with the 10-channel thermocouple comb shown in Fig. 4.4. The ten thermocouple junctions were connected to a Comark 1602 Al/Cr unit. This distribution is used as an independent check on the accuracy of the computer reconstructed solutions.

Temperature error due to conduction along the leads of the thermocouples was considered negligible when the junctions had reached steady state in the temperature field. Minor fluctuations in temperature reading occurred but care was taken to record only the true stable temperatures.

The 10-channel thermocouple comb traverse covered an area measuring 3.43 cm x 4.27 cm, as shown in Fig. 4.5. The thermocouples were equally spaced at intervals of 0.381 cm, and the comb was traversed in steps of 0.5334 cm. This procedure gave values at the centre of pixels representing a temperature field or picture with a resolution of 9 x 10 over an area of 3.81 cm x 4.803 cm. After each traversing step of the comb, a period variable up to four minutes was given to each selected one of the ten thermocouples before a reading of the temperature (or temperature band) was finally recorded according to the reading on the scale of the Comark where the needle most frequently settled. A complete traverse took approximately three hours and over this time the overall temperatures did not change significantly. These traverse results were checked by making several such complete traverses over a period of several days, and were found to be consistent. Temperature fluctuation occurred more significantly over an area just inside the boundary edges of the block.

Another technique of measurement was tried - the use of an automatic traversing mechanism. Instead of a comb array of thermocouples, a single

thermocouple probe was attached vertically to a horizontal traversing arm which moved along a preset distance and then dwelled for a preset length of time before repeating itself. The output from this thermocouple was fed to a JJ Instruments Chart Recorder set to read 20mV/cm. However, the results produced were difficult to interpret as the response of the recorder was too fast making it very sensitive to minor disturbances. A complete traverse of the temperature field was also found to be very time consuming indeed.

The rationale for a resolution of 10 x 9 was based on the normally available core storage of the CDC Cyber 73 computer at the University of Leicester, 32768<sub>10</sub> words for a batch job submitted from a computer terminal. Ideally one would like to be able to resolve to finer details. However, it was found that when the direct inversion least squares method of Golub (1965) was implemented to solve for 90 unknowns using say 120 digitised pathlength measurements of  $\phi_i$ , two large working matrices, one containing the coefficients of [A], were required, both totalling 21600 words. Storage was also required for the program and other necessary working matrices and this had almost taken up all the available memory space of the computer. In any case, increasing the resolution did not produce any significantly better results from this type of smoothly varying temperature field as no large temperature gradients were detected by the thermocouples. In fact, if the comb had more thermocouples the thermocouple traverse results could have been unreliable. There is likely to be much more disturbance to the flow caused by the greater number of thermocouples.

### 4.3 RELATIONSHIP BETWEEN FRINGE NUMBER AND TEMPERATURE

Fringes are formed on the holographic interferogram when there is a change in the shape of the propagating object wavefront through the refractive index field of the test section between the first and second exposure.

The fringe order number is given by the expression:

$$N = \frac{1}{\lambda} \int_{-\infty}^{\infty} (n(x,y,z) - n_0) \, dS \quad (4.5)$$

where

$n(x,y,z) - n_0$  denotes the change in refractive index at  $(x,y,z)$ ,

$\lambda$  is the wavelength of the laser light source being used,

$S$  is the optical pathlength of the refracting medium.

On the interferogram successive dark fringes are designated with half odd numbers as in  $N = \frac{1}{2}, \frac{3}{2}, \frac{5}{2}, \frac{7}{2}, \dots$ , and bright fringes have integer values of  $N$ .

The refractive index that changes the speed of the laser light and hence the propagating phase of the wavefront is a function of pressure, temperature and wavelength of light source used, and is related by the Gladstone-Dale equation

$$(n - 1) = K \rho \quad (4.6)$$

where  $K$  = Gladstone-Dale constant which is nearly independent of pressure and temperature, but has a small dependence on wavelength  $\lambda$  as shown in table 4.1,

$\rho$  = density of the gas, related by the ideal gas equation of state  $\rho = (M.p / R.T)$  where  $M$  is the molecular weight of the gas,  $p$ (Pa) the pressure,  $R = 8.3143 \text{ J/mol } ^\circ\text{K}$  the gas constant and  $T$ ( $^\circ\text{K}$ ) is the absolute temperature.

$\lambda$ (nm)	K (m <sup>3</sup> /kg)
509.7	0.2274x10 <sup>-3</sup>
567.7	0.2264
607.4	0.2259
644.0	0.2255
703.4	0.2250
912.5	0.2239

Table 4.1 Some values of K for air at 15°C  
Source Vest (1979)

Vest (1979) obtained an accurate relationship between refractive index and temperature for air at the wavelength 632 nm by utilising the Gladstone-Dale equation and the empirical data of Meggers and Peters (1918-19), and also including small corrections introduced by Tilton (1935) at a pressure of 760 mm Hg:

$$n - 1 = \frac{0.000292015}{1 + 0.00368184 \cdot T} \quad (4.7)$$

Following Smithsonian Physical Tables a pressure correction can be applied to give

$$n - 1 = \frac{0.000292015}{1 + 0.00368184 \cdot T} \cdot \frac{p}{760} \quad (4.8)$$

where p is in mm Hg, and T in °C.

By holding the pressure and wavelength of the laser light source constant in the two exposures, and providing that  $n(x,y,z)$  can be determined from eqn. (4.5), the temperature T can thus be determined from eqn. (4.7).

#### 4.4 PRACTICAL LIMITATIONS OF HOLOGRAPHIC INTERFEROMETRY

It is noted in Section 4.1, and also in Chapter 5, that there is considerable difficulty in obtaining holographic projection data over a viewing angle of  $180^\circ$  theoretically required for good general reconstruction. Even if there are no optical obstructions which prevent the building of a complicated multiple beam holographic interferometer around any proposed test section with a range of viewing angles close to the ideal of  $180^\circ$ , the laser has to provide sufficient energy to expose the plates. From trial tests it was found that the University's J.K.Lasers pulsed ruby laser, producing an output of 30mJ in 25ns and with the main beam split to produce two object and two reference beams all expanded to diameters of 14.5 cm, gave enough energy only to expose simultaneously two holographic plates (8E75HD type) giving a viewing angle from a small test object of approximately  $125^\circ$ . It was also found that repeated firing of the pulsed laser to increase the energy falling on the plates seemed to have hardly any effect in attempts to improve the quality of the image due to initial under-exposure cause by the reduced intensity of the pulsed laser light. Although it is possible to fit an oscillator amplifier in front of the laser to boost this power output up to twenty times, this facility was not available.

Increased range of viewing angles could be obtained by increasing the number of pairs of object and reference beams. In this laboratory a continuous wave laser with long exposure times would then be necessary. If one of the 5mW Spectra-Physics He-Ne lasers in the lab were used on a two object /reference beam holographic interferometer an exposure time of between 20 - 30 seconds is necessary. This is much too long since due to the vibration levels in the laboratory interferograms would be completely degraded. The lab has available a more powerful 15mW

Scientifica & Cook He-Ne laser used for reconstruction. This was invariably found not as good at making any holograms as the Spectra-Physics laser. Mainly its power output was not as steady, and as it emits incandescent light through the ventilation holes the laser ideally has to be mounted on the floor or in another room well away from the interferometer thereby magnifying the vibration problem.

However, reconstruction with data from a limited range of viewing angles is still possible, but the solutions produced are most likely to be less than perfect. In real, as opposed to simulated situations, digitised experimental interferometric data from projections are invariably noisy and interferograms are often covered with unwanted finite background fringes. Therefore, the reconstructions may not even resemble the expected temperature field particularly using straight forward direct inversion methods, even when solved in the least squares sense, due to instability. It was noticed in the digitised experimental projection data that the smaller values of fringe order numbers have large errors in them, and Radulovic (1977) suggested that these should be discarded. But this is unsatisfactory from the reconstruction point of view because having some low values of fringe numbers is better than not having any. This is to prevent the reconstruction program producing badly constrained solutions.

#### 4.5 METHOD OF DIGITISATION OF INTERFEROGRAMS

A good interferogram, one with very little or no background fringes, was illuminated with the reconstruction laser, the Scientifica & Cook at 15mW and 632.8nm, in a reconstruction set-up similar to that shown in fig. 2.5. A 35mm Nikon FM camera, placed approximately 1.4 m away from the interferogram, recorded the fringe distribution on 400ASA Kodak Tri-X Pan film from a number of projection angles. The holographic image

appeared slightly magnified on reconstruction due to the shift in wavelength from 694nm on recording with the pulsed laser to 632.8nm on reconstruction with the He-Ne laser, but this was not considered to affect the fringe distribution. The camera took three frames from each projection angle with exposure times varied from half to two seconds, and the clearest picture was taken for digitisation. The Nikon FM camera had LED metering facility which was used as a rough guide to the mean exposure time.

After developing the negatives, 12.7 cm x 17.8 cm prints were produced for viewing angles  $0^\circ$  to  $70^\circ$  inclusive. The magnification factor of each print was calculated on the basis of geometrically measuring the length from one vertical edge of the image of the copper block to the other and comparing this to the actual geometry of the block at that angle. They were in the range 1.41 to 1.48. A line representing a horizontal plane 1.27 cm above the block was scratched on each print with a sharp compass needle with two marks at each end to show the boundary edges of the proposed 9 x 10 resolution picture to be reconstructed. In between these two marks ten short strips of equal widths were scratched on the print, thus dividing the reconstructing plane into ten segments, and the fringe number corresponding to the centre of each of these strips was recorded with together the distance  $r$  measured from the left hand corner or boundary edge of this plane. All the recorded measurements of  $r$  from each projection angle were then demagnified to their true values, producing a compatible set of data for analysis. On two of the prints there were finite background fringes due to a slight distortion of the reference beam by the heated copper block in taking the second exposure. This was corrected by noting the number of background fringes appearing at a particular location on the print and then removing this number of fringes from the fringe number measurement taken at that location. These background fringes appeared on the right hand side of these two prints.

#### 4.6 RESULTS FROM DIGITISATION

The projection data obtained from digitising the interferometric prints of the heated copper block are plotted in fig. 4.6 (a) and fig. (4.6 (b). They are compared with simulated projection data obtained by numerically computing the thermocouple readings. A grid element model with a resolution of  $9 \times 10$  was used in this simulation, and each pixel (picture element) within this model was assumed to have a constant value of refractive index  $n$  corresponding to the thermocouple temperature at that point. By utilising the system of co-ordinates  $\phi(\rho, \theta)$  used in the process of digitising the interferometric prints and eqns. 4.5 and 4.7 sets of simulated fringe numbers corresponding to the same points from each projection angle were obtained. The axes labelled fringe number in fig. 4.6 (a) and fig. 4.6 (b) are graduated in whole number of wavelengths corresponding to  $N$  in eqn. 4.5.

A grid element with a greater resolution was tested to established whether there was any significant difference in the simulated projection data. By halving the sides of each of the pixels the modified model had a resolution of  $18 \times 20$ . A value of temperature obtained by interpolating from the thermocouple traverse was assigned to each of the new pixels. There was a problem in the computer memory in attempting to hold the weight matrix  $[A]$  containing elements of the pathlengths  $dS_i$ . This problem was overcome by generating rather than retrieving particular values of pathlength elements required in calculating the simulated fringe number for each of the rays. The fringe numbers obtained do not any significant differences suggesting that the  $9 \times 10$  model was sufficiently accurate.

A complete set of these interferometric prints were sent to Dr. Walklate at his request during a visit to Harwell in Didcot,

Oxfordshire, in which thermal tomographic techniques and problems were discussed. The prints were digitised and tested on his computer program. The digitised projection data are reproduced here, fig. 4.6 (a) and fig. 4.6 (b), and they in general show good agreement with those obtained by the author, except for the one at  $50^\circ$  which was likely to be caused by an error in the scaling factor. There was however a difference in the way prints were digitised. The method of Walklate appeared to be that of locating every bright and dark fringe. In plotting the projection data of Walklate in fig. 4.6 (a) and fig. 4.6 (b) calculations were made to take into account the difference in location of the origin on Walklate's data. Although both origins were taken about the centre of a corner pixel within the tomographic models the resolutions were different -  $4 \times 4$  against  $9 \times 10$ .

The numerical discrepancy between the author's digitised data with those obtained by computation of the thermocouple temperature field is discussed in section 4.6.1. By comparing the curves obtained by Walklate's digitisation, denoted by x, to those obtained by the author, denoted by o, figs. 4.6 (a) & 4.6 (b) show that, with the exception of the  $50^\circ$  plot from Walklate's digitisation, fringes can be digitised to within or better than one half of a whole fringe which is from one dark band to the next, or vice versa. This is mainly due to the relatively high fringe density around the block, so making fringe numbers easier to locate and to an extent interpolate. Furthermore, because data are collected over a large number of points in the digitisation process, the magnitude of error from interpolation for more data, or for data from selected points, should be quite small.

The computed curves in figs. 4.6 (a) & 4.6 (b) show differences of between half and two fringes with the author's digitised data curves, but

they are following similar paths within the half to two fringe error band. On a number of the plots from 30° onwards, the computed values near the edges seem higher than digitised values. This suggests there is likely to be an effect on taking thermocouple readings over a discrete number of points over a period of time, because there was a slight degree of unsteadiness within the plume near these edge regions as discussed earlier. Therefore, the thermocouple readings taken were actually time averaged values for the thermal plume. So as well as experimental errors due to digitisation from interferograms there is also the error due to the slight unsteadiness within the plume.

#### 4.6.1 ERRORS IN DIGITISED DATA

The error  $e_i$  for each value of projection data and the average error  $e_{av}$  for all the projection data are defined as

$$e_i = \left( \frac{\phi_{act} - \phi_{dig}}{\phi_{act}} \right)_i \quad (4.9)$$

$$e_{av} = \frac{1}{M} \sum_{i=1}^M |e_i| \quad (4.10)$$

where  $\phi_{act}$  and  $\phi_{dig}$  represent the actual and digitised pathlength difference measurement respectively, and M the total number of rays collected in the projection data. Also defined is the mean error as

$$e_m = \frac{1}{M} \sum_{i=1}^M e_i \quad (4.11)$$

Using these definitions, the authors digitised projection data in fig. 4.6 (a) and fig. 4.6 (b) indicate an average error  $e_{av}$  of 24.2% and the largest error  $e_{i_{max}}$  found is 73%. This occurs at a low fringe number. It can be seen from these plots that the percentage error band gets larger as the fringe number order gets lower. There are two factors which contribute to an error of this magnitude, (i) theoretically the fringe number  $N$  could only be measured to a value within  $\pm\frac{1}{2}$ , and (ii) correction for finite background fringes could only be estimated. Therefore if the fringe number is less than say 2 the signal to noise ratio is bad approaching one giving 100% error, and data with values up to 2 fringes would thus seem to be buried in noise. However, using the dispersion about the simulated curves measure  $e_m$  as in eqn. 4.11 the error is somewhat smaller with  $e_m = 15.58\%$ .

This shows that fringes on the holographic interferograms can be digitised, but with an uncertainty of 2 fringes. This would be totally unacceptable for reconstruction if digitised experimental projection data do not also contain higher order fringe numbers in order to reduce the overall average error  $e_{av}$  of the data.

#### 4.7 RESULTS FROM COMPUTER RECONSTRUCTIONS

Having obtained the digitised projection data from the interferograms, noisy but by no means untypical of a laboratory experiment, the mathematical models in conjunction with the inversion schemes, described in Chapter 3, are tested to discover which combination of mathematical model and inversion scheme could produce a good or sensible reconstruction. The tests were carried out first of all with reconstruction techniques having the smallest estimated execution time in order to reduce cost and

turnround time on the computer.

Although quantitatively there would be significant improvement in the reconstructed thermal tomographs by visually smoothing out any irregularly reconstructed point to point variation of refractive index  $n$  within the reconstructing model, no attempt has been made in this respect on any of the reconstructed temperature fields in this thesis as this would not have indicated truly the performance of the reconstruction techniques. For example, the appearance of contour level 3 on the left hand side of plot 4.4 is not physically possible or expected on that temperature field and thus could be blended-in with the surrounding elements. This is possible because a knowledge of the type of three-dimensional temperature fields could determine the form certain points on the reconstructing grid could take. However, should smoothing be done the overall shape of the reconstructed temperature field should not depart significantly from the unsmoothed version otherwise it could be misleading.

But in this thesis the average error, mean error, and maximum error in the reconstructed temperature fields are to be the actual unsmoothed reconstructed values from the program.

#### 4.7.1 A DIRECT INVERSION TECHNIQUE

First of all it was decided that the direct inversion procedure of Golub (1965), a standard computer NAG library numerical routine named F04 AMF should be implemented as a method of solution by solving the simultaneous set of projection equations in the least squares sense.

The grid element model is used to represent the reconstructed temperature field with the proposed resolution of  $9 \times 10$ , on the premise of mathematical simplicity. This is because pathlengths within each of

the pixels from any light ray could be interpreted and calculated simply according to section 3.2.1 thus giving the coefficients elements or weights of matrix  $A_{mn}(\theta, \rho)$  as in eqn. 3.8. The overall matrix  $[A_{ij}]$  in eqn. (3.3) could be obtained by calculating the coefficients from each of the rays in the projection data. For this 9 x 10 model a single row of  $[A_{ij}]$  has 90 coefficients many of which are zeros. As the size of each pixel is small and some redundant data are used the effect of instability caused by the error term  $e_i$  becomes less. With 13 values of fringe number  $N$  from each of the 8 projections spread over a viewing angle range of  $70^\circ$  entered into the column matrix  $[b_i]$ , eqn (3.3) is now solved by calling F04 AMF.

However, the computer program produced an unintelligible spurious set of 'random' numbers, some very large, supposedly representing the reconstructed temperature field. A typical plane from a cross-section of this temperature field is shown in fig. 4.7 with errors of up to 500% or more appearing in most places. Also, there were just as many negative values of temperatures, known to be non-existent, as there were positive values.

Similar results have also been obtained by Walklate (1977) in studies of simulated temperature field reconstruction using the grid and the sinc series of Sweeney and Vest (1973) when the resolution was increased from 3x5 to 5x5. The mathematical description of the grid series is similar to the one used by the author, and that of the sinc series is based on a sampling theory, which should give a smoother reconstructed picture. In this study Walklate (1977) used simulated noise free pathlength data collected over  $45^\circ$ .

The computer program was checked for the possibility of errors using the computed projection data from the thermocouple traverse. Approximately

90% of the values of temperature obtained are in exact agreement, and the rest in very good agreement with those corresponding to the measured temperatures. Because of the very large core storage needed by F04 AMF the University CDC Cyber 73 would not accept any more digitised redundant projection data to test the method. An attempt was made to reconstruct with a coarser plane by halving the number of pixels and using the same number of digitised projection data, 108. The method was still found to be quite hopeless with no satisfactory solution produced.

This study has shown that the direct inversion procedure, F04 AMF, is not a suitable scheme for reconstructing a slice of the three-dimensional temperature field using data from noisy interferometric pathlength measurements from a limited range of viewing angles for the following reasons:

(i) digitised projection data with low values are buried in noise, and so any attempt to recover a value of  $x_j$  with a procedure of the form  $x_j = (b_i/a'_{ij})$  where  $i$  and  $j$  are ray and pixel numbers respectively, and  $a'_{ij}$  is a (transformed) coefficient of  $[A_{ij}]$ , is unlikely to be successful; when the resolution is increased the pixels becomes smaller and so does  $a'_{ij}$  and thus error in the value of  $x_j$  becomes much greater.

(ii) the pathlength coefficients in  $[A_{ij}]$  are in effect only approximate because of the assumption that the value of temperature on each pixel is constant throughout. When inversion is carried out by back-substitution from an upper triangular form of this matrix a problem of instability arises caused by errors piling up on each other as each value of refractive index  $n_j$  is evaluated in reconstructing the temperature field.

So the use of redundant data with this method does not necessarily

guarantee a satisfactory solution. Walklate (1977) also discovered that by increasing the resolution the optimal degree of redundant data required does not seem to increase proportionately in the ratio 1 to 1, but at a greater rate.

#### 4.7.2 ITERATIVE INVERSION TECHNIQUES

These techniques are used in the reconstruction of the three-dimensional temperature fields in this thesis because there are no viable alternative techniques capable of suppressing the instability problem encountered in the previous section. Iterative techniques cost more to run on the computer because they require more computation time, but there are genuine reasons to believe that they could produce better results:

- i ) a relaxation parameter can be incorporated allowing the thermo-tomogram to be reconstructed gradually,
- ii ) the error terms  $e_i$  caused by noisy projection data and approximate modelling of the reconstructing plane could be dumped or accounted for in the residuals as there is no need to evaluate the simultaneous equations exactly,
- iii) coefficients of  $[A_{ij}]$  are not used directly in inversion,
- iv ) constraints can be introduced to produce tomograms with positive values of temperatures only, or temperature above that of the environment around the test section.

Another advantage to be gained from using these techniques is that the number of rays from the projection data that can be used can be increased considerably. This is because the coefficients of  $[A_{ij}]$  need not be stored - they can be generated whenever required in the computation. It is evident from the printouts obtained that most of these coefficients are zeros, typically between 2/3 to 3/4 on a grid element model. Thus to save

computing time a method was developed for storing and recalling the non-zero coefficients only.

This method is incorporated in the computer program FERECON in Appendix 1 for reconstructing, either from the Grid element or Finite element mathematical model, using non-zero coefficients of  $[A_{ij}]$  in the much shortened format in storage. All the iterative inverting schemes together with the conservatively initialised pixels sub-program KAISYM in the program FERECON are written such that these coefficients could be recalled for use easily. The program in Appendix 1 is set to solve with a resolution of 9 x 5. This program also contains commented out codes which when uncommented could invert with greater or smaller resolution. These codes were used in initial trial tests with the iterative techniques.

The iterative technique technique ART was chosen first as it is the least time consuming procedure to reconstruct the temperature field from the heated copper block. In the reconstruction process two matrices were needed; one containing exact pathlength elements in order that the residual from each ray path could be calculated, and the other one containing the pixel numbers for a given ray path that need their values of refractive index  $n$  changed according to eqn 3.25 in section 3.3.1 for each ray.

As mentioned above, a wide range of reconstruction plane resolution were tried from 9x10, 13x7, 3x4, 6x6, 5x9, to 2x1, but it was found that the 13 x 7 reconstructs temperatures closest to that on the 9x10 thermocouple traverse grid. The 13 x 7 model was preferred because the centre points of the pixels correspond to the nodal points on a 6 x 3 Finite element model.

In trial tests made on ART it was noticeable that when the 108 values

of fringe numbers from the digitised projection data were almost doubled to 200 by linearly interpolating for the fringe number that is half way in between the projection data points, the reconstructed temperature field was much smoother in that it was not so peppered with lumps and 'spikes' on the reconstructed temperature surface. With the 108 rays used on the 13 x 7 model, after some 15 iterations certain values of temperature on the reconstruction grid tended to behave erratically by progressively increasing their net values much more after each iteration than those surrounding them. So 200 fringe numbers were used in the reconstruction.

The optimal value of  $\lambda$ , the relaxation parameter, was found by trial tests to be 1/30. When  $\lambda$  was reduced to 1/10 ART was found to behave very erratically after 4 cycles of iteration. A value of  $\lambda$  smaller than 1/30 would just take more time to produce the required reconstruction. Minor improvement was also seen when the rays from the digitised projection data were sampled at regular intervals by reprocessing the data according to eqn. 3.6. If more than one projection data point were to lie within the sampled ray of width  $w_\theta$ , the average value is usually taken. Strictly speaking, however, all rays lying within the sampled ray width but not through the centre should be interpolated to obtain the exact fringe number value at the sampled ray centre, but in practise the pixels are small and so is  $w_\theta$  and the temperature field, and such detail calculations for exact sampled data did not show a reconstruction to be significantly different to that obtained using data processed by averaging. But when  $\lambda$  was reduced to a value as small as 1/30 the reconstructed temperature field was not significantly different to that reconstructed with unprocessed data. The objective of sampling in this form was to use the sampled projection data to change each pixel value on the reconstructing plane once only for an iteration with data from a given projection angle.

After a large number of tests in which a wide range of values were tried in each of the parameters,

relaxation parameter  $\lambda$  :  $1/2$  to  $1/100$ ; also variable with iteration number  $k$ , e.g.  $\lambda = 1/3$  for  $k \leq 2$ ,  $\lambda = 1/10$  for  $k \leq 8$ , and  $\lambda = 1/30$  for  $k > 8$

resolution :  $13 \times 7$  to  $2 \times 1$

number of rays : 108 and 200

sampled width of rays :  $0.2 \cdot \Delta x$  to  $\Delta x$ ; and  $0.2 \cdot \Delta x \cdot \cos\theta$  to  $\Delta x \cdot \cos\theta$ ,

the best reconstructions of the temperature distribution with the ART algorithm are shown in plots 4.2 - 4.4. Using the simulated thermocouple projection data the shape of the reconstructed temperature field matches with the original very well. Plot 4.1 shows a contours plot of the measured temperature field from the thermocouple probe traverse over the plane - 1.27 cm above the top surface of the block. The boundaries of the plane traversed and the edges of the copper block are shown in dotted lines. All other contour plots, i.e. plots 4.2 - 4.7, in this chapter are reconstructed fields and would therefore be compared with plot 4.1 for evaluation of the accuracy with which numerical techniques can reconstruct from the limited range viewing angle projection data from the holographic interferogram.

Plots 4.2 - 4.4 are ART reconstructions with resolutions of  $13 \times 7$  Grid elements. In plot 4.2 the ART algorithm is tested using the computed projection data. A comparison of this with plot 4.1 shows a very good reconstruction, with hardly any significant amount of instability even though the iteration cycle number is as high as 100. Instability is characterised by artifacts or random errors such as peaking or dipping of levels occurring over the reconstructed field, such as contour levels 1, which is quite low, on the l.h.s. and also on the r.h.s. bottom corner of plot 4.2. Plots 4.3 and 4.3 show the best reconstructed temperature fields

obtainable with this ART algorithm on using the digitised projection data, and these two plots are shown to illustrate the performance of this algorithm at iteration cycle numbers 17 and 53. Improvements on plot 4.4 over plot 4.3 are chiefly on the upper boundary as shown by the change in contours from 5 to 4, and in the shape of the contours in that they are not so elongated diagonally: but the plume of plot 4.4 is generally narrower with the maximum temperature shot up to level 12 from 10 (c.f. only a 9 in plot 4.1). Plot 4.4 also shows that the artifact contour levels are beginning to get worse, increasing from level 2 to 3 on the l.h.s.

Plot 4.5 is also an ART reconstruction, but using a 6 x 3 Finite element model as the reconstructing plane. Digitised projection data were used, but comparing this with plot 4.3 it can be seen that there is no real improvement even though the model is supposed to fit the data better by describing the surface of each reconstructing element with a second degree polynomial.

Reconstructions with the LSRT algorithm are shown in plots 4.6 and 4.7, with resolutions of 9 x 5 Grid elements which were found to be adequate for this type of smoothly varying temperature field. However, when a higher resolution was tried some improvements were seen on the reconstructed field but not considerable, even though the computation time increased considerably. This model with a maximum of 9 x 5 Grid elements was chosen mainly because it gave the best reconstructions obtainable with the digitised interferometric projection data from the enclosure model experiment which will be describe later. The LRST reconstruction with the digitised projection data from the plume is shown in plot 4.6. Compared with plot 4.3, plot 4.6 is slightly better in that the highest contour values on the boundaries are 2's rather than 5's, and also there are no artifacts with a level of 2 or higher. Nevertheless, when

compared with plot 4.1, which also has contour levels of 2 on the boundaries, some of the contours in plot 4.6 appeared somewhat elongated diagonally or biased in certain directions. This was attributed to the limited range of viewing angles in the projection data. There is a reduction in this kind of bias when the computed or simulated projection data were used as shown in plot 4.7. Plot 4.7 is almost comparable with plot 4.2, except for some diagonal contours on the bottom r.h.s. corner, but then these types of contours also appear in plot 4.1 though not so pronounced. Plot 4.2, however, contains some quite low artifact contours whereas plot 4.7 does not.

Errors are evaluated using the measures the form of which are defined in eqns. 4.9, 4.10, and 4.11 for the maximum, average, and mean error respectively, where  $\phi_{act}$  and  $\phi_{dig}$  now become  $T_{act}$  and  $T_{rec}$ , the measured and reconstructed temperature, and  $i$  now refers to pixel number from 1 to  $(M \times N)$ . For plot 4.2, average error = 31.24%, mean error = -15.49%, and maximum error = 65%. Using digitised projection data the reconstructed temperature fields on the same plane are shown in plot 4.3 and 4.4. Plot 4.3 shows the temperature distribution obtained when the iteration was terminated using the a method to be described later developed by the author at which point the equations were nearly satisfied after 17 iterations. The maximum temperature was reconstructed to be in the centre of the plane and its value close to the original. Average error = 45%, mean error = 11.14%, and maximum error = 290.00%. On continued iteration, as shown in plot 4.4, after 53 iterations, the temperature in the centre got much worse; the reconstructed shape of the surface was better, not so elongated diagonally; temperature on the top boundary edge of the reconstructed plane causing the 290.00% error in plot 4.3 dropped from contour level 5 to 4. However, there were signs of instability starting to occur characterised by artifacts

or lumps peppering the surface of the reconstructing plane - see contour level 3 on the left hand edge and also 1 on the top left hand corner. Average error = 47.30%, mean error = 9.93%, and maximum error = 480.00%.

Trial tests showed that when values of the parameters as described above are not chosen carefully to take into account of the pathlength measurement and mathematical modelling errors when inverting iteratively the reconstructions are likely to be useless because the whole of the reconstructing plane could be peppered with artifacts. Values of these parameters, shown on the plots, were obtained by trial tests in which each parametric value was adjusted until reconstructions were produced with magnitude and number of artifacts reduced to the minimum possible.

A description of the method which was used in terminating the iteration of ART to produce plot 4.3 is given: Some of the elements on the reconstruction plane are selected, between 1/5 to 1/10 of all elements. This selection is based on those elements with the largest increases in value of temperature between the first and second iteration. The values from these elements, all of which would be positive, are added up to give a number. Any changes in the temperatures from these elements after each successive complete cycle of iteration are added again giving another number. By using 1/9 of all the elements in the 13 x 7 grid element model, these numbers were found to decrease rapidly in the first 15 iterations after which number this decrement was very much less, suggesting that the projection equations were almost satisfied. After 15 cycles of iteration, iteration could be continued provided there is no visual appearance of artifacts cropping up on the reconstruction surface. For plot 4.3 the series for these numbers was as follows: 685, 255, 108, 57, 38, 30, 26, 24 (best reconstruction), 24, 23, 23, 23, 22, 22, 22, etc (recorded after iteration number 2,3,5,7,9,11, etc.).

The iteration criteria by which the change in variance is measured according to inequality (3.28) proved very unsatisfactory. A good reconstruction could not be achieved when the digitised projection data were used because the criteria is insensitive to the continual growth of artifact values which appeared on only a small number of the pixels on the reconstruction surface whilst the reconstructing temperature field is also building up gradually using the small value of  $\lambda$ , the relaxation parameter. This criteria was tested by calculating

$$\sum_j T_j^2 \quad (4.12)$$

where  $T$  is temperature and  $j$  the pixel number, after each iteration, and then a comparison was made on the variance of the values from (4.12) using the experimentally digitised, and also the thermocouple derivative, projection data with respect to the true temperature field from the thermocouple traverse. Iteration should be terminated when

$$(\sum_j T_j^2)_{k+1} - (\sum_j T_j^2)_k < \frac{1}{100} (\sum_j T_j^2)_k \quad (4.13)$$

In practise, though this condition could be achieved with good projection data as the reconstruction process is more stable, the reconstructed temperature field obtained from this criteria is not necessarily the correct let alone the best one.

Also, preliminary tests were performed on ART with a measure called the maximum entropy criteria but it produced no satisfactory results yet from this preliminary laboratory experiment. Basically this criteria states that the reconstruction with the smoothest surface which is also consistent with the data supplied is most likely to be the true solution, subject to

$$\text{Maximising } - \sum_j \left( \frac{T_j}{(M \times N) \cdot T} \right) \cdot \ln \left( \frac{T_j}{(M \times N) \cdot T} \right) \quad (4.14)$$

where T was calculated as

$$\sum_i \left( \frac{\phi_i}{L_i} \right) .$$

When the Grid Element model was replaced by the 3x6 Finite Element model with each element now being described by the second degree polynomial of eqn. (3.9), the reconstructed temperature field as shown in plot 4.5 looks more elongated along the directions where the projection data were collected. This suggests that the linking of 8 nodal values of refractive index n to a short string of inter-related terms in order to define the surface of only a single element is not an appropriate choice of mathematical model in view of the digitised experimental projection data being non-omnidirectional and as such each of the nodal values of n is more prone to produce an error in reconstruction using an incomplete set of projection equations - because of the non-availability of data from all projection angles. The values at the nodal points were evaluated by ART, using the appropriate weighting matrix for changing nodal point values in the process of iteration. Each nodal point was considered as at the centre of a pixel. Thus for one finite element there would be nine pixels, the ninth pixel being artificially introduced in the centre of the FE element enabling the ART weight matrix to be formed. Here the simultaneous projection equations from the Finite Element model were merely used to calculate the residuals after each iteration. For plot 4.5, average error = 64.59%, mean error = -28.90%, and maximum error = 277.80%.

SIRT was also tried but the reconstruction at the optimal point was found not to be as smooth as ART, although the peak temperature was approaching 300°C.

However, on the basis of evaluating point to point values of temperature the least squares of residuals technique LSRT produced slightly

better reconstructions than ART. The reconstruction using the digitised projection data is shown in plot 4.6. Average error = 44.60%, mean error = 10.92%, and maximum error = 83%. Using simulated thermocouple projection data a much more closer fit to the original was obtained as shown by the reconstructed temperature field in plot 4.7. Average error = 27.70%, mean error = 18.81%, maximum error = 61.20%.

With LSRT it was found that with the digitised projection data the best temperature field was reconstructed when the change in the sum of the squares of all the residuals became very small on further iteration. Plot 4.6 was obtained after iteration number 37. However, provided there are no artifacts cropping up on the reconstructing surface, the iteration process could be continued to improve the reconstructed field very slightly. Using the simulated thermocouple projection data changes in values of  $n$  were found quite small after iteration number 35 and up to iteration number 200. But when compared with the original the reconstruction from iteration number 200 would fit closer. Fig. 4.8 shows the sum of squares of all the residuals against the iteration numbers for the reconstruction shown in plot 4.6 using digitised projection data, and that shown in plot 4.7 using simulated projection data.

The main consideration of this study has been to establish the ability of the proposed mathematical models and inversion techniques to reconstruct the shape of the temperature fields as well as to obtain the point to point values of temperature. Satisfactory reconstructed temperature fields were obtained with the ART inversion algorithm, represented by the Grid Element model. The stability of this technique depends very much on the use of a good set of projection data. With digitised experimental projection data it was difficult to find an objective measure of minor instability which is characterised by the appearance of artifacts peppered on only a few of

the pixels on the reconstructing surface. Because the iteration process was terminated by criteria which are insensitive to artifacts and also because reconstruction are thus produced without having to satisfy the projection equations exactly, it was found useful to list the reconstructed temperature field after each iteration, and then select the best field by eye near the iteration number for best reconstruction according to the selected elemental value criteria described above. LSRT was demonstrated, again represented using the Grid Element model. For this temperature field it produced a reconstruction only marginally better than ART. The formulation of LSRT, by which a value of  $n$  on any pixel is changed using all the projection data intersecting that pixel instead of only a single projection data, handled the inconsistent digitised projection data much more effectively because each value of  $n$  that was changed after each cycle of iteration had also satisfied the built-in least squares criteria.

However, errors on the reconstructed temperature field cannot be attributed entirely to the reconstruction techniques as the relationship between the refractive index and temperature is non-linear in the range  $20^{\circ}\text{C}$  to  $300^{\circ}\text{C}$ , see fig. 4.9 because

$$\frac{dT}{dn}_{20^{\circ}\text{C}} = 4.24 \frac{dT}{dn}_{300^{\circ}\text{C}}$$

and thus a unit error in  $n$  produces a much more than proportionate increase in  $T$  as  $n$  becomes greater. So errors on the reconstructed temperature field appear to be much more magnified than that on the reconstruction with values of  $n$ . The reconstructed temperature field was obtained by converting values of  $\Delta n(x,y)$  to  $\Delta T$  about the ambient temperature.

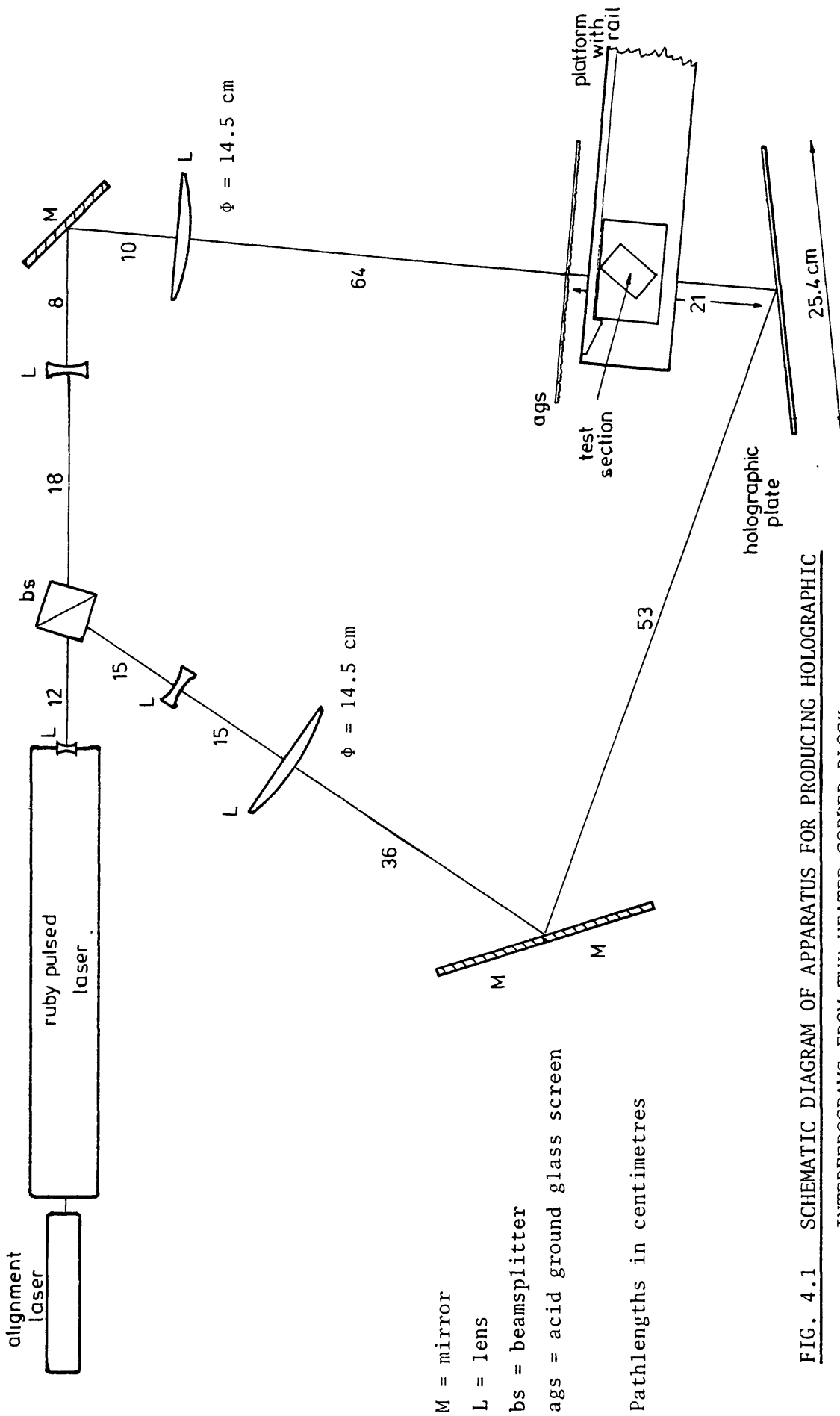


**FIG. 4.1 SCHEMATIC DIAGRAM OF APPARATUS FOR PRODUCING HOLOGRAPHIC INTERFEROGRAMS FROM THE HEATED COPPER BLOCK**

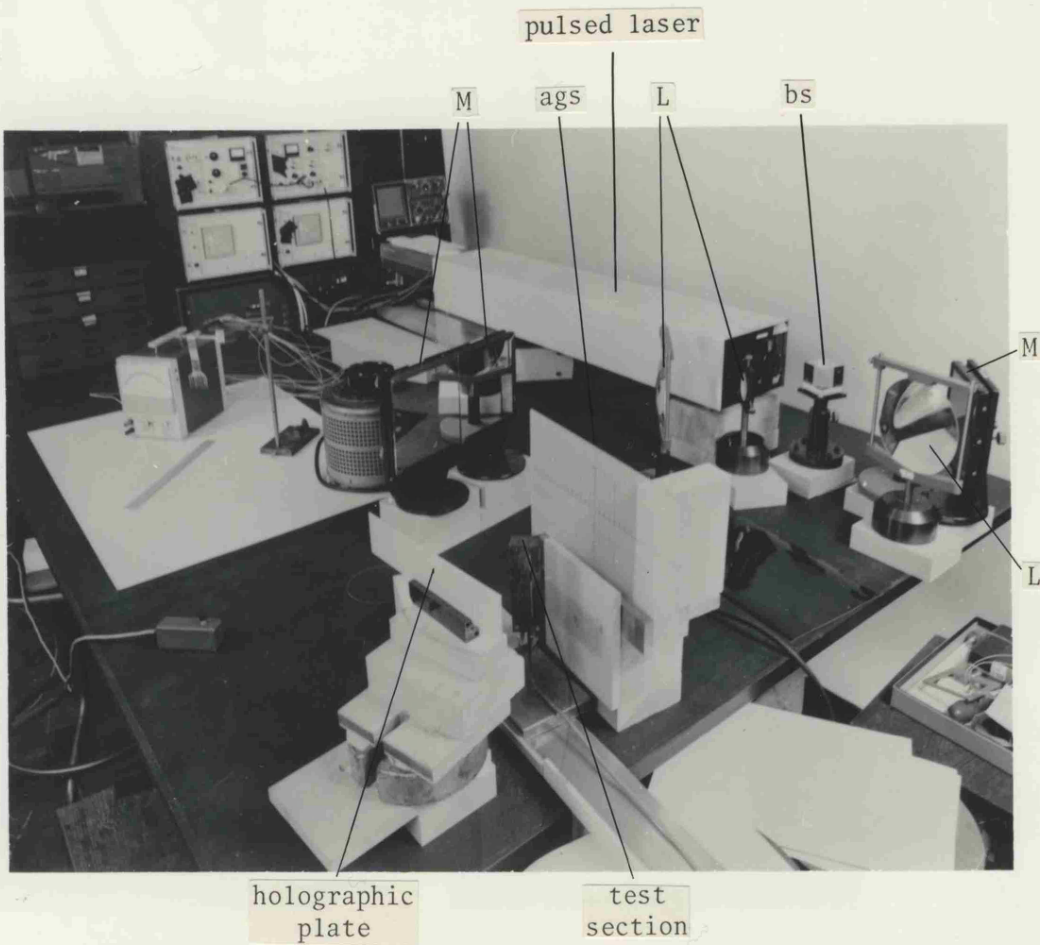


FIG. 4.2 A PHOTOGRAPH SHOWING THE OPTICAL SYSTEM

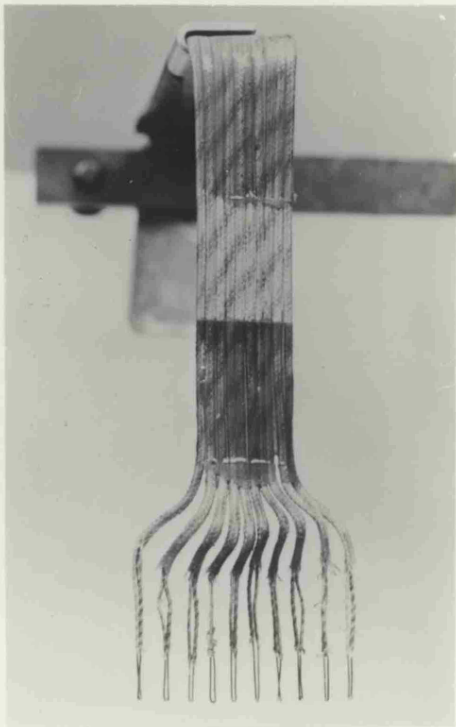
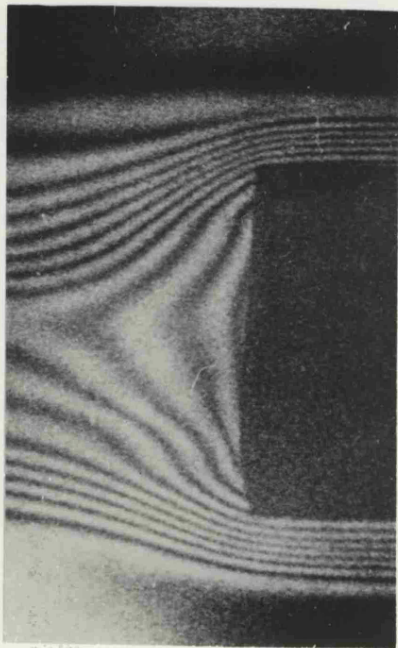


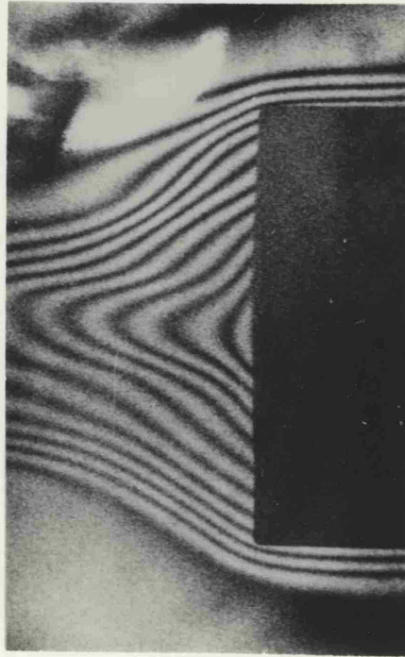
FIG. 4.4 ACTUAL TEMPERATURES OBTAINED WITH THIS 10-CHANNEL THERMOCOUPLE COMB



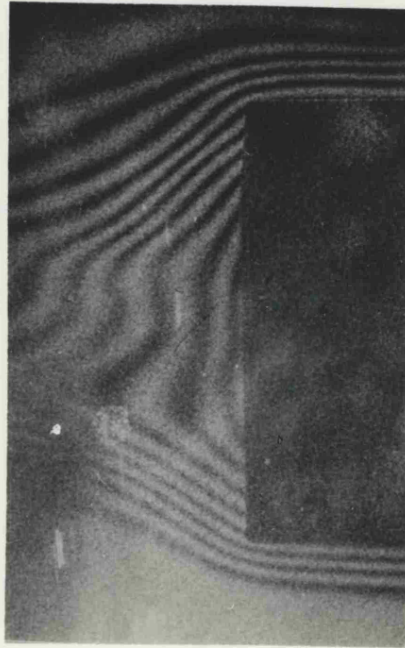
10° FROM NORMAL



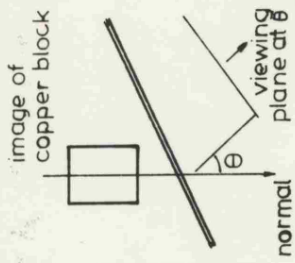
30° FROM NORMAL



50° FROM NORMAL



60° FROM NORMAL



near corner of block

FIG. 4.3 FOUR VIEWS FROM A HOLOGRAPHIC INTERFEROGRAM OF THE HEATED COPPER BLOCK

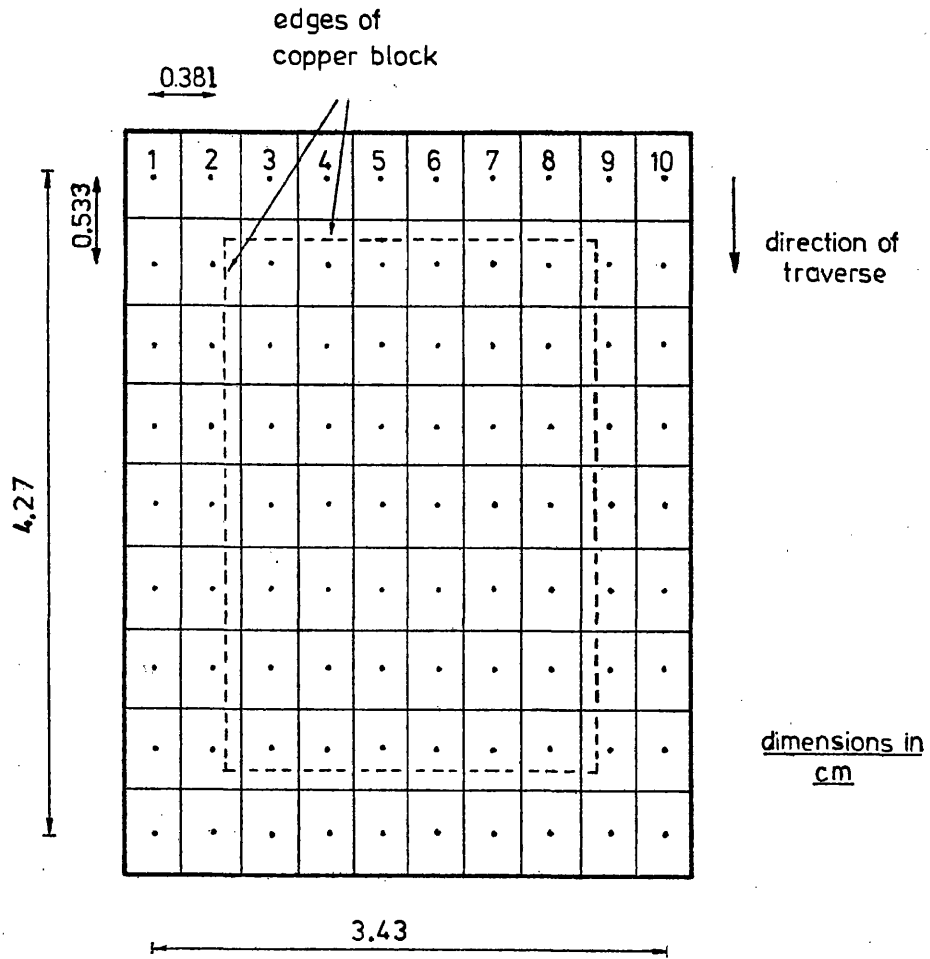


FIG. 4.5 REGION COVERED BY THERMOCOUPLE TRAVERSE

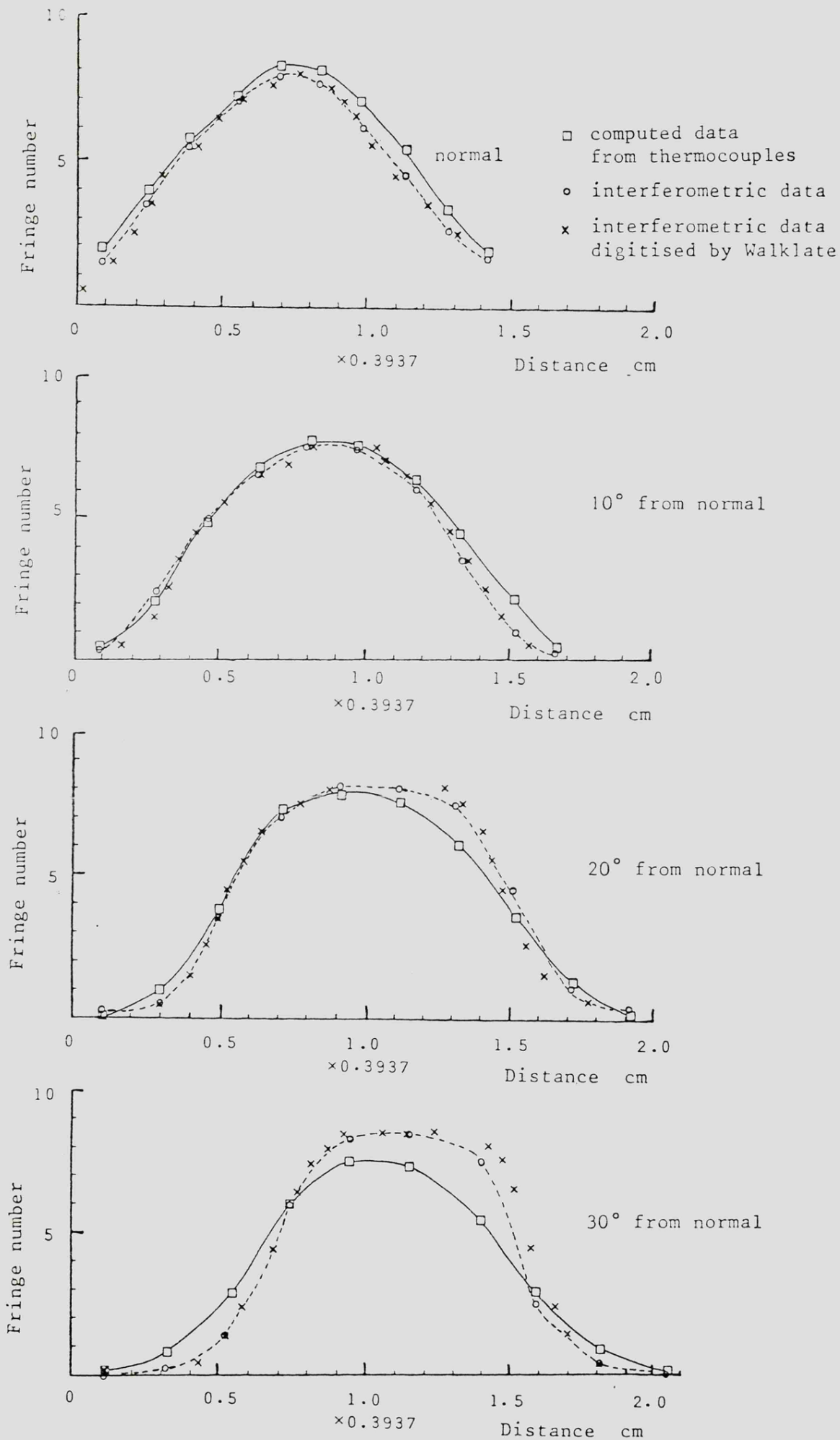


FIG. 4.6(a) COMPARISON OF DIGITISED PATHLENGTH DIFFERENCES FROM (i) INTERFEROGRAM AND (ii) WALKLATE'S DIGITISATION, TO THOSE OBTAINED BY COMPUTATION OF THERMOCOUPLE READINGS. VIEWING ANGLES  $0^{\circ}$ - $30^{\circ}$  INCL.

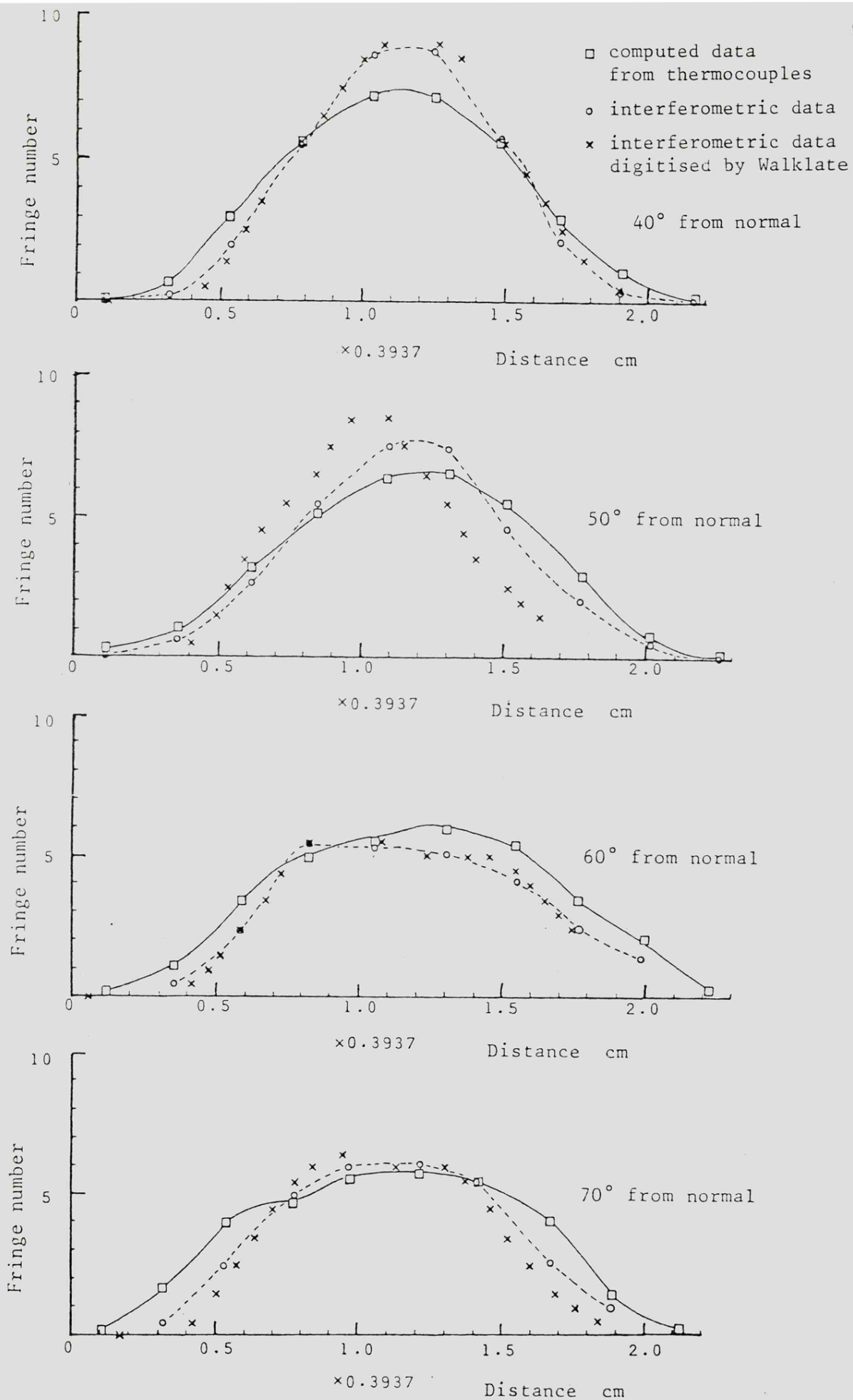


FIG. 4.6(b) COMPARISON OF DIGITISED PATHLENGTH DIFFERENCES FROM (i) INTERFEROGRAM AND (ii) WALKLATE'S DIGITISATION, TO THOSE OBTAINED BY COMPUTATION OF THERMOCOUPLE READINGS. VIEWING ANGLES 40°-70° INCL.

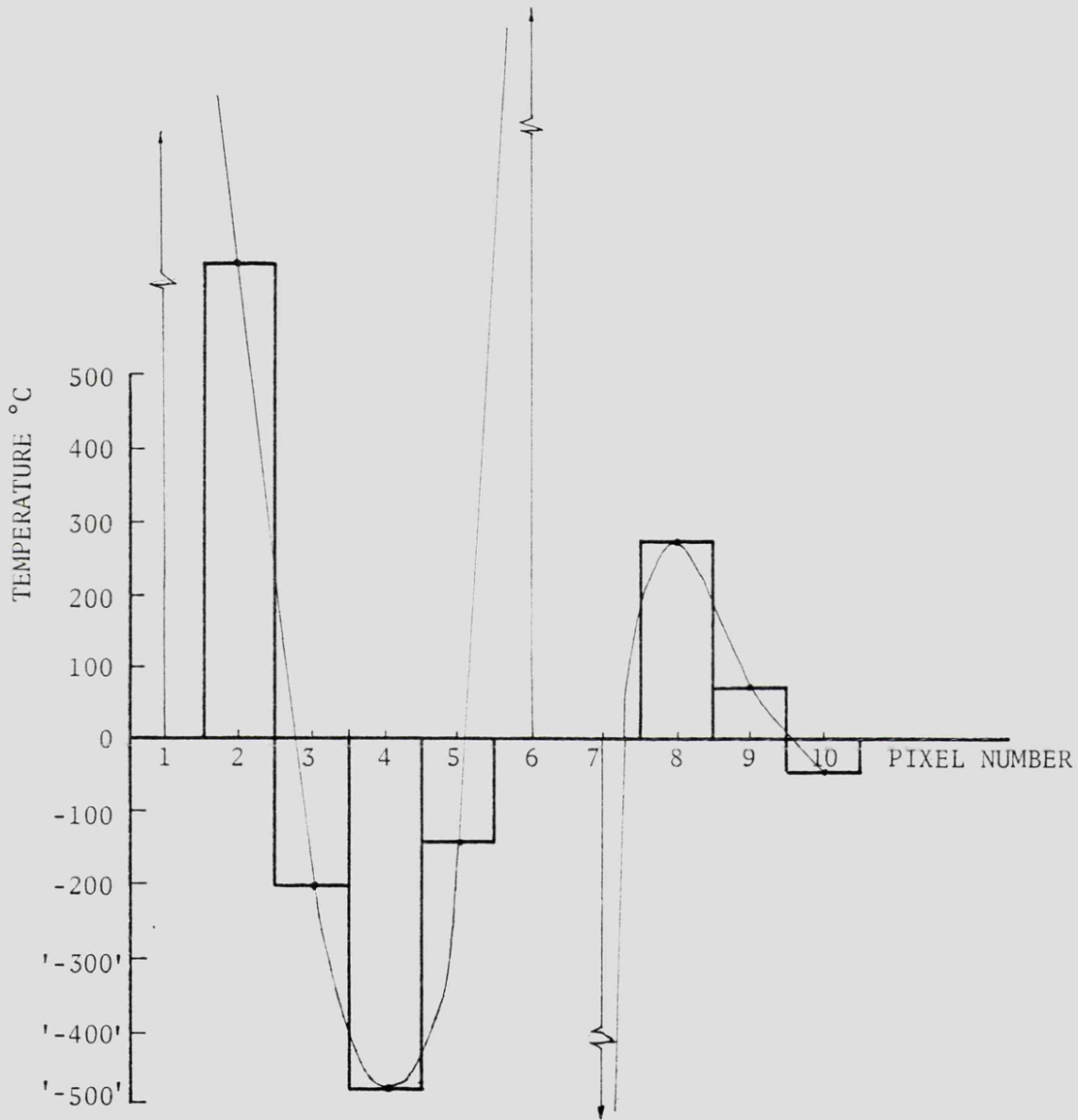
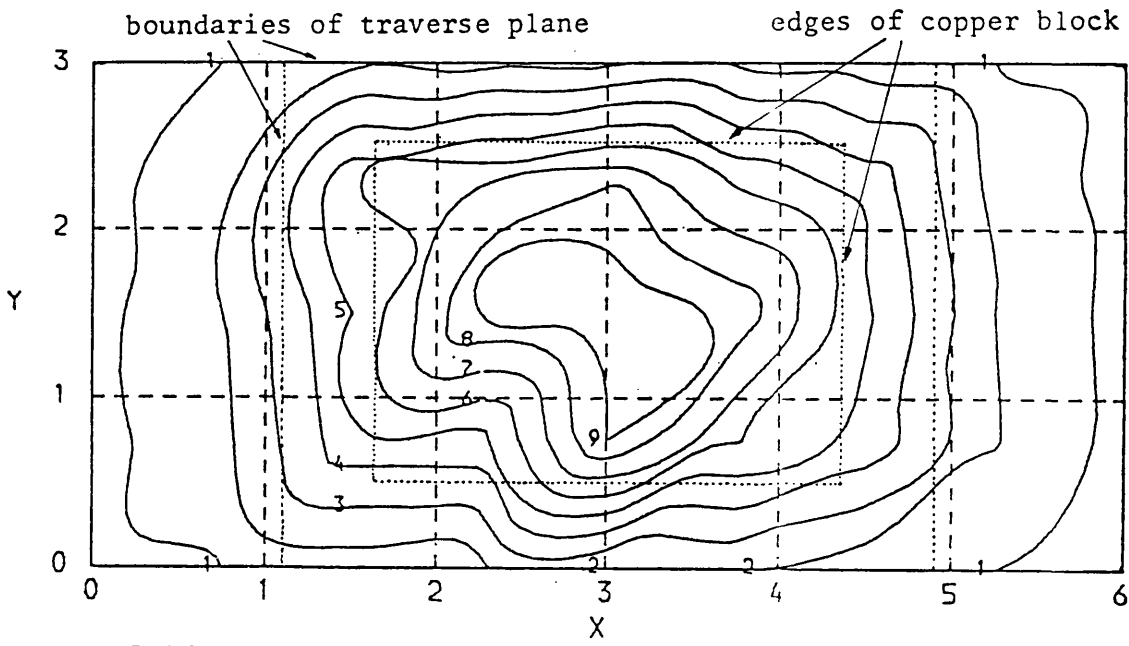


FIG. 4.7 PROFILE SHOWING INSTABILITY IN RECONSTRUCTION OF A SMOOTHLY VARYING TEMPERATURE DISTRIBUTION



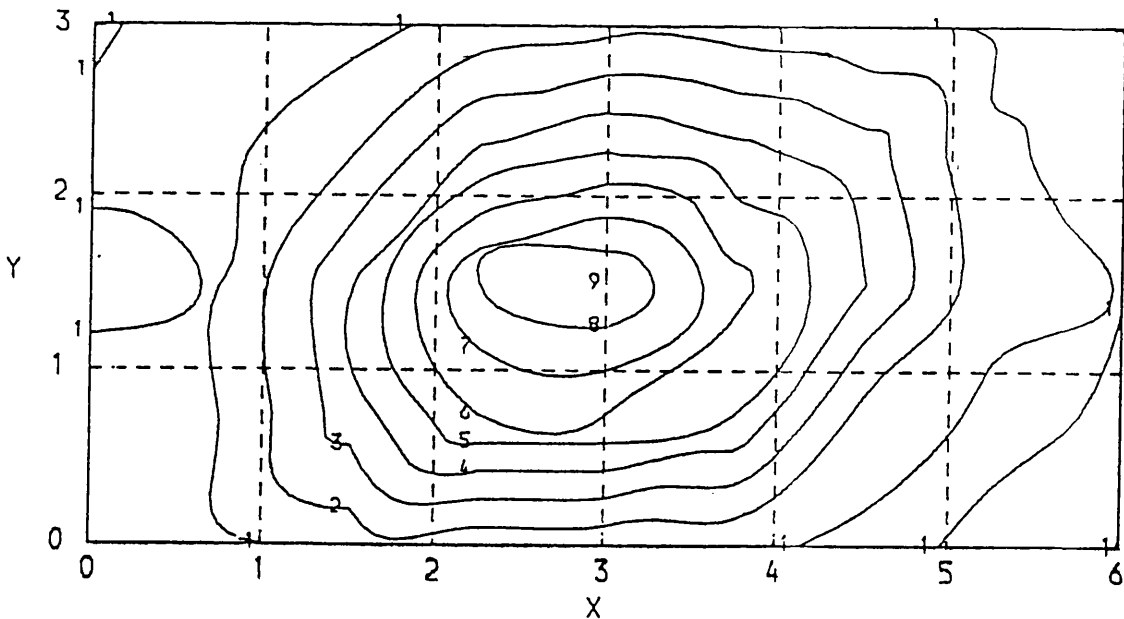
PLOT 4.1 TEST FIELD FROM THE THERMOCOUPLE TRAVERSE

Plane: 1.27 cm above top surface  
 and horizontal  
 Resolution: 9x10  
 Room temp: 20°C  
 Min & max temp: 24°C\*, 298°C

CONTOURS IN DEG C

- 1= 30.00
- 2= 60.00
- 3= 90.00
- 4= 120.00
- 5= 150.00
- 6= 180.00
- 7= 210.00
- 8= 240.00
- 9= 270.00
- 10= 300.00 ETC.

\*at a point outside plane  
 traversed but within plane plotted



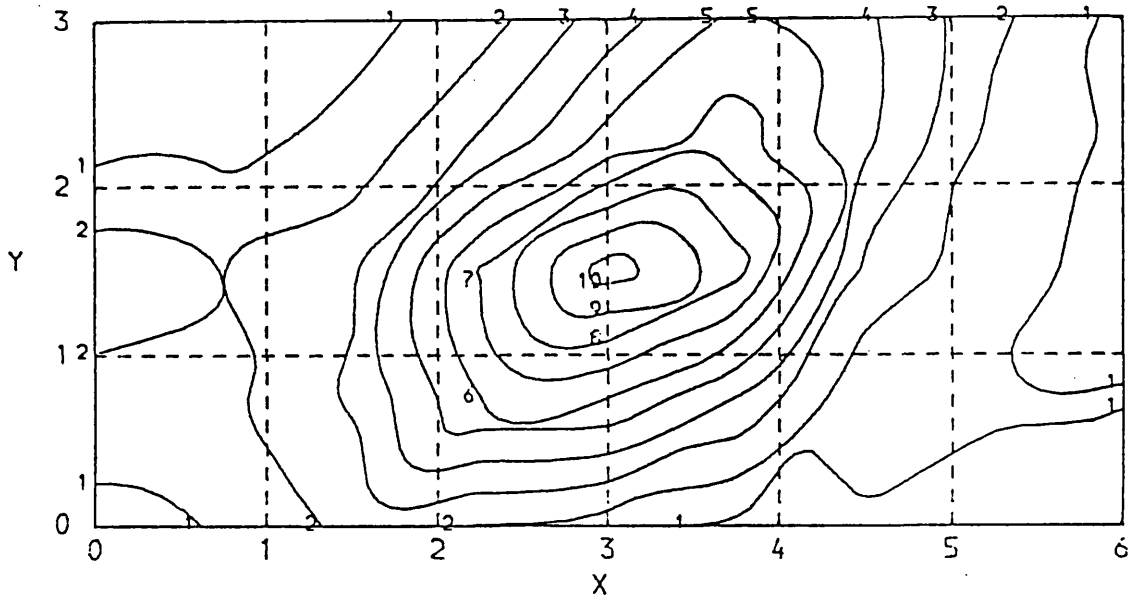
PLOT 4.2 RECONSTRUCTED FIELD USING ART & SIMULATED DATA

Plane: 1.27 cm above top surface  
 Model: Grid element  
 Resolution: 13x7  
 Angle range: 70°  
 No. of rays: 200  
 No. of projections: 8  
 No. of iterations : 100  
 Min & max temp: 20°C, 270°C

CONTOURS IN DEG C

- 1= 30.00
- 2= 60.00
- 3= 90.00
- 4= 120.00
- 5= 150.00
- 6= 180.00
- 7= 210.00
- 8= 240.00
- 9= 270.00
- 10= 300.00 ETC.

Computation time: 39s cpu, k=101



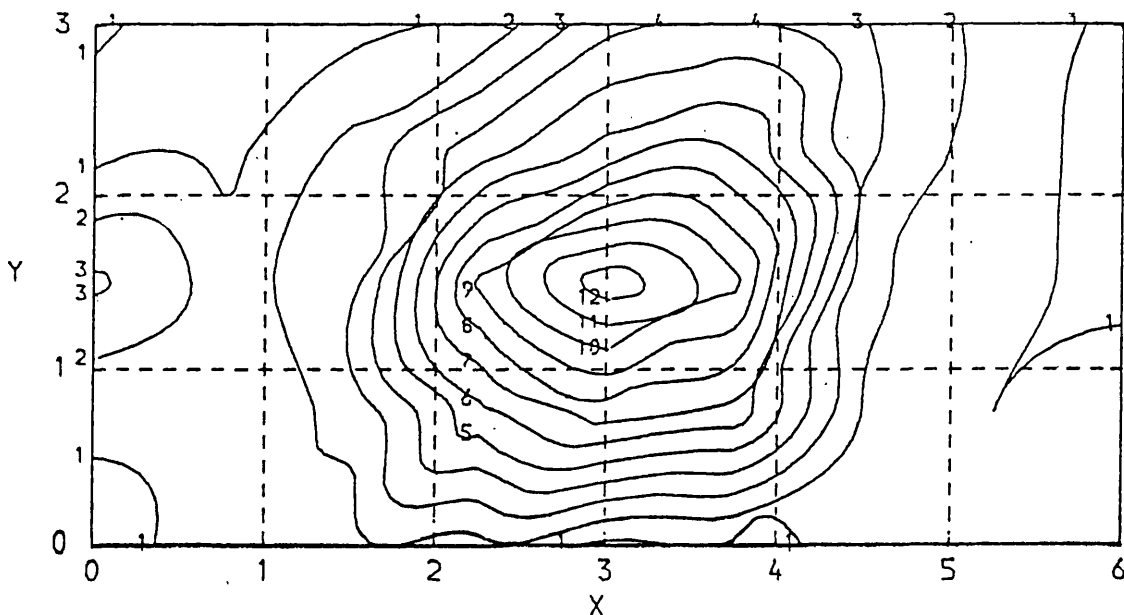
PLOT 4.3 RECONSTRUCTED FIELD USING ART & DIGITISED DATA

CONTOURS IN DEG C

Plane: 1.27 cm above top surface  
 Model: Grid element  
 Resolution: 13x7  
 Angle range: 70°  
 No. of rays: 200  
 No. of projections: 8  
 No. of iterations k: 17  
 Min & max temp: 20°C, 315°C

1= 30.00  
 2= 60.00  
 3= 90.00  
 4= 120.00  
 5= 150.00  
 6= 180.00  
 7= 210.00  
 8= 240.00  
 9= 270.00  
 10= 300.00 ETC.

Computation time: 32s cpu, k=101



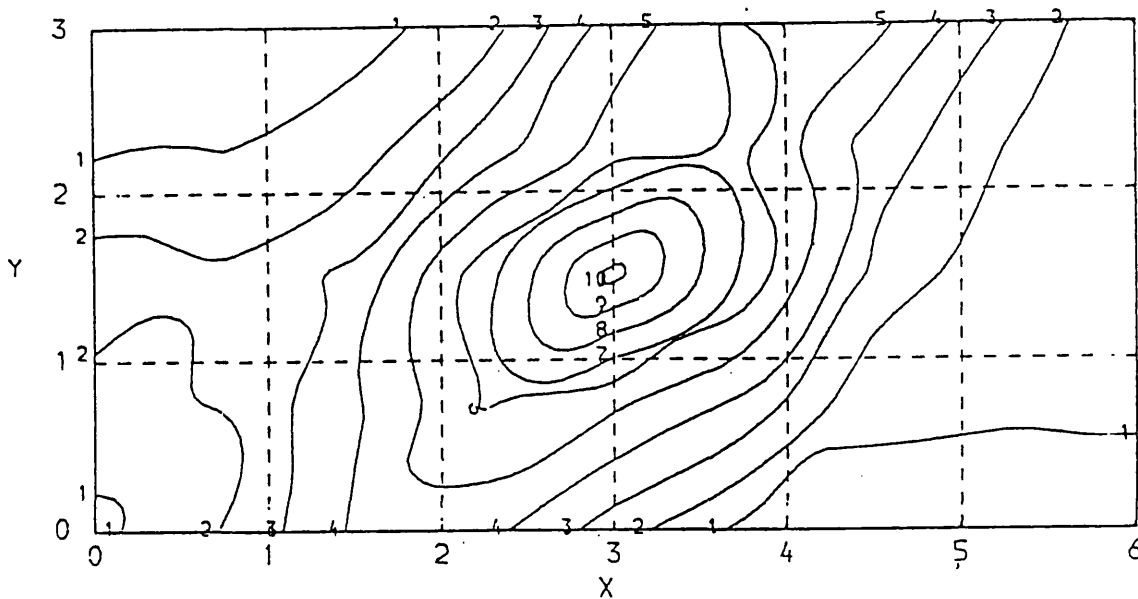
PLOT 4.4 RECONSTRUCTED FIELD USING ART & DIGITISED DATA

CONTOURS IN DEG C

Plane: 1.27 cm above top surface  
 Model: Grid element  
 Resolution: 13x7  
 Angle range: 70°  
 No. of rays: 200  
 No. of projections: 8  
 No. of iterations k: 53  
 Min & max temp: 20°C, 382°C

1= 30.00  
 2= 60.00  
 3= 90.00  
 4= 120.00  
 5= 150.00  
 6= 180.00  
 7= 210.00  
 8= 240.00  
 9= 270.00  
 10= 300.00 ETC.

Computation time: 32s cpu, k=101



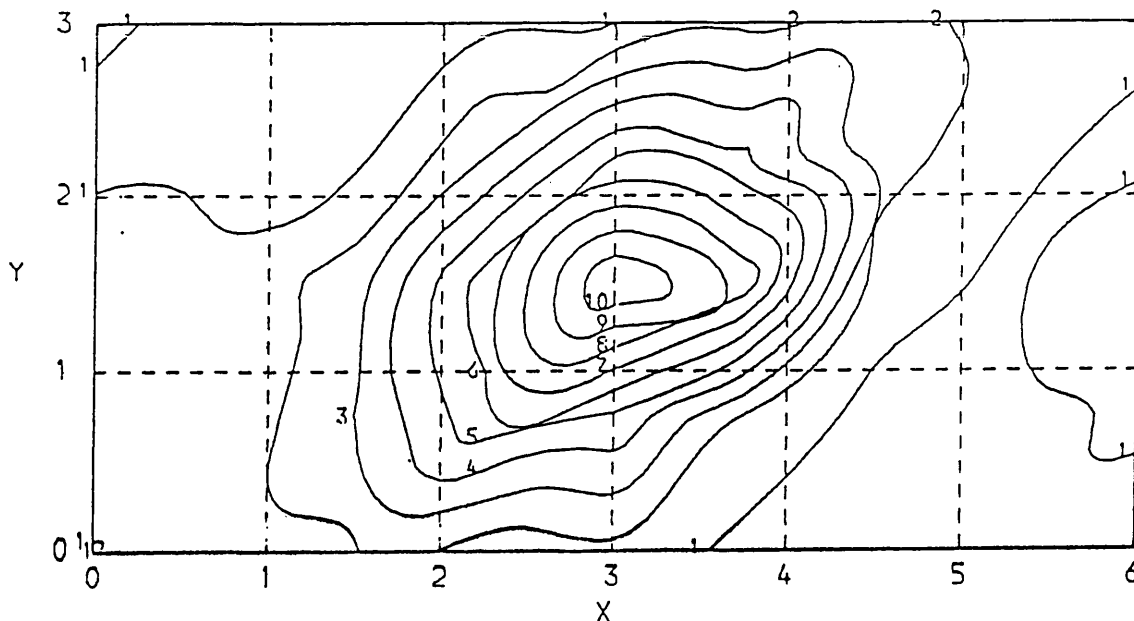
PLOT 4.5 RECONSTRUCTED FIELD USING ART & DIGITISED DATA

CONTOURS IN DEG C

Plane: 1.27 cm above top surface  
 Model: Finite element  
 Resolution: 6x3  
 Angle range: 70°  
 No. of rays: 200  
 No. of projections: 8  
 No. of iterations k: 27  
 Min & max temp: 20°C, 309°C

1= 30.00  
 2= 60.00  
 3= 90.00  
 4= 120.00  
 5= 150.00  
 6= 180.00  
 7= 210.00  
 8= 240.00  
 9= 270.00  
 10= 300.00 ETC.

Computation time: 114s cpu, k=84



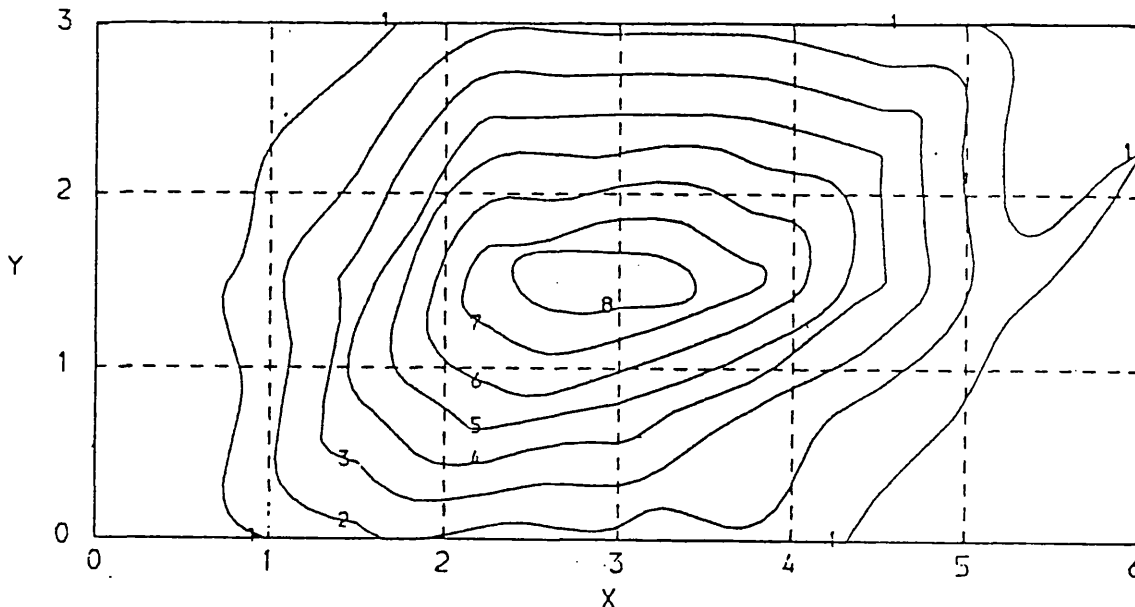
PLOT 4.6 RECONSTRUCTED FIELD USING LSRT & DIGITISED DATA

CONTOURS IN DEG C

Plane: 1.27 cm above top surface  
 Model: Grid element  
 Resolution: 9x5  
 Angle range: 70°  
 No. of rays: 200  
 No. of projections: 8  
 No. of iterations k: 37  
 Min & max temp: 20°C, 331°C  
 Computation time: 114s cpu, k=200

1= 30.00  
 2= 60.00  
 3= 90.00  
 4= 120.00  
 5= 150.00  
 6= 180.00  
 7= 210.00  
 8= 240.00  
 9= 270.00  
 10= 300.00 ETC.

Sum of square of @ residual  
 17.9 (cf. 1468.7 at k=2)



PLGT 4.7 RECONSTRUCTED FIELD USING LSRT & SIMULATED DATA

Plane: 1.27 cm above top surface

Model: Grid element

Resolution: 9x5

Angle range: 70°

No. of rays: 200

No. of projections: 8

No. of iterations k: 200

Min & max temp: 19.4°C, 256°C

Computation time: 98s cpu, k=200

CONTOURS IN DEG C

1= 30.00  
 2= 60.00  
 3= 90.00  
 4= 120.00  
 5= 150.00  
 6= 180.00  
 7= 210.00  
 8= 240.00  
 9= 270.00  
 10= 300.00 ETC.

Sum of square of @ residual:

1.82 (cf. 1292.2 at k=2)

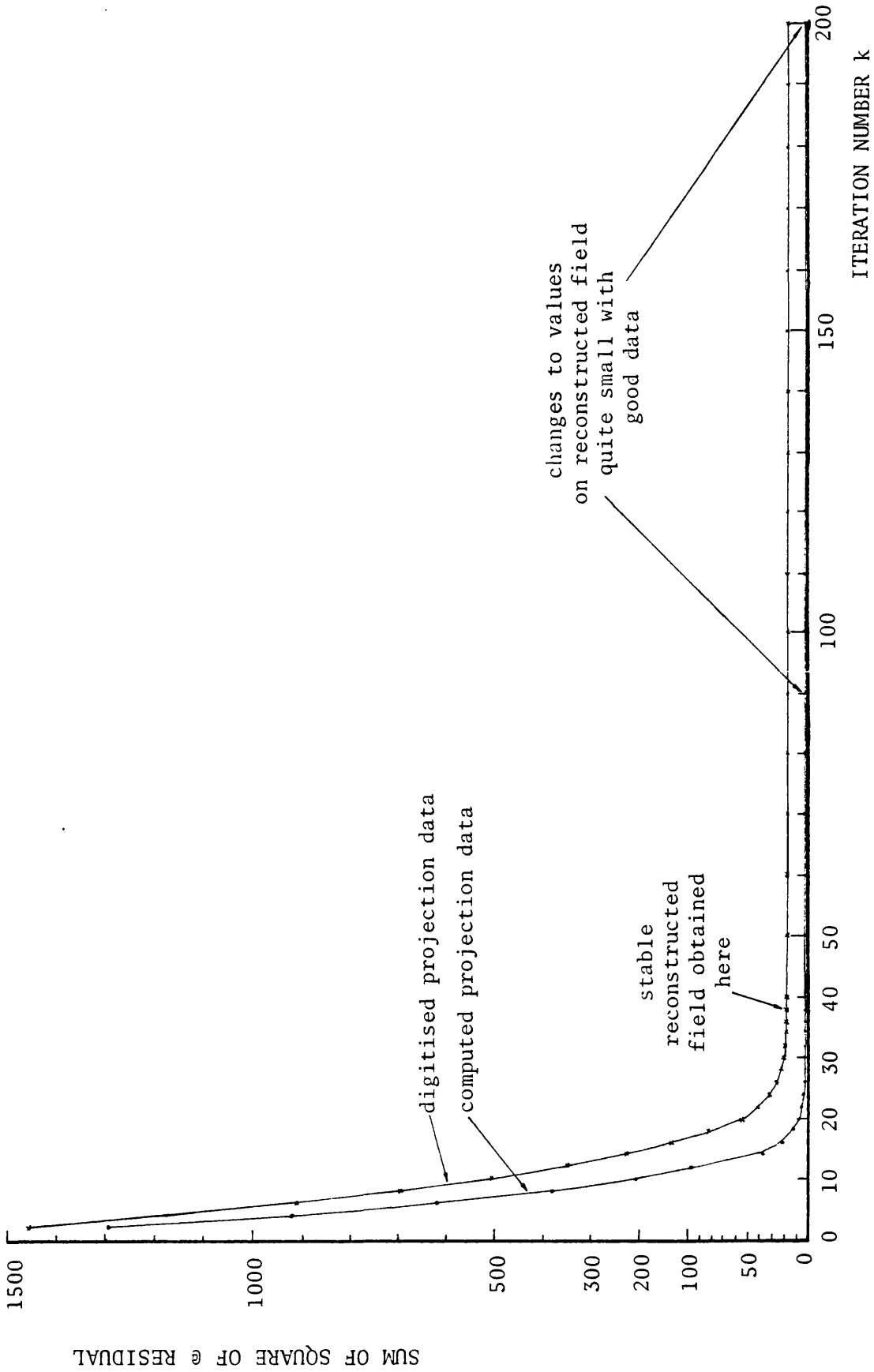


FIG. 4.8 SUM OF SQUARE OF @ RESIDUAL AGAINST ITERATION NUMBER k  
ON RECONSTRUCTION WITH LSRT

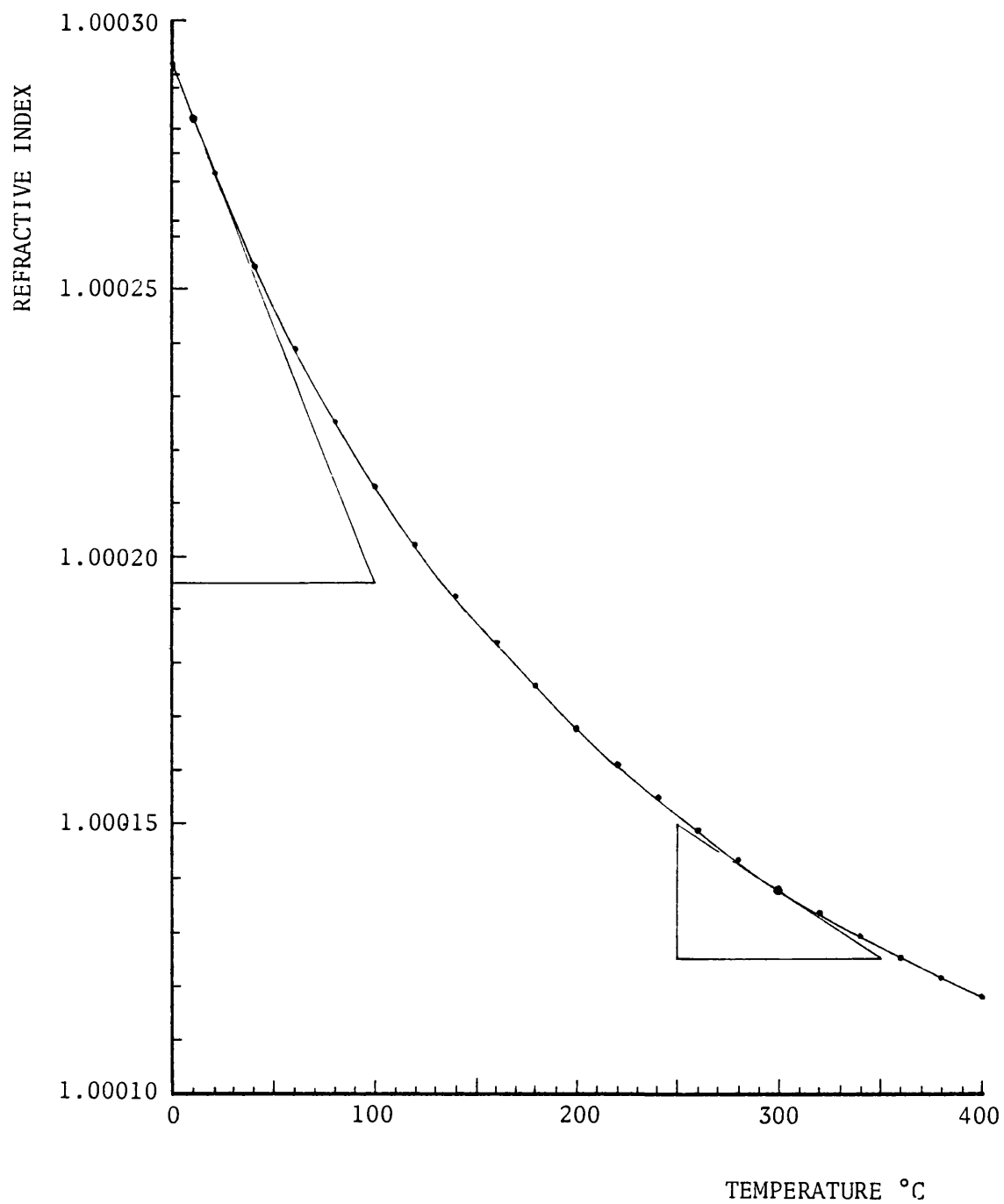


FIG. 4.9 RELATIONSHIP BETWEEN REFRACTIVE INDEX AND TEMPERATURE  
FOR AIR AT 632.8 nm

SYNOPSISCHAPTER 5FABRICATION OF MODEL OF LOCALISED HEATING IN AN ENCLOSURE

As mentioned in Chapter 1 the 3-D temperature field of interest is that due to a heated spot on the floor of an enclosure with constant temperature walls, ceiling and floor. The design and construction of this apparatus, including the pulsed laser holographic interferometer are described. To obtain digitised projection data over a wide range of viewing angles it has been found necessary to build the interferometer with multiple object/reference beam pairs. A description is also made of the set-up for re-illuminating the interferograms to gather the fringe data.

In reconstructing the temperature fields from this experiment utilising numerical techniques similar in principle to those used for reconstructing the test temperature field from the heated copper block of Chapter 4, the computer program requires the relationship between the refractive index and temperature for water, and this has been found.

## CHAPTER 5

### FABRICATION OF MODEL OF LOCALISED HEATING IN AN ENCLOSURE

#### 5.1 INTRODUCTION

This experiment determines the 3-D temperature distribution from the natural convection of a localised heat source in an enclosure having double skin walls maintained at a constant temperature.

The design of the apparatus follows a set of practical constraints within which interferograms with a wide range of viewing angles can be produced with ease. The constraints are:-

- (i) due to the limited energy output of the pulsed laser the holographic interferometer to be built can only have two reference/object beam pairs,
- (ii) no collimated beams can have a diameter greater than 14.5 cm, this being the maximum size of commercially available optics.

For good temperature field reconstruction at least the same number of accurately located values of  $N$ , the fringe number, is needed as the number of pixels in the picture. For example, in reconstruction of a picture with a resolution of  $10 \times 9$  or less, with data from nine viewing angles spread over a  $70^\circ$  field of view, interferograms with 10 or more fringes are desirable. These would give measurements of  $N$  at distance  $r$  from the origin to an accuracy to within  $\pm 5\%$ .<sup>\*</sup> If however there are only two to three fringes then to obtain the same number of data points, most of the values will be unreliable, obtained by interpolating between fringes.

The number of fringes on an interferogram is a function of the pathlength

\* For an object to be covered with ten interferometric fringes there will be twenty-one bright and dark bands. Each of these bands can thus be located with an accuracy of  $\pm 1/21$  of the entire fringe pattern or to within  $\pm 5\%$ .

through the test region, the temperature changes within that region and the variation of refractive index with temperature of the test medium. As already mentioned test enclosure size is limited by the available optics and this in turn means the localised heater is fairly small.

Preliminary tests were made, using a Mach-Zehnder interferometer on a short square heater of dimension 15mm x 15mm x 7mm in free air. This heater was made by sandwiching a heating element between two thick pieces of copper clamped together by screws. With the heater glowing at a dark reddish orange colour fringe shifts of only three wavelengths were produced. The heater glowing red implies quite high air temperatures. It was noted in Chapter 4 that it is better to have a temperature field with small changes of temperature because the behavior of refractive index with temperature is non-linear.

Pressurising the air in the system is a way of producing a greater number of fringes due to the effect on refractive index value (see eqn. 4.7). However this method was not pursued due to the complexity of producing a pressurised container with walls cooled and with sufficient wall area transparent to give the required field of view.

An alternative test medium is water. At the sizes involved this can produce the required number of fringes with relatively small temperature changes so that operation remains in the linear portion of the refractive index - temperature curve. Since the test enclosure need not be pressurised and since the wall cooling medium and the test medium - water - can be the same, a simple rig is possible.

In the following sections the design and construction of the apparatus, including the multiple beam holographic interferometer are described.

## 5.2 THE TEST ENCLOSURE

Trial tests were made using an acid ground glass diffusing screen of width 23 cm with two object beams shining on it at angles of approximately  $27^\circ$  from the normal, as in fig. 5.1. A pair of holographic plates placed in front of this, as shown, could record the diffusing screen and were able to give a viewing angle range of approximately  $120^\circ$ . It was found that by moving the holographic plates away from the diffusing screen beyond 25 cm there was an appreciable drop in the intensity of the diffused light reaching the plates, making recording difficult. This sets limits on the available space for the test section.

A 10 x 5 cm floor plan, with an effective floor area of 9.5 x 4.5 cm, and with an effective height of 6 cm, was chosen as the dimensions of the test enclosure which would fit adequately in the test section of fig. 5.1.

The basic chamber required was a rectangular box having a metal base and a top with side walls of transparent material. The outside faces of this box have to be kept at a constant temperature. Initially the method tried was to set such a test chamber in a large tank of water. However preliminary double exposure holograms showed the fringe system extending into the region just outside the walls of this chamber representing the enclosure. The form of this temperature boundary layer indicated that the requirement of constant wall temperature was not achieved.

To overcome this a box was made in which the side wall were double skinned so that water could be continually drained through the space so formed. The top and bottom plates had cooling passages in them through which water could flow.

Two open boxes were made. An outer "open top" box had a copper floor 1.5 mm thick in which ten grooves 1.2 mm deep were milled. A 1.0 mm

thick copper sheet was stuck across the top of these grooves thereby forming the cooling passages. Around the periphery this plate had small holes drilled through its thickness, at 4.5 mm intervals, so that they came within the thickness of the side wall skin. Small stub lengths of stainless steel hyperdermic tube were fixed into these holes on the underside to which were attached flexible nylon drain tubes. Across the centre similar holes were drilled from the underside through into the cooling passages. Again stub tubes and nylon drain tubes were attached. Outer side walls of 1.5 mm thick glass were fixed to this floor plate strengthen by metal corner guide posts.

An inner "open box" was made. The metal top was made with cooling passage in the same way as the bottom plate. However, no holes were drilled. Small stub tubes were fixed in one end of these grooves and drain tubes attached. The other end was left open.

The transparent side walls of this box presented a problem. A material was required which was transparent. It had to be very thin, so that little thermal resistance was offered, to conduct heat away into cooling water flowing past it thereby keeping the walls at constant temperature. Yet it had to be stiff enough to adequately define the wall. Very thin materials such as overhead projector transparency film or chocolate box wrapping were far too flexible and had a tendency to curl although they filled the other criteria. Kodak Pan-X sheet film backing, 5" x 4", was found the most useful. The emulsion coating was quite easily removed by scraping with a plastic scraper the film which were soaked in ordinary concentrated household bleach.

This inner "open box" representing the actual test enclosure was made so that it slides into the slightly larger open top box guided by the

corner posts. The bottom edge of the inner transparent side wall sat squarely on the bottom plate which had thin transparent 2 mm square L shape section defining the inner wall and making the inner enclosure draught free. When in place a double skin wall with an open top and drain holes at the bottom was formed. Araldite adhesive was used throughout for fixing the parts together. However in water some of the glass joints on the glass windows to the guide posts became weak after a period of approximately one month. Because of the guide posts defining the double skin walls the effective floor area of enclosure was therefore 4.5 x 9.5 cm - a size appropriate to the space available between the ground glass screen and the holographic plates. A plan view is shown in fig. 5.2.

This test enclosure sat in a much larger transparent wall tank filled with water. Water from the tank drained under gravity through the double skin of the wall and the cooling passages in the top and bottom plates. The water then flowed through the drain tubes out of the tank to waste.

In practice this system worked very well and interferograms shown later in Chapter 5 indicate the constant wall temperature requirement is largely met.

#### 5.2.1 THE TEST TANK

The large tank just referred to had an additional function as well as acting as a reservoir of cooling water.

With the test enclosure in air difficulties are encountered when collecting projection data at a viewing angle which encompasses a corner due to the refractive effects at adjacent sides at right angles. Two parallel rays each passing through one of the sides in such a way that they cross. By surrounding the test enclosure with water this difficulty is overcome.

This outer test tank was made long and narrow so that the two reference beams could pass through undisturbed.

Glass walls of thickness 3 mm were sealed onto the aluminium frames with EVO-Stick silicone rubber. The detachable base was made out of two layers of 12.6 mm machined perspex. The 47 draining tubes were passed through the base. Fig. 5.3 shows a photograph of the tank with the enclosure in place.

The dimensions of this tank are length 61.0 cm, height 13.6 cm and depth 11.9 cm.

#### 5.2.2 THE COOLING SYSTEM

During an experiment the whole of the enclosure was cooled by draining the water in the test tank through the ducts in the top and floor plates, and the four double skin walls. Water at a constant temperature from a reservoir tank holding 68.2 litres refills the tank continually to the top level through a regulating valve at the bottom of the reservoir. The draining tubes from the top plate of the enclosure with some from the bottom plate were joined onto a perspex connecting tube which lead to a drain exit valve. The rest of the tubes in two bundles were also joined to similar connecting tubes, as shown in fig. 5.3a, and were lead to another drain exit valve. The flow of water from the reservoir to the test tank, and from the enclosure to the drain was by gravity. The top level of the reservoir was 0.5 m above the exit, and the top level of the test tank above the test tank was 1.2 m above the drain exit valves.

The rate of coolant flow was monitored visually through the vertical perspex drainage tubings connected to the drain exit valves, fig. 5.3b. Double exposure holograms showed satisfactory results, with only one or two background fringes, when the coolant flowrate was regulated to

63.6 litres /hour.

Finite background fringes should not appear if the temperature of the water in the test tank was constant during the two exposures. Calculations indicated two fringes would appear if the temperature change by  $0.1^{\circ}\text{C}$  in the test tank.

### 5.2.3 THE HEATERS

Two flat coils of heating elements sandwiched in between three pieces of thin copper plates formed the heater. A 30 V, 2 A stabilised direct current supply provided the input power. The heating elements were made from wires from an element similar to that used in making the heated copper block. It was found necessary to seal all electrical parts from the water as electrolytic erosion causes an open circuit very quickly. Araldite adhesive was used.

Heater size : 15 mm x 15 mm x 7 mm  
Input voltage : 17.5 V dc  
Input current : 0.75 A

A taller heater measuring 35 mm x 35 mm x 15 mm was also made to compare the flow circulation pattern. Input power was 39.0 W.

### 5.3 THE HOLOGRAPHIC INTERFEROMETER

A two object/reference beam holographic interferometer was designed to produce the wide angle interferograms of the temperature field in the constant temperature test enclosure. The use of more than two pairs of object/reference beams would not give a substantial increase in the range of viewing angles because incident rays striking the window on the test tank from acute angles are diffracted much more than those rays coming

at angles closer towards the normal. Moreover the limited output of the pulsed laser which was used as the light source would distribute an unacceptably low level of intensity on the holographic plates. The resulting interferograms would have a much weaker image, unlikely to be clear enough for digitising.

In building this interferometer, concave rather than convex lenses were used for expanding the beams. They have no real focal points, and thus the air cannot be ionised whenever the laser is fired. The laser also had a built-in concave lens which made the output beams diverging to reduce the intensity level. However, steering and splitting this continuously expanding main beam to the holographic plates, ending up with the correct magnification so as to illuminate the whole of the holographic plates, proved awkward and cumbersome. If the built-in lens were removed, it would be much easier to steer the unexpanded practically parallel main beam with a nominal diameter of only 1.5 mm. However this could not be regarded as practical. In tests involving firing the pulsed laser directly onto optical elements, laser damage to the cement in the beam splitting cube, surfaces of semi-reflecting and fully reflecting mirrors was clearly visible.

The most effective method found was to expand and collimate in two stages. The first stage was to collimate the expanding beam at some small and yet safe diameter standard size, small optical elements to be used. With the built-in concave lens in position, test firing of the laser onto a lightly coated semi-transparent mirror showed no discoloration at a distance where the beam had expanded to 10 mm in diameter. The collimating convex lens, calculated to have a focal length of 10 cm, was placed at this distance. This collimated main beam was divided into two beams, and each of these was divided again to produce the object and reference beam pairs -

see fig. 5.4. When all the beams were aligned to pass through the test tank and to the photographic plates, the pathlengths from each of the secondary beamsplitters to the holographic plate was adjusted to match one another. In this interferometer all pathlengths were matched right back to the main beamsplitter to within 5 cm, which is the coherence length of this pulsed laser. The second stage involved expanding each of the beams further with a 20 mm fl concave lens, and collimating or condensing most of these with 33 cm fl semi-convex lenses.

The optics were aligned using a 5mW helium-neon Spectra-Physics model 126 laser, the beams of which was shone through the back of the pulsed laser. First, the beam of the helium-neon laser had to be aligned with the pulsed laser. This was accomplished by allowing the pulsed laser without the built-in lens in place to make a burn mark at a distance of some 1.5 m away on to a black piece of print paper, (made by developing and fixing a piece of photographic paper exposed to bright ordinary light). The beam from the He-Ne laser was then adjusted to line up with this burn mark. Finally, with the built-in lens put back in place, the laser was fired again, and fine adjustments were made to the expanded He-Ne beam until it matched up with that from the pulsed laser.

Two pieces of white cards were mounted onto the holographic plate holder and the mirrors were adjusted carefully until the maximum intensity, especially from the object beams, fell on the cards. At this stage the holographic system was ready to be tested. Two pieces of 8E75HD holographic plates measuring 85 mm x 203 mm cut from a 8" x 10" piece were placed in the holders. Holograms produced showed a good image over a good range of angles. Near the edges of the holograms, where the intensity of the object beam was lower, the image was not so good but still visible. In

making the holographic interferograms it was found essential to maintain the temperature of the coolant to the ruby laser rod in the range 15 - 19°C. At less than 15°C the laser output increases slightly to more than the rated 30mJ, and produced streaks of vertical dark bands at approximately 10 mm apart all the way across the interferograms.

Fig. 5.5 is a photograph showing the completed interferometer. Also shown on the left hand side at the front of the wooden surface optical table is the optical set-up for flow visualisation . The piece of apparatus with vane blades shown at the bottom was used to produce stroboscopic flow visualisation photographs.

#### 5.4 COLLECTION OF FRINGE DATA FROM INTERFEROGRAMS

The interferograms were illuminated in pairs using two re-illuminating reference beams. In order to produce a good image the re-illuminating beams came from two continuous wave He-Ne lasers available in the Department instead of one. Fig. 5.6 shows the optical set-up for reconstruction.

The fringe patterns from the various projection angles were recorded, as described in Chapters 2 and 4, with the Nikon FM camera fitted with a 200 mm fl telephoto lens on an extension tube. The projection angles were determined by reading off from the scale of a protractor, a calibrated semi-circular disc, placed on top of the interferograms, as shown in fig. 5.7. The camera using Ilford fine grain ASA 100 FP4 film took three frames with varying exposure times from 0.5 to 30 seconds from each of the projection angles at intervals of approximately 10°. The sharpest one of each three was used for digitising. After digitisation of each print the true projection angle through the enclosure and the magnification factor of that print were calculated to produce a complete input data set.

Fig. 5.8 is a photograph showing the paths of the laser beams.

Because the centres of these beams had the highest intensities the contrast of the interference patterns in places was improved by shifting these beams slightly to the desired regions on the interferograms. The resulting image distortion from such a move was negligible.

### 5.5 RELATIONSHIP BETWEEN REFRACTIVE INDEX OF WATER AND TEMPERATURE

The fringe pattern on the interferogram results from the change in optical pathlength between the two exposures. This change is determined by refractive index variations along that pathlength. The reconstruction program evaluates the refractive index difference value for each pixel. These values are then changed to temperature values using an appropriate expression for the temperature dependence of refractive index.

Tilton and Taylor (1938) produced a tabulated set of results for the refractive index of water over a range of temperatures from 0°C to 60°C at 5°C intervals for a number of spectral lines. There were however no tabulated values at the ruby laser wavelength of 694nm, nor at 632.8nm for the helium-neon laser. To deduce the relationship between the refractive index and temperature for the line at 694nm, some of Tilton and Taylor's results were plotted as shown in fig. 5.9. Replotting as shown in fig. 5.10 in the form of refractive index versus wavelength for a constant temperature allowed easy reading of values at 694nm. These interpolated values are replotted on fig. 5.9. In the 0°C to 40°C range within which reconstruction was required a good fit for the wavelength at 694nm is the equation

$$(n - 1.33118) = -(1.26T + 0.172T^2) \times 10^5 \quad (5.1)$$

or

$$T = - \left[ \frac{1.26}{2 \times 0.172} \right] + \left[ \frac{1}{2 \times 0.172} \right] \cdot \left[ 1.26^2 - 4.0 \times 0.172 \times [(n-1.33118) \times 10^5] \right]^{0.5}$$

..... (5.2)

where T is in °C, and  $(n-1.33118)$  is the change in refractive index.

The quadratic form of eqn. 5.1 is based on the work of Dobbins and Peck (1973).

At the time of developing the temperature field reconstruction program, Taylor and Tilton's results were not available, and the relationship of Radulovic (1977) was actually used as a temporary measure in converting refractive index difference values to temperatures:

$$(n - 1.3331733) = -(1.936xT + 0.1699xT^2) \times 10^{-5} \quad (5.3)$$

Fortunately when the results of Tilton and Taylor were obtained and plotted, the refractive index difference values against temperature difference values are similar in the range 18°C to 25°C, over which temperatures were reconstructed, and therefore eqn. 5.1 was not being used. Eqn. 5.1 is at 694nm for water while eqn. 5.3 is at 632.8nm for water.

As a point of interest it was noted that the absolute values of refractive index from eqn. 5.3 are slightly shifted or over-estimated as shown in fig. 5.9 it should be

$$(n - 1.33275) = -(0.85xT + 0.185xT^2) \times 10^{-5} \quad (5.4)$$

As a means of checking, Tilton and Taylor's results were compared with other sources such as those from Smithsonian Physical Tables and the American Institute of Physics Handbook, and were found to be in good agreement.

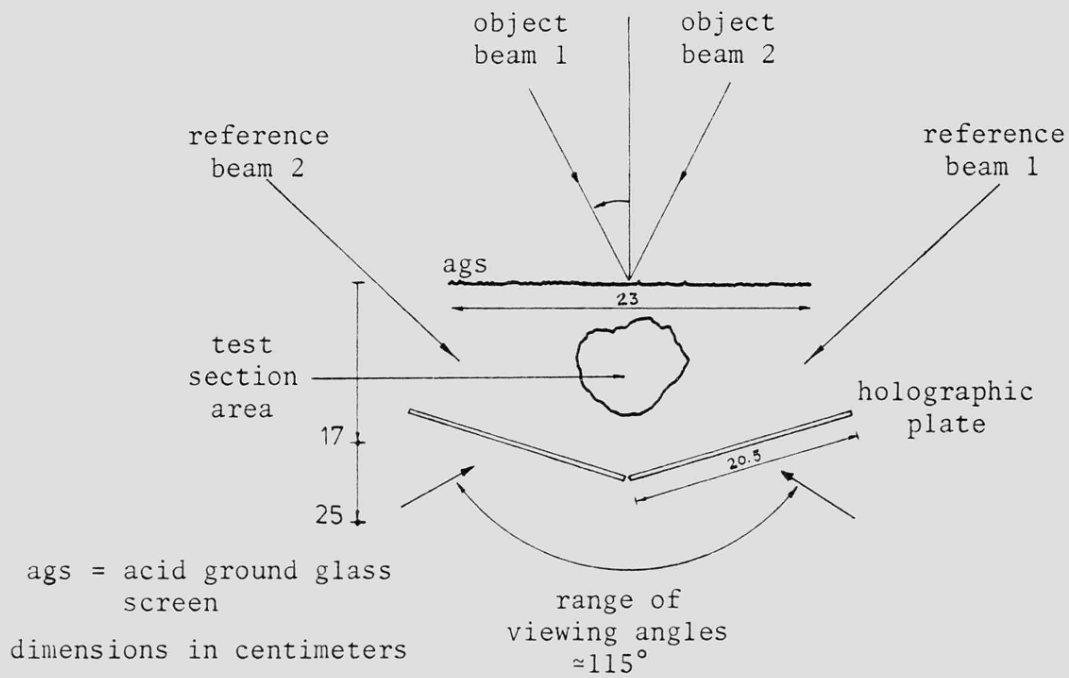


FIG. 5.1 ARRANGEMENT FOR PRODUCING PULSED LASER HOLOGRAMS WITH A WIDE RANGE OF VIEWING ANGLES

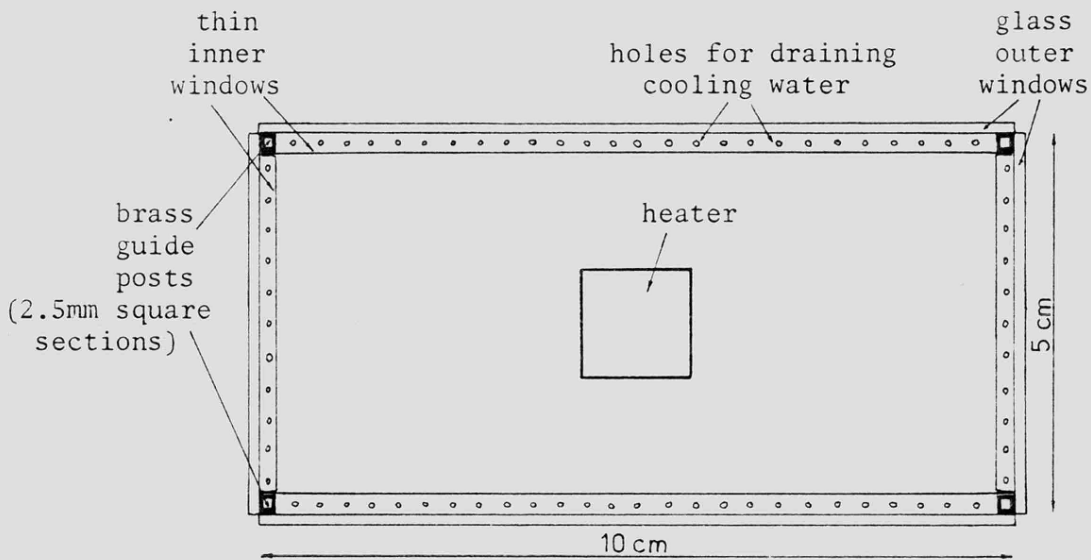


FIG. 5.2 PLAN VIEW THROUGH A SECTION OF THE CONSTANT TEMPERATURE ENCLOSURE

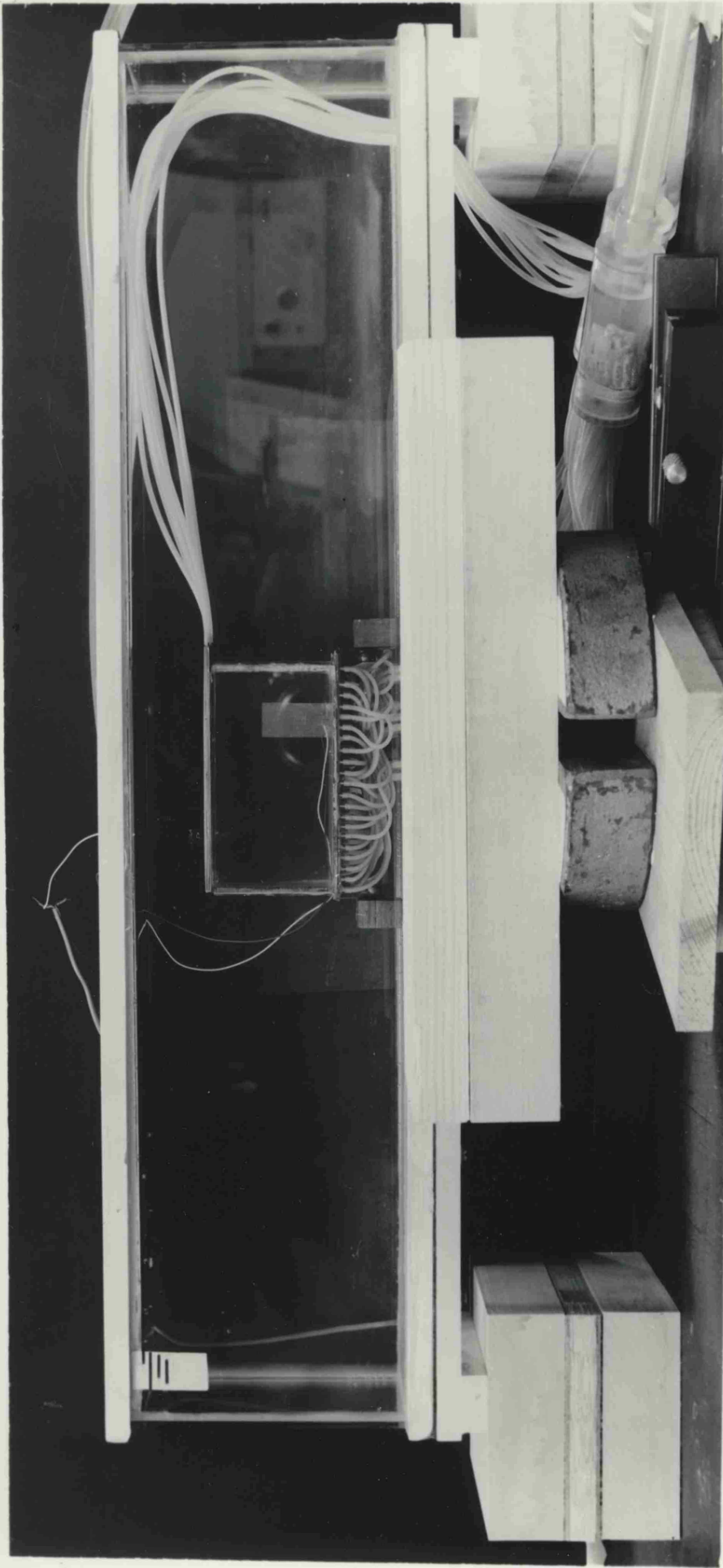


FIG. 5.3 TEST TANK WITH THE CONSTANT TEMPERATURE ENCLOSURE INSIDE

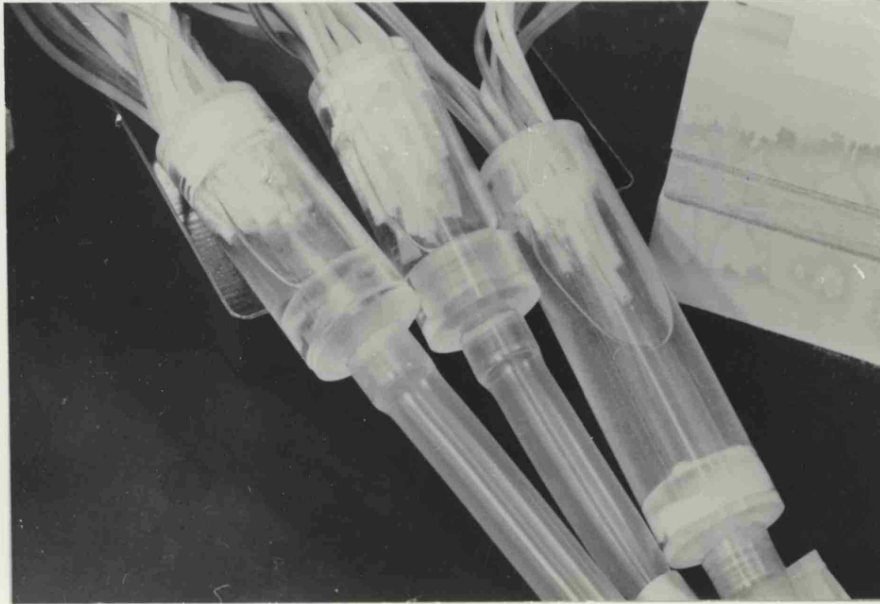


FIG. 5.3a COOLANT OUTLET TUBES JOINED  
ONTO THREE MANIFOLDS

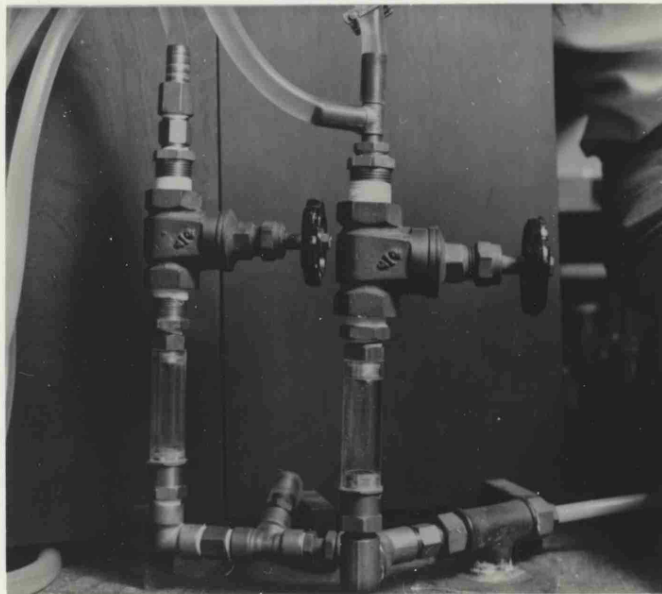
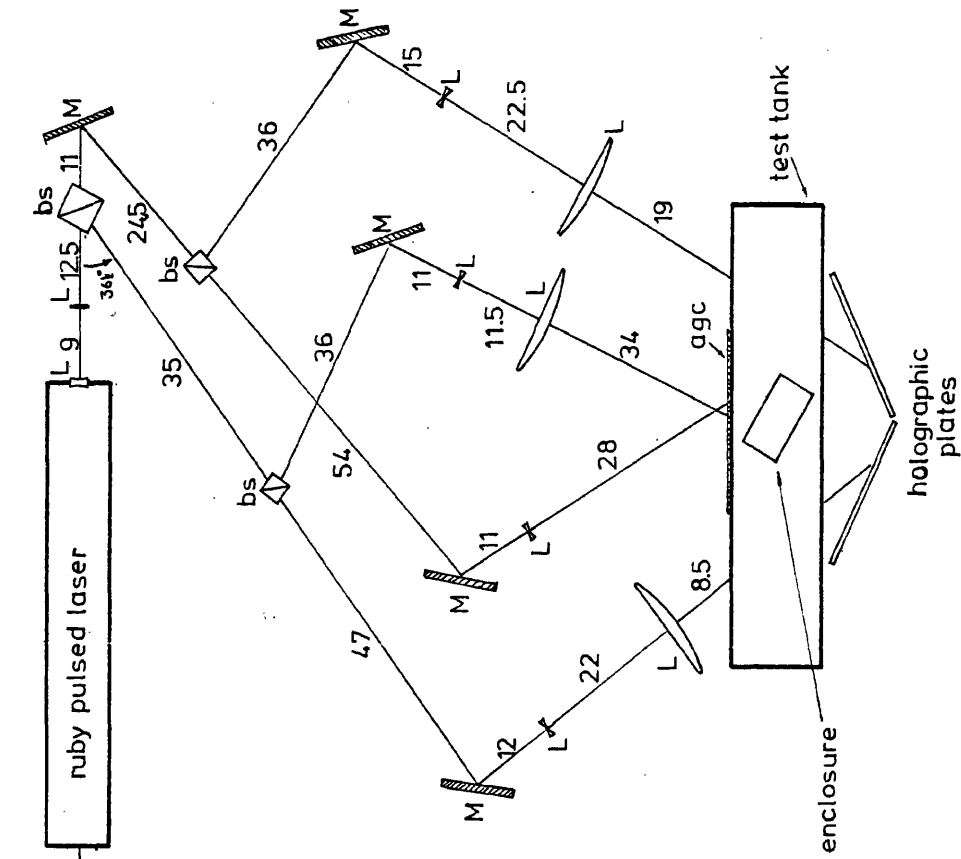


FIG. 5.3b COOLANT FLOW REGULATING VALVES  
WITH SHORT TRANSPARENT SECTIONS TO MONITOR  
FLOW



M = mirror  
 L = lens  
 bs = beamsplitter  
 ags = acid ground glass screen

Pathlengths in centimeters

FIG. 5.4 SCHEMATIC DIAGRAM OF THE 2 OBJECT/REFERENCE BEAM HOLOGRAPHIC INTERFEROMETER BUILT AROUND THE ENCLOSURE

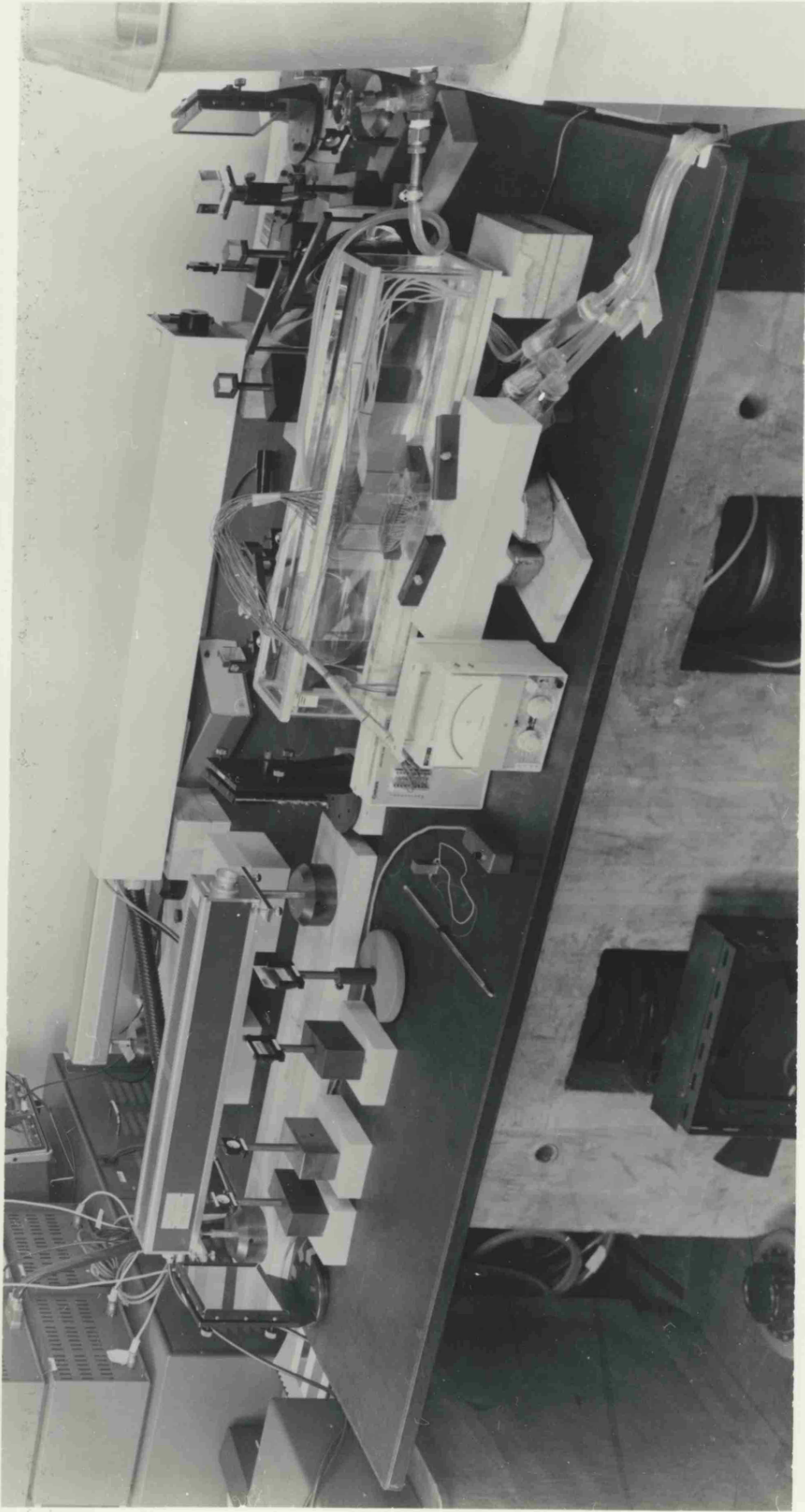


FIG. 5.5 PHOTOGRAPH OF THE TWO OBJECT/REFERENCE BEAM HOLOGRAPHIC INTERFEROMETER (TOP RIGHT SECTION), TOGETHER WITH OTHER MEASUREMENT FACILITIES (BOTTOM LEFT SECTION)

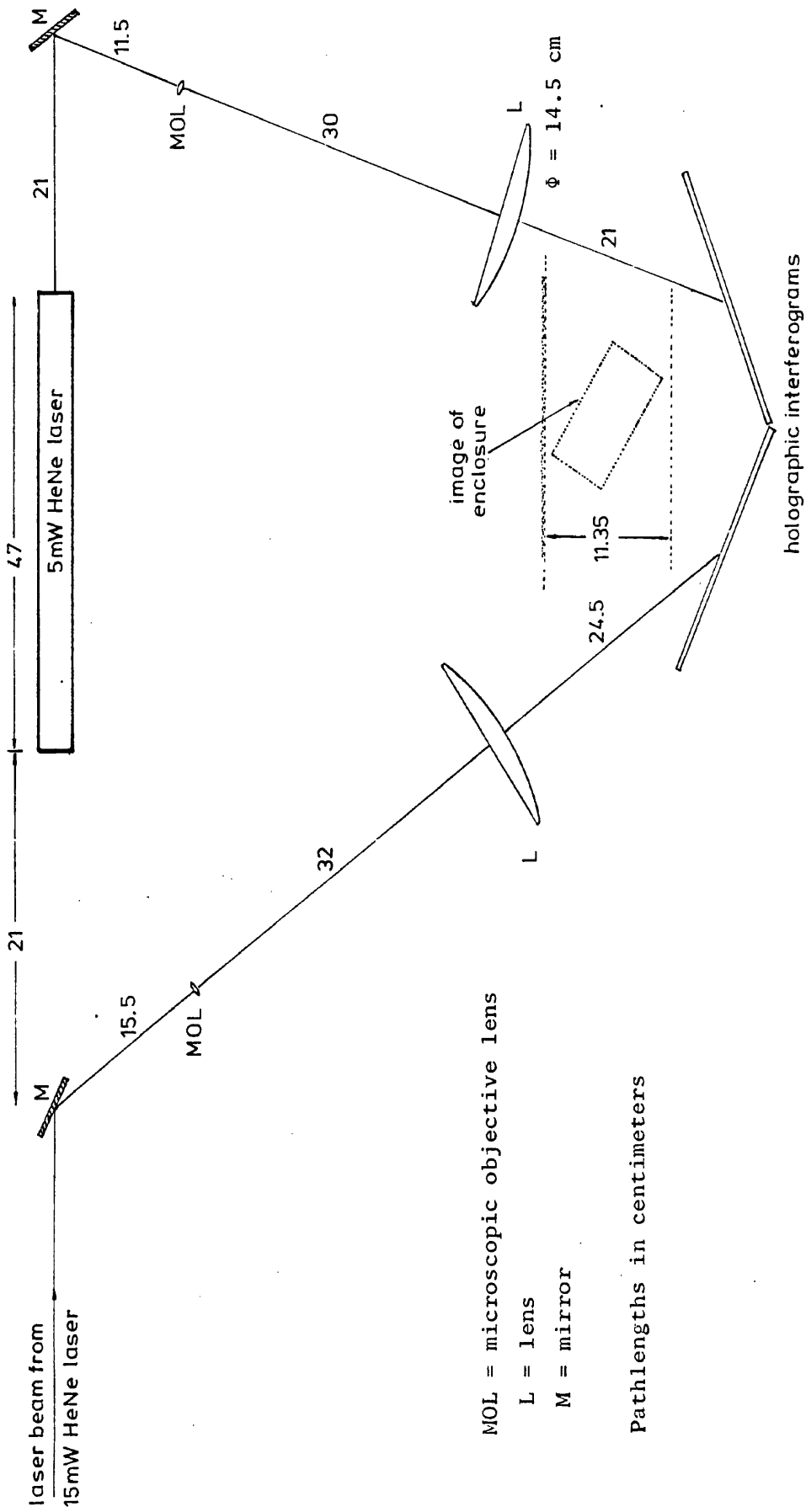


FIG. 5.6 SCHEMATIC DIAGRAM OF THE OPTICAL RECONSTRUCTION SYSTEM FOR THE ENCLOSURE

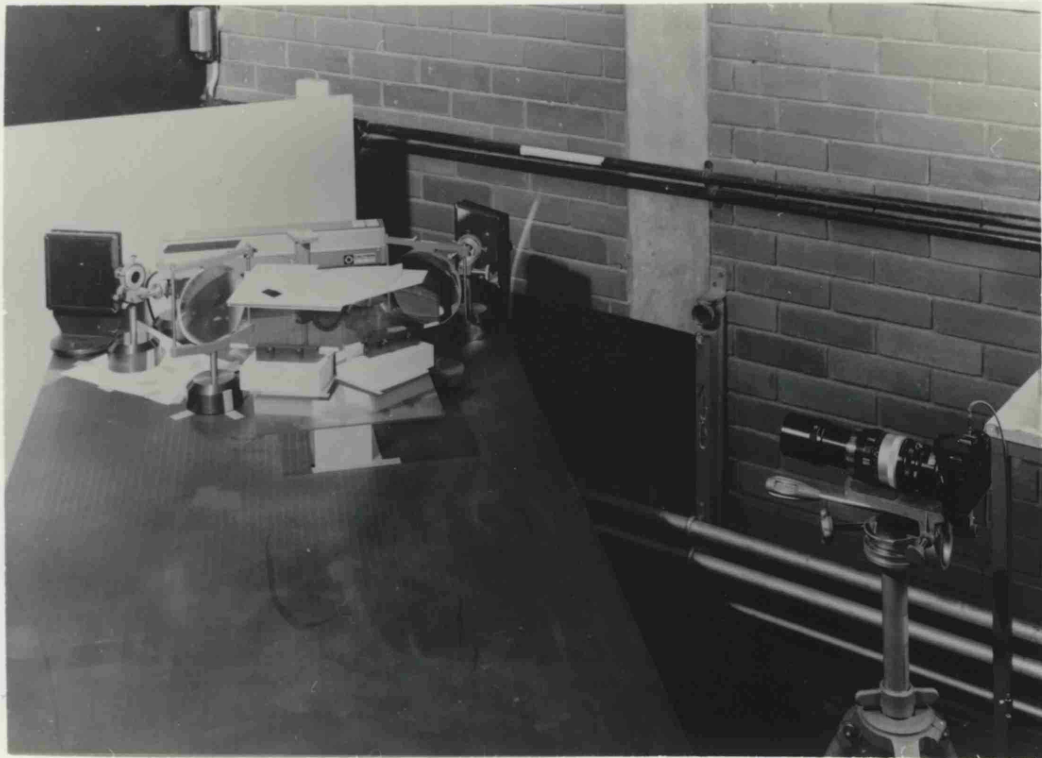


FIG. 5.7 OPTICAL RECONSTRUCTION-IMAGING SYSTEM FOR RECORDING INTERFEROMETRIC FRINGES

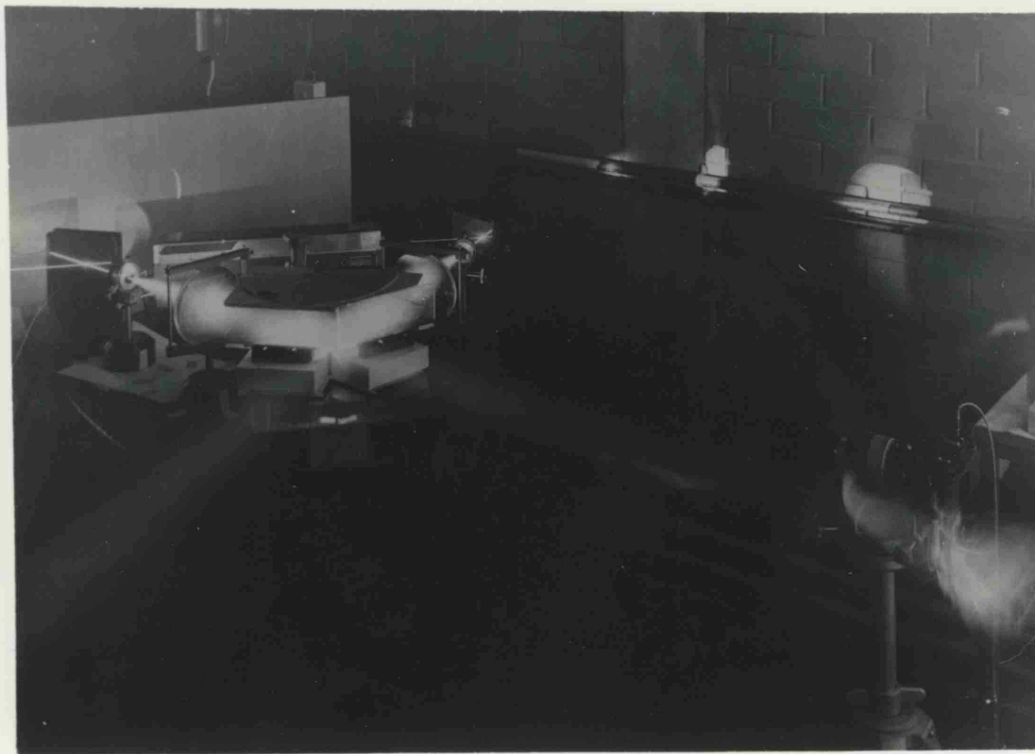


FIG. 5.8 AS FIG. 5.7 BUT WITH PATHS OF RE-ILLUMINATION LASER BEAMS MADE VISIBLE

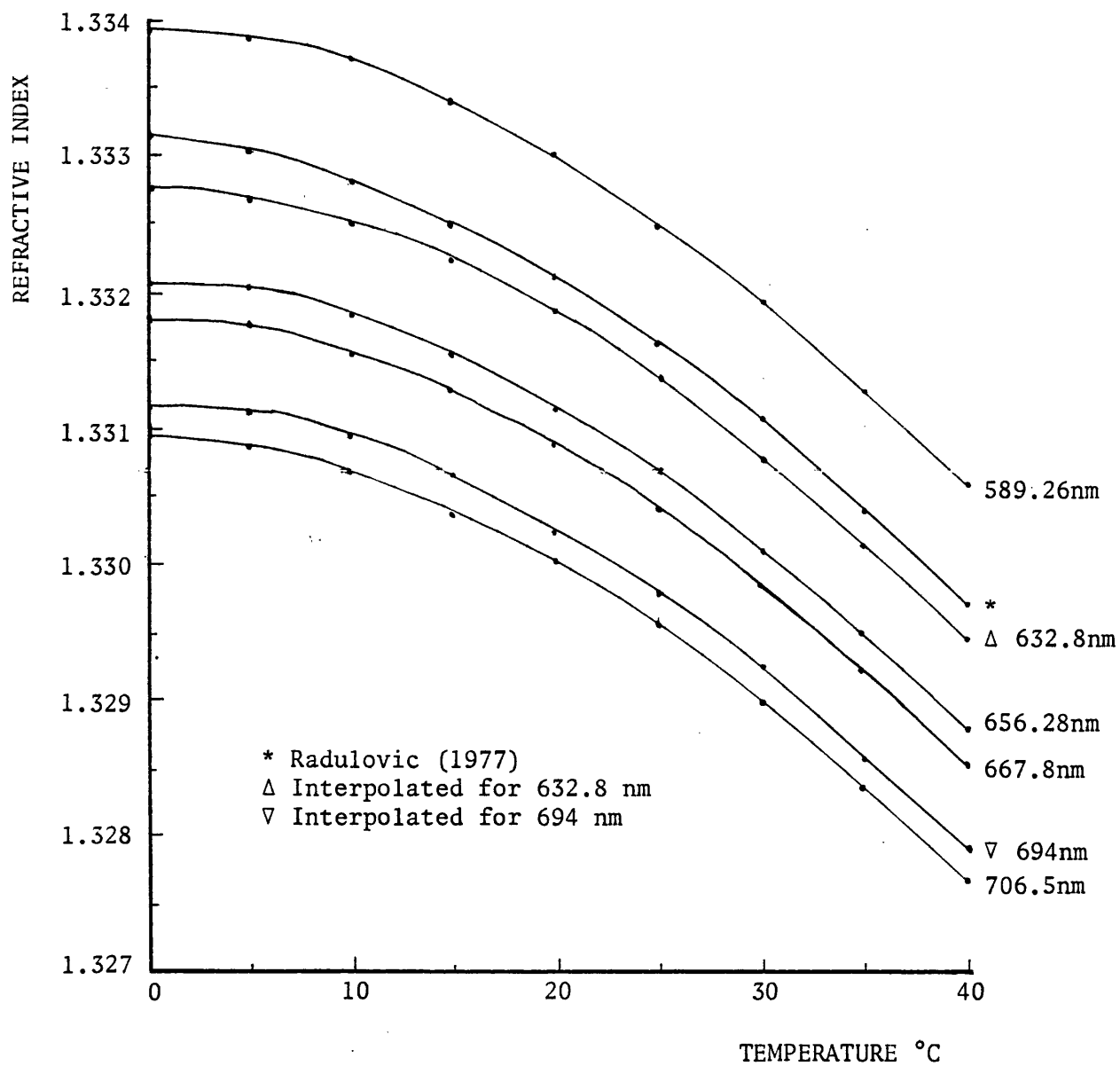


FIG. 5.9 REFRACTIVE INDEX AGAINST TEMPERATURE FOR WATER  
OVER SEVERAL WAVELENGTHS

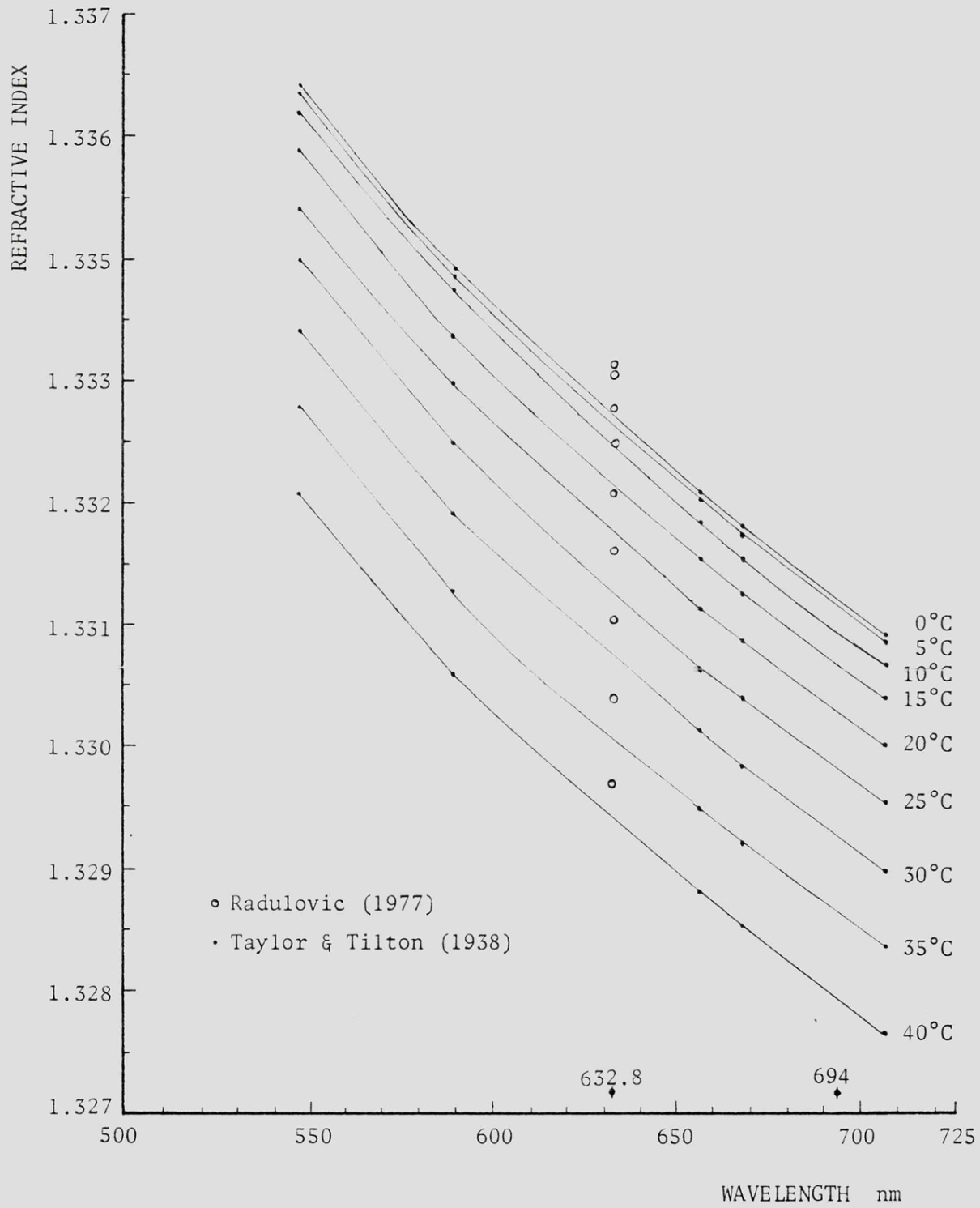


FIG. 5.10 REFRACTIVE INDEX AGAINST WAVELENGTH FOR WATER  
OVER A RANGE OF TEMPERATURES

SYNOPSISCHAPTER 6ANALYSIS OF RESULTS FROM THE CONSTANT TEMPERATURE ENCLOSURE

Double exposure holograms of the natural convection process within the constant wall temperature enclosure were produced from the two object/reference beam holographic interferometer described in the previous chapter. The programme of experimentation was therefore to make the interferograms, then the prints from these interferograms from various projection angles, and subsequently digitising from the prints. In this experiment the heater could be located at four different spots on the floor. Interferograms from each of these configurations were produced.

To reconstruct the 3-D temperature field four slices of two-dimensional planes at different heights from the floor of the enclosure were selected to be digitised for projection data. The reconstructed temperature fields from these planes were then stacked up to give the 3-D picture. Because of refraction causing light rays inside the test tank to converge the true range of viewing angles obtained from the collected projection data was therefore only  $62.7^\circ$ . For each of the four heater in enclosure configurations, the four 2-D planes selected for digitisation were the same. The data were then tested on the proven techniques developed in Chapter 4. However in reconstruction, sensible numerical solutions could only be obtained from the least squares of residuals technique.

Finally, stroboscopic photographs are shown of the flow circulation pattern within the enclosure in which Cayenne pepper was introduced as tracers illuminated by a thin sheet of laser light of thickness 2 mm.

CHAPTER 6ANALYSIS OF RESULTS FROM THE CONSTANT TEMPERATURE ENCLOSURE6.1 EXPERIMENTAL RESULTS

Holographic interferograms of the natural convection process in the constant temperature enclosure from localised heating were made using the pulsed laser interferometer described in the previous chapter. Two holographic plates, each of width 20.3 cm and height 8.5 cm, were exposed at the same time to produce a wide angle of view of the fringe patterns.

Digitisation was carried out from these interferograms at four differing heights indicated by 1, 2, 3, and 4 in fig. 6.1 (a), producing data for the computer program to reconstruct a quantitative picture of the temperature distribution in 3-D.

Figs. 6.2, 6.3, 6.4, and 6.5 show the holographic results in terms of fringe patterns in the enclosure, with the heater located at four different spots on the floor. Each of the figures shows three views each at a differing viewing angle. Angles are shown according to Fig. 6.1(b).

The maximum range of viewing angles achieved was  $125^\circ$  about a vertical axis through the centre of the enclosure. However the true range of viewing angles within the enclosure was in the region of  $75^\circ$  due to the refractive effect of water, and while complete scans were also required in the digitisation this range was further reduced to  $62.7^\circ$ .

Interferometric test results from the system showed that the flow pattern near the top surface plate, from the point of view of the fringe

profiles, was formed in the first 3 to 5 minutes after switching on the heater, but the full pattern did not begin to appear until 15 minutes after this. After some 30 minutes from switching the heater on, the flow pattern was stabilised.

Most of the interferograms were taken late in the evenings when the lab became a good darkroom to prevent the holographic plates from fogging, as the time delay between the first and second exposure was 40 minutes at least. After making an interferogram the water in the reservoir tank was refilled, and a minimum of six hours was given to allow the water to settle down to a constant temperature throughout the system. Over the period when these experiments were performed the temperature in the lab was between 18 to 20°C.

Finite fringes sometimes appeared on the interferograms and required the experiment to be repeated all over again. However, two steps were taken to eliminate or reduce these fringes. First, water was allowed to flow through the double skin enclosure for ten minutes before taking the first exposure so as to overcome any temperature differences, usually of 0.5°C or less, between the temperature of the water in the reservoir tank and in the test tank which was 0.5 m lower down. Second, the minimum rate of coolant flow was found which could still keep the enclosure surfaces cool enough, and yet allow the water in the reservoir to last throughout the experiment. This flow rate was measured to be at 54.6 litres/hour. The temperature of the water in each of the holographic experiments producing figs. 6.2 to 6.5 was as follows: for fig. 6.2 - 18.6°C, fig. 6.3 - 18.7°C, fig. 6.4 - 19.0°C, and fig. 6.5 - 18.0°C.

A stabilised direct current power supply was connected to the

heater. 0.73 A at 17.0 V was found to be the safe maximum current handling capacity of this heater, and this setting was needed to produce the necessary number of fringes on the interferograms.

## 6.2 RECONSTRUCTIONS

The results of the digitisation were fed into the ART type computer program similar to that used in Chapter 4 as a first step to test for possibility of reconstruction. This technique however encountered severe instability problems and was unable to produce interpretable solutions. The cause appeared to be that the temperature distribution over the thermal plume above the heater was quite narrow and peaky, and also that the rise in temperature between the liquid on the walls of the enclosure and that in the enclosure for a distance of approximately 2.5 mm away from the walls was quite sharp. As such the size of the uniform temperature pixels needed to be small. It thus seemed that a resolution of 13 x 7 used was inadequate, and that too much noise was introduced in the iteration process from the residuals.

A finer resolution was not used because the size of each grid element pixels at 8.3 x 8.3 mm, for the resolution of 13 x 7, should be sufficiently small to give

- (i) a good approximation to a 2-D slice of the 3-D temperature field,
- (ii) short turn-round time for a reconstruction on the University Cyber 73 computer.

Any increase on this number of pixels increases computation time and storage requirement, and the computer would classify the job as low priority sometimes taking a lot longer than 15 minutes for a turnround. Moreover, increasing the number of pixels would also aggravate the

instability problem.

The next stage was to implement SIRT, which had been shown by Herman et. al. (1975) to be capable of handling noisy data. Although this technique produced slightly better solutions, it was felt that they were still unsatisfactory. On a typical reconstructed temperature field in some regions, quite large artifacts, such as lumps or spots as that appeared on the left hand side of fig. 4.4, shown by contour level 3, or a strong directional bias as in fig. 4.3, shown by the elongated reconstructed field, were present due to the lack of constraint in the data because of the limited range of viewing angles of  $62.7^\circ$ .

The problem of instability as a result of noise from the experimental data, and that generated from the process of reconstructing from an approximated mathematical model lead to the search and formulation of a new algorithm. The method with the least squares of residuals as a measuring criteria described in Chapter 3 was used and seemed to give the best reconstructions that could be obtained. Plots 6.1, 6.2, 6.3, and 6.4 show the best possible solutions obtainable from the digitised data collected over a true range of viewing angles of approximately  $62.7^\circ$ .

Plots 6.1 to 6.4 are reconstructed by the LRST algorithm with resolutions of  $9 \times 5$  Grid elements. In all plots digitised projection data from the holographic interferograms were used. Each plot shows reconstructed temperature fields from four horizontal planes within the double skin wall enclosure. The position of these planes is shown by plane number 1, 2, 3, & 4 in fig. 6.1(a), plane 1 being closest to the ceiling and 4 closest to the heater, and can be identified on the contour maps by the number in brackets following each plot number such as plot 6.1(1), 6.1(2), etc. Dashed lines on the first plane of each plot are used to

Following pages: 125A, 125B, 125C, 125D and then 126.

indicate the location on the heater on the floor. There are four plots, therefore four different temperature fields within the enclosure were set up.

Plot 6.1 shows the reconstructed contour maps of the temperature field within the enclosure with the heater located centrally on the floor. Not only in this but in all the other three plots as well, plots 6.2 - 6.4, it can be seen from the physics of the experimental set-up that plane 4 should have a value of temperature higher than that on any of the other planes i.e. 1, 2, and 3. In this respect, the overall reconstructed temperature field within the enclosure cannot be regarded as good because in plot 6.1(4), the maximum contour level is only 8 whereas a level of 14 appears in plot 6.1(2), but these maximum values are reconstructed in their proper positions i.e. in the central region and not elsewhere. The lower value of the maximum in plane 4 is caused by the relatively large size of the pixel or Grid element compared to the hottest region of the thermal plume above the heater, which was expected to have a mean diameter around 0.48 of that of one of the sides of a pixel at 12.5 mm. The lower maximum contour level of 7 in plot 6.1(3) as against plot 6.1(4) would seem to indicate a lower temperature over this region, but if the maximum contour level of 14 in plot 6.1(2) is assumed most likely to be true then this would suggest that the central plume in plot 6.1(3) is thinner than that in plot 6.1(4) rather than at a lower temperature.

Contours also seem to be crossed over from one to another in places, caused by computer programming error in plotting, producing ill-defined contour levels, as can be seen in plots 6.1(1), 6.1(2), and 6.1(4). These occur when there are peaks and dips of contour levels plotted over a relatively coarse mesh size which is determined by the number of temperature points available for contouring. It seems that more than the present 9 x 5 temperature points are required to produce contour maps with better accuracy

from these temperature fields. The GHOST contouring routine used calls a cubic curve fitting procedure which draws a curve between successive intersected points ensuring continuity of slope over the drawn curve. The intersected points represent contour level values and are obtained by dividing each square in the mesh into two triangles and using inverse linear interpolation to determine the intersection with the sides of the triangles, with temperature points assigned to the corners of each triangle by the data. For example, if the size of the squares in the mesh is halved by using more temperature points (i.e. data) the two level 10 contours in plot 6.1(1) would join together at each of the intersected points without crossing over: this is achieved by splitting into two the length of the mesh diagonal, which at present in this region is ill-defined, having two level 10 intersections with a level 11 on either side producing the two intersecting arcs on the diagonal. With more points used the bottom curve of one of the level 10 contours would join the bottom of one of the other, and similarly with the level 10 curves at the top, and with possibly contour levels 11 joining together by very narrow lines. The crossing over of level 3 contours in plot 6.1(4) should appear as a single line were more temperature points available.

Besides plot 6.1, in virtually all other plots as well, plots 6.2 - 6.4, the region around the top l.h.s. corner and bottom r.h.s. corner boundaries seem to have much higher values than those around the top r.h.s. corner and bottom r.h.s. corner boundaries. The effect of directional bias in temperature field reconstruction from experimental digitised projection data from a limited range of viewing angles is thus clearly shown here. The projection data were collected from the interferograms in a direction from bottom to top as on these contour maps for the  $90^\circ$  set to a set from the maximum angle that could be obtained in a direction from approximately the bottom r.h.s. corner to the top l.h.s. corner. However, if good error free

data were available and the temperature field to be reconstructed were more smoothly varying than these then such an effect is not so noticeable, because the projection equations would then match the reconstruction mathematical model better. As can be seen in later plots, some of these errors on the boundaries are so large that the reconstruction is badly distorted.

Artifacts or random errors can also be seen to appear such as peaks and dips shown by contours 2 & 5 within the contour maps such as in plot 6.1(3) and also contour 1 in plot 6.1(4).

Plot 6.2 shows contour maps of the temperature field within the enclosure with heating located across to one side, as shown by the dashed lines. Plot 6.2(2) is possibly the worse reconstruction in this work in that the directional bias is very bad indeed. The contour level 8 is possibly in error as well compared to the higher value 9 in the first plane, plot 6.2(1). The plume region has disappeared altogether on plot 6.2(3). In plot 6.2(4) contour levels 5 cross, where they should have joined together, and contour 5 and 3 in the bottom r.h.s. corner region and top l.h.s. corner region respectively are expected to be artifacts.

Plot 6.3 is a reconstruction of the temperature field with heating located near one of the corners on the floor. There are artifacts on every contour map and the boundaries in plots 6.3(1) and 6.3(2) contain some quite high values of temperature which is expected to be erroneous.

Criticisms similar to the above hold for the reconstructed temperature field shown by plot 6.4, with heating located along to one side as shown by plot 6.4(1).

As can be seen from these contour plots temperature field reconstruction from experimental projection data from a limited range of viewing angles causes a direction bias to appear. Firstly, this would produce a distorted three-dimensional temperature field.

Secondly, because each observation is an integrated value of the refractive index change from a projected ray through the entire test field, it is likely that such a distortion has affected the absolute value of temperature on every point within the reconstruction grid. Thirdly, because the temperature fields to be reconstructed do not vary as smoothly as that in Chapter 4, reducing the grid size to increase the resolution did not improve matters as the number of artifacts was found to increase. Of these four plots the best reconstructions obtained are those shown in plot 6.1, followed by those in plot 6.4, but in absolute terms when compared with the physics of the constant temperature enclosure set-up with localised heating on the floor, these are not good reconstructions because of the unexpectedly high temperature values on the boundaries caused mainly by reconstruction from a limited range of viewing angles from the digitised projection data.

### 6.3 FLOW VISUALISATION RESULTS

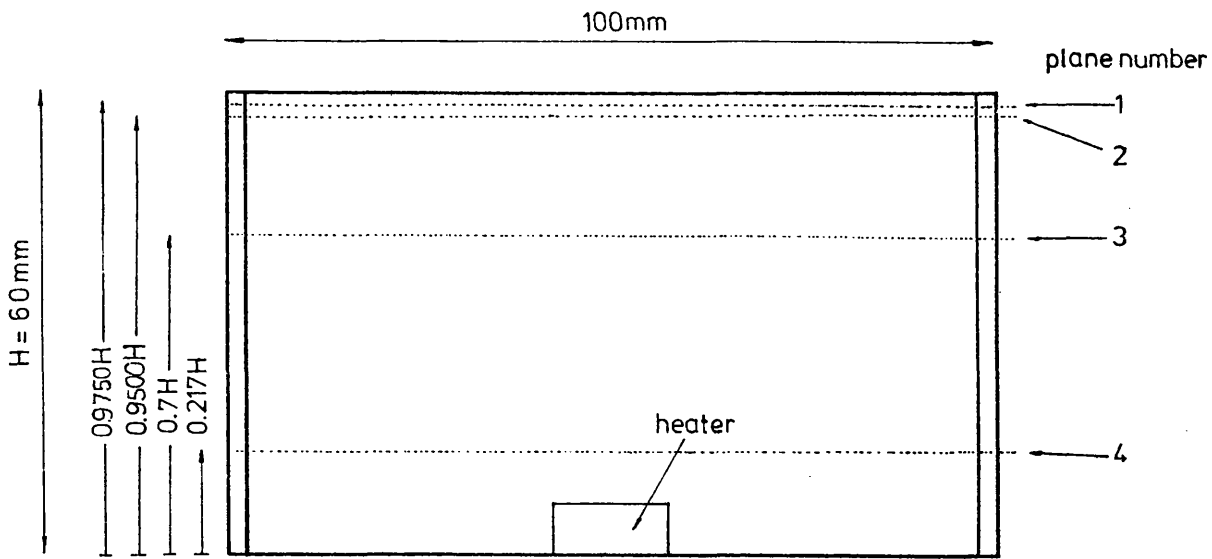
Another aspect that was investigated was the flow due to the natural convective current in the enclosure. The flow was made visible by introducing reflective particles of cayenne pepper in the enclosure just before the test. In tests it was found that these particles could remain suspended in stagnant water for up to 20 minutes. One of the other substances tried was 0.8 mm - 100  $\mu$ m diameter polystyrene particles as used by Buranathanitt (1979). He described that these particles, which have a specific gravity between 1.03 and 1.05, could have a specific

gravity of about 1.0 by immersing them in water at 95°C for 5 seconds and then quenching them to below 60°C. However during tests the sinking time with these particles was found to be relatively fast, and no particles could be seen still suspended after two minutes.

A narrow sheet of light of thickness 2.0 mm from the 15 mW Scientifica and Cook He-Ne laser illuminated the particles in a vertical plane, first along and then across the enclosure. The plane taken passes through the centre of the heater as shown in fig 6.6.

Stroboscopic photographs of the flow circulation patterns were obtained with the 35 mm Nikon camera fitted with a 200 mm telephoto lens placed at a distance of approximately 2.0 m away. The condition that showed a fairly steady state appeared 5 minutes after switching on the heater and coolant flow, but the pictures taken were within the period 15 - 20 minutes after switching on. By this time the flow appeared stabilised. The streaking flow circulation pattern from which component of velocity could be determined was produced by intermittently interrupting the sheet of laser light with an equally spaced 6 vane wheel rotating at 30.0 rpm. Ilford HP5 400 ASA film was used. Exposure times are given on the photographs of results.

Figs. 6.6, 6.7, 6.8, and 6.9 show the results of the flow circulation with the heater located at four different positions on the floor, and also as an example for the purpose of comparison of flow circulation pattern, stroboscopic pictures were produced with a taller and also more powerful heater in the enclosure, fig. 6.10.



Inside dimensions of enclosure: 95mm x 45mm x 60mm  
 Dimensions of heater: 15.0mm x 15.0mm x 6.5mm

FIG. 6.1 (a) DIAGRAM SHOWING THE 4 PLANES SELECTED FOR RECONSTRUCTION

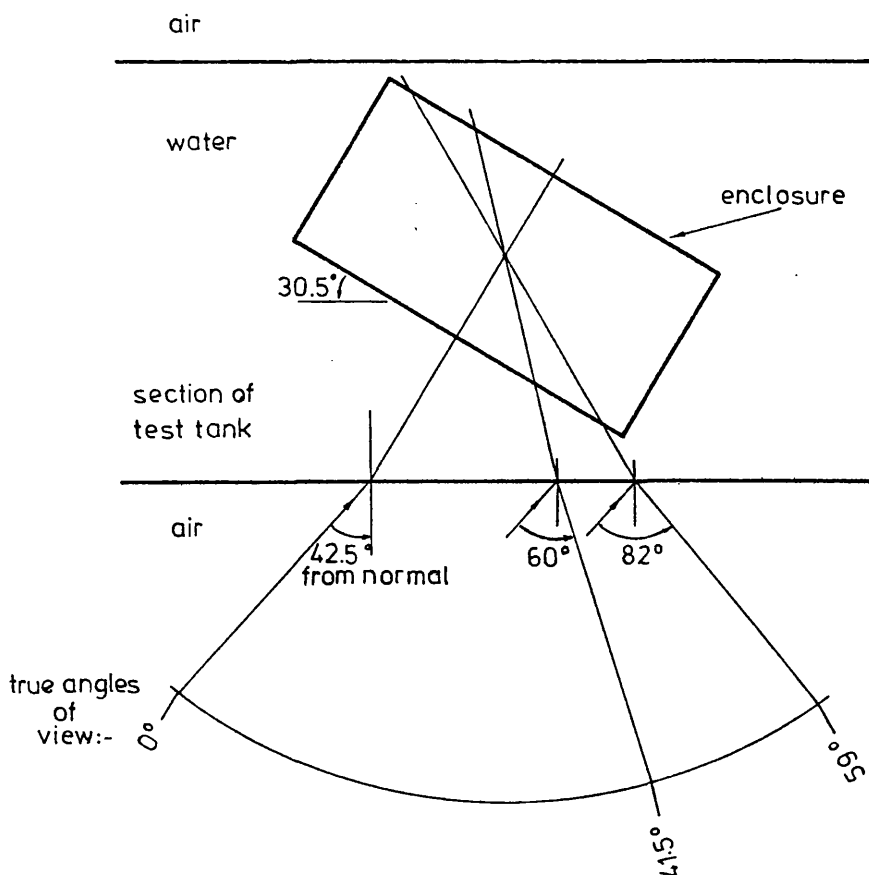
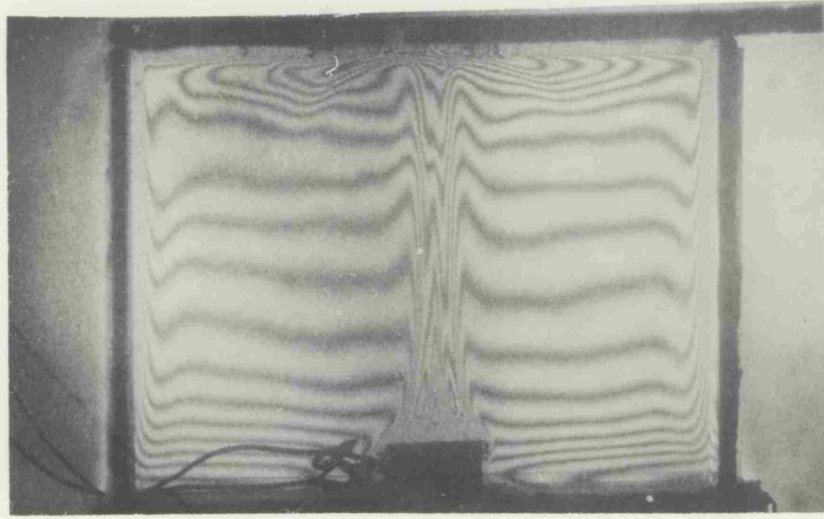
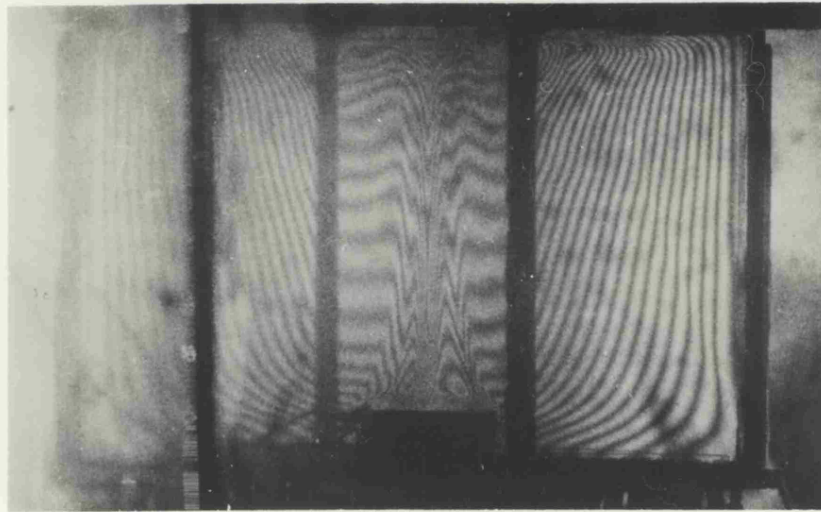


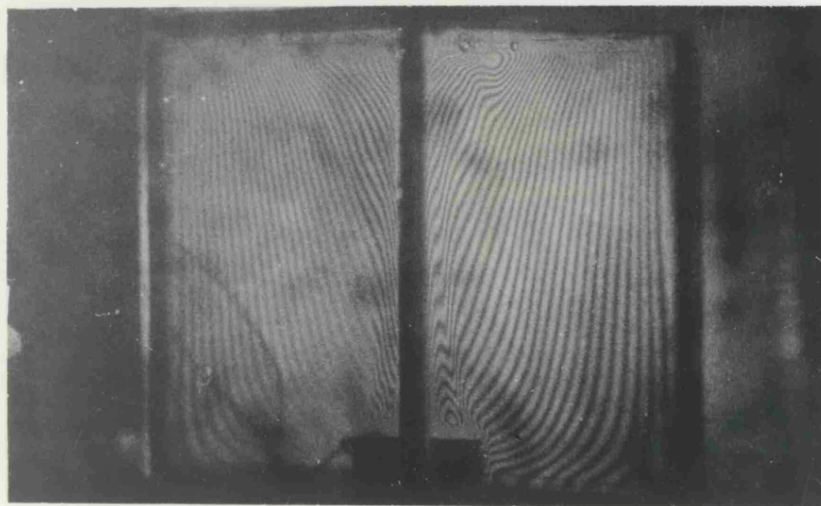
FIG. 6.1 (b) CONFIGURATION SHOWING TRUE VIEWING ANGLES FROM ENCLOSURE



(a)

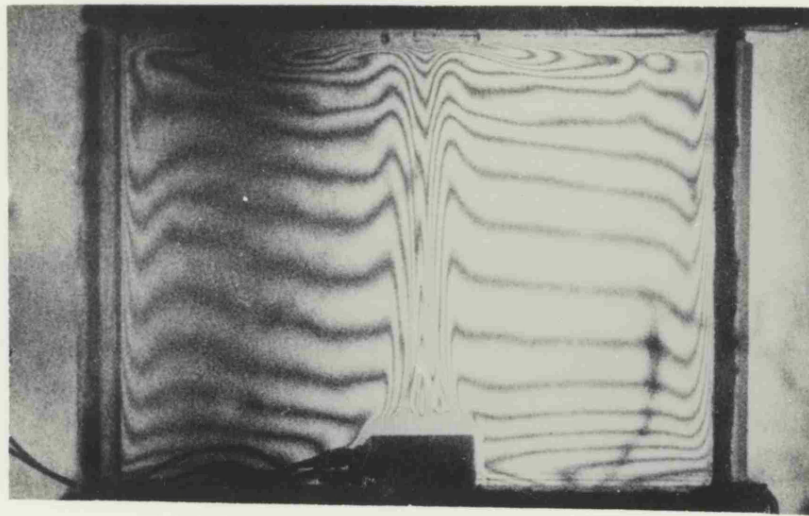


(b)

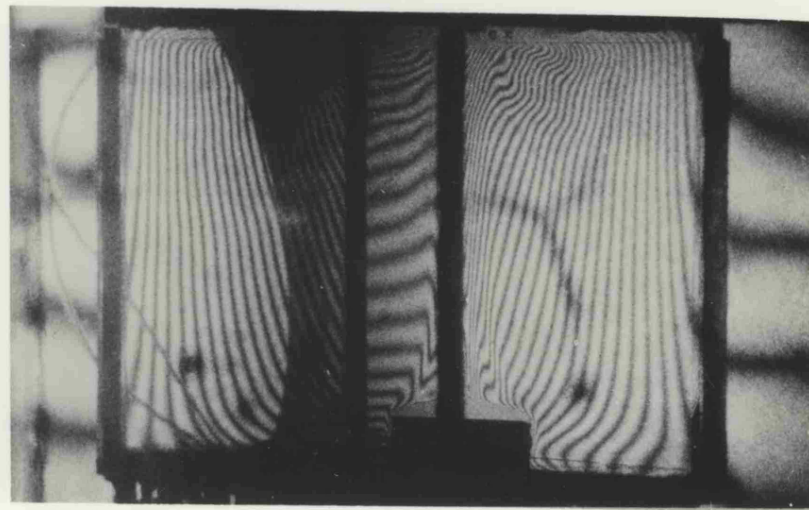


(c)

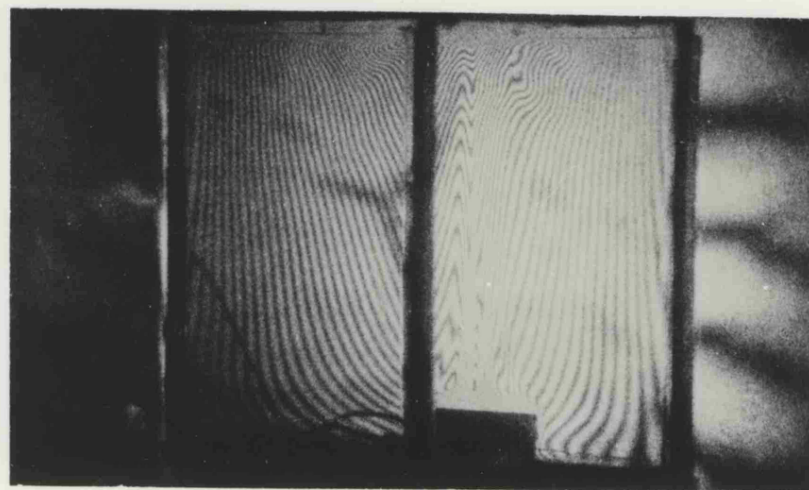
Fig. 6.2 Natural convection from localised heating in the constant temperature enclosure at different viewing angles, (a)  $0^\circ$ , (b)  $60^\circ$ , (c)  $82^\circ$ . Power = 13.1 Watts. Location of heater = central.



(a)

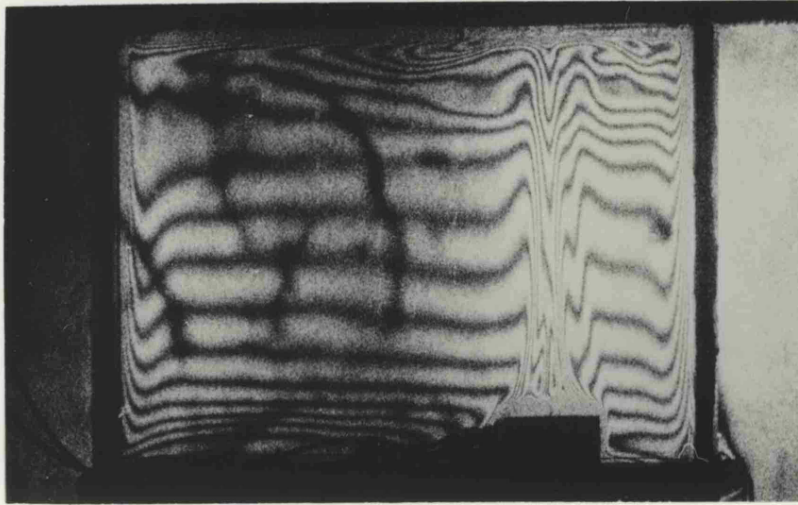


(b)

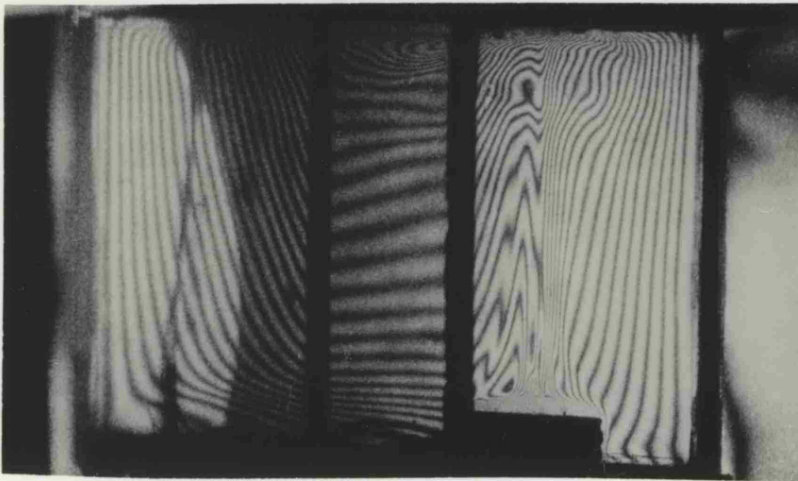


(c)

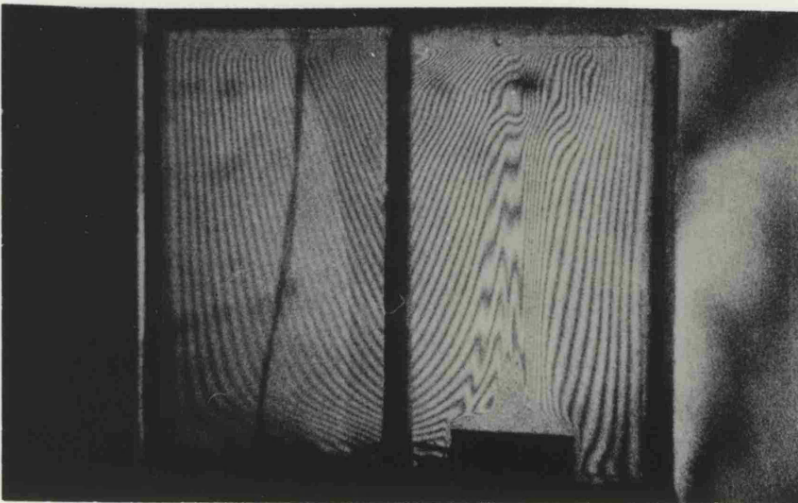
Fig. 6.3 Natural convection from localised heating in the constant temperature enclosure at different viewing angles, (a)  $0^\circ$ , (b)  $70^\circ$ , (c)  $80^\circ$ . Power = 13.1 Watts. Location of heater = 0.5 way along, 0.75 way across



(a)

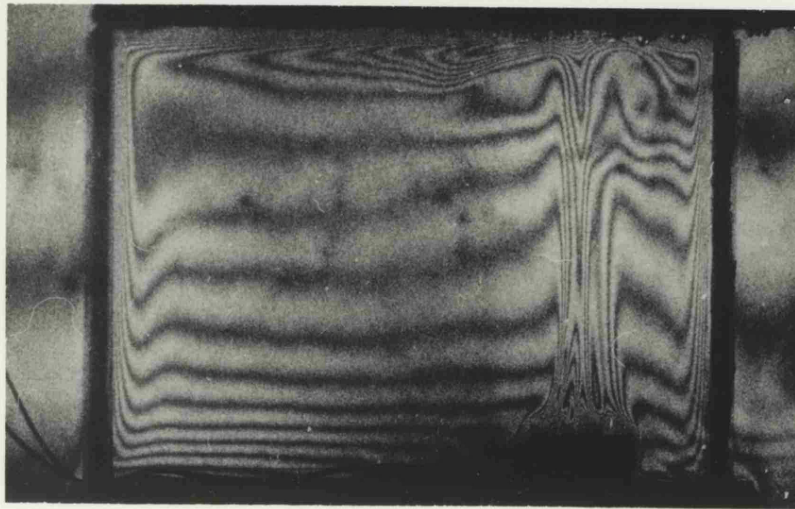


(b)

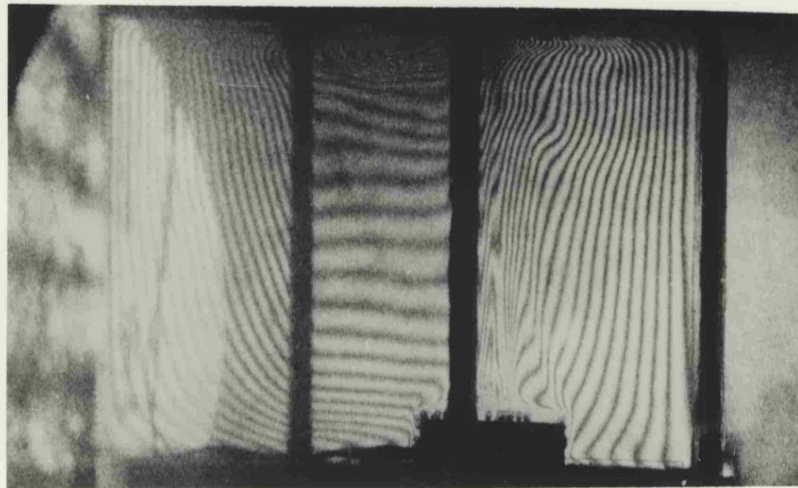


(c)

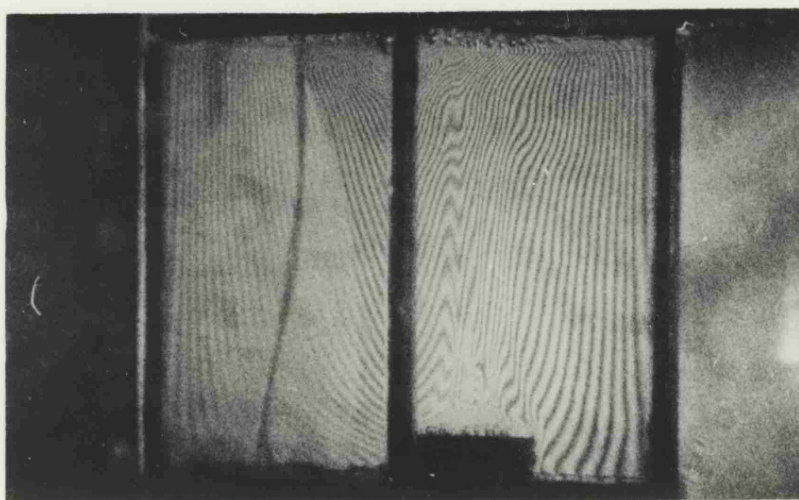
Fig. 6.4 Natural convection from localised heating in the constant temperature enclosure at different viewing angles, (a)  $0^\circ$ , (b)  $63^\circ$ , (c)  $79^\circ$ . Power = 13.1 Watts. Location of heater = 0.75 way along, 0.75 way across.



(a)



(b)



(c)

Fig. 6.5 Natural convection from localised heating in the constant temperature enclosure at different viewing angles, (a)  $0^\circ$ , (b)  $60^\circ$ , (c)  $79^\circ$ . Power = 13.1 Watts. Location of heater = 0.75 way along, 0.5 way across.

PLOT 6.1 RECONSTRUCTED 3-D TEMPERATURE FIELD WITH HEAT SOURCE

LOCATED CENTRALLY

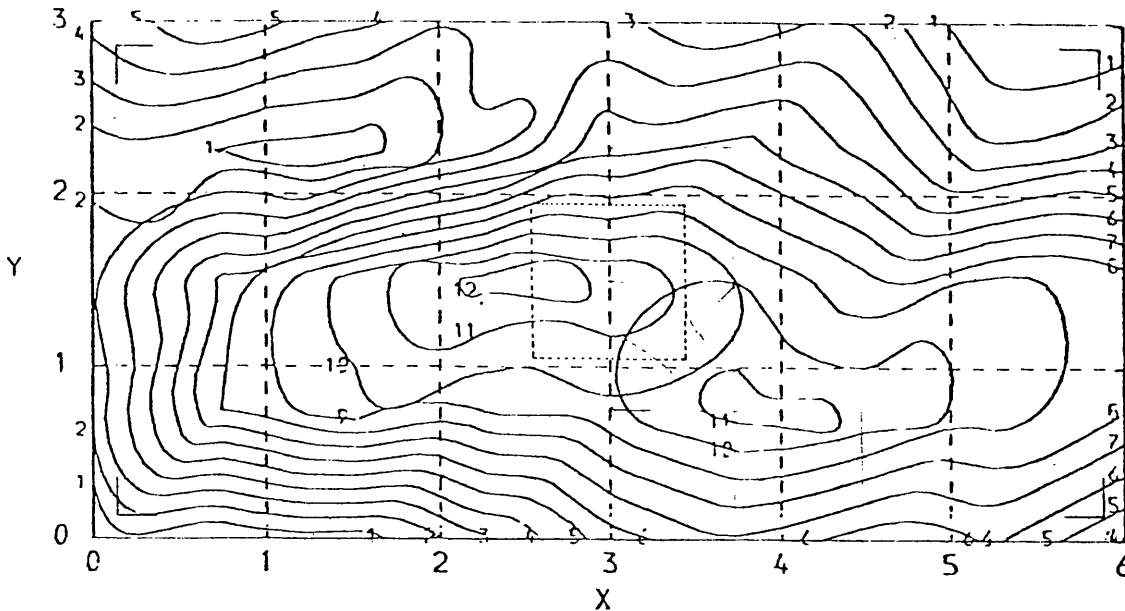
Four 2-D planes as labelled 1, 2, 3, and 4 in fig. 6.1 (a) were reconstructed, and are represented by contour plots.

Resolution: 9 x 5

Model: Grid element

Technique of inversion: LSRT

Contours represent changes in temperature



PLOT 6.1(1) RECONSTRUCTED FIELD USING LSRT & DIGITISED DATA

PLANE H= 0.975  
 ANGLE MIN= 0.0 DEG  
 ANGLE MAX= 60.9 DEG  
 TOTAL NUMBER OF RAYS USED = 246  
 NUMBER OF PROJECTIONS USED = 8

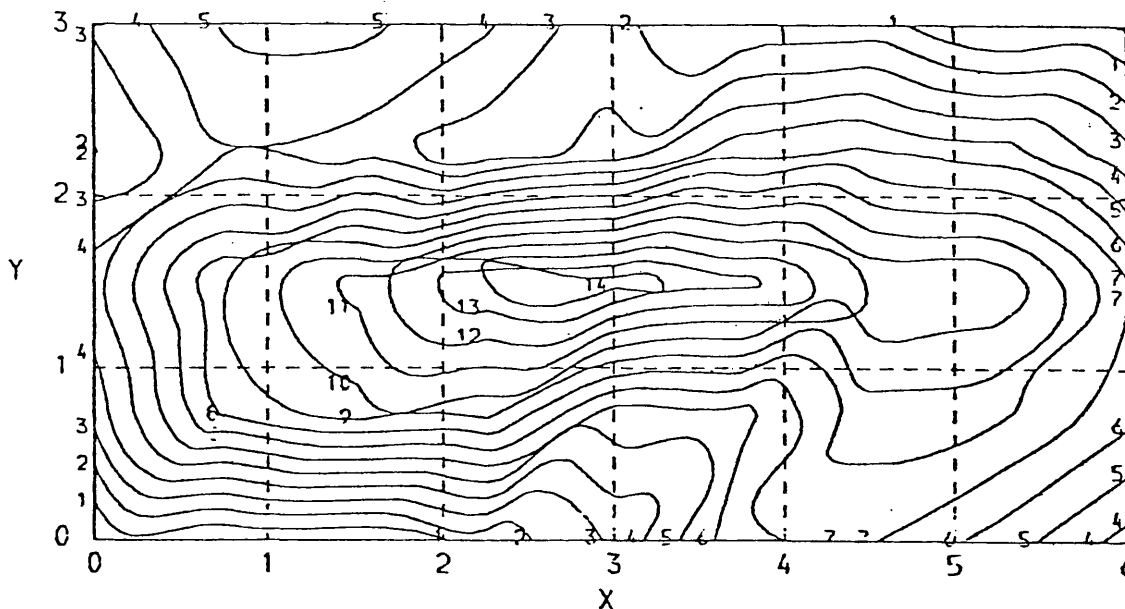
ORIGINAL TEMP = 18.5°C  
 RECONSTRUCTED MEAN TEMP = 20.14°C  
 RECONSTRUCTED MAX TEMP = 22.20°C  
 RECONSTRUCTED MIN TEMP = 18.50°C

↑  
 min viewing  
 angle

CONTOURS IN DEG C  
 1= 0.30  
 2= 0.60  
 3= 0.90  
 4= 1.20  
 5= 1.50  
 6= 1.80  
 7= 2.10  
 8= 2.40  
 9= 2.70  
 10= 3.00 ETC.

↙ ↘  
 60.9°  
 max viewing  
 angle

SUM OF SQUARE OF @ RESIDUAL = 46 (CF. 2584 AT K=2)  
 COMPUTING TIME = 140.00 SEC, CPU (K=200).



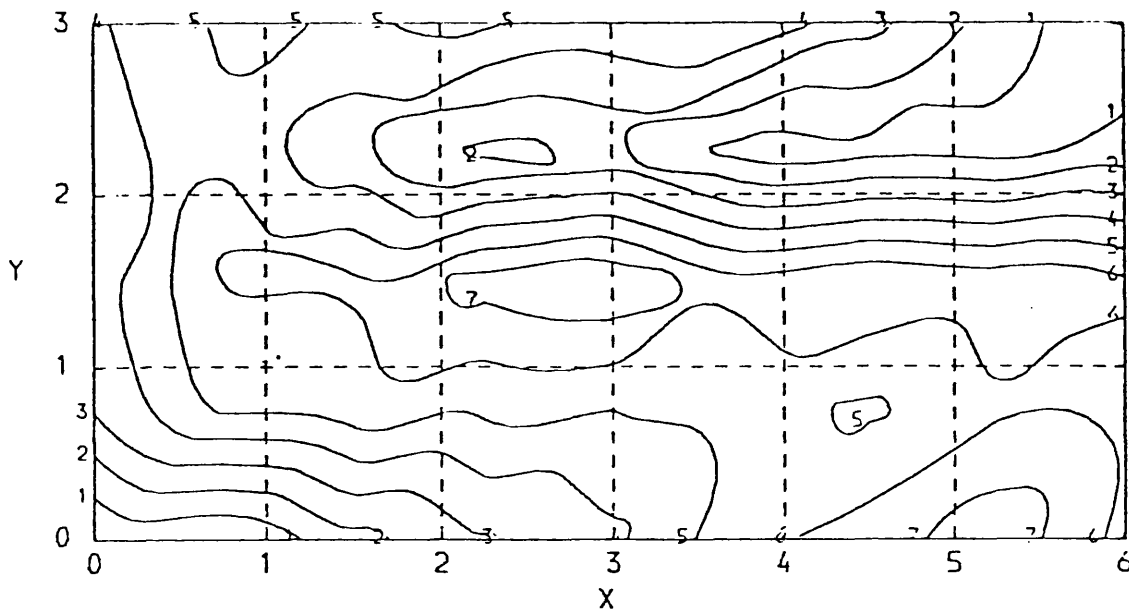
PLOT 6.1(2) RECONSTRUCTED FIELD USING LSRT & DIGITISED DATA

PLANE H= 0.950  
 ANGLE MIN= 0.0 DEG  
 ANGLE MAX= 60.9 DEG  
 TOTAL NUMBER OF RAYS USED = 281  
 NUMBER OF PROJECTIONS USED = 9

ORIGINAL TEMP = 18.5°C  
 RECONSTRUCTED MEAN TEMP = 20.15°C  
 RECONSTRUCTED MAX TEMP = 22.81°C  
 RECONSTRUCTED MIN TEMP = 18.50°C

CONTOURS IN DEG C  
 1= 0.30  
 2= 0.60  
 3= 0.90  
 4= 1.20  
 5= 1.50  
 6= 1.80  
 7= 2.10  
 8= 2.40  
 9= 2.70  
 10= 3.00 ETC.

SUM OF SQUARE OF @ RESIDUAL = 56 (CF. 2578 AT K=2)  
 COMPUTING TIME = 152.00 SEC, CPU (K=200).



PLOT 6.1(3) RECONSTRUCTED FIELD USING LSRT & DIGITISED DATA

PLANE H = 0.700

ANGLE MIN = 0.0 DEG

ANGLE MAX = 60.9 DEG

TOTAL NUMBER OF RAYS USED = 280

NUMBER OF PROJECTIONS USED = 9

ORIGINAL TEMP = 18.5 °C

RECONSTRUCTED MEAN TEMP = 19.76 °C

RECONSTRUCTED MAX TEMP = 20.90 °C

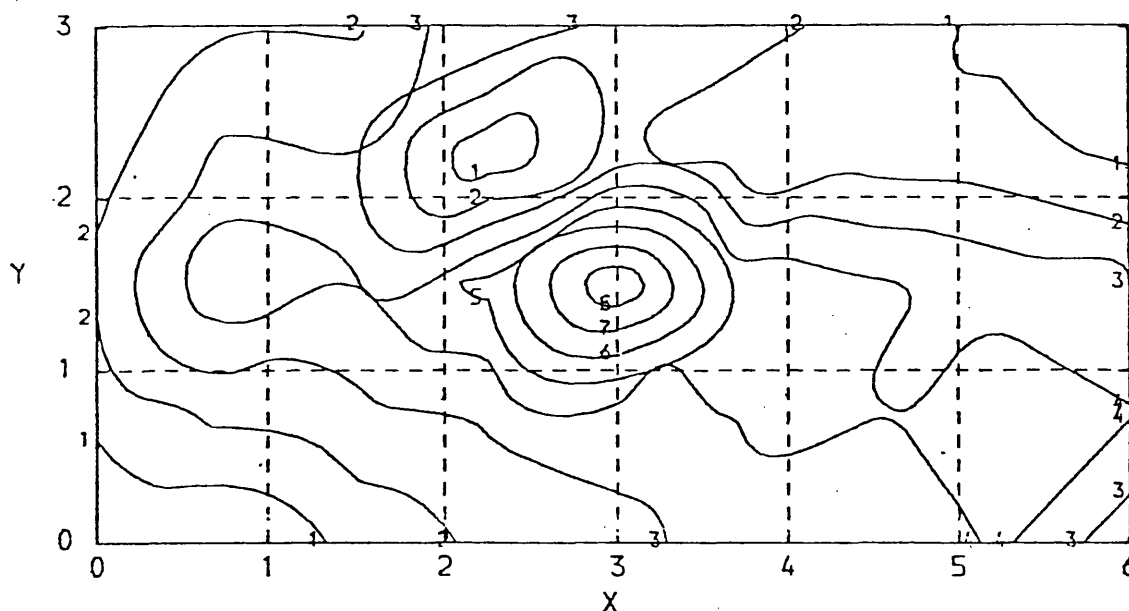
RECONSTRUCTED MIN TEMP = 18.50 °C

CONTOURS IN DEG C

1 = 0.30  
 2 = 0.30  
 3 = 0.90  
 4 = 1.20  
 5 = 1.50  
 6 = 1.50  
 7 = 2.10  
 8 = 2.40  
 9 = 2.70  
 10 = 3.00 ETC.

SUM OF SQUARE OF @ RESIDUAL = 28 (CF. 1310 AT K=2)

COMPUTING TIME = 152.00 SEC, CPU (K=200).



PLOT 6.1(4) RECONSTRUCTED FIELD USING LSRT & DIGITISED DATA

PLANE H = 0.217

ANGLE MIN = 0.0 DEG

ANGLE MAX = 60.9 DEG

TOTAL NUMBER OF RAYS USED = 290

NUMBER OF PROJECTIONS USED = 9

ORIGINAL TEMP = 18.5 °C

RECONSTRUCTED MEAN TEMP = 19.31 °C

RECONSTRUCTED MAX TEMP = 21.11 °C

RECONSTRUCTED MIN TEMP = 18.50 °C

CONTOURS IN DEG C

1 = 0.30  
 2 = 0.60  
 3 = 0.90  
 4 = 1.20  
 5 = 1.50  
 6 = 1.80  
 7 = 2.10  
 8 = 2.40  
 9 = 2.70  
 10 = 3.00 ETC.

SUM OF SQUARE OF @ RESIDUAL = 23.8 (CF. 360.0 AT K=2)

COMPUTING TIME = 154.00 SEC, CPU (K=200).

PLOT 6.2 RECONSTRUCTED 3-D TEMPERATURE FIELD WITH HEAT SOURCE

LOCATED 0.5 WAY ALONG, 0.75 WAY ACROSS

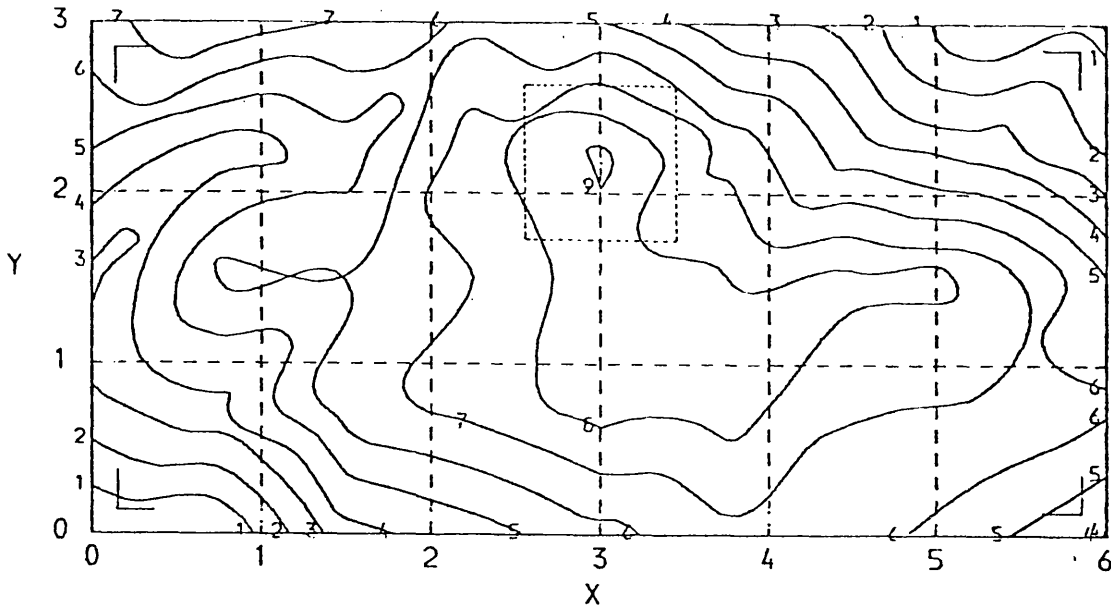
Four 2-D planes as labelled 1, 2, 3, and 4 in fig. 6.1 (a) were reconstructed, and are represented by contour plots.

Resolution: 9 x 5

Model: Grid element

Technique of inversion: LSRT

Contours represent changes in temperature



PLOT 6.2(1) RECONSTRUCTED FIELD USING LSRT & DIGITISED DATA

PLANE H = 0.975

ANGLE MIN = 0.0 DEG

ANGLE MAX = 58.7 DEG

TOTAL NUMBER OF RAYS USED = 223

NUMBER OF PROJECTIONS USED = 8

ORIGINAL TEMP = 18.8 °C

RECONSTRUCTED MEAN TEMP = 20.4 °C

RECONSTRUCTED MAX TEMP = 22.25 °C

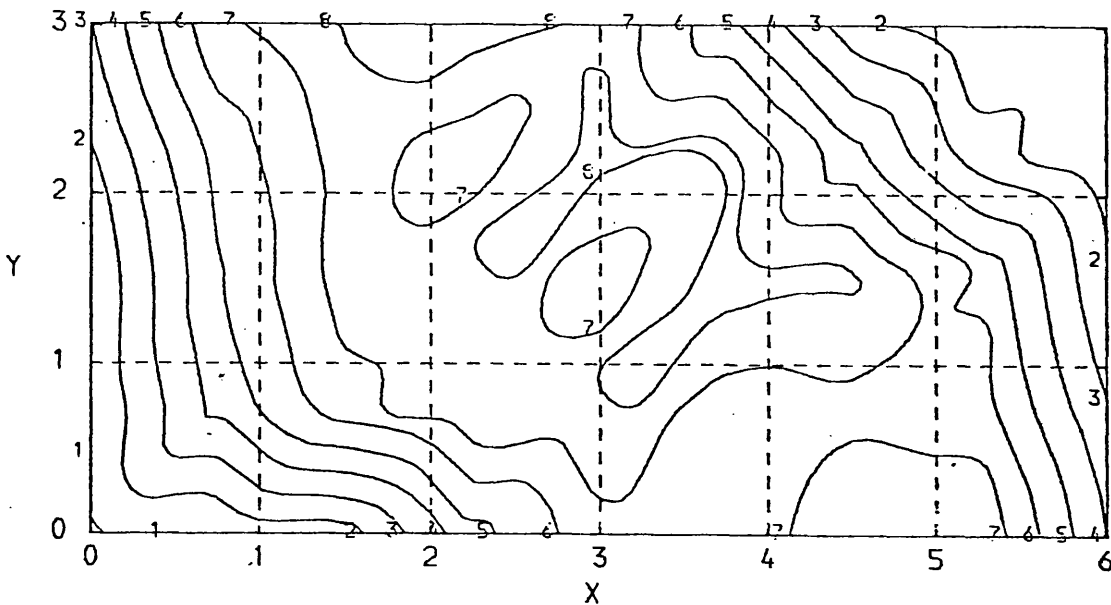
RECONSTRUCTED MIN TEMP = 18.72 °C

CONTOURS IN DEG C

- 1 = 0.30
- 2 = 0.60
- 3 = 0.90
- 4 = 1.20
- 5 = 1.50
- 6 = 1.80
- 7 = 2.10
- 8 = 2.40
- 9 = 2.70
- 10 = 3.00 ETC.

SUM OF SQUARE OF @ RESIDUAL = 27.7 (CF. 2459 AT K=2)

COMPUTING TIME = 154.00 SEC, CPU (K=200)



PLOT 6.2(2) RECONSTRUCTED FIELD USING LSRT & DIGITISED DATA

PLANE H = 0.950

ANGLE MIN = 0.0 DEG

ANGLE MAX = 58.7 DEG

TOTAL NUMBER OF RAYS USED = 241

NUMBER OF PROJECTIONS USED = 8

ORIGINAL TEMP = 18.8 °C

RECONSTRUCTED MEAN TEMP = 20.37 °C

RECONSTRUCTED MAX TEMP = 22.08 °C

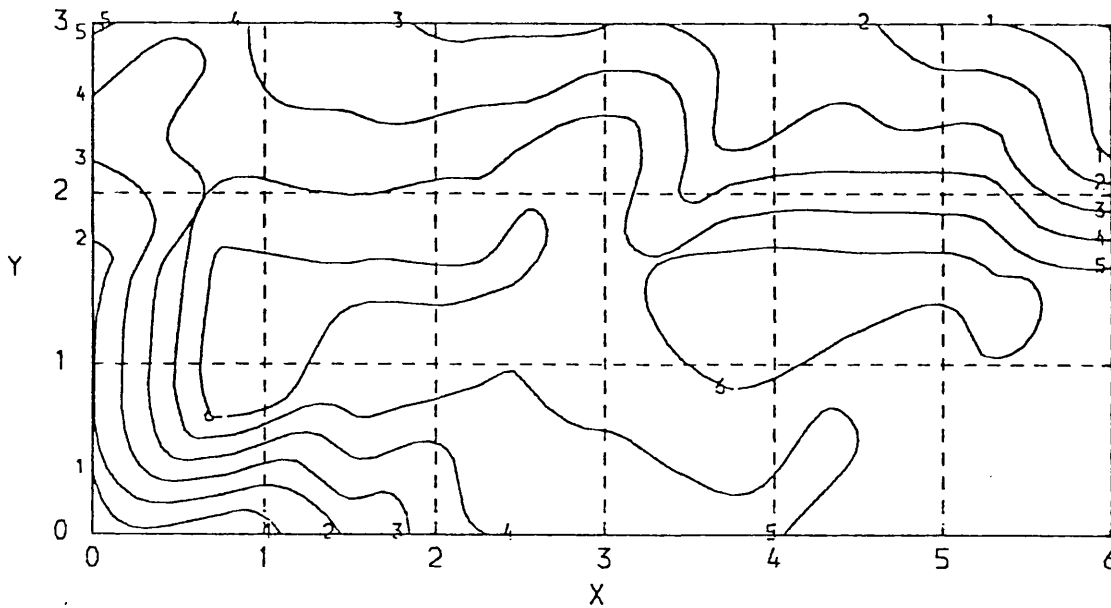
RECONSTRUCTED MIN TEMP = 18.80 °C

CONTOURS IN DEG C

- 1 = 0.30
- 2 = 0.60
- 3 = 0.90
- 4 = 1.20
- 5 = 1.50
- 6 = 1.80
- 7 = 2.10
- 8 = 2.40
- 9 = 2.70
- 10 = 3.00 ETC.

SUM OF SQUARE OF @ RESIDUAL = 22.5 (CF. 2262 AT K=2)

COMPUTING TIME = 158.00 SEC, CPU (K=200)



PLOT 6.2(3) RECONSTRUCTED FIELD USING LSRT & DIGITISED DATA

PLANE H= 0.700

ANGLE MIN= 0.0 DEG

ANGLE MAX= 58.7 DEG

TOTAL NUMBER OF RAYS USED = 224

NUMBER OF PROJECTIONS USED = 8

ORIGINAL TEMP = 18.8 °C

RECONSTRUCTED MEAN TEMP = 20.04 °C

RECONSTRUCTED MAX TEMP = 21.20 °C

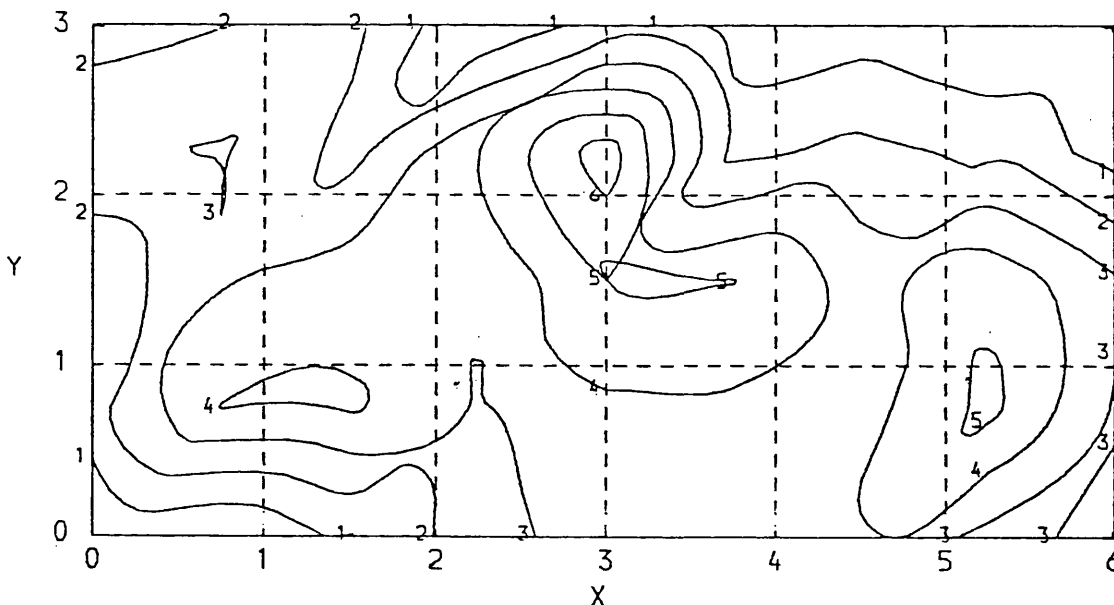
RECONSTRUCTED MIN TEMP = 18.80 °C

CONTOURS IN DEG C

- 1= 0.30
- 2= 0.60
- 3= 0.90
- 4= 1.20
- 5= 1.50
- 6= 1.80
- 7= 2.10
- 8= 2.40
- 9= 2.70
- 10= 3.00 ETC.

SUM OF SQUARE OF @ RESIDUAL = 22.3 (CF.1250 AT K=2)

COMPUTING TIME = 157.00 SEC, CPU (K=200)



PLOT 6.2(4) RECONSTRUCTED FIELD USING LSRT & DIGITISED DATA

PLANE H= 0.217

ANGLE MIN= 0.0 DEG

ANGLE MAX= 58.7 DEG

TOTAL NUMBER OF RAYS USED = 219

NUMBER OF PROJECTIONS USED = 8

ORIGINAL TEMP = 18.8 °C

RECONSTRUCTED MEAN TEMP = 19.58 °C

RECONSTRUCTED MAX TEMP = 21.33 °C

RECONSTRUCTED MIN TEMP = 18.80 °C

CONTOURS IN DEG C

- 1= 0.30
- 2= 0.60
- 3= 0.90
- 4= 1.20
- 5= 1.50
- 6= 1.80
- 7= 2.10
- 8= 2.40
- 9= 2.70
- 10= 3.00 ETC.

SUM OF SQUARE OF @ RESIDUAL = 13.3 (CF. 585 AT K=2)

COMPUTING TIME = 152.00 SEC, CPU (K=200)

PLOT 6.3 RECONSTRUCTED 3-D TEMPERATURE FIELD WITH HEAT SOURCE  
LOCATED 0.75 WAY ALONG, 0.75 WAY ACROSS

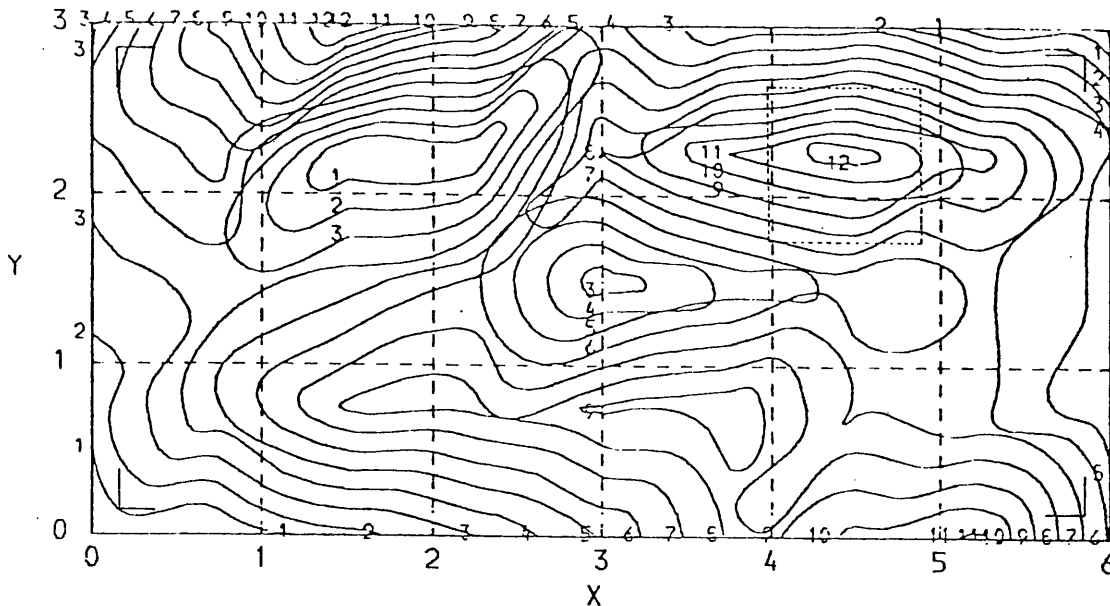
Four 2-D planes as labelled 1, 2, 3, and 4 in fig. 6.1 (a) were reconstructed, and are represented by contour plots.

Resolution: 9 x 5

Model: Grid element

Technique of inversion: LSRT

Contours represent changes in temperature



PLOT 6.3(1) RECONSTRUCTED FIELD USING LSRT & DIGITISED DATA

PLANE H = 0.975

ANGLE MIN = 0.0 DEG

ANGLE MAX = 62.8 DEG

TOTAL NUMBER OF RAYS USED = 300

NUMBER OF PROJECTIONS USED = 10

ORIGINAL TEMP = 19.0 °C

RECONSTRUCTED MEAN TEMP = 20.6 °C

RECONSTRUCTED MAX TEMP = 23.28 °C

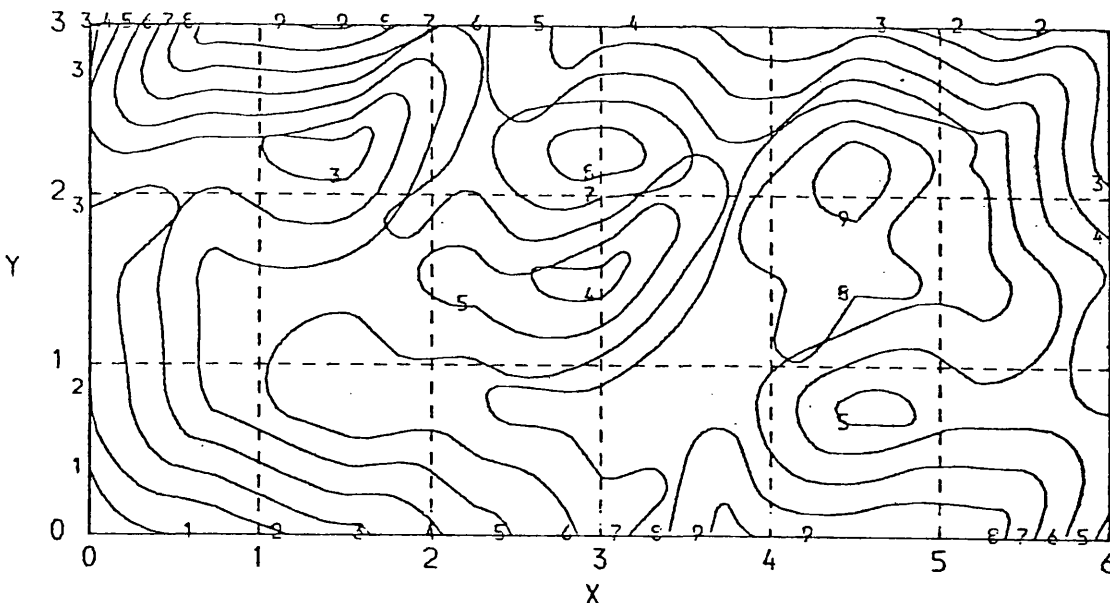
RECONSTRUCTED MIN TEMP = 19.0 °C

CONTOURS IN DEG C

1 = 0.30  
 2 = 0.60  
 3 = 0.90  
 4 = 1.20  
 5 = 1.50  
 6 = 1.80  
 7 = 2.10  
 8 = 2.40  
 9 = 2.70  
 10 = 3.00 ETC.

SUM OF SQUARE OF  $\sigma$  RESIDUAL = 84.9 (CF. 2095 AT K=2)

COMPUTING TIME = 197.90 SEC, CPU (K=200)



PLOT 6.3(2) RECONSTRUCTED FIELD USING LSRT & DIGITISED DATA

PLANE H = 0.950

ANGLE MIN = 0.0 DEG

ANGLE MAX = 62.7 DEG

TOTAL NUMBER OF RAYS USED = 284

NUMBER OF PROJECTIONS USED = 10

ORIGINAL TEMP = 19.0 °C

RECONSTRUCTED MEAN TEMP = 20.58 °C

RECONSTRUCTED MAX TEMP = 23.66 °C

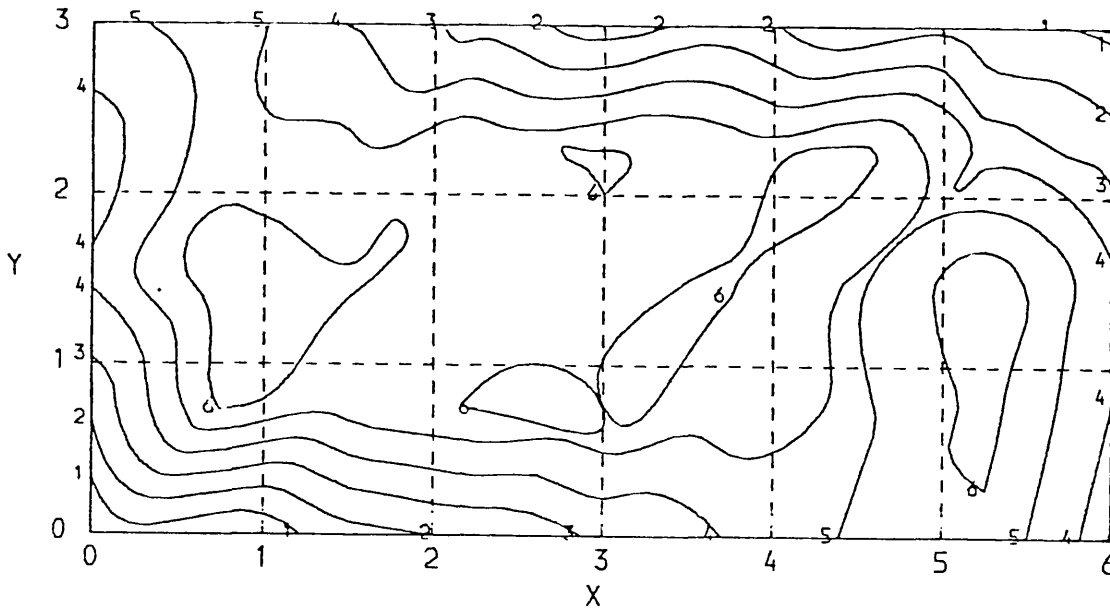
RECONSTRUCTED MIN TEMP = 19.00 °C

CONTOURS IN DEG C

1 = 0.30  
 2 = 0.60  
 3 = 0.90  
 4 = 1.20  
 5 = 1.50  
 6 = 1.80  
 7 = 2.10  
 8 = 2.40  
 9 = 2.70  
 10 = 3.00 ETC.

SUM OF SQUARE OF  $\sigma$  RESIDUAL = 65.6 (CF. 3460 AT K=2)

COMPUTING TIME = 195.00 SEC, CPU (K=200)



PLOT 6.3(3) RECONSTRUCTED FIELD USING LSRT & DIGITISED DATA

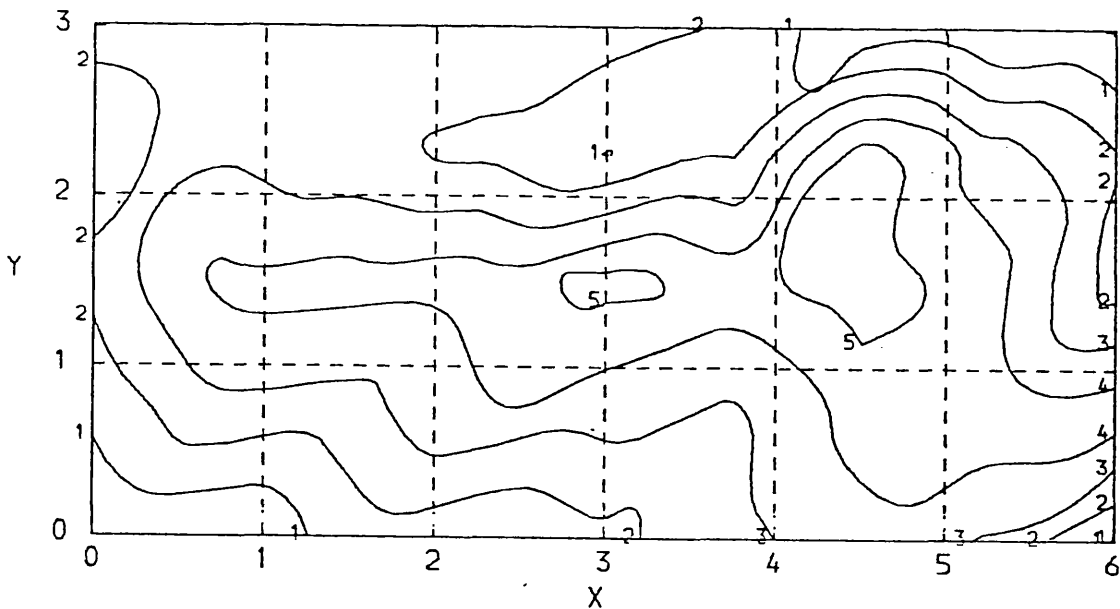
PLANE H = 0.700  
 ANGLE MIN = 0.0 DEG  
 ANGLE MAX = 62.7 DEG  
 TOTAL NUMBER OF RAYS USED = 265  
 NUMBER OF PROJECTIONS USED = 10

CONTOURS IN DEG C

- 1 = 0.30
- 2 = 0.60
- 3 = 0.90
- 4 = 1.20
- 5 = 1.50
- 6 = 1.80
- 7 = 2.10
- 8 = 2.40
- 9 = 2.70
- 10 = 3.00 ETC.

ORIGINAL TEMP = 19.0 °C  
 RECONSTRUCTED MEAN TEMP = 20.26 °C  
 RECONSTRUCTED MAX TEMP = 21.02 °C  
 RECONSTRUCTED MIN TEMP = 19.00 °C

SUM OF SQUARE OF RESIDUAL = 22.4 (CF. 1761 AT K=2)  
 COMPUTING TIME = 203.60 SEC, CPU (K=200).



PLOT 6.3(4) RECONSTRUCTED FIELD USING LSRT & DIGITISED DATA

PLANE H = 0.217  
 ANGLE MIN = 0.0 DEG  
 ANGLE MAX = 62.7 DEG  
 TOTAL NUMBER OF RAYS USED = 264  
 NUMBER OF PROJECTIONS USED = 10

CONTOURS IN DEG C

- 1 = 0.30
- 2 = 0.60
- 3 = 0.90
- 4 = 1.20
- 5 = 1.50
- 6 = 1.80
- 7 = 2.10
- 8 = 2.40
- 9 = 2.70
- 10 = 3.00 ETC.

ORIGINAL TEMP = 19.0 °C  
 RECONSTRUCTED MEAN TEMP = 19.8 °C  
 RECONSTRUCTED MAX TEMP = 20.74 °C  
 RECONSTRUCTED MIN TEMP = 19.99 °C

SUM OF SQUARE OF RESIDUAL = 7.4 (CF 691 AT K=2)  
 COMPUTING TIME = 197.00 SEC, CPU (K=200)

PLOT 6.4 RECONSTRUCTED 3-D TEMPERATURE FIELD WITH HEAT SOURCE  
LOCATED 0.75 WAY ALONG, 0.5 WAY ACROSS

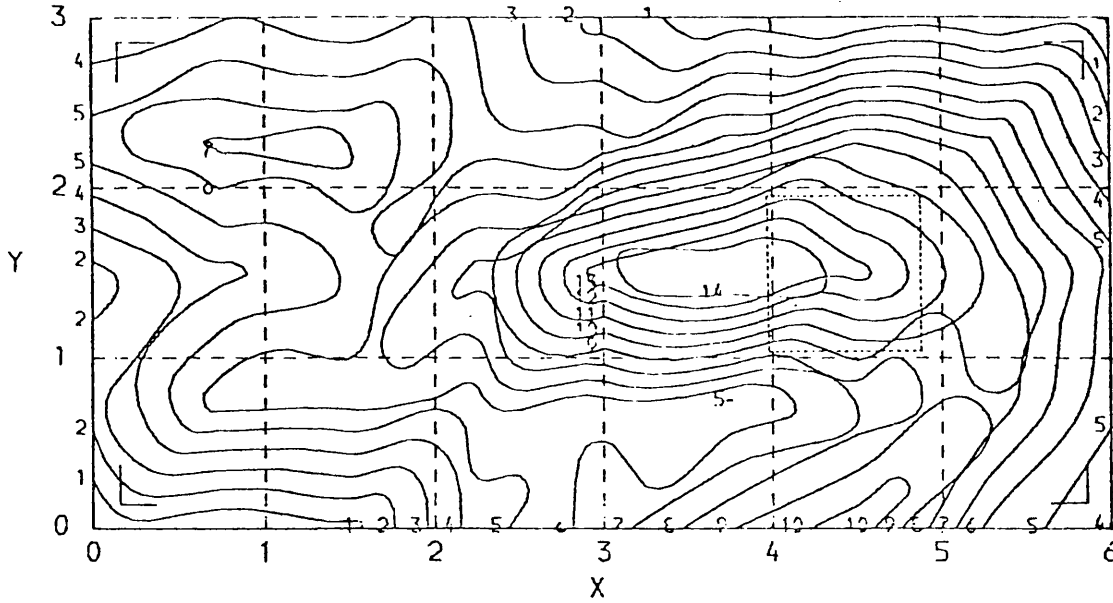
Four 2-D planes as labelled 1, 2, 3, and 4 in fig. 6.1 (a) were reconstructed, and are represented by contour plots.

Resolution: 9 x 5

Model: Grid element

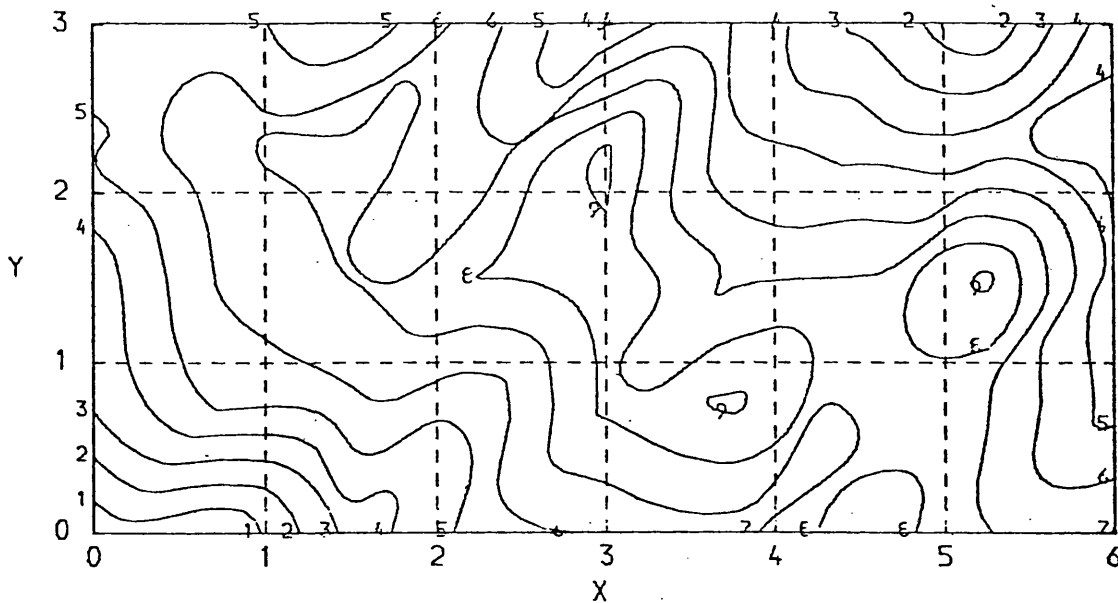
Technique of inversion: LSRT

Contours represent changes in temperature



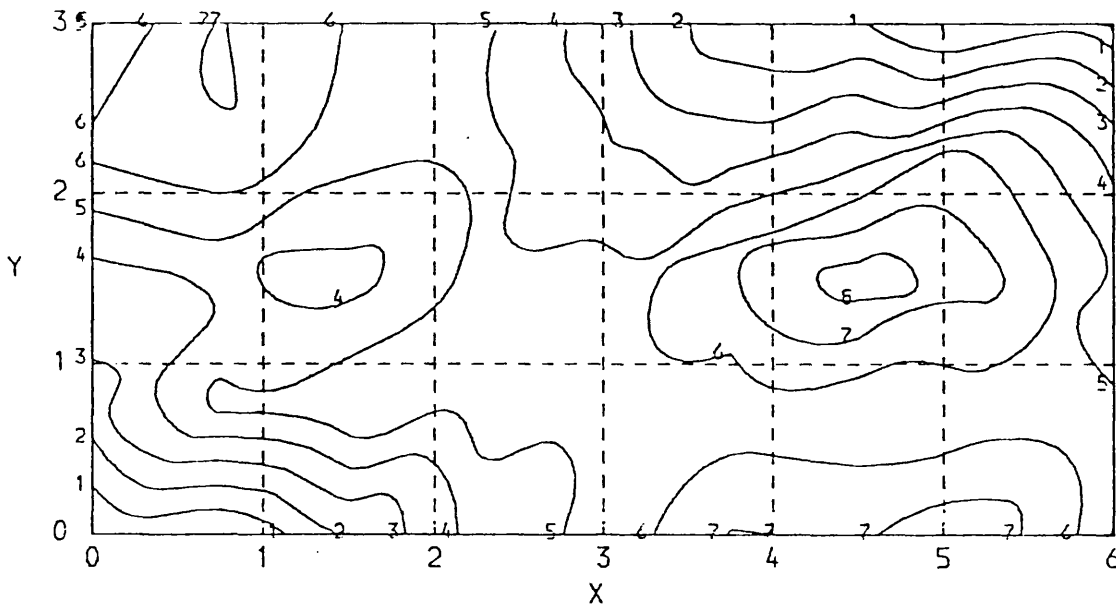
PLOT 6.4(1) RECONSTRUCTED FIELD USING LSRT & DIGITISED DATA

PLANE H= 0.975	CONTOURS IN DEG C
ANGLE MIN= 0.0 DEG	1= 0.30
ANGLE MAX= 59.5 DEG	2= 0.60
TOTAL NUMBER OF RAYS USED = 273	3= 0.90
NUMBER OF PROJECTIONS USED = 8	4= 1.20
	5= 1.50
ORIGINAL TEMP = 18.0°C	6= 1.80
RECONSTRUCTED MEAN TEMP = 19.61°C	7= 2.10
RECONSTRUCTED MAX TEMP = 22.59°C	8= 2.40
RECONSTRUCTED MIN TEMP = 18.00°C	9= 2.70
	10= 3.00 ETC.
	SUM OF SQUARE OF e RESIDUAL = 47.3 (CF. 2727 AT K=2)
	COMPUTING TIME = 172.00 SEC, CPU (K=200)



PLOT 6.4(2) RECONSTRUCTED FIELD USING LSRT & DIGITISED DATA

PLANE H= 0.950	CONTOURS IN DEG C
ANGLE MIN= 0.0 DEG	1= 0.30
ANGLE MAX= 59.5 DEG	2= 0.60
TOTAL NUMBER OF RAYS USED = 251	3= 0.90
NUMBER OF PROJECTIONS USED = 8	4= 1.20
	5= 1.50
ORIGINAL TEMP = 18.0°C	6= 1.80
RECONSTRUCTED MEAN TEMP = 19.66°C	7= 2.10
RECONSTRUCTED MAX TEMP = 22.53°C	8= 2.40
RECONSTRUCTED MIN TEMP = 17.92°C	9= 2.70
	10= 3.00 ETC.
	SUM OF SQUARE OF e RESIDUAL = 49.3 (CF. 2486 AT K=2)
	COMPUTING TIME = 156.00 SEC, CPU (K=200).



PLOT 6.4(3) RECONSTRUCTED FIELD USING LSRT & DIGITISED DATA

PLANE H= 0.700

ANGLE MIN= 0.0 DEG

ANGLE MAX= 59.5 DEG

TOTAL NUMBER OF RAYS USED = 218

NUMBER OF PROJECTIONS USED = 8

ORIGINAL TEMP = 18.0 °C

RECONSTRUCTED MEAN TEMP = 19.38 °C

RECONSTRUCTED MAX TEMP = 20.37 °C

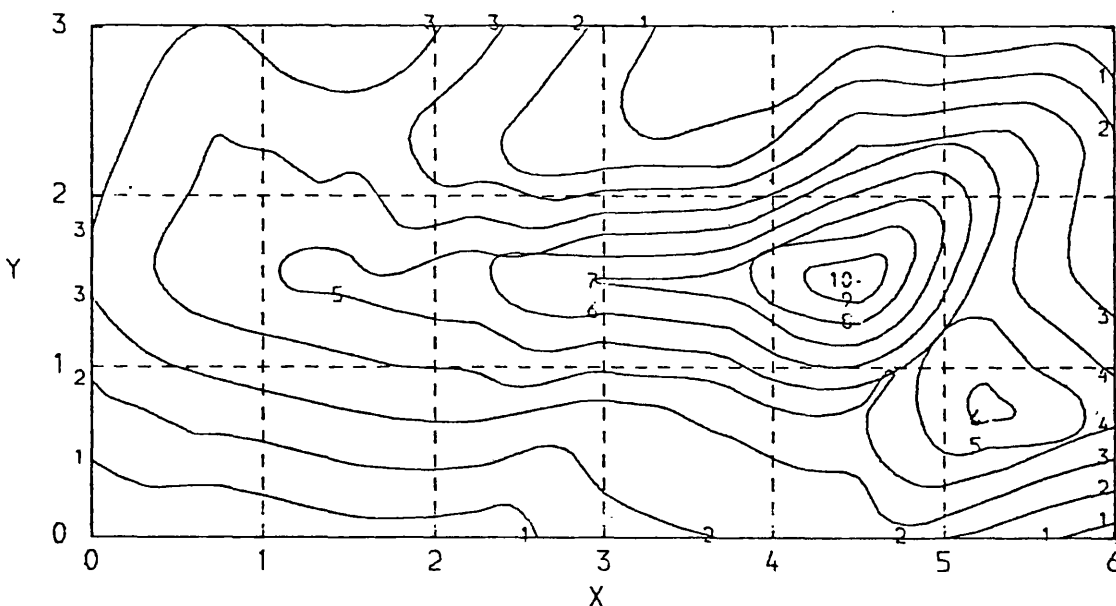
RECONSTRUCTED MIN TEMP = 17.97 °C

CONTOURS IN DEG C

1= 0.30  
2= 0.60  
3= 0.90  
4= 1.20  
5= 1.50  
6= 1.80  
7= 2.10  
8= 2.40  
9= 2.70  
10= 3.00 ETC.

SUM OF SQUARE OF e RESIDUAL = 28.0 (CF. 1472 AT K=2)

COMPUTING TIME = 158.23 SEC, CPU (K=200)



PLOT 6.4(4) RECONSTRUCTED FIELD USING LSRT & DIGITISED DATA

PLANE H= 0.217

ANGLE MIN= 0.0 DEG

ANGLE MAX= 59.5 DEG

TOTAL NUMBER OF RAYS USED = 204

NUMBER OF PROJECTIONS USED = 8

ORIGINAL TEMP = 18.0 °C

RECONSTRUCTED MEAN TEMP = 18.87 °C

RECONSTRUCTED MAX TEMP = 21.01 °C

RECONSTRUCTED MIN TEMP = 17.95 °C

CONTOURS IN DEG C

1= 0.30  
2= 0.60  
3= 0.90  
4= 1.20  
5= 1.50  
6= 1.80  
7= 2.10  
8= 2.40  
9= 2.70  
10= 3.00 ETC.

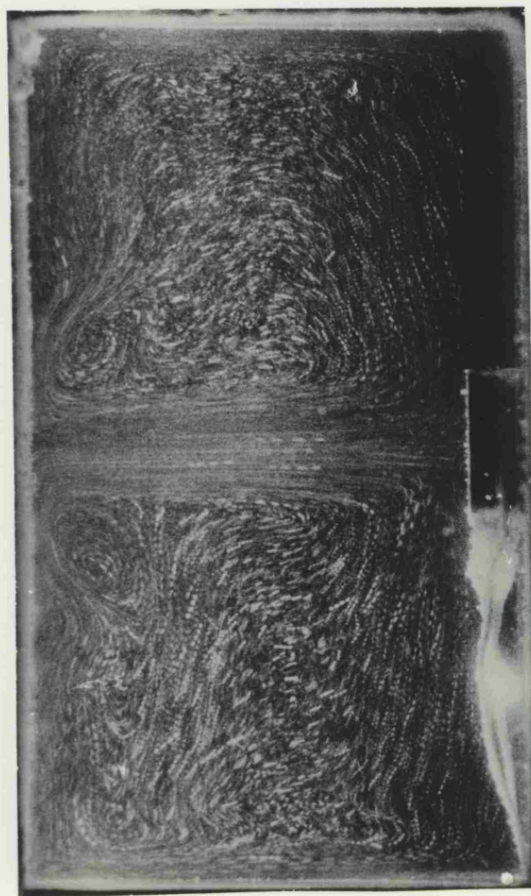
SUM OF SQUARE OF e RESIDUAL = 10.8 (CF. 637 AT K=2)

COMPUTING TIME = 157.07 SEC, CPU (K=200)

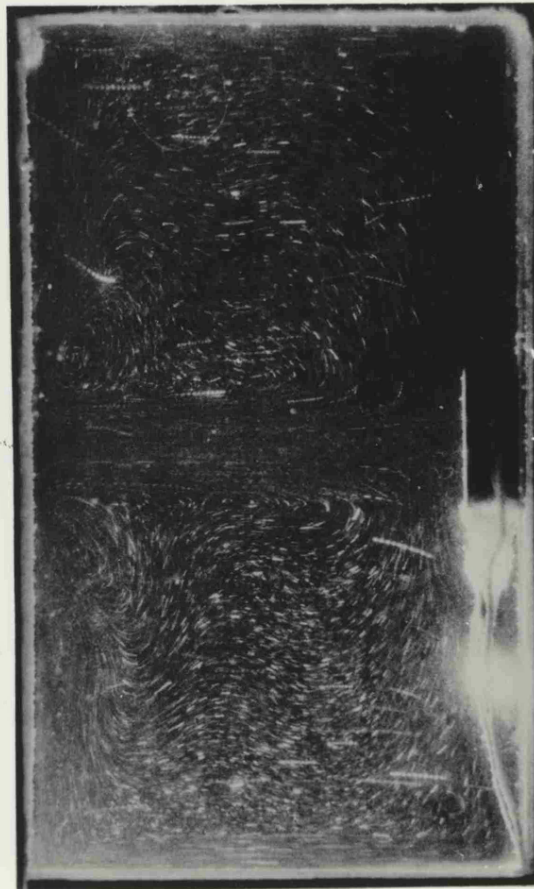
FIG. 6.6

STROBOSCOPIC PHOTOGRAPHS OF  
THE CIRCULATION FLOW PATTERN  
IN THE VERTICAL PLANES THRO'  
THE CENTRE OF THE HEATER

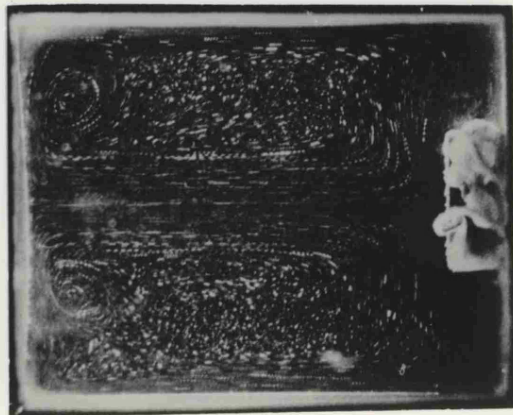
STROBE PERIOD =  $1/6$  sec  
HEATER LOCATION = CENTRAL  
EXPOSURE TIMES (EXP):-  
(i) 4 sec, (ii) 2 sec.



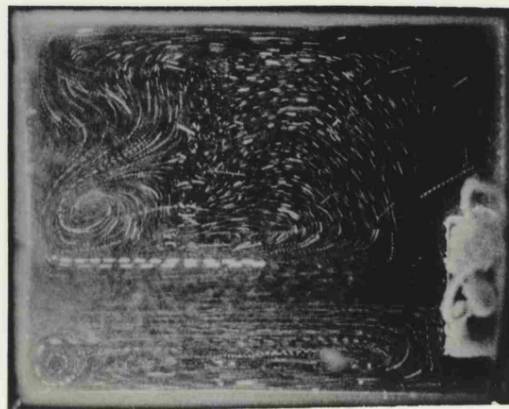
(i)



(ii)



(i)

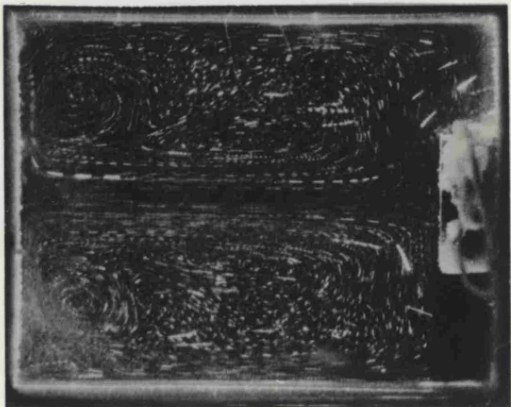


(ii)

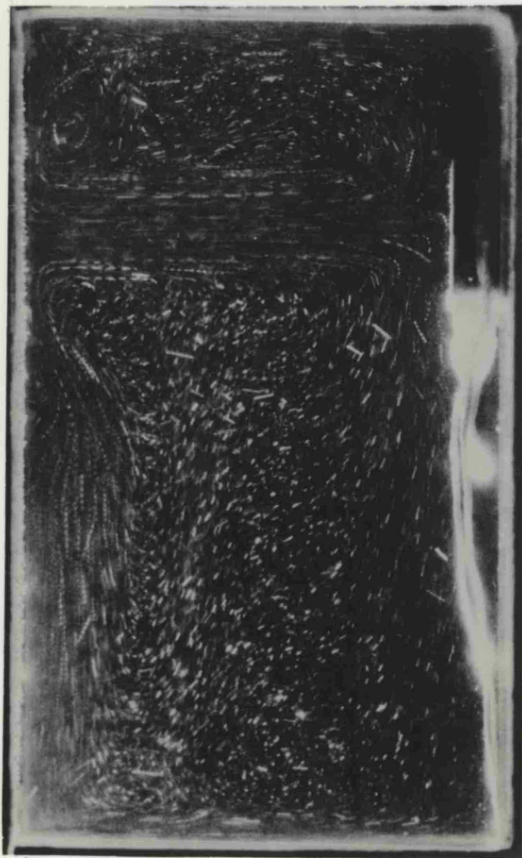
FIG. 6.7

STROBOSCOPIC PHOTOGRAPHS OF  
THE CIRCULATION FLOW PATTERN

STROBE PERIOD =  $1/6$  sec  
HEATER LOCATION :-  
 $\frac{1}{2}$  WAY ALONG,  $\frac{3}{4}$  WAY ACROSS  
EXP = 4 s for (i), 4 s for (ii)



(ii)



(i)

FIG. 6.8

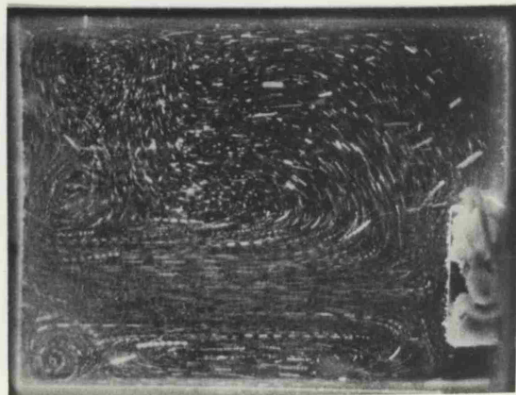
STROBOSCOPIC PHOTOGRAPHS OF  
THE CIRCULATION FLOW PATTERN

STROBE PERIOD =  $1/6$  sec

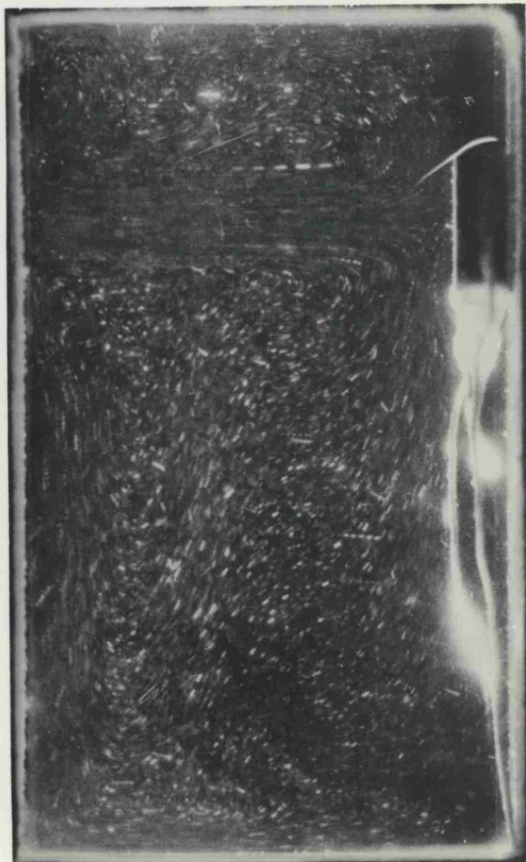
HEATER LOCATION :-

$\frac{3}{4}$  WAY ALONG,  $\frac{1}{2}$  WAY ACROSS

EXP = 2s for (i), 2s for (ii).



(ii)



(i)

FIG. 6.9

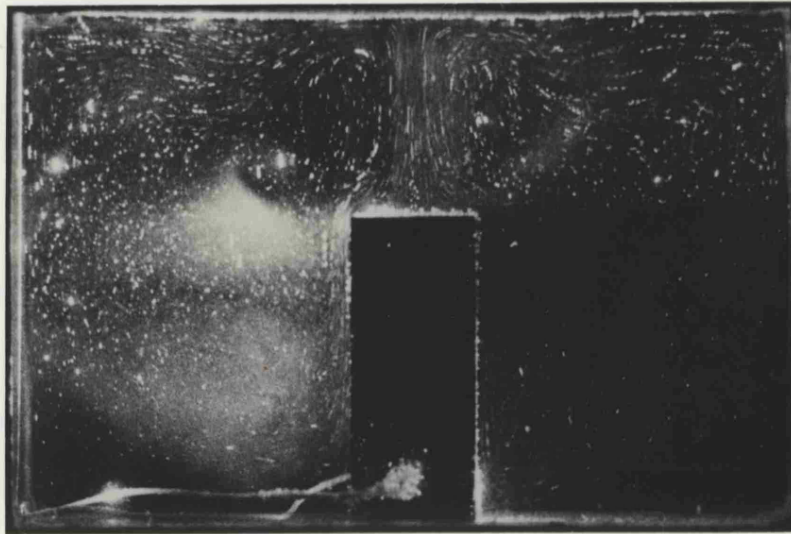
STROBOSCOPIC PHOTOGRAPHS OF  
THE CIRCULATION FLOW PATTERN

STROBE PERIOD =  $1/6$  sec

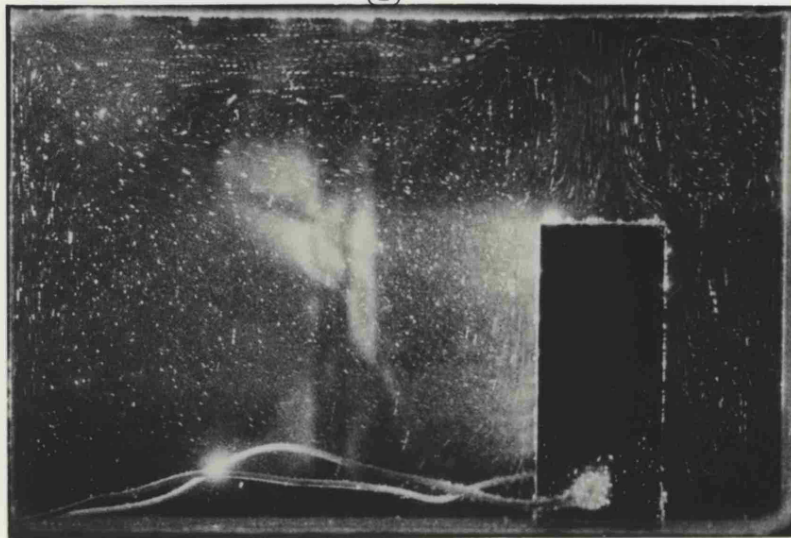
HEATER LOCATION :-

$\frac{3}{4}$  WAY ALONG,  $\frac{3}{4}$  WAY ACROSS

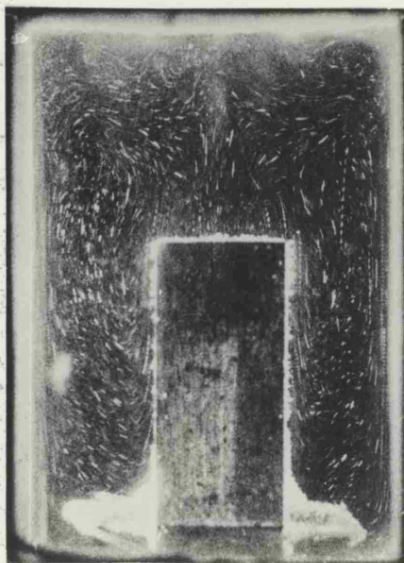
EXP = 1s for (i), 2s for (ii).



(i)



(ii)



(iii)

FIG. 6.10

STROBOSCOPIC PHOTOGRAPHS OBTAINED  
WITH THE 39W TALL HEATER LOCATED  
 $\frac{1}{2}$  WAY ACROSS IN THE ENCLOSURE

STROBE PERIOD =  $\frac{1}{6}$  sec

- (i) WITH HEATER  $\frac{1}{2}$  WAY ALONG, EXP=1sec.
- (ii) WITH HEATER  $\frac{3}{4}$  WAY ALONG, EXP=1sec
- (iii) SIDE VIEW OF (i), EXP=4sec.

SYNOPSISCHAPTER 7CONCLUSIONS

The capability of pulsed laser holographic interferometry for gathering projection data is assessed in this chapter. A viewing angle range of approximately  $125^\circ$  was achieved, but the actual range of viewing angles within the test object that was used was considerably less than this due to refraction effects. In the two laboratory experiments performed involving (i) the heated copper block, and (ii) the constant temperature wall enclosure, it seemed that a  $63^\circ - 70^\circ$  continuous range can be obtained easily. A wider range of viewing angles was not achievable by holography. It is however possible to rotate the test section slightly and make a second set of interferograms but this would be impractical as there would be problems in maintaining exactly similar test conditions everywhere.

Conclusions are also drawn as to the accuracy of the digitised projection data, and also with respect to the numerical techniques used. The digitised projection data were found to be inconsistent with the projection equations because of (i) experimental errors in fringe number measurement, and (ii) errors caused by approximations in the mathematical models. Iterative techniques with very low relaxation parameters were the only procedures able to invert these equations without a significant amount of instability. Chapters 4 and 6 show the results. ART and LSRT techniques, and Grid and Finite Element mathematical models were employed. In terms of engineering measurement accuracy, these results are degraded by computational errors caused by use of an incomplete set of projection data obtained from a restricted range of viewing angles. This is characterised by a directional bias in the shape of the reconstructed temperature field. A viewing angle range of  $180^\circ$  is considered to be the ideal for numerical analysis.

CHAPTER 7CONCLUSIONS7.1 3-D TEMPERATURE MEASUREMENT BY PULSED LASER HOLOGRAPHIC INTERFEROMETRY

The main concern of this project was to determine the usefulness of the technique of holographic interferometry as a means of gathering experimental projection data from heat transfer processes in which three-dimensional temperature fields were set up. This was followed by an investigation into the possibility of reliably reconstructing the three-dimensional temperature fields from the collected data processed by appropriate numerical algorithms using the University Cyber 73 computer. Two approximate mathematical models were proposed to represent the reconstructed surface of the temperature field, and a number of numerical algorithms was tested based on these reconstructing models.

Therefore in this research programme there were two stages:

(1) Investigation of the hot plume above a heated copper block from which both projection data and direct temperature measurements by thermocouple were obtained. This allows a comparison between the temperature field reconstructed from the projection data and the directly measured temperatures. Good agreement here builds confidence in results obtained from a situation where only projection data is available. Also by simulating projection data by calculation from the directly measured temperature an estimate of the effect of noise in the projection data on the temperature field reconstruction is possible. Good reconstruction were obtainable with the ART and LSRT techniques based on the Grid element model. Tests on these and other methods are fully discussed in Chapter 4.

(2) Investigation of the reconstruction of a three-dimensional temperature field which was more complicated. The temperature field used resulted from the natural convection current in an enclosure with a heated spot on the floor and all the walls maintained at constant temperature. To obtain a sufficiently high number of fringes for accurate digitisation from interferograms it was necessary to have water as the medium in the enclosure. Maintaining the walls at a constant temperature was being achieved by immersing the enclosure in a glass tank full of flowing water. Refraction effects meant that it was necessary to build a two object/reference beam holographic interferometer to achieve a wide field of view in the enclosure. The location of the heated spot on the floor was variable. For each location the three-dimensional temperature field was built up by reconstructing the two dimensional field on each of the four planes at different heights above the enclosure floor.

In this case the temperature field was more complicated than that above the heated copper block. In attempting to reconstruct using the Grid element model and the ART numerical inversion algorithm, as described in Chapter 3 and used in Chapter 4, severe instability problems were encountered characterised by large artifacts peppering the reconstructing field. A version of the SIRT inversion algorithm was tried but similar problems still persisted. In an attempt to overcome these problems the author developed a technique, LSRT, where the criteria of least squares of residuals was measured iteratively. Successful reconstructions were obtained using this technique.

More details with regards to each of the various aspects of this research are concluded in the following sections.

## 7.2 THE METHOD OF HOLOGRAPHIC INTERFEROMETRY AND DATA DIGITISATION

The single object/reference beam holographic interferometer built for the heated copper block experiment gave a maximum useful viewing angle of approximately  $79^\circ$ . However, digitisation over an entire viewing plane could only be carried out from  $0^\circ$  to  $70^\circ$  inclusive. This was being done at  $10^\circ$  intervals. A wider range of viewing angles would be difficult to achieve in this case because a pathway was required to slide the copper block into the test region after it was heated to a stabilised temperature. This reduced the disturbance to the reference beam due to the radiation causing the interferometer to warm up and hence the air in the path of the reference beam.

Although it was impractical to build an interferometer with more than one object/reference beam for the heated copper block, the results obtained were representative in terms of the maximum range of viewing angles obtainable from holographic experiments. As such they were used to test the numerical techniques for the possibility of reconstruction.

To obtain a similar range of actual viewing angles from the constant temperature enclosure, rays from the diffusing screen had to be diffused over a much wider angle because of the refraction of the rays in going through the water tank. So it was necessary to build the two object/reference beam holographic interferometer. The maximum viewing angle range obtainable from this interferometer was approximately  $125^\circ$ , but digitisation over entire viewing planes was possible only over  $95^\circ$  or less. Taking refraction into account the true range of viewing angles obtained was  $62.7^\circ$ . Though the quality of these interferograms were not as good as that from the single object/reference beam interferometer, they were adequate and very fine fringes, up to 5 per mm, could be resolved.

A range of viewing angles much wider than this was very difficult to achieve because

- (i) the maximum output of the recording pulsed laser was 30mJ; further splitting of the main beam and losses in the optical elements caused insufficient exposure on the holographic plates making the resulting interferograms extremely difficult to analyse,
- (ii) light rays were refracted more as rays were made to diffuse over a greater range of angles at the air/water interface of the water tank containing the enclosure.

These experiments have thus shown that pulsed laser holographic interferometry cannot easily be used to collect projection data over the ideally  $180^\circ$  for reconstruction purposes. In addition to the optical problems the field of interest must also be largely free from any opaque obstacles.

Photographs of the fringe pattern at the various angles on the interferogram were produced by the method described in Chapter 2, in which a 35mm LED metering SLR camera fitted with a 200mm f.1. telephoto lens and an extension tube was used. Digitisation was carried out on these enlarged photographs which were taken with the camera placed at least 1.3 m away from the holographic image so that the maximum estimated average error near the edges of the reconstructed image was  $2^\circ$  for the copper block, or  $3.5^\circ$  for the constant temperature enclosure. Viewing planes were mostly taken at  $10^\circ$  intervals although for the enclosure it was more convenient to digitise on planes in which fringes were clearly sharper over the entire viewing plane than at similarly close intervals.

This method used by the author proved much more successful than the spatial filtering technique which theoretically is more accurate. This

filtering technique was very difficult to implement because the test sections were diffusely illuminated, and as such reconstructing an image from absolutely parallel rays from a certain direction requires a more powerful reconstructing laser. It was found that the continuous wave reconstructing laser from the lab with a maximum output of 15 mW was not strong enough to produce any good images.

### 7.3 A COMPARISION OF THE HOLOGRAPHIC DATA

The level of noise in the experimental holographic data was found by making a comparision with the results of the thermocouple traverse from a horizontal plane over the heated copper block. The thermocouple readings were then converted by computation to fringe numbers along ray paths. A resolution of  $9 \times 10$  was used and was found adequate. The plots of computed and experimental fringe numbers in Chapter 4 showed that fringe numbers with low values have a much bigger error band,  $\pm 100\%$  in error not being uncommon. Also these occurred at the edges of the thermal plume where the frequency was already quite low making measurements unreliable. At the higher values the fringe numbers were in good general agreement with the exception of only a few which were out by not much more than 30%.

It was considered unlikely that the errors between the computed and digitised experimental fringe numbers were due to the discrete method by which computed fringe numbers were obtained because calculations performed using a horizontal reconstructing plane extended beyond the thermal plume region indicated that the temperature increase was only slight and that the thermocouple readings in this extended region was not sufficient to cause any significant under-estimation in the computation. The cause was thus determined to be experimental because

- (i) there was thermal disturbance to the air in and around the test region and also to the reference beam in between the first and second exposure, and
- (ii) there was also slight physical movement of the optical elements due to vibration in between the two exposures causing some finite background fringes to appear.

#### 7.4 THE TECHNIQUES FOR RECONSTRUCTING 3-D TEMPERATURE FIELDS

Trial temperature field reconstructions by all the three iterative inversion algorithms showed that they could reconstruct much better than the direct least squares back-substitution procedure, when experimental interferometric projection data were used which were invariably noisy. However, the feasibility of the iterative inversion techniques does not mean that holographic interferometry is a viable technique for the measurement of three-dimensional temperature fields. In practise, apart from the possibility of disturbance to the environment around the test section, the biggest problem is the restricted range of viewing angles over which data are obtainable from the holographic interferometer. The preliminary laboratory experiment on the heated copper block showed a tendency for the reconstructed field to be biased in the directions from which projected data were collected. This was much more pronounced when experimental projection data were used, instead of accurate simulated data. The reconstructions thus imply that the missing projection data were necessary to constrain the shape of the reconstruction. They would also be useful in constraining the value pixels could have. The study in Chapter 4 also showed that the Grid element model produces better reconstructions than the more sophisticated Finite element model used as a basis for representing the surface of the 3-D temperature fields. In the Grid element each value of  $n$  is independent of others neighbouring it

so the directional bias in the reconstructions became less noticeable.

Three types of errors were identified as described in Chapter 3. They are due to (i) digitisation or measurement, (ii) modelling, and (iii) restricted range of viewing angles. In the presence of errors of type (ii) and (iii) satisfactory reconstructions depend largely on the test temperature field being smoothly varying rather than peaky. Combined with the error of type (i) significant degradation in the reconstructed field is likely.

ART and SIRT, using the Grid element model, could produce acceptably good reconstructions from the heated copper block experiment, using either simulated or digitised projection data. However, these techniques, when applied to the digitised projection data from the constant temperature wall enclosure, produced practically useless and unstable reconstructions even though redundant data were being used. The problem arose from the complicated nature of the temperature field. This field could not be adequately represented by the model containing the optimal number of pixels necessary for reconstructing without much instability with projection data from the restricted viewing angles. A narrow spiky profile was expected to occur over the heated spot and temperature changes near the boundary walls were present as implied by the downward velocities from the flow visualisation photographs shown in Chapter 6. Error of type (ii) therefore became more significant. The reconstruction if good would therefore show these features as averaged out over the pixels concerned. In attempts to overcome this problem the least squares of residuals technique (LSRT) was developed which reconstructed the projection data. The best possible reconstructed fields are shown in Chapter 6.

Tests made using the experimental projection data from the heated copper block experiment showed that each of the iterative inversion techniques produced a temperature field which differed to one another in values on some (up to half) of the pixels. A closer match with one another and also to the true temperature field obtained from the thermocouple traverse was found possible provided pixels were initialised with some suitable values before the iteration process. But at the optimal number of iterations some of these differences in values on pixels corresponding to those obtained by thermocouples could still easily be in the order of 20% - 35%. To handle experimental or inconsistent projection data a subprogram called KAISYM was developed to determine, based on the input projection data, the optimal weights or values to be initialised or used on the pixels to obtain the general shape of the field first and then let subsequent iterations with the inversion technique to improve on this. In the computer listing in Appendix 1 KAISYM is shown implemented on the LSRT technique.

When dealing with such highly inconsistent projection data as that from the enclosure model, pixel initialisation together with use of variable relaxation parameters which acted like filters, or dampers, was found to be essential in achieving a sensible reconstruction. Trial tests showed that the use of smaller and smaller relaxation factors or parameters, 0.1 or less, was desirable to allow the field to be formed gradually though this takes more computing time. Without the relaxation parameters the reconstruction process is corrupted after the first few iterations and useless reconstructions produced.

ART was rejected in the enclosure experiment because of its inability to adequately handle the inconsistent and noisy projection data as explained in Chapters 3 and 4. SIRT was also rejected as it could not produce the desired form of reconstruction on convergence.

LSRT produced the best reconstructed fields with resolutions of 13x7 and 9x5, but there were still some artifacts appearing on the surface of the 3-D temperature field. Various tests were tried, sampling data at different intervals, increasing resolution etc., but there was no improvement. A greater resolution was thought to be useful but the subsequent appearance of artifacts and directional bias on the reconstructed temperature surface could not be controlled. Digitised projection data from a much wider range of viewing angles are necessary to overcome this.

APPENDIX 1COMPUTER PROGRAM LISTING

The computer program FERECON used to reconstruct a 2-D slice of the 3-D temperature field is included. The 3-D temperature field is obtained by stacking a number of such 2-D reconstructions on top of one another. During trial tests many versions of this program were developed to search for the best values for the various parameters such as the relaxation factor, resolution, mathematical model, inversion technique, and criteria for terminating the iteration process. The version included is therefore considered to be representative for the reconstructed temperature field work reported in this thesis.

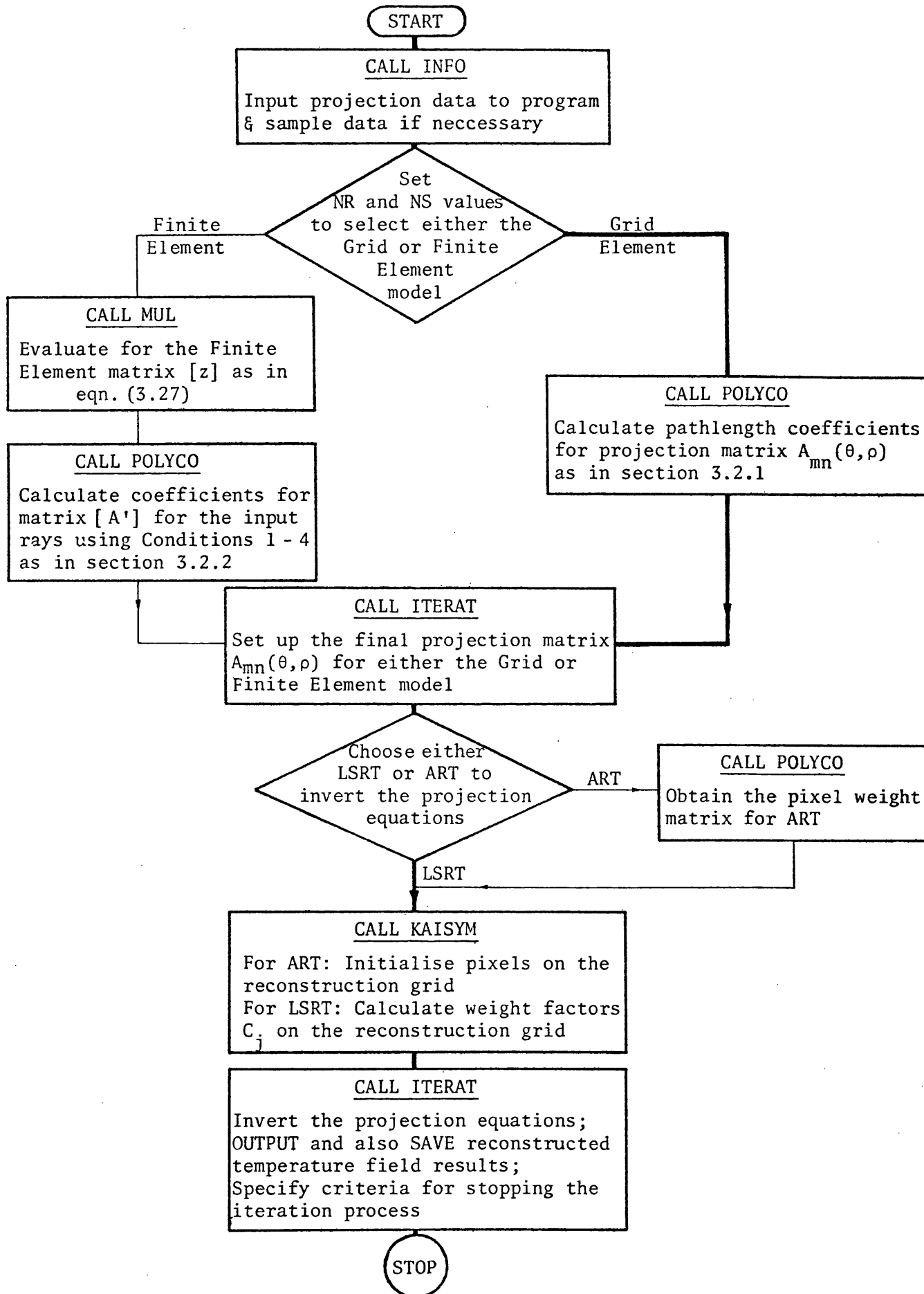
This version was actually used on the four sets of digitised projection data to reconstruct the temperature field in the enclosure with the heater centrally located, using the Grid Element model with a resolution of 9 x 5, and LSRT to invert for the temperature field. The extension to use the ART technique, or the Finite Element mathematical model, or a change in resolution, or even to the heated copper block temperature field reconstruction is quite straightforward as this version contains a lot of written but commented out Fortran codes and is also documented.

Also included in this Appendix are the sets of digitised projection data obtained from holographic interferograms of the enclosure model, each set corresponds in sequence to the reconstructed fields shown in Chapter 6. Each set contains the following inputs to the program:-

1. (a) Number of projections, (b) total number of rays, (c) 2 now redundant integers
2. Number of rays from each projection
3. The projection or viewing angles in degrees according to convention used in fig. 3.1
4. The magnification factor on each print that was digitised for projection data
5. The digitised data, each input in terms of the fringe number  $N$  together with a value of located distance of ray  $\rho$  for that fringe number.

The program PLOT was used to draw the reconstructed temperature fields, which uses a graphic computer package called GHOST. Changing the values of the quantities appearing immediately below each plot is again quite straightforward from the PLOT program.

A condensed flowchart illustrating the major operations of the main program FERECON is given.



MAJOR OPERATIONS PERFORMED BY THE MAIN PROGRAM FERECON

FERECON OPERATION NOTES

The 9 x 5 Grid element method chosen follows the paths indicated by thick lines on the flowchart. Basically, projection data are read in by the program, in subroutine INFO, and are then processed by the routine, on pages 163 & 164, which assigns a ray, and hence a pathlength fringe number, over a certain width so that they are more evenly distributed on the reconstruction grid. The width for the enclosure data is determined by  $\Delta x \cdot \sin \theta$  which was found to be adequate without the need to change  $\sin \theta$  to  $\cos \theta$  when  $\theta > 45^\circ$  because the maximum angle of view was only  $-27.3^\circ$  (starting from  $-90^\circ$ ). The difference shown by reconstructions when  $\cos \theta$  was used when  $\theta > 45^\circ$  was quite small and produced no noticeable improvement.

The subroutine MUL calculates elemental values for the second matrix on the l.h.s. of eqn.(3.28), for a 4 x 2 Finite element model, but is defunct when the Grid element model is used. Calculated values of the elements in array POLY(I,J), where I and J are row and column numbers respectively, are then transposed to facilitate subsequent manipulation in subroutine ITERAT with [A'] the first matrix on the l.h.s. of eqn.(3.28). The transposed values are stored in ZX1(I) which disregards any zero-valued elements because of the limited amount of core storage memory available on the University's Cyber 73 computer.

Subroutine POLYCO evaluates the weight projection matrix [A] for the 9 x 5 Grid element model according to the location of the rays on the reconstruction grid. For the 4 x 2 Finite element model, this subroutine evaluates the projection matrix [A'] as in eqn.(3.27).

Having evaluated the weights of [A] or [A'], and with the input

projection data sampled to a reasonably distributed form, FERECON now calls subroutine ITERAT which first evaluates for the final projection matrix [A] if the 4 x 2 Finite element model is used, or if the 9 x 5 Grid element model is used proceeds by calling subroutine KAISYM to produce a set of conservative weight factors based on the projection data. The latter part of ITERAT performs the iterative inversion process with the algorithm LSRT. The algorithm preceding this in ITERAT is ART but is defunct when LSRT is used.

The iteration inversion process continues for 200 complete cycles of iterations, during which time at the end of each iteration a number of measuring criteria, such as the sum of the squares of each residual, sum of the residuals, maximum and minimum temperatures on the reconstructed field, iteration cycle number, were also evaluated and printed out together together with the reconstructed temperature field for the purpose of evaluation by the author.

FERECON has also been used to produce temperature field reconstructions using the holographic projection data from the heated copper block experiment. The following symbols are used in FERECON on the r.h.s. of the computer codes to indicate the changes required to adapt the program to invert using the holographic projection data from the copper block:

- o - comment out this line
- \* - uncomment this line
- \*o - an alteration required as per comments

A description of the main variables used by FERECON is given below.

MAIN VARIABLES USED BY FERRECON

(arranged in order to follow FERRECON)

S( $\theta, \rho$ ) = fringe number

RD( $\theta, \rho$ ) = distance from origin

AG( $\theta$ ) = projection angle

NODE(I,J) = numbering sequence of the nodes on the Finite element mesh  
where I and J are pixel and node numbers respectively

BASIC(I,J) = nodal coefficients as from eqn.(3.18) in section 3.2.2  
where I and J are row and column numbers respectively

POLY(I,J) = the matrix [z] as in section 3.2.2, elements of [z] to  
be stored permanently in ZX1(I). Also the matrix [A] when  
in subroutine ITERAT for the Finite element model as in p.176

KZ(J) = no. of non-zero elements in row J of the matrix [z]

KP(II) = the column number corresponding to the IIth non-zero element

ZX1(II) = the value of the IIth non-zero element

ZMAG( $\theta$ ) = magnification factor in the digitised projection data from  
the prints

X(I) = value of the pixel I

XVALUE(I) = a working store for X(I)

ZX(I) = total physical pathlength intersecting the entire  
reconstruction grid

ICOUNT(I) = number of non-zero elements in ray I

NODE2(I) = working node identifier for output of results, used with  
Finite element model only

IZ(I) = number of non-zero coefficients in the Finite element  
model weight matrix [A] for ray I

POLYCD(I) = pathlength elemental coefficients

XX(I) = used as a store for the solution vector

```

PROGRAM FERECON(INPUT,OUTPUT,TAPE3,TAPE1=INPUT,TAPE2=OUTPUT)
C
C PROGRAM TO RECONSTRUCT A 2-D SLICE OF AN UNKNOWN 3-D TEMPERATURE
C FIELD, USING PROJECTION DATA OBTAINED BY PULSED LASER HOLOGRAPHIC
C INTERFEROMETRY, THE RECONSTRUCTED 3-D TEMPERATURE FIELD IS
C OBTAINED BY STACKING UP A NUMBER OF THESE RECONSTRUCTED 2-D
C TEMPERATURE DISTRIBUTIONS.
C
DIMENSION S(10,50),RD(10,50),AG(20)
DIMENSION KZ(144),KP(730),ZX1(730)
COMMON POLYCD(10412),ZX(300),POLYC(1,144),ISUB,KOZ(10),ICOUNT(300)
1,NR,IOP,M4,PMAG,NS,MS,NR55
C
C INPUT AND PROCESS THE PROJECTION DATA
C
CALL INFO(S,RD,AG,IO,KO)
C
NOTE: TO OVERCOME LIMITED CORE STORAGE SPACE ONE-DIMENSIONAL
C ARRAYS ARE USED THROUGHOUT FOR THE WEIGHTING MATRICES
C WHICH ARE TWO-DIMENSIONAL. THESE 1-D MATRICES ARE
C DEVELOPED TO STORE ONLY THOSE COEFFICIENTS WITH
C NON-ZERO COEFFICIENTS, E.G. MATRICES POLYCD(10412) ,
C ZX1(730) IN SUBROUTINE MUL, & POLY(8420) IN SUBROUTINE
C ITERAT.
C
FOR THE FINITE ELEMENT MODEL ONLY - SETTING UP THE COEFFICIENT MATRIX
C DESCRIBING THIS MATHEMATICAL MODEL. (THE VECTOR Z IN SECTION 3.2.2)
C
CALL MUL(KZ,KP,ZX1)
C
THE MODE OF THE VARIABLES AT PRESENT IS SET TO CALCULATE USING A 9X5
C GRID ELEMENT MODEL , AND THE LSRT ALGORITHM
C
NR=1
NS=1
C (FOR THE GRID ELEMENT MODEL SET NR=1, NS=1. HOWEVER IF NR=1 AND
C NS=0 OPTICAL PATHLENGTH DIFFERENCES CAN BE CALCULATED ONLY
C APPROXIMATELY FROM THE RECONSTRUCTED FIELD UTILISING THE GRID
C ELEMENT MODEL. FOR THE FINITE ELEMENT MODEL NR & NS SHOULD BE
C SET TO 0 & 1 RESPECTIVELY HERE)
C
NR55=0
C EVALUATE COEFFICIENTS OF WEIGHTING MATRIX (A OR A') USING PROJECTION
C DATA RAYS.
C
CALL POLYCO(S,RD,AG,IO,KO)
C
INVERT THE RECONSTRUCTION EQUATION FROM THE CHOSEN MATHEMATICAL
C MODEL USING EITHER ART OR LRST
C
CALL ITERAT(S,RD,AG,KZ,KP,ZX1)
STOP
END
C
C

```

```

C
C
C
  SUBROUTINE INFO(S,RD,AG,IO,KO)
  DIMENSION ZMAG(10)
  DIMENSION S(10,50),RD(10,50),AG(20)
  DIMENSION R5(50),S5(50)
  COMMON POLYCD(10412),ZX(300),POLYC(1,144),ISUR,KOZ(10),ICOUNT(300)
  1,NR,IOP,M4,PMAG,NS,M5,NR55

C
C  PROJECTION=IO, RAYS=KO, CENTRE 'NODES' X=LO,Y=MO, ANGLES=A(I)
C
C  NO. OF PIXELS
  M5=45
C
C  MAGNIFICATION FACTOR TO FIT TEST FIELD (FLOOR OF ENCLOSURE) ON
C  TO RECONSTRUCTING PLANE.
  PMAG=0.4
C
C*** FOR COPPER BLOCK:
C*** PMAG=1.333333 : for 9x5 Grid elements, with Cu block data *
C** PMAG=2.0000 : for 13x7 Grid elements, with Cu block data
C  INPUT NO. OF PROJECTIONS IO, & TOTAL NUMBER OF RAYS KO
C  LO & MO ARE REDUNDANT SET TO 9 & 5 OR ANY OTHER VALUES
  READ(1,1)IO,KO,LO,MO
  IOP=IO
  M4=KO
C  INPUT NUMBER OF RAYS FROM EACH PROJECTION
  READ (1,8) (KOZ(I),I=1,IO)
  8 FORMAT(10(I3))
C  INPUT PROJECTION ANGLES IN DEGREES
  READ(1,4)(AG(I),I=1,IO)
C  INPUT MAGNIFICATION FACTOR OF & PRINT FROM WHICH DIGITISED DATA
C  WERE OBTAINED.
C  ZMAG NOT REQUIRED ON CU (COPPER) BLOCK DATA. THIS CAN EITHER BE
C  COMMENTED OUT, OR SET EACH ELEMENT TO EQUAL 1.00
  READ(1,4) (ZMAG(I),I=1,IO)
C
C  4 FORMAT(8F9.2)
C  4 FORMAT(10F7.3)
C  1 FORMAT(4I3)
C  CHECK DATA ENTRY VALUES=
  WRITE(2,7)
  WRITE(2,100)IO,KO,LO,MO
  7 FORMAT(1H1,1X,12H IO KO LO MO)
  100 FORMAT(1H0,4I3,/)
C
C  WRITE(2,9)
C  WRITE(2,400)(AG(I),I=1,IO)
  9 FORMAT(1H0,13HVIEW ANGLE A=,/)
  400 FORMAT(1H0,F9.4)
C
C  INPUT THE FRINGE NUMBERS IN ARRAY S, AND THE CORRESPONDING
C  DISTANCE OF RAYS FROM ORIGIN IN ARRAY RD
C
  DO 3 I=1,IO
  KOZI=KOZ(I)
  READ(1,11)(S(I,K),RD(I,K),K=1,KOZI)
C 11 FORMAT(10(F3.0,F5.3))
  11 FORMAT(8(F4.2,F6.4))
  DO 103 K=1,KOZI

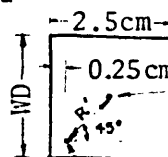
```

checking data  
entered

```

C READ(1,5) S(I,K),RD(I,K) : [not in use]
C FOR ENCLOSURE, FIRST DARK FRINGE WAS COUNTED AS 1 IN ALL
C PROJECTION DATA, AND NEED TO BE CORRECTED HERE.
C REMOVE 0.5 FOR CU BLOCK DATA
S(I,K)=-S(I,K)+0.5 *O
C RD(I,K)=RD(I,K)*1.939 : for 4x4 square Finite elements & Cu data
C RD(I,K)=RD(I,K)*2.2222 : for 4x4 rect. Finite element & Cu data
C*** RD(I,K)=RD(I,K)*PMAG [ or Grid " " " " ]
C CALCULATE ACTUAL DISTANCE OF PROJECTION RAYS ON THE RECONSTRUCTING
C PLANE
C FOE CU BLOCK, INITIALISE ZMAG AS 1.00
RD(I,K)=RD(I,K)*PMAG/ZMAG(I) O
C CONVERT INPUT DATA OF DISTANCE FROM MM TO CM
C NOT NEEDED FOR COPPER BLOCK DATA:
RD(I,K)=RD(I,K)/10.0 O
C PROCESSING DATA TO FOLLOW CONVENTION : IN NEXT TWO IF STATEMENTS
IF(ABS(AG(I)).GT.90.0) RD(I,K)=-RD(I,K) O
103 CONTINUE
C
C 5 FORMAT(2F12.4)
C
C IF(ABS(AG(I)).GT.90.0) AG(I)=180.0+AG(I) O
C
C
C WRITE(2,10)
C WRITE(2,500)((RD(I,K)/PMAG),S(I,K)),K=1,KOZI) } checking data
10 FORMAT(//,1H0,3X,2HR=,8X,2HS=,/) entered
500 FORMAT(1H ,2F10.4)
C
C 3 CONTINUE
C
C
C DO 6 I=1,IO
C FOR CU BLOCK, COMMENT OUT NEXT LINE & UNCOMMENT THE LINE
C FOLLOWING : ORIENTATES TEST REGION ONTO RECONSTRUCTION PLANE
AG(I)=AG(I)*4.0*ATAN(1.0)/180.0 O
C*** AG(I)=(AG(I)+90.0)*4.0*ATAN(1.0)/180.0 *
C DO 1000 K=1,KO
C S(I,K)=(S(I,K)*0.0000006328)/0.254
C1000 CONTINUE
C 6 CONTINUE
C
C SHIFT ORIGIN TO PIXEL M=2, N=2, THEN TO M=1, N=1 FOR GRID
C ELEMENT MODEL. FOR FINITE ELEMENTS, CENTER OF FIRST ELEMENT
C IS THE ORIGIN CORRESPONDING TO "M=2, N=2" ON EVALUATION OF
C NODAL POINTS WITH TEMPERATURE FIELD RECONSTRUCTION TECHNIQUES.
C LENGTH OF ONE SIDE OF SQUARE PIXEL =0.5
C CHANGE DATA ORIGIN
DO 20 I=1,IO
A=AG(I)
AR=0.785398-AG(I) : [0.785398 rad = 45°] *O
C FOR CU BLOCK AR=A+0.1511165, COMMENT OUT LINE ABOVE *
ARO=0.785398-AG(I)
KOZI=KOZ(I)
DO 21 K=1,KOZI
C FOR CU BLOCK, CHANGE 0.5656 TO 2.6562
Normalising WD as 1.0 gives R'= 0.5656
from  $\sqrt{(0.4^2 + 0.4^2)}$ 

```



centre of  
square Finite  
element

origin from digitised data  
new origin required here

```

Shift origin from data set to centre of 1st Finite element
and then to 1st node i.e. centre of 1st Grid element
RD(I,K)=RD(I,K)-(0.5656*SIN(AR))
RD(I,K)=RD(I,K)+(0.7071*SIN(AR))
CB-ARTIF(A.GT.0.0)RD(I,K)=-RD(I,K)
IF(A.GT.0.0)RD(I,K)=-RD(I,K)
21 CONTINUE
20 CONTINUE

C
C SAMPLE PROJECTION DATA IF KART=0, ACCORDING TO DX
KART=0
IF(KART.EQ.1) GOTO 71
C BANDED ART
M4=0
DO 55 I=1,10 : Sample data from each projection angle
A=AG(I)
R=0.0
K55=0
C FOR CU BLOCK, CHANGE SIN(A) TO COS(A)
DX=0.25*ABS(SIN(AG(I))) : for data with(viewing angle)max ≤70° *o
C DX=0.15 :trial constant width spacing
C****DX=0.3535534*ABS(SIN(0.7853982-AG(I)))/2.0 : trial spacing with max. width
C****IF(A.GT.0.0) DX=0.3535534*ABS(SIN(0.7853982+AG(I)))/2.0 : at 45°
C****R=R-DX [0.25 x √2 = 0.3535534]
XYZ=RD(I,1)
62 IF(XYZ.GE.(R-DX)) GOTO 58
R=R-2*DX
GOTO 62

C
58 N=0
S55=0.0
C R55B=0.0
R55=R-DX
R55A=R+DX
KOZI=KOZ(I)

C
DO 56 K=1,KOZI
XYZ=RD(I,K) : distance of ray from given projection I
IF(XYZ.LE.R55A .AND. XYZ .GE. R55) N=N+1 : no. of projn data counter
IF(XYZ.LE.R55A .AND. XYZ .GE. R55) S55=S55+S(I,K)
C*****
C IF THE LINE OF CODES ABOVE IS UNCOMMENTED THE NEXT 8
C LINE BELOW MAY BE COMMENTED OUT
C IF(XYZ.LE.R55A .AND. XYZ .GE. R55.AND.N.EQ.1)S55=S(I,K)
C IF(XYZ.LE.R55A .AND. XYZ .GE. R55.AND.N.EQ.1) R55B=XYZ
C AR5=ABS(R55B-R)
C ASS=ABS(XYZ-R)
C IF(XYZ.LE.R55A .AND. XYZ .GE. R55.AND.N.GT.1.AND.ASS.LT.AR5)S55=
C 1S(I,K)
C IF(XYZ.LE.R55A .AND. XYZ .GE. R55.AND.N.GT.1.AND.ASS.LT.AR5)R55B
C 1=XYZ
C*****
IF(XYZ .GE. R55A) GOTO 57
IF(K .EQ. KOZI) GOTO 60
56 CONTINUE

C
60 IF(N .EQ. 0) GOTO 61
C
57 IF(N.EQ.0) S55=0.0

```

```

IF(N.EQ.0) N=100000000
S55=S55/FLOAT(N)
K55=K55+1
R5(K55)=R
C   R5(K55)=R55B
S5(K55)=S55
C   IF(K.EQ.KOZI) GOTO 61
R=R+(2.0*DX)
GOTO 58
C
61 KOZ(I)=K55 : routine to check that data are sampled at regular
KOZ=KOZ(I) intervals
DO 68 K=1,KOZI
RD(I,K)=R5(K)
IF(A.GT.0.0) RD(I,K)=-RD(I,K)
SE=S5(K)
C   RD4=R5(K)
IF(K.GT.1.AND.K.LT.KOZI .AND. SE.EQ.0.0) SE=(S5(K-1)+S5(K+1))/2.0
C   IF(K.GT.1.AND.K.LT.KOZI .AND. SE.EQ.0.0) RD4=(R5(K-1)+R5(K+1))/2.0
C   RD(I,K)=RD4
S(I,K)=SE
68 CONTINUE
M4=M4+KOZI
WRITE(2,65) KOZI
C   PRINT OUT NEW CALCULATED CO-ORDINATES
WRITE(2,500)((RD(I,K)/PMAG),S(I,K),K=1,KOZI) : NOTE USE OF PMAG
65 FORMAT(1H0,6HKOZI= ,I5)
C
C*****
C
55 CONTINUE
C
WRITE(2,70) M4
70 FORMAT(1H0,4HM4= ,I5)
C
71 CONTINUE
C   NOTE: MAGNIFICATION FACTOR PMAG NOT BEING APPLIED TO S(I,K) DATA YET,
RETURN [SEE PAGE 177]
END
C
C
C
C
C
SUBROUTINE MUL(KZ,KP,ZX1)
DIMENSION NODE(8,8),BASIC(8,8)
DIMENSION POLY(64,37)
DIMENSION KZ(144),KP(730),ZX1(730)
COMMON POLYCD(10412),ZX(300),POLYC(1,144),ISUB,KOZ(10),ICOUNT(300)
1,NR,IOP,M4,PMAG,NS,M5,NR55
EQUIVALENCE(POLY(1,1),POLYCD(1))
C
C   THE FOLLOWING DATA ARE FOR EVALUATING Z FOR A 2X4 FINITE ELEMENT
C   RECONSTRUCTION MODEL. MATRIX BASIC CONTAINS THE WEIGHTING
C   COEFFICIENTS FOR A SINGLE ELEMENT. NODES ARE NUMBERED ACCORDING
C   TO FIG. 3.1, WHERE CENTRE OF NODE = CENTRE OF PIXEL ON GRID
C   ELEMENT MODEL

```

```

C   SETTING UP 2ND L.H.S. MATRIX AS INEQN. (3.28) - FOR 2x4 ELEMENT MODEL
C   NOTE: VALUES OF NODE AND BASIC IN DATA STATEMENTS ARE TRANSPOSED
      DATA NODE/1,3,6,8,16,18,24,26,
12,9,7,12,17,20,25,28,
23,10,8,13,18,21,26,29,
34,5,14,15,22,23,30,31,
45,11,15,19,23,27,31,35,
56,8,16,18,24,26,32,34,
67,12,17,20,25,28,33,36,
78,13,18,21,26,29,34,37/
C   SQUARE ELEMENT USED:
      DATA BASIC/-.25,0.0,0.0,1.0,1.0,1.0,-2.0,-2.0, 0.5,-1.0,0.0,0.
10,0.0,-2.0,4.0,0.0,
2-0.25,0.0,0.0,-1.0,1.0,1.0,-2.0,2.0, 0.5,0.0,-1.0,0.0,-2.0,0.0,0.0
3,4.0, 0.5,0.0,1.0,0.0,-2.0,0.0,0.0,-4.0, -0.25,0.0,0.0,-1.0,1.0,1.
40,2.0,-2.0, 0.5,1.0,0.0,0.0,0.0,-2.0,-4.0,0.0, -0.25,0.0,0.0,1.0,1
5.0,1.0,2.0,2.0/
C   POLY= MATRIX Z AS IN SECTION 3.2.2
C   SET EACH COEFFICIENT OF MATRIX POLY TO ZERO
C   37 UNKNOWNNS, AND 8 ELEMENTS (EACH WITH 8 NODAL POINTS) -
      IROW=64
      ICOL=37
      DO 10 I=1,IROW
      DO 11 J=1,ICOL
      POLY(I,J)=0.0
11 CONTINUE
      KZ(I)=0
10 CONTINUE
C
C   EVALUATING OVERALL MATRIX POLY (128,65) USING NUMBERS FROM BASIC(8,8)
C   AND NODE (16,8)
C   FOR THIS MODEL MATRICES HAVE SIZES: POLY(64,37) AND NODE(8,8)
C
C
      K=0
      L=0
      I=1
20 K=K+1
      L=L+1
      DO 30 J=1,8
      POLY(K,NODE(I,J))=BASIC(L,J)
30 CONTINUE
      IF(L.EQ.8) I=I+1
      IF(L.EQ.8) L=0
      IF(K.LT.IROW) GO TO 20
C
C
      II=0
      DO 50 J=1,ICOL
      DO 40 I=1,IROW
      IF(POLY(I,J).EQ.0.00000) GOTO 40
      KZ(J)=KZ(J)+1
      II=II+1
      KP(II)=I
      ZX1(II)=POLY(I,J) : transposed here to facilitate manipulation
      POLY(I,J)=0.000000

```

```

40 CONTINUE
50 CONTINUE
  WRITE(2,306)II
306 FORMAT(1H ,3HII=,I6)
  RETURN
  END
C
C
C
C
C
  SUBROUTINE POLYCD(S,RD,AG,IO,KO)
  DIMENSION S(10,50),RD(10,50),AG(20)
  DIMENSION CB(8),GT(8),ST(8),ET(8)
C1  COMMON POLYC(120,128),ZX(128)
  COMMON POLYCD(10412),ZX(300),POLYC(1,144),ISUB,KOZ(10),ICOUNT(300)
  1,NR,IOP,M4,PMAG,NS,M5,NR55
  PI=4.0*ATAN(1.0)
  IF(NR.EQ.1) GOTO 150
C  FOR THE FINITE ELEMENT ONLY:
C  LENGTH OF ONE SIDE OF SQUARE ELEMENT=1.0
  LO=4
  MO=2
  NRETAN=0
  XM=4.0
  IF(NRETAN.EQ.1) XM=8.0
  YM=2.0
  GOTO 151
C  FOR GRID ELEMENT MODEL:
C  LENGTH OF ONE SIDE OF SQUARE PIXEL= 0.5
150 LO=9
  MO=5
  NRETAN=0
  XM=4.5
  IF(NRETAN.EQ.1) XM=9.0
  YM=2.5
151 T3=XM/(FLOAT(LO))
  T4=YM/(FLOAT(MO))
  T1=T4/T3
C
C  SETTING ALL COEFFICIENTS IN POLYC TO ZERO
C  POLYC IS A ROW OR A LINE OF THE WEIGHT PROJECTION MATRIX A OR A'
C
C1  DO 1 I=1,120
  I=1
  DO 101 J=1,144
  POLYC(I,J)=0.0
101 CONTINUE
C1 1 CONTINUE
C
C
C
  I1A=0
  ISUB=0
C  TAKE A PROJECTION AND CONSIDER EACH ONE OF THE RAYS
  DO 2 I=1,IO
C1  DO 3 K=1,KO

```

```

C
  KOZI=K0Z(I)
  DO 3 K=1,KOZI
C
  T2=TAN(AG(I))
  A=AG(I)
  R=RD(I,K)
C
  THE NEXT 14 LINES ARE OF NO USE NOW, BUT WERE USED FOR TESTING
C
  PURPOSES. :changes origin of data to fit on the reconstruction
C
  R=RD(I,K)-(6.0*SIN(A)) :for 4x4 Finite elements, Cu block data[plane
C
  HYPOTENUSE IS 4.085 FROM SQRT(X*X+Y*Y) WHERE X=(0.21*PHAG)*9=3.78 PLUS 0.5
C
  AND Y=(0.5-0.15)=0.35
C
  ANGLE IS INV(TAN(Y/X))=4.915 DEG OR 0.085784 RADS
C*** AR=A+0.083736           :for 13x7 Finite elements, Cu data
C
  AR=A+0.463647           :used for Walklate's
C
  R=RD(I,K)-(1.118034*SIN(AR)) :data set
C*** R=RD(I,K)-(4.185*SIN(AR)) :for 13x7 Finite elements, Cu data
C*NA AR=0.785398-A
C*** R=RD(I,K)-(0.49497*SIN(AR)) :for 6x3 Finite elements, R'=0.49497
C*NA R=RD(I,K)-(0.56568*SIN(AR)) [from  $\sqrt{(0.35^2 + 0.35^2)}$ , because 0.25cm = 0.15 WD.
C1 I1=K+(I-1)*KO        [see page 162.
C
  SHIFT ORIGIN
C
  45 DEG =0.7854 RADIANS, AND SQRT(0.5*0.5+0.5*0.5)=0.7071
  ARD=0.7854-A : shifts origin to one corner, from centre of a
  IF(NR.EQ.0 .AND.R.EQ.0.0000) R=0.00001 [Finite element
  IF(NR.EQ.0) R=R-(0.707109*SIN(ARD))
  I1A=I1A+1
C
  ZX(I1A) = LENGTH OF RAY INTERSECTING THE RECONSTRUCTION REGION.
C1 ZX(I1)=0.0
  ZX(I1A)=0.0
  ICOUNT(I1A)=0
  I1=1
C
C
  DX, R55, R55A, B55, & B55A ARE NOT USED BECAUSE NR55 WAS SET TO
C
  0 IN FERECON. THIS GIVES 0 OR 1 WEIGHTS IN A IF NR=1
  DX=0.25*ABS(SIN(A)) }
  R55=R+DX              } [not in use]
  R55A=R-DX
C
C
  EVALUATE COEFFICIENTS BY CONSIDERING INTERSECTION OF EACH OF THE
C
  PIXELS IN TURN - PROCEED UPWARDS (M) AND THEN ALONG (L), SEE FIG. 3.1.
  DO 4 L=1,LD
  DO 5 M=1,MD
  W=0.0
  I2=M+(L-1)*MD
C
  I7 IS USED ON THE FINITE ELEMENT ONLY
  I7=1+(I2-1)*8
C
C
  EVALUATING COEFFICIENTS ACCORDING TO EQN. 3.8A AND 3.8B FOR USE
C
  ON BOTH THE FINITE AND GRID ELEMENT.
  IF(ABS(A).EQ.(PI/2.0))R=10.0**5
  IF(ABS(A).EQ.(PI/2.0))GO TO 7
  B1=((R/COS(A))+T3*(L-1)*T2-T4*(M-1))
C*NA *****
C
  NEXT 5 LINES FOR 0 OR 1 WEIGHTS ONLY, PROVIDED N55=1
  B55=0.0
  B55A=0.0

```

```

IF(NR55.EQ.1)B55=(R55/COS(A))+T3*(L-1)*T2-T4*(M-1)
IF(NR55.EQ.1)B55A=(R55A/COS(A))+T3*(L-1)*T2-T4*(M-1)
IF(NR55.EQ.1 .AND. B55.GE.0.0.AND.B55A.LT.0.0) POLYC(1,I2)=1.0
} [not in use]
C THIS SECTION JUMPS OUT AFTER LABEL 49
C*NA *****
B=ABS(B1)
T6=(T4-T3*ABS(T2))/2.0
IF(B.LE.T6.AND.ABS(T2).LE.T1) GO TO 10
T6=(T3*ABS(T2)-T4)/2.0
IF(B.LE.T6.AND.ABS(T2).GT.T1) GOTO 20
T6=ABS(T4-T3*ABS(T2))/2.0
T7=(T3*ABS(T2)+T4)/2.0
IF(T6.LT.B.AND.B.LE.T7) GOTO 30
IF(B.GT.(T3*ABS(T2)+T4)/2.0) GOTO 49
GOTO 40
49 IF(NR.EQ.1.AND.NR55.EQ.0) POLYC(1,I2)=0.0
IF(NR.EQ.1) GOTO 40
C USE ON FINITE ELEMENT ONLY
I5=I7+7
DO 48 I3=I7,I5
POLYC(I1,I3)=0.0
48 CONTINUE
GOTO 40
7 IF(A.GT.0.0)C=R+(L-1)*T3
IF(A.LT.0.0)C=R-(L-1)*T3
IF(ABS(C).LE.T3/2.0.AND.ABS(A).EQ.PI/2.0) GOTO 41
GOTO 40
C
C ANGLE =90 DEGREES
41 W=T4
C CALCULATE LENGTH OF RAY AND ALSO PUT VALUE OF COEFFICIENT IN A',
C EQ. 3.8(A)
C1 ZX(I1)=ZX(I1)+W
ZX(I1A)=ZX(I1A)+W
IF(NR.EQ.1) POLYC(1,I2)=T4
IF(NR.EQ.1) GOTO 40
C
C USE N FINITE ELEMENTS ONLY: CONDITION 3
ET(1)=1.0
ET(2)=C
ET(3)=0.00
ET(4)=0.00
ET(5)=C*C
ET(6)=1.0/12.0
ET(7)=C
ET(8)=0.00
I4=0
I5=I7+7
DO 11 I3=I7,I5
I4=I4+1
POLYC(I1,I3)=ET(I4)
11 CONTINUE
GOTO 40
C FOR ANGLES FROM 0 TO LESS THAN 45 DEG:
10 H=SQRT(1.0+T2**2)
W=H*T3
C1 ZX(I1)=ZX(I1)+W

```

```

ZX(I1A)=ZX(I1A)+W
IF(NR.EQ.1.AND.NR55.EQ.0) POLYC(1,I2)=W
IF(NR.EQ.1) GOTO 40
IF(NRETAN.EQ.1) GOTO 16
C   USE ON FINITE ELEMENT ONLY: CONDITION 1
ST(1)=H
ST(2)=0.0
ST(3)=B1*H
ST(4)=(T2/12.0)*H
ST(5)=(H/12.0)
ST(6)=((B1*B1)+(T2*T2)/12.0)*H
ST(7)=B1*(T2/6.0)*H
ST(8)=(B1/12.0)*H
IF(NRETAN.EQ.0) GOTO 17
C   RECTANGULAR FINITE ELEMENT: CONDITION 1
16 ST(1)=H*2.0
ST(2)=0.0
ST(3)=B1*H*2.0
ST(4)=(T2/12.0)*H*8.0
ST(5)=(H/12.0)*8.0
ST(6)=((2.0*B1*B1)+(8.0*T2*T2)/12.0)*H
ST(7)=B1*(T2/6.0)*H*8.0
ST(8)=(B1/12.0)*H*8.0
17 I4=0
I5=I7+7
DO 12 I3=I7,I5
I4=I4+1
POLYC(I1,I3)=ST(I4)
12 CONTINUE
GOTO 40
C   FOR ANGLES FROM 45 TO LESS THAN 90 DEG:
20 H=SQRT(1.0+(1.0/(T2*T2)))
W=SQRT(1.0+T2**2)*T4/(ABS(T2))
C1  ZX(I1)=ZX(I1)+W
ZX(I1A)=ZX(I1A)+W
IF(NR.EQ.1.AND.NR55.EQ.0) POLYC(1,I2)=W
IF(NR.EQ.1) GOTO 40
C   USE ON FINITE ELEMENT ONLY: CONDITION 2
GT(1)=H
GT(2)=-B1/T2)*H
GT(3)=0.25*H
GT(4)=(1.0/(12.0*T2))*H
GT(5)=((1.0/12.0+(B1*B1))/(T2*T2))*H
GT(6)=H/12.0
GT(7)=(-B1/(12.0*T2))*H
GT(8)=(B1/(6.0*T2*T2))*H
I4=0
C
I5=I7+7
DO 14 I3=I7,I5
I4=I4+1
POLYC(I1,I3)=GT(I4)
14 CONTINUE
GOTO 40
C   FOR RAYS PASSING THROUGH ADJACENT SIDES:
30 SS=(SQRT(1.0+T2**2)/ABS(T2))*((T3*ABS(T2)+T4)/2.0-B)
C

```

```

      W=SS
C1  ZX(I1)=ZX(I1)+W
      ZX(I1A)=ZX(I1A)+W
C
      IF(NR55.EQ.1) GOTO 55
      W1=1.0
      IF(NR.EQ.1.AND.ABS(T2).LE.T1) W1=T3*SQRT(1.0+T2**2)
      IF(NR.EQ.1.AND.ABS(T2).GT.T1) W1=SQRT(1.0+T2**2)*T4/ABS(T2)
C   COEFFICIENTS SMALLER THAN SOME FRACTION OF THE MAXIMUM POSSIBLE
C   LENGTH THAT CAN INTERSECT THE PIXEL FROM THE GIVEN PROJECTION ANGLE
C   CAN BE IGNORED, E.G. SAY LESS THAN 0.83, IF NS=0 IN FERECON.
      IF(NR.EQ.1.AND.(W/W1).GE.0.83) POLYC(1,I2)=W
C   PUT THE EXACT VALUE OF COEFFICIENT IN WEIGHT PROJECTION MATRIX TO
C   BE USED FOR CALCULATING THE RECONSTRUCTED PICTURE PATHLENGTH
C   DIFFERENCE
      IF(NR.EQ.1.AND.NS.EQ.1) POLYC(1,I2)=W
C   FOR USE ON FINITE ELEMENT ONLY:
55  IF(NR.EQ.1) GOTO 40
      IF(B1.GT.0.0.AND.A.LT.0.0) GOTO 33
      IF(B1.GT.0.0.AND.A.GT.0.0) GOTO 32
      IF(B1.LT.0.0.AND.A.LT.0.0) GOTO 32
      IF(B1.LT.0.0.AND.A.GT.0.0) GOTO 33
32  RMAX=-0.5+SS*COS(A)
      RMIN=-0.5
      GOTO 34
33  RMAX=0.5
      RMIN=0.5-SS*COS(A)
C   NOT POSSIBLE FOR B1 TO EQUAL ZERO TO ENTER FERECON
      IF(B1.EQ.0.0) WRITE(2,31)
31  FORMAT(21H ERROR DETECTED IN B1)
34  R2=RMAX
      R1=RMIN
      H=SQRT(1.0+(T2*T2))
      CB(1)=R2-R1
      CB(2)=(R2*R2)/2.0-(R1*R1)/2.0
      CB(3)=(B1*R2+((R2*R2)*T2/2.0)-(B1*R1+((R1*R1)*T2/2.0)))
      CB(4)=((B1*R2*R2)/2.0+(R2**3)*T2/3.0)-((B1*R1*R1)/2.0+(R1**3)*T2/3
1.0)
      CB(5)=(R2**3)/3.0-(R1**3)/3.0
      CB(6)=((B1*B1*R2)+(R2**3)*T2*T2/3.0+B1*R2*R2*T2)-(B1*B1*R1+(R1**3)
1*T2*T2/3.0+B1*R1*R1*T2)
      CB(7)=(B1*B1*R2*R2/2.0+(R2**4)*T2*T2/4.0+B1*(R2**3)*T2*2.0/3.0)-(B
11*B1*R1*R1/2.0+(R1**4)*T2*T2/4.0+B1*(R1**3)*T2*2.0/3.0)
      CB(8)=((B1*R2**3)/3.0+(R2**4)*T2/4.0)-(B1*(R1**3)/3.0+(R1**4)*T2/4
1.0)
      I4=0
      I5=I7+7
      DO 15 I3=I7,I5
      I4=I4+1
      POLYC(I1,I3)=CB(I4)*H
15  CONTINUE
40  CONTINUE
5   CONTINUE
4   CONTINUE
C
C   8 ELEMENTS, 8 NODES. THEREFORE IV=64
      IV=64

```

```

C   FOR GRID ELEMENT THERE ARE 45 PIXELS 9X5
C   IF(NR.EQ.1) IV=M5
C   DO 999 J=1,IV
C   CALCULATE NUMERICAL LOCATION FOR PIXEL NUMBER
C   VSUB=(FLOAT(J)+1000.0)*100.0
C   WSUB=VSUB+10.00000
C   NUMBER OF ELEMENTS BEING FILLED IN POLYCD MATRIX
C   IF (ABS(POLYC(1,J)).GT.0.00000) ISUB=ISUB+1
C   NUMBER OF NON-ZERO VALUES OF COEFFICIENTS FROM A RAY OF A PROJECTION
C   IF (ABS(POLYC(1,J)).GT.0.00000) ICOUNT(I1A)=ICOUNT(I1A)+1
C   STORE THE PROJECTION WEIGHT COEFFICIENT IN POLYCD, TOGETHER WITH
C   THE PIXEL NUMBER
C   IF (ABS(POLYC(1,J)).GT.0.00000) POLYCD(ISUB)=POLYC(1,J)+WSUB
C   RESET LINE PROJECTION MATRIX
C   POLYC(1,J)=0.000000
999 CONTINUE
C
C   3 CONTINUE
C   2 CONTINUE
C   RETURN
C   END
C
C
C
C
C   SUBROUTINE KAISYM(ACTLS,DIFF,X,POLY,IZ,NODE2,ARTS)
C
C   THIS ROUTINE IS CALLED FROM SUBROUTINE ITERAT (READ FIRST)
C
C   A ROUTINE TO PRODUCE A FACTOR, OR AN INITIAL STARTING VALUE, FOR
C   EACH OF THE PIXELS BASED ON THE MINIMUM, OR CONSERVATIVE, AVERAGE
C   VALUE OF REFRACTIVE INDEX CHANGE A PIXEL COULD HAVE WHICH COULD
C   PRODUCE A PICTURE WITHOUT OVER-ESTIMATING ANY OF THE PROJECTION
C   DATA, IF NO CONSTRAINT IS APPLIED.
C   DIMENSION POLY(8420),IZ(300),NODE2(45)
C   DIMENSION XVALUE(91),ACTLS(300),DIFF(300), X(91),ZM(300),ARTS(300)
C   COMMON POLYCD(10412),ZX(300),POLYC(1,144),ISUB,KOZ(10),ICOUNT(300)
C   1,NR,IOP,M4,PHAG,NS,M5,NR55
C   M4=246 [not in use]
C*** M4=287 [not in use]
C   INITIALISE VALUES OF PIXELS
C   DO 15 I=1,M5
C   X(I)=0.00000
C   XVALUE(I)=0.0
15 CONTINUE
C   I2=1
C   CHANGE "I2.EQ.6" TO "I2.EQ.1" IF THIS ROUTINE IS NOT REQUIRED IN TEST
C   IF(I2.EQ.6) GOTO 6
C   IF PROJECTION DATA IS GOOD, ICE MAY GO UP TO 3, FOR THE ART ALGORITHM
C   DO 2 ICE=1,1
C   RESET AUXILLARY PIXEL ARRAY TO RECORD FURTHER CHANGES IF ANY
C   DO 16 I=1,91
C   XVALUE(I)=0.0
16 CONTINUE
C   FOR EACH RAY CALCULATE THE AVERAGE CHANGE IN REFRACTIVE INDEX
C   DO 5 I=1,M4

```

```

IF(ZX(I).EQ.0.0) ZH(I)=0.0
IF(ZX(I).EQ.0.0) GOTO 5
ZH(I)=DIFF(I)/(ZX(I)*1.0)
IF(ICE.GT.I2) ZH(I)=ZH(I)/1.0
5 CONTINUE
C USED FOR SIRT, UNLIKELY TO BE OF FURTHER USE.
IF(ICE.GT.I2) GOTO 100
C FOR EACH PIXEL UP TO M5 INITIALISE IT WITH ANY AVERAGE VALUES OF
C REFRACTIVE INDEX CHANGE.
DO 10 J=1,M5
DO 12 I=1,ISUR
IX=(POLYCD(I)/100.0)-1000
IF(IX.EQ.J) GOTO 11
12 CONTINUE
C THIS ALSO TAKES CARE OF AN X WITH NO COEFFICIENT
GOTO 10
11 JP=0
DO 14 IJ=1,M4
JP=JP+ICOUNT(IJ)
JS=JP+1-ICOUNT(IJ)
IF(ICOUNT(IJ).EQ.1) JS=JP
IF(ICOUNT(IJ).EQ.0) GOTO 14
IF(I.GE.JS.AND.I.LE.JP) GOTO 13
14 CONTINUE
GOTO 10
13 XVALUE(J)=ZH(IJ)
10 CONTINUE
100 CONTINUE
DO 20 IX=1,M5
N=0
AVGE=0.0 } [not in use]
JP=0
DO 21 K=1,M4
JP=JP+ICOUNT(K)
JS=JP-(ICOUNT(K)-1)
IF(ICOUNT(K).EQ.1) JS=JP
IF(ICOUNT(K).EQ.0) GOTO 21
DO 22 L=JS,JP
I=(POLYCD(L)/100.0)-1000
IF(ICE.GT.I2) GOTO 101
IF(I.EQ.IX.AND.XVALUE(I).GT.ZH(K)) XVALUE(I)=ZH(K)
101 IF(ICE.LE.I2) GOTO 102
IF(I.EQ.IX) N=N+1
IF(I.EQ.IX) AVGE=AVGE+ZH(K) } [not in use]
C METHOD TO FIND AVERAGE VALUE OF EACH PIXEL - FOUND TO BE OF NO
C FURTHER USE.
102 CONTINUE
22 CONTINUE
21 CONTINUE
IF(ICE.GT.I2) XVALUE(IX)=AVGE/N
20 CONTINUE
DO 30 I=1,M5
X(I)=X(I)+XVALUE(I)
C LSO XVALUE(NODE2(I))=X(I)
XVALUE(I)=X(I)
30 CONTINUE
PJ=-300.0 : find the largest value of pixel X(I) as PJ

```

```

DO 53 J=1,M5
IF(X(J).GT,PJ) MAX=J
IF(X(J).GT,PJ) PJ=X(J)
53 CONTINUE
C PRODUCE THE C'J FACTORS:
DO 54 J=1,M5
XRX=X(J)
X(J)=(XRX/PJ)*1.25
IF(ICE,LT,I2) GOTO 54
IF(X(J),LT,0.15) X(J)=0.15 :minimum factor set as 0.15
54 CONTINUE
WRITE(2,819) (X(J),J=1,M5)
WRITE(2,829) MAX,PJ : pixel X(MAX) contains the largest value as PJ
829 FORMAT(1H0,I5,F10.6)
C*****
C C'J FACTORS CAN BE PRODUCE WITHOUT CONSTRAINTS: : jumps to label 68
IF(ICE,EQ,I2) GOTO 68
DO 55 J=1,M5
XRX=X(J)
X(J)=(XRX*PJ)/1.25
55 CONTINUE
C*****
LSQ=1
C C'J FACTORS DO NOT NEED THE FOLLOWING CODES TO PRODUCE A
C PICTURE OF THE TEMPORARY RECONSTRUCTED FIELD.
IF(LSQ,EQ,1) GOTO 66
DO 36 J=1,M5
C ZH(J)=((0.000292015/(0.0002719868+(-XVALUE(J)*0.0000249134)))-1.0)
C 1/0.00368184
C X(J)=ZH(J)
C FOR CU BLOCK THE 3 LINES ABOVE AND COMMENT OUT THE 3 LINES BELOW.
ZH(J)=-5.6974691+2.9429076*SQRT(3.748096-(67960.0*(-0.000939
16428+(-X(J)*0.00006328))))
ZH(J)=ZH(J)-18.5
C AT 18.5 DEG C, N-1.3331733=-0.0009396428
C AT 20 DEG C, N-1.3331733=-0.0010668
C AT 50 DEG C, N-1.3331733=-0.0052155
36 CONTINUE
WRITE(2,819)(ZH(J),J=1,M5)
819 FORMAT(1H0,5(4X,F8.3))
66 JS=0
C CODES UP TO LABEL 227 WORK OUT RESIDUALS:
DO 227 I=1,M4
JS=JS+IZ(I)
JP=JS-IZ(I)+1
IF(IZ(I),EQ,1) JP=JS
IF(IZ(I),EQ,0) GOTO 227
DO 229 J=JP,JS
IX=(POLY(J)/100.0)-1000
CO=POLY(J)-FLOAT((1000+IX)*100)-10.00000
IF(J,EQ,JP) ARTS(I)=0.0
ARTS(I)=ARTS(I)+XVALUE(IX)*CO
229 CONTINUE
DIFF(I)=ACTLS(I)-ARTS(I)
227 CONTINUE
C IF FURTHER REDUCTION OF RESIDUALS IS NEEDED BASED ON THE SAME
C PROCEDURE, THIS ROUTINE CAN BE RE-ITERATED IN WHICH A MODIFIED

```

```

C   PICTURE CAN STILL BE PRODUCED WITHOUT OVER-ESTIMATING ANY OF
C   THE RESIDUALS.
C
  2 CONTINUE
    GOTO 2
  68 DO 67 I=1,MA
      DIFF(I)=ACTLS(I)
  67 CONTINUE
  6 CONTINUE
    RETURN
    END

C
C
C
C
C   SUBROUTINE ITERAT(S,RD,AG,KZ,KP,ZX1)
C
C   THIS ROUTINE CONTAINS THE ART AND LSRT ITERATIVE INVERSION
C   ALGORITHMS FOR SOLVING THE RECONSTRUCTION EQUATIONS SET UP
C   BASED ON EITHER THE GRID ELEMENT OR FINITE ELEMENT MODEL.
C
C   IT ALSO CONTAINS SOME ROUTINES TO OBTAIN THE FINAL WEIGHT
C   PROJECTION MATRIX OR MATRICES.
C
C   DIMENSION S(10,50),RD(10,50),AG(20)
C   DIMENSION Z(300),ZH(300),DIFF(300),ARTS(300),XVALUE(120)
C   1,ACTLS(300),POLY(8420)
C
C   DIMENSION NODE(8,8),NODE2(45) ,T(8),X(91)
C   DIMENSION KZ(144),KP(730),ZX1(730)
C   DIMENSION XX(91)
C   DIMENSION CONVEG(100)
C   DIMENSION CH(91),TA(91),MA(91),SA(200)
C*****
C   DIMENSION XX5(91),XVALU5(120),DIFF5(300),XT(91)
C*****
C
C   COMMON POLYCD(10412),ZX(300),POLYC(1,144),ISUB,KOZ(10),ICOUNT(300)
C   1,NR,IOP,MA,PMAG,NS,M5,NR55
C
C   DIMENSION IZ(300)
C
C   EQUIVALENCE (DIFF5(1),Z(1))
C   DATA NODE/1,3,6,8,16,18,24,26, : 2x4 Finite element model
C   12,9,7,12,17,20,25,28,      [node numbers
C   23,10,8,13,18,21,26,29,
C   34,5,14,15,22,23,30,31,
C   45,11,15,19,23,27,31,35,
C   56,8,16,18,24,26,32,34,
C   67,12,17,20,25,28,33,36,
C   78,13,18,21,26,29,34,37/
C   NODE SEQUENCE ARRAY, NODE2, NUMBERED ACCORDING TO FIG. 3.1.
C   DATA NODE2/1,2,3,9,10,4,100,5,100,11,6,7,8,12,13,14,100,
C   115,100,19,
C   216,17,18,20,21,22,100,      23,100,27,
C   324,25,26,28,29, 30,100,31,100,35,

```

```

432,33,34,36,37/
C
C
  IO=IOP
C*** PHAG=2.0000
C*** PHAG=0.6
C   M4=246
C*** M4=287
C   INITIALISE PIXELS IN ARRAY X, AND SELECTED ELEMENTAL CHANGE
C   CRITERIA SA
  DO 494 I=1,200
  -SA(I)=0.0
  IF(I.LE.91) X(I)=0.0
494 CONTINUE
  DO 32 I=1,M4
C   M4 = TOTAL NUMBER OF RAYS FROM PROJECTION DATA, VECTOR Z = LENGTH
C   OF EACH RAY INTERSECTING THE TEST SECTION.
  Z(I)=ZX(I)
  IZ(I)=0
32 CONTINUE
C
  TT=0.0
  J=0
  JZ=0
  IF(NR.EQ.1) GOTO 493
C   INSTRUCTIONS UP TO LABEL 918 ARE FOR FINITE ELEMENT ONLY - TO
C   EVALUATE THE FINAL PROJECTION MATRIX (AS AT END OF SECTION 3.2.2
C   ) BY CALCULATING THE COEFFICIENT PRODUCTS OF POLYCD FROM
C   SUBROUTINE POLYCD AND POLY FROM SUBROUTINE POLY. : 2x4 elements model
  DO 40 IK=1,M4
  IF(ICOUNT(IK).EQ.0) GOTO 51
  J=J+ICOUNT(IK)
  KMIN=J-(ICOUNT(IK)-1)
  IF(ICOUNT(IK).EQ.1) KMIN=J
  JK=0
  DO 30 K=1,37
  JK=JK+KZ(K)
  JL=JK-KZ(K)+1
  IF(KZ(K).EQ.1) JL=JK
  DO 50 L=KMIN,J : no. of columns from [A'] with non-zero coefficients
  IX=POLYCD(L)/100.0 [from a ray]
  IX=IX-1000 : column number from [A']
  DO 919 JO=JL,JK : number of rows with non-zero coefficients from
  IF(KP(JO).EQ.IX) GOTO 929 [2nd l.h.s. matrix in eqn.(3.28)]
  IF(KP(JO).GT.IX) GOTO 50 : column number from the 2nd l.h.s. matrix
919 CONTINUE
  GOTO 50
929 CO=POLYCD(L)-FLOAT((1000+IX)*100)
  CO=CO-10.00000
C   ARRAY ZX1 CONTAINS THE VALUES OF MATRIX Z AS IN SECTION 3.2.2
  TT=ZX1(JO)*CO+TT
50 CONTINUE
C
  IF(TT.NE.0.000000) GOTO 65
  GOTO 55
65 IZ(IK)=IZ(IK)+1
  JZ=JZ+1

```

```

C POLY IS THE FINAL WEIGHT PROJECTION MATRIX FOR THE FINITE ELEMENT
C RECONSTRUCTION MODEL.
POLY(JZ)=(TT+10.00000)+(K*100)+100000
55 CONTINUE
TT=0.0
30 CONTINUE
51 CONTINUE
TT=0.0
40 CONTINUE
-- WRITE(2,939)(IZ(I),I=1,M4) : number of non-zero elements in each ray, I
939 FORMAT(1H ,22(1X,I5))
C
493 JR=0
IF(JR.EQ.0) GOTO 918
C PRINT COEFFICIENTS OF POLY FOR CHECKING IF REQUIRED
DO 305 I=1,M4
JR=JR+IZ(I)
JP=JR-(IZ(I)-1)
IF(IZ(I).EQ.1) JP=JR
IF(IZ(I).EQ.0) GOTO 306
WRITE(2,302)(POLY(J),J=JP,JR)
306 WRITE(2,307)
305 CONTINUE
918 CONTINUE
307 FORMAT(1H )
302 FORMAT(1H ,10(1X,F12.3))
WRITE(2,41)(Z(I),I=1,M4)
41 FORMAT(1H ,9(4X,F7.5))
C
C IF NS=1, EXACT PATHLENGTH COEFFICIENTS ARE NEEDED TO CALCULATE
C THE RESIDUALS FROM THE RECONSTRUCTING PICTURE FOR THE GRID MODEL
C FOR WHICH NR=1
IF(NR.EQ.0) GOTO 75
IF(NS.EQ.0) GOTO 75
DO 76 I=1,M4
IZ(I)=ICOUNT(I)
76 CONTINUE
DO 77 I=1,ISUR
POLY(I)=POLYCD(I) : pathlength coefficient store
77 CONTINUE
75 CONTINUE
C
C FOR TEST PURPOSES ONLY, FRINGE NUMBERS CAN BE INPUT HERE PROVIDED
C RAYS WERE NOT SAMPLED IN SUBROUTINE INFO
C READ(1,27)(ACTLS(I),I=1,M4)
27 FORMAT(9F10.8)
C PHAG=1.939 : for 4x4 square Finite elements, Cu block data
C PHAG=2.2222 : for 4x4 rectangular Finite elements, Cu block data
C PHAG=2.0000 : for 13x7 Grid elements, Cu block data
C IO=9
C KO IS REDUNDANT
KO=18
N=0
SFR=0.0
SPA=0.0
DO 25 I=1,IO
KOZI=KOZ(I)

```

```

DO 26 K=1,KOZI
C   THOUGH THE SIGN OF (N(X,Y)-N(REF)) IS ACTUALLY NEGATIVE, BECAUSE
C   THE VALUE OF REFRACTIVE INDEX DECREASES WITH INCREASE IN TEMPERATURE
C   , POSITIVE VALUES OF PROJECTION DATA ARE USED FIRST TO RECONSTRUCT
C   A 2-D FIELD SHOWING THE VARIATION OF REFRACTIVE INDEX.  CONVERSION
C   TO VALUES OF TEMPERATURE OR REFRACTIVE INDEX CAN BE CARRIED OUT AFTER
C   EACH ITERATION IF NEEDED, OR WHEN THE FINAL RECONSTRUCTED FIELD IS
C   OBTAINED.
C
N=N+1
C
C   N.B.  PRINT MAGNIFICATION FACTORS ZMAG(I) NOT USED HERE - THEY ARE
C   INDEPENDENT OF THE FRINGE NUMBER.
DIFF(N)=-S(I,K)*PMAG
ACTLS(N)=-S(I,K)*PMAG
C
C   DIFF(N)=-ACTLS(N)*PMAG
C   ACTLS(N)=-ACTLS(N)*PMAG
SFR=SFR+ACTLS(N)
SPA=SPA+Z(N)
26 CONTINUE
25 CONTINUE
C   DEFINE AVERAGE VALUE OF REFRACTIVE INDEX CHANGE AS SME
SME=SFR/SPA
C   NORMALISED INITIALISATION OF AUXILLARY PIXELS IN XVALUE!
DO 633 I=1,100
XVALUE(I)=SME
633 CONTINUE
C
C   USE UNWEIGHTED COEFFICIENTS FOR EVALUATING RESIDUALS
C   FOR TEST PURPOSES - OF NO FURTHER USE NOW.
IF(NS.EQ.1) GOTO 928
DO 924 I=1,M4
IZ(I)=ICOUNT(I)
924 CONTINUE
DO 925 I=1,ISUB
POLY(I)=POLYCD(I)
925 CONTINUE
C
928 NR=1
IF(NS.EQ.0) GOTO 74
C   CALCULATE AN UNWEIGHTED PROJECTION MATRIX FOR ART IF NEEDED (FOUND
C   TO BE UNNECESSARY)
NS=0
NR55=1
C-LSQ CALL POLYCD(S,RD,AG,IO,KO) : [required for ART algorithm]
74 CALL KAISYM(ACTLS,DIFF,XX,POLY,IZ,NODE2,ARTS)
C   INITIALISE I'J FACTORS IN VECTOR XT
DO 635 I=1,M5
C-LSQ XVALUE(NODE2(I))=XX(I)
XT(I)=XX(I)
XX(I)=0.0
C   XVALUE(I)=XX(I)
635 CONTINUE
C   WRITE THE VALUE OF PATHLENGTH FOR EACH RAY, & NUMBER OF NON-ZERO
C   COEFFICIENTS IN EACH RAY
WRITE(2,41) (ZX(I),I=1,M4)

```

```

WRITE(2,939)(ICOUNT(I),I=1,M4)
K=0
SIGN=1.0
231 K=K+1
C IF(K.GT.1) GOTO 1000
C IF KCD=1 USE LSRT
KCD=1 : i.e. use LSRT algorithm
IF(KCD.EQ.1) GOTO 1000
C VARIABLE RELAXATION PARAMETERS FOR ART BASED ON TRIAL TESTS
IF(K.EQ.1) XRT=2.0
IF(K.EQ.2) XRT=10.0
IF(K.GE.3) XRT=15.0
IF(K.GE.7) XRT=30.0
C*****
LAZ=0
GOW1=0.0
N=0
C FOR USE ON FINITE ELEMENT ONLY
I5=0
I8=0
IF(K.LE.2) GOTO 110
111 LAZ=1
I5=I5+1
XRT=15.0
IF(NODE2(I5).EQ.100) GOTO 112
N=1
IF(N.EQ.1) GOTO 110
C
113 XXX=XX(I5)-(XX(I5)/10.0)
C*****
N=N+1
DO 122 I6=1,M4
DIFF5(I6)=DIFF(I6)
IF(I6.LE.M5) XX5(I6)=XX(I6)
IF(I6.LE.M5) XVALU5(NODE2(I6))=XX(I6)
IF(I6.EQ.I5) XX5(I6)=XXX
IF(I6.EQ.I5) XVALU5(NODE2(I6))=XXX
122 CONTINUE
GOTO 121
C*****
110 CONTINUE
GOTO 116
C
114 LAZ=0
XRT=3.0
GOW1=0.0
I8=1
DO 115 I6=1,M5
XX(I6)=XT(I6)
115 CONTINUE
C
116 DO 117 I6=1,M4
DIFF5(I6)=DIFF(I6)
IF(I6.LE.M5) XX5(I6)=XX(I6)
IF(I6.LE.M5) XVALU5(NODE2(I6))=XX(I6)
117 CONTINUE
C

```

```

121 IF(N.EQ.1 .AND. I5.GT.1) GOTO 118
C*****
C
C   ART TYPE ALGORITHM:
   JS=0
   JSG=0
   DO 227 II=1,M4
   IF (II,EQ.1) I=1
C
   JS=JS+IZ(II)
   JP=JS-IZ(II)+1
   IF(IZ(II),EQ.1) JP=JS
   JSG=JSG+ICOUNT(II)
   JPG=JSG-ICOUNT(II)+1
   IF(ICOUNT(II),EQ.1)JPG=JSG
C
C
   IF(ABS(ZX(I)),LE.0.01)ZH(I)=0.0
   IF(ABS(ZX(I)),LE.0.01)GOTO 78
C
   ZH(I)=DIFF5(I)/(ZX(I)*XRT)
   DO 28 J=JPG,JSG
C   CHANGING THE VALUE OF A PIXEL USING EITHER WEIGHTED OR UNWEIGHTED
C   COEFFICIENTS FROM MATRIX POLYCD
   IX=(POLYCD(J)/100.0)-1000
   XX5(IX)=XX5(IX)+ZH(I)
   IF(XX5(IX),LT.0.0) XX5(IX)=0.0
   XVALUS(NODE2(IX))=XX5(IX)
28 CONTINUE
78 IF(II,LT,M4)I=II+1
   JS1=JS+IZ(I)
   JP1=JS1-IZ(I)+1
   IF(IZ(I),EQ.1) JP1=JS1
   IF(II,EQ,M4) I=1
   IF(II,EQ,M4) JS1=IZ(I)
   IF(II,EQ,M4) JP1=1
   IF(IZ(I),EQ.0) GOTO 227
   DO 229 J=JP1,JS1
   IX=(POLY(J)/100.0)-1000
   CO=POLY(J)-FLOAT((1000+IX)*100)-10.00000
   IF(J,EQ,JP1)ARTS(I)=0.0
C   CALCULATE RESIDUALS USING MATRIX POLY CONTAINING ACCURATELY
C   WEIGHTED COEFFICIENTS.
   ARTS(I)=ARTS(I)+(XVALUS(IX)*CO)
229 CONTINUE
   DIFF5(I)=ACTLS(I)-ARTS(I)
227 CONTINUE
C   A CRITERIA USED BY AUTHOR FOR TEST PURPOSES (UP TO LABEL 39)
   GOV=0.0
   GOW=0.0
   DO 79 J=1,M4
   GOV=GOV+DIFF5(J)
   GOW=GOW+(DIFF5(J)*DIFF5(J))
79 CONTINUE
   IF(N,EQ.1) GOW1=GOW
118 IF(N,EQ.1) GOTO 113
   IF(GOW,LT,GOW1) GOTO 119

```

```

      GOTO 112
119 CONTINUE
      DO 120 I6=1,M4
C      DIFF(I6)=DIFF5(I6)
C      IF(I6.LE.M5)XVALUE(I6)=XVALU5(I6)
C      IF(I6.LE.M5) XX(I6)=XX5(I6)
120 CONTINUE
      XT(I5)=XXX
C
112 CONTINUE
C
      IF(I5.LT.M5 .AND.LAZ.EQ.1) GOTO 111
      IF(I8.EQ.1) GOTO 125
      IF(I5.EQ.M5) GOTO 114
125 DO 39 I=1,M4
      DIFF(I)=DIFF5(I)
      IF(I.LE.M5) XX(I)=XX5(I)+(4.0*SME)
      IF(I.LE.M5) XT(I)=XX(I)
      IF(I.LE.M5) XVALUE(NODE2(I))=XX(I)
39 CONTINUE
} [not in use]
C*****
C
C
1000 KD=1
      IF(KD.EQ.0) GOTO 108
      IF(K.GT.1) GOTO 109
      KCDL=0
C      IF KCDL=0 USE LSRT
      IF(KCDL.EQ.0) GOTO 1003
      JS=0
      DO 1001 I=1,M4
      JS=JS+IZ(I)
      JP=JS-(IZ(I)-1)
      IF(IZ(I).EQ.1) JP=JS
      IF(IZ(I).EQ.0) GOTO 1001
C*****
      DO 1002 J=JS,JP
      IX=(POLY(J)/100.0)-1000
      CO=POLY(J)-FLOAT((1000+IX)*100)-10.0000
      IF(J.EQ.JS) ARTS(I)=0.0
      ARTS(I)=ARTS(I)+(XVALUE(IX)*CO)
1002 CONTINUE
      DIFF(I)=ACTLS(I)-ARTS(I)
1001 CONTINUE
C*****
C      START LSRT:
1003 CONTINUE
C
C
      GOW=0.0
C
      DO 80 J=1,M4
      GOW=GOW+(DIFF(J)*DIFF(J))
80 CONTINUE
C
      GOW1=GOW
109 CONTINUE

```

```

*****
C  VARIABLE RELAXATION PARAMETERS FOR LSRT FOUND BY A PROCESS OF
C  TRIAL TESTS
    XRT5=3.0
    IF(K.GT.30) XRT5=9.0
    IF(K.GT.50) XRT5=25.0
    IF(K.GT.80) XRT5=40.0
    IF(K.GT.110) XRT5=60.0
    IF(K.GT.140) XRT5=80.0
C  PRODUCTION OF A CONSTANT VALUE SME/XRT5 AS D'K OF SECTION 3.3.3 TO
C  DETERMINE WHETHER OR NOT A PIXEL NEEDS ITS VALUE CHANGING
    XXXX=(SME/XRT5)*SIGN
C
C  CONSIDERING ONE PIXEL AT A TIME UP TO PIXEL M5:
    DO 20 I=1,M5
      INOD=I
C      INOD=NODE2(I)
      IF(INOD.EQ.100) GOTO 20
C      IF VALUE OF PIXEL IS ZERO, & SIGN IS -VE MOVE ON TO THE NEXT PIXEL
      IF(XX(I).LE.0.0.AND.SIGN.LT.0.0) GOTO 20
C
      XXXX=XXXX*XT(I) : XT(I) are weight factors
C      THE QUANTITY TO ADD TO PIXEL (I) IF REQUIRED IS XXXX
      DO 21 J=1,M4 : ray numbers
C      PERMANENT RESIDUAL REGISTER ID DIFF5
      DIFF5(J)=DIFF(J)
21 CONTINUE
C
      JS=0
C      TAKING EACH RAY IN TURN UP TO RAY M4:
      DO 105 J=1,M4
        JS=JS+IZ(J)
        JP=JS-(IZ(J)-1)
        IF(IZ(J).EQ.1) JP=JS
        IF(IZ(J).EQ.0) GOTO 105
C
        DO 107 JX=JP,JS
C      IF RAY INTERSECTS PIXEL INOD WHICH IS UNDER CONSIDERATION THEN GO
C      TO 101 AND ADD THE QUANTITY TO INOD
        LX=(POLY(JX)/100.0)-1000
        IF(LX.GT.INOD) GOTO 105
        IF(LX.EQ.INOD) GOTO 101
        GOTO 107
101 CD=POLY(JX)-FLOAT((1000+LX)*100)-10.0000
        CHANGE= CD*XXXX
        DIFF5(J)=DIFF5(J)-CHANGE
107 CONTINUE
C
105 CONTINUE
*****
C
C  EVALUATING NEW VALUES FOR CRITERIONS:
    GOV=0.0
    GOW=0.0
    DO 89 J=1,M4
      GOV=GOV+DIFF5(J)
      GOW=GOW+(DIFF5(J)*DIFF5(J))

```

```

89 CONTINUE
C   IF SUM OF SQUARE OF EACH RESIDUAL IS SMALLER, THEN CHANGE THAT VALUE
C   OF N ON PIXEL
      IF(GOW.LT.GOW1) GOTO 102
      GOTO 22
102 DO 104 J=1,M4
      DIFF(J)=DIFF5(J)
104 CONTINUE
C
      GOW1=GOW
      XX(I)=XX(I)+XXXX
      22 XXXX=XXXX/XT(I)
      20 CONTINUE
108 SIGN=SIGN*(-1.0)
C*****
C
C           - end of LSRT algorithm -
C
      EN=0.0
      ET=0.0
      THAX=-100.0
      THIN=100.0
      TMEAN=0.0
C
      JS=0
C   CONVERTING VALUE OF REFRACTIVE INDEX CHANGE TO TEMPERATURE
      DO 36 J=1,M5
C   ZH(J)=(((0.000292015/(0.0002719868+(-XVALUE(J)*0.0000249134)))-1.0)
*
C   1/0.00368184
*
C   X(J)=ZH(J)
*
C   FOR CU BLOCK, UNCOMMENT THE 3 LINES ABOVE AND COMMENT OUT THE
C   3 LINES BELOW
      ZH(J)=-5.6974691+2.9429076*SQRT(3.748096-(67960.0*(-0.000939
O
      16428+(-XX(J)*0.00006328))))
O
      X(J)=ZH(J)-18.5
O
C*****
C
      IF(X(J).LT.THIN) THIN=X(J)
      IF(X(J).GT.THAX) THAX=X(J)
      TMEAN=TMEAN+X(J)
C
C   EVALUATING FOR A CRUDE FORM OF ENTROPY HERE
      IF(XX(J).LE.0.000000) XXJ=XX(J)
      IF(XX(J).LE.0.000000) XX(J)=0.000001
      IF(X(J).LE.0.000000) XJ=X(J)
      IF(X(J).LE.0.000000) X(J)=0.000001
      EN=EN+(XX(J)*ALOG(XX(J)))
      ET=ET+(X(J)*ALOG(X(J)))
C*****
C   AT 18.5 DEG C, N-1.3331733=-0.0009396428
C   AT 20 DEG C, N-1.3331733=-0.0010668
C   AT 50 DEG C, N-1.3331733=-0.0052155
      IF(XX(J).EQ.0.000001) XX(J)=XXJ
      IF(X(J).EQ.0.000001) X(J)=XJ
      36 CONTINUE
C
C*****

```

```

C   FOR CU BLOCK COMMENT OUT NEXT TWO LINES & REMOVE THE 18.5 ON 3RD LINE
    THAX=THAX+18.5
    THIN=THIN+18.5
    THEAN=(THEAN/FLOAT(M5))+18.5
C*****
    IF(NR.EQ.0) GOTO 205
    GOTO 484
C   FOR THE FINITE ELEMENT MODEL ONLY
205 DO 1 I=1,18
    TH=0.0
    DO 2 J=1,8
      TH=TH+ZM(NODE(I,J))
    2 CONTINUE
    T(I)=TH/8.0
    1 CONTINUE
    IT=0
    DO 3 I=1,M5
      X(I)=ZM(NODE2(I))
      IF(NODE2(I).EQ.100) IT=IT+1
      IF(NODE2(I).EQ.100)X(I)=T(IT)
    3 CONTINUE
484 CONTINUE
C
C   INSTRUCTION UP TO LABEL 54 CALCULATE VALUES FOR THE SELECTED
C   ELEMENTS CRITERIA ACCORDING TO SECTION 4.7.2
    IF(K.EQ.1) GOTO 208
    LZ=K/2
    MZ=LZ*2
CDEF IF((MZ+1).NE.K) GOTO 209
C 208 WRITE(2,819)(ZM(J),J=1,73)
C
208 IF(K.EQ.1) GOTO 57
    IF(K.EQ.2) GOTO 58
    IF(K.GT.2) GOTO 59
58 DO 60 I=1,M5
    CH(I)=ZM(I)-TA(I)
60 CONTINUE
C
    DO 52 I=1,M5
    PJ=-300.0
    DO 53 J=1,M5
      IF(CH(J).GT.PJ) MA(I)=J
      IF(CH(J).GT.PJ) PJ=CH(J)
    53 CONTINUE
    CH(MA(I))=-300.0
    SA(I)=0.0
    52 CONTINUE
    WRITE(2,939)(MA(I),I=1,M5)
C
C   NUMBER OF ELEMENTS CHOSEN = 7
59 DO 54 I=1,7
    CH(MA(I))=ZM(MA(I))-TA(MA(I))
    SA(K)=SA(K)+CH(MA(I))
54 CONTINUE
    WRITE(2,210) EN,ET,GOV,GOW,SA(K)
    WRITE(2,210) THAX,THIN,THEAN
210 FORMAT(1H ,73X,F10.3,3X,F10.3,3X,F10.4,3X,F10.4,3X,F8.3)

```

```
IF(K.LT.3) GOTO 57
C THE INCREMENTS AFTER EACH ITERATION FOR THE SELECTED ELEMENTS
C CRITERIA ARE CONTAINED IN VECTOR CONVEG
CONVEG(K)=SA(K-1)-SA(K)
C IF(CONVEG(K).LE.0.2 .OR. SA(K).LE. 0.0) GOTO 5
C IF(CONVEG(K).LE.0.009) GOTO 5
C
57 DO 56 I=1,M5
TA(I)=ZM(I)
56 CONTINUE
WRITE(2,819)(X(J),J=1,M5)
209 WRITE(2,207) K
207 FORMAT(1H0,20X,I4)
819 FORMAT(5(4X,FB.2))
C IF(K.EQ.60) GOTO 5
IF (K.LT.200) GO TO 231
C IF (K.LE.60) GO TO 231
5 M1=5
N1=9
K1=M1*M1
WRITE(3,888) N1,M1,(X(J),J=1,K1)
888 FORMAT(1H ;I3,1X,I3,/ (5(4X,FB.2)))
RETURN
END
/
```

— END OF MAIN PROGRAM FERECON —

```

PROGRAM PLOT(INPUT,OUTPUT,TAPE3,TAPE2=OUTPUT)
C
C PROGRAM TO PLOT THE TWO-DIMENSIONAL RECONSTRUCTED TEMPERATURE
C FIELDS, FROM SELECTED Z=CONSTANT PLANES, BY USING THE GHOST LIBRARY
C ROUTINES.
C
DIMENSION X(9,5),H(14)
DO 1 I=1,14
H(I)=I*0.3
1 CONTINUE
NUMBER=0
C
GOTO 31
30 NUMBER=1
Z=0.100
A=0.0
AH=60.9
M4=281
IQ=9
RT=18.5
TM=20.15
TMAX=22.81
TMIN=18.5
C
EN1=108.5
EN2=-11.7
SSR1=46.9
SSR2=1306.0
SEC=180.0
C
READ(3,1000)((X(I,J),J=1,5),I=1,9)
GOTO 32
C*****
31 CONTINUE
C
Z=0.05
A=0.0
AH=60.9
M4=246
IQ=8
RT=18.5
TM=20.14
TMAX=22.2
TMIN=18.5
C
EN1=300.0
EN2=-11.5
SSR1=7
SSR2=1500.0
SEC=120.0
C
READ(3,1000)((X(I,J),J=1,5),I=1,9)
1000 FORMAT(5(4X,F8.2))
C*****
C
C

```

```

C
C*****
 32 CALL PAPER (1)
    IF (NUMBER.EQ.1) GOTO 10
    CALL PSPACE(0,1333,0,5666,0,7,0,91666)
C
    GOTO 20
 10 CALL PSPACE(0,1333,0,5666,0,266,0,4833)
C
 20 CONTINUE
C
C
    CALL CTRMAG(8)
    CALL CSPACE(0,0,1,0,0,0,1,0)
C
    CALL MAP(0,0,6,01,0,0,3,01)
    CALL SCALSI(1,00,1,00)
    CALL BORDER
    CALL CONTRA(X,1,9,9,1,5,5,H,1,14)
    CALL BROKEN(5,5,5,5)
    CALL GRATSI(1,0016,1,003)
    CALL FULL
C
    YY=-0,077*6,01
    XX=0,492*6,01
    CALL PLOTCS (YY,1,55,1HY,1)
    CALL PLOTCS (XX,-0,37,1HX,1)
C
    IF (NUMBER.EQ.0) CALL CSPACE(0,1500,0,6166,0,5,0,6666)
    IF (NUMBER.EQ.1) CALL CSPACE(0,1500,0,6166,0,066,0,2333)
C
    CALL PLACE(1,1)
    CALL TYPECS(5HPL0T ,5)
    CALL CRLNFD
C
    CALL CTRMAG(5)
    CALL PLACE(3,4)
    CALL TYPECS("PLANE Z= ",9)
    CALL TYPENF(Z,3)
C
    CALL PLACE (3,6)
    CALL TYPECS ("ANGLE MIN= ",11)
    CALL TYPENF (A,1)
    CALL TYPECS(" DEG",4)
C
    CALL PLACE(3,8)
    CALL TYPECS ("ANGLE MAX= ",11)
    CALL TYPENF (AH,1)
    CALL TYPECS (" DEG",4)
C
    CALL PLACE (3,10)
    CALL TYPECS ("TOTAL NUMBER OF RAYS USED = ",28)
    CALL TYPENI(M4)
C
    CALL PLACE (3,12)
    CALL TYPECS ("NUMBER OF PROJECTIONS USED = ",29)
    CALL TYPENI (IO)

```

```

C
CALL PLACE (4,15)
CALL TYPECS ('ORIGINAL TEMP = ',16)
CALL TYPENF (RT,1)
CALL TYPECS (' C',2)

C
CALL PLACE (4,17)
CALL TYPECS ('RECONSTRUCTED MEAN TEMP = ',26)
CALL TYPENF (TM,2)
CALL TYPECS (' C',2)

C
CALL PLACE (4,19)
CALL TYPECS ('RECONSTRUCTED MAX TEMP = ',25)
CALL TYPENF (TMAX,2)
CALL TYPECS (' C',2)

C
CALL PLACE (4,21)
CALL TYPECS ('RECONSTRUCTED MIN TEMP = ',25)
CALL TYPENF (TMIN,2)
CALL TYPECS (' C',2)

C
C
CALL PLACE (60,4)
CALL TYPECS ('CONTOURS IN DEG C ',18)
CALL CRLNFD
DO 90 I=1,10
V=FLOAT(I)*0.3
CALL CRLNFD
IF(I.LT.10) CALL SPACE (64)
IF(I.GE.10) CALL SPACE (63)
CALL TYPENI (I)
CALL TYPECS (2H= ,2)
CALL TYPENF (V,2)
90 CONTINUE
CALL TYPECS (' ETC.',5)

C
C
CALL PLACE (47,17)
CALL TYPECS ('ENTROPY = ',10)
CALL TYPENF (EN1,2)
CALL TYPECS (' ( ',3)
CALL TYPENF (EN2,2)
CALL TYPECS (' )',2)

C
CALL PLACE (47,19)
CALL TYPECS ('SUM OF SQUARE OF @ RESIDUAL = ',30)
CALL TYPENF (SSR1,1)
CALL TYPECS (' ( ',2)
CALL TYPENF (SSR2,1)
CALL TYPECS (' )',1)

C
CALL PLACE (47,21)
CALL TYPECS ('COMPUTING TIME = ',17)
CALL TYPENF (SEC,2)
CALL TYPECS (' SEC.',5)
IF(NUMBER.EQ,0) GOTO 30

C

```

```
CALL GREND  
C  
STOP  
END
```

SIXTEEN SETS OF DIGITISED PROJECTION DATA  
FROM THE CONSTANT TEMPERATURE WALL ENCLOSURE MODEL.  
EACH OF THE SIXTEEN SETS HAS PRODUCED A RECONSTRUCTION.  
THE RECONSTRUCTED FIELDS ARE SHOWN IN CHAPTER 6.

An extract is given below showing the layout of the digitised data set,  
and numbers in square brackets represent quantities described on page 158.  
Each set is identified by a plot number which refers to a particular contour  
plot in Chapter 6.

[1(a)]	[1(b)]	[1(c)]	[ 2 ]	[ 4 ]	[ 3 ]	[ 5 ]	
8246	6	3					
28 21 28 37 23	41 39 29						
-90.0	-81.9	-74.8	-59.85	-50.87	-44.98	-37.15	-29.10
1.3684	1.4290	1.420	1.417	1.293	-1.234	1.448	1.424
1.0 0.8 5.0 2.0 8.0 3.0	9.0 4.0 9.5 11.0 10.0 18.0	11.0 25.0 12.0 35.7					
13.0 47.0 14.0 52.0 15.0 53.4	16.0 55.0 17.0 60.0 17.0 66.0	18.0 68.0 18.0 74.0					
18.0 81.5 17.0 85.2 16.0 90.2	15.0 94.0 14.0 104.2 13.0 109.0	12.3 115.2 12.0 121.0					
11.0 125.5 10.0 127.0 9.0 128.0	5.0 130.0						
5.0 9.0 11.0 20.0 12.0 22.0	12.5 30.0 13.0 41.0 14.0 53.0	15.0 57.0 16.0 59.0					
17.0 62.0 17.0 68.8 18.0 72.0	19.0 76.4 20.0 82.3 18.0 90.0	17.0 92.5 16.0 95.5					
15.0 100.4 14.0 109.2 13.0 115.0	12.0 130.0 11.0 134.0						
1.0 2.5 5.0 8.0 10.0 13.2	12.0 28.0 13.0 34.3 13.0 40.0	14.0 53.0 15.0 56.0					
16.0 57.0 17.0 60.0 18.0 62.5							

## PLOT 6.1(1)

8246 6 3  
28 21 28 37 23 41 39 29  
-90.0 -81.9 -74.8 -59.85 -50.87 -44.98 -37.15 -29.10  
1.3684 1.4290 1.420 1.417 1.293 1.234 1.448 1.424  
1.0 0.8 5.0 2.0 8.0 3.0 9.0 4.0 9.5 11.0 10.0 18.0 11.0 25.0 12.0 35.7  
13.0 47.0 14.0 52.0 15.0 53.4 16.0 55.0 17.0 60.0 17.0 66.0 18.0 68.0 18.0 74.0  
18.0 81.5 17.0 85.2 16.0 90.2 15.0 94.0 14.0104.2 13.0109.0 12.3115.2 12.0121.0  
11.0125.5 10.0127.0 9.0128.0 5.0130.0  
5.0 9.0 11.0 20.0 12.0 22.0 12.5 30.0 13.0 41.0 14.0 53.0 15.0 57.0 16.0 59.0  
17.0 62.0 17.0 68.8 18.0 72.0 19.0 76.4 20.0 82.3 18.0 90.0 17.0 92.5 16.0 95.5  
15.0100.4 14.0109.2 13.0115.0 12.0130.0 11.0134.0  
1.0 2.5 5.0 8.0 10.0 13.2 12.0 28.0 13.0 34.3 13.0 40.0 14.0 53.0 15.0 56.0  
16.0 57.0 17.0 60.0 18.0 62.5 18.0 71.2 19.0 75.2 20.0 77.5 20.0 86.0 19.0 88.0  
18.0 93.0 17.0 96.3 16.0100.0 15.0108.0 14.0116.0 13.0125.0 9.0138.0 6.0140.3  
5.0141.8 4.0143.0 3.0145.0 1.0146.0  
1.0 2.5 3.0 6.8 5.0 12.0 7.0 15.0 9.0 18.0 11.0 22.0 13.0 25.0 15.0 28.0  
17.0 33.0 18.0 28.0 19.0 34.5 20.0 40.0 20.0 48.3 21.0 52.6 21.5 55.0 22.0 57.0  
22.0 62.1 21.0 66.5 22.0 69.0 23.0 71.5 24.0 75.5 23.0 77.5 21.0 81.2 22.0 90.2  
20.5116.0 20.0113.2 20.4116.2 17.0122.0 15.0123.5 12.0129.5 10.0137.0 7.0138.0  
5.0141.5 4.0144.0 3.0145.0 2.0147.0 1.0148.0  
1.0 2.0 3.0 7.0 5.0 11.0 7.0 15.6 9.0 19.8 10.0 21.0 13.0 25.0 15.0 28.0  
17.0 31.0 20.0 36.0 21.0 44.0 22.0 49.5 23.0 59.0 24.0 63.5 23.0 87.5 18.0102.5  
16.0106.3 13.0111.0 10.0115.0 7.0119.6 5.0124.0 4.0126.2 2.0130.0  
1.0 3.0 3.0 9.0 5.0 12.3 7.0 16.0 9.0 20.4 10.0 22.5 12.0 25.0 14.0 29.0  
15.0 30.0 17.0 33.0 19.0 35.5 20.0 37.0 22.0 41.0 24.0 44.6 25.0 49.9 26.0 52.5  
27.0 60.5 29.0 65.5 30.0 67.5 30.0 70.0 29.0 75.0 27.0 83.5 25.0 90.5 22.0 95.3  
20.0 99.1 19.0101.0 18.0102.0 17.0103.0 15.0105.0 13.0107.2 11.0110.1 10.0111.0  
9.0113.0 8.0114.5 7.0116.1 6.0118.8 5.0120.0 4.0122.0 3.0124.0 2.0126.0  
1.0128.8  
2.0 4.0 3.0 7.0 4.0 9.0 6.0 12.2 8.0 17.0 10.0 20.0 12.0 24.0 14.0 27.5  
16.0 30.0 18.0 33.0 20.0 36.2 24.0 42.8 26.0 45.0 27.0 46.0 28.0 47.0 29.5 50.0  
30.0 55.0 31.0 61.0 32.0 62.0 33.0 63.5 34.0 67.0 32.0 72.2 31.0 75.0 30.0 80.2  
28.0 83.5 27.0 85.5 25.0 91.0 23.0 95.4 20.0 99.1 17.0103.0 15.0106.0 13.0108.8  
11.0112.2 9.0114.5 7.0118.0 5.0122.1 3.0127.1 2.0129.4 1.0133.0  
1.0 3.0 2.0 5.1 3.0 7.2 5.0 10.1 9.0 14.6 15.0 22.4 17.0 24.5 20.0 28.5  
25.0 33.0 29.0 36.9 30.0 40.9 32.0 45.0 34.0 47.1 36.0 53.0 37.0 54.5 36.0 61.0  
35.0 63.0 34.0 68.5 33.0 70.5 30.0 73.6 28.0 79.5 25.0 85.0 20.0 90.0 15.0 95.0  
10.0101.5 8.0104.9 6.0108.1 4.0111.1 2.0115.0  
1.0 2.0 3.0 7.0 5.0 11.0 7.0 15.6 9.0 19.8 10.0 21.0 13.0 25.0 15.0 28.0  
17.0 31.0 20.0 36.0 21.0 44.0 22.0 49.5 23.0 59.0 24.0 63.5 23.0 87.5 18.0102.5  
16.0106.3 13.0111.0 10.0115.0 7.0119.6 5.0124.0 4.0126.2 2.0130.0  
11.0 6.0 11.0 15.0 12.0 22.1 13.0 33.8 14.0 45.0 15.0 48.0 16.0 50.1 16.0 57.4  
17.0 63.0 18.0 66.9 18.0 79.0 17.0 88.2 16.0 94.0 15.0 96.9 14.0102.2 13.0105.0  
12.0118.5

## PLOT 6.1(2)

9281 6 3  
 27 27 28 27 32 33 36 40 31  
 -90.0 -93.2 -81.9 -74.8 -59.85 -50.87 -44.98 -37.15 -29.10  
 1.3684 1.2841 1.4290 1.420 1.417 1.293 1.234 1.448 1.424  
 5.0 1.5 10.0 3.5 11.0 4.0 12.0 13.1 13.0 19.6 14.0 32.2 15.0 36.0 16.0 46.9  
 15.0 51.5 14.0 54.0 13.0 58.0 13.0 62.5 14.0 64.0 15.5 66.2 15.0 71.0 15.0 77.0  
 16.0 81.0 17.0 85.5 17.0 91.8 16.0 99.2 15.0106.6 14.0112.5 13.0122.8 12.0127.0  
 11.0128.0 10.0128.5 5.0129.5  
 4.0 3.5 8.0 4.0 11.0 6.0 13.0 7.0 14.0 17.0 14.0 30.5 15.0 34.5 16.0 40.5  
 16.0 46.0 15.0 50.6 14.0 53.2 13.0 58.9 13.0 61.2 14.0 63.0 15.0 64.0 15.0 69.5  
 14.0 71.0 15.0 76.5 16.0 80.6 17.0 84.0 17.0 90.9 16.0 99.0 15.0105.0 14.0110.0  
 13.0118.5 12.0120.1 4.0123.0  
 2.0 2.0 4.0 3.5 12.0 9.5 12.0 15.9 13.0 19.6 14.0 32.0 15.0 38.0 16.0 43.0  
 17.0 50.4 16.0 54.6 15.0 56.5 14.0 60.4 13.0 65.6 14.0 68.9 15.0 70.8 16.0 74.5  
 15.0 78.2 16.0 83.6 17.0 87.3 17.0101.6 16.0110.6 15.0117.4 14.0125.8 13.0133.0  
 12.0135.0 4.0140.0 2.0142.0 1.0143.0  
 2.0 3.0 4.0 6.0 6.0 8.6 8.0 11.0 10.0 14.0 13.0 20.1 15.0 30.9 16.0 43.5  
 17.0 47.9 18.0 54.6 17.0 58.5 16.0 59.9 15.0 61.1 14.0 67.0 15.0 70.9 16.0 73.6  
 17.0 76.4 16.0 81.0 17.0 84.0 18.0 86.5 18.0100.3 17.0118.2 16.0116.6 14.0128.1  
 10.0137.0 5.0141.9 1.0146.2  
 1.0 1.9 2.0 4.1 3.0 6.5 5.0 10.2 7.0 13.4 10.0 18.0 12.0 22.8 15.0 26.5  
 17.0 29.0 19.0 34.0 21.0 43.0 23.0 50.6 22.0 54.0 21.0 56.0 20.0 59.5 19.0 67.5  
 20.0 71.0 21.0 73.0 21.0 75.6 20.0 78.4 19.0 81.0 19.0 88.5 17.0120.4 15.0124.0  
~~13.0128.0~~ 11.0130.7 9.0133.8 7.0136.1 5.0140.0 3.0142.9 2.0145.0 1.0147.6  
 1.0 1.6 3.0 6.5 5.0 9.6 8.0 15.0 10.0 18.5 12.0 21.4 13.0 23.0 15.0 26.0  
 17.0 29.5 19.0 32.0 20.0 33.5 21.0 40.0 22.0 43.0 23.0 45.0 23.0 62.0 23.0 67.1  
 24.0 68.5 25.0 73.0 25.0 75.5 24.0 80.1 22.0 91.1 20.0 99.8 18.0103.0 17.0104.9  
 15.0107.9 14.0109.3 12.0113.0 10.0116.0 9.0117.7 7.0120.2 5.0123.4 4.0125.0  
 2.0128.2  
 1.0 2.5 2.0 5.0 3.0 7.5 4.0 9.1 5.0 11.0 8.0 17.5 10.0 23.4 11.0 25.2  
 13.0 29.0 15.0 32.1 16.0 34.0 18.0 37.0 20.0 39.2 22.0 42.2 24.0 44.0 25.0 45.6  
 26.0 52.4 26.0 59.0 26.0 63.9 27.0 66.0 28.0 67.4 28.0 70.4 27.0 73.0 26.0 81.0  
 25.0 92.0 22.0 95.8 20.0100.0 18.0103.0 15.0106.9 12.0110.6 10.0114.0 8.0117.0  
 6.0120.1 5.0122.0 3.0125.1 1.0129.6  
 1.0 1.8 2.0 4.2 3.0 6.8 5.0 10.0 7.0 13.9 8.0 15.9 10.0 19.5 13.0 23.5  
 15.0 25.6 17.0 28.0 18.0 19.4 20.0 33.0 22.0 36.1 25.0 40.5 26.0 42.0 28.0 44.9  
 30.0 48.9 31.0 59.9 31.0 64.0 32.0 65.0 33.0 66.8 33.0 68.0 32.0 70.0 31.0 73.1  
 30.0 84.9 29.0 87.1 26.0 90.1 25.0 92.0 22.0 97.0 20.0100.1 17.0104.5 15.0107.8  
 13.0110.4 10.0115.8 8.0119.0 7.0120.5 5.0124.6 3.0128.1 2.0130.1 1.0133.0  
 1.0 1.2 2.0 3.9 3.0 5.6 6.0 10.0 10.0 15.8 15.0 22.0 18.0 25.0 22.0 29.8  
 25.0 33.1 29.0 38.5 30.0 41.4 31.0 45.0 33.0 49.0 35.0 51.2 36.0 54.2 38.0 61.1  
 35.0 66.0 33.0 69.9 30.0 73.3 28.0 81.0 25.0 84.6 23.0 87.0 20.0 90.6 18.0 82.9  
 17.0 94.0 13.0 99.0 10.0103.0 7.0107.0 5.0110.5 3.0113.8 1.0118.0

## PLOT 6.1(3)

9280 6 3  
 26 27 30 28 36 32 34 31 36  
 -90.0 -93.2 -81.9 -74.8 -59.85 -50.87 -44.98 -37.15 -29.10  
 1.3684 1.2841 1.4290 1.420 1.417 1.293 1.234 1.448 1.424  
 5.0 2.0 9.0 4.0 10.0 5.0 10.4 8.3 10.0 15.0 9.8 19.9 10.0 31.0 10.0 40.0  
 10.0 54.4 9.5 60.5 10.0 63.2 11.0 64.5 12.0 66.0 12.0 68.0 11.0 71.0 10.0 72.5  
 9.6 74.5 11.0 76.8 10.1 88.0 10.2 97.2 10.2107.2 10.2117.2 10.7123.0 10.0125.1  
 9.0126.0 6.0127.9  
 5.0 3.0 10.0 4.8 11.0 5.3 11.8 9.0 11.1 17.0 11.2 25.0 11.2 31.2 11.3 40.0  
 11.2 49.0 11.0 56.9 10.7 59.1 11.0 61.1 12.0 62.2 12.8 63.9 13.0 65.5 13.0 67.5  
 12.0 68.6 10.7 71.0 11.0 74.0 11.2 87.0 11.2 94.8 11.2103.0 11.1112.0 11.8116.4  
 11.0119.3 9.0120.5 5.0123.1  
 1.0 0.5 3.0 2.1 4.0 3.0 5.0 5.0 10.0 9.5 10.6 13.3 10.2 20.4 10.1 25.1  
 10.2 29.5 10.6 39.0 11.0 45.0 11.0 52.8 10.7 61.0 10.0 68.1 11.0 70.8 12.0 72.0  
 12.0 74.1 13.0 76.5 12.0 78.0 11.0 79.5 10.0 81.0 10.8 94.0 10.9106.0 10.8118.1  
 10.8126.0 11.0129.4 11.2132.9 11.0135.0 10.0136.0 7.0139.0  
 2.0 2.5 4.0 5.1 5.0 6.4 6.0 8.1 8.0 11.0 10.0 14.0 11.0 20.5 11.0 26.3  
 11.1 33.8 11.2 44.5 11.4 53.6 11.3 62.4 11.0 67.4 12.0 71.0 13.0 74.3 13.0 77.5  
 11.0 80.1 11.0 83.5 11.5 88.5 11.5101.9 11.4110.8 11.4120.1 11.8125.8 10.0133.6  
 8.0136.0 5.0139.3 3.0141.9 1.0145.0  
 1.0 2.1 2.0 4.3 3.0 6.6 5.0 10.1 7.0 13.0 8.0 14.6 10.0 17.5 11.0 19.3  
 13.0 23.1 15.0 26.7 16.0 28.0 16.1 39.0 16.2 45.1 16.4 34.2 16.3 60.5 16.0 66.4  
 18.0 72.0 19.0 73.0 19.0 74.0 18.0 75.2 17.0 79.9 16.0 83.1 16.3 87.8 16.8 93.5  
 16.5100.0 15.0120.0 13.0123.2 11.0126.5 10.0128.5 9.0131.1 7.0134.8 6.0136.6  
 5.0138.8 3.0142.4 2.0144.2 1.0146.0  
 1.0 3.5 2.0 5.4 3.0 8.0 5.0 12.0 7.0 15.7 9.0 20.0 11.0 24.3 13.0 28.0  
 14.0 30.4 16.0 34.2 17.0 36.0 17.0 44.0 17.0 46.5 16.5 63.0 18.0 69.0 19.0 70.0  
 19.0 72.0 18.0 73.5 17.0 75.0 16.5 77.5 17.0 81.0 17.0 87.0 17.0 92.0 17.0 99.0  
 14.0104.0 12.0107.5 10.0111.0 8.0115.0 6.0119.3 4.0123.0 3.0125.4 2.0128.0  
 1.0 2.0 2.0 4.0 4.0 9.0 5.0 11.2 6.0 13.9 7.0 16.8 10.0 28.7 12.0 32.4  
 15.0 38.1 19.0 46.0 19.0 54.6 19.0 58.9 18.3 62.1 19.0 63.9 20.0 65.9 21.0 67.4  
 21.0 68.9 20.0 70.0 19.0 70.9 19.0 73.0 18.5 75.9 19.0 80.9 18.0 91.5 16.0 96.0  
 15.0 98.1 13.0102.0 11.0106.6 10.0109.0 8.0113.0 6.0118.0 5.0120.0 4.0122.0  
 3.0124.3 1.0129.0  
 1.0 1.0 2.0 3.2 4.0 7.3 6.0 11.8 8.0 16.0 10.0 20.3 12.0 24.1 14.0 28.9  
 16.0 33.9 18.0 38.7 20.0 43.4 22.0 46.6 23.0 57.0 24.0 62.6 25.0 66.6 25.0 64.2  
 24.0 67.8 23.0 73.0 23.0 80.5 22.0 83.0 20.0 87.5 18.0 92.3 16.0 96.0 15.0 98.2  
 13.0102.0 11.0108.0 9.0113.0 7.0118.0 5.0122.5 3.0127.3 1.0132.8  
 1.0 3.0 3.0 6.3 5.0 10.0 7.0 13.1 8.0 16.3 10.0 19.1 12.0 22.4 14.0 25.8  
 15.0 27.5 17.0 31.0 18.0 32.5 19.0 34.5 20.0 36.4 22.0 40.2 24.0 44.0 25.0 46.1  
 27.0 50.0 29.0 52.8 28.0 60.4 26.0 64.1 25.0 66.0 24.0 67.5 23.0 69.4 21.0 75.2  
 19.0 79.5 17.0 82.5 15.0 86.2 13.0 90.0 12.0 91.9 10.0 96.2 8.0 99.2 6.0104.4  
 5.0106.4 3.0110.0 2.0112.2 1.0114.3

## PLOT 6.1(4)

```

9290 6 3
31 26 36 33 31 30 32 34 37
-90.0 -93.2 -81.9 -74.8 -59.85 -50.87 -44.98 -37.15 -29.10
1.3684 1.2841 1.4290 1.420 1.417 1.293 1.234 1.448 1.424
1.0 1.0 3.0 2.5 5.0 5.0 5.4 7.2 5.1 12.5 5.3 24.0 5.5 35.0 5.7 44.0
5.9 48.0 6.0 56.0 6.0 60.5 7.0 62.0 10.0 63.5 10.0 64.5 11.0 67.0 10.0 69.5
11.0 71.0 9.0 73.0 7.0 74.5 6.0 76.0 6.0 79.5 6.1 85.0 6.1 95.5 6.1 102.5
6.0113.0 6.0116.5 6.2121.5 6.0124.5 5.0126.0 3.0128.0 1.0129.0
1.0 1.0 3.0 3.0 4.0 4.2 5.0 5.25 5.5 9.0 5.2 15.0 5.5 25.0 6.0 38.5
6.0 51.0 6.0 58.0 7.0 60.2 9.0 62.5 10.0 64.0 11.0 65.0 10.0 66.0 9.0 67.2
10.0 68.0 8.0 70.2 6.0 73.0 6.1 88.4 6.2 98.0 6.0107.5 6.0117.2 5.0120.0
4.0121.5 2.0123.5
1.0 1.5 2.0 3.2 4.0 5.5 5.0 7.7 5.7 13.7 5.5 21.8 5.6 27.0 6.0 34.8
6.0 37.5 6.0 40.0 6.4 50.0 6.5 58.0 7.0 65.0 9.0 67.0 10.0 69.0 11.0 70.0
11.0 71.0 12.0 72.0 12.0 73.1 10.0 74.8 9.0 76.3 9.0 78.5 8.0 80.0 7.0 81.3
6.6 82.6 6.4 85.0 6.8 93.1 6.8100.9 6.8108.2 6.8116.3 6.6123.3 6.9130.0
6.0134.4 4.0140.0 1.0143.2 0.5 161.0
1.0 3.5 2.0 7.0 3.0 9.5 5.0 13.0 6.2 23.0 6.4 28.2 6.6 34.2 6.8 39.5
7.0 46.2 7.2 53.8 7.3 60.0 7.4 65.8 8.0 67.2 10.0 70.3 10.0 72.0 12.0 75.2
12.0 76.8 11.0 77.5 11.0 79.0 10.0 80.5 10.0 81.7 9.0 82.8 8.0 84.0 7.3 86.8
7.5 92.0 7.5101.5 7.5108.5 7.4120.0 7.5126.0 6.0135.0 4.0139.0 2.0143.0
1.0145.0
1.0 1.5 2.0 4.0 3.0 7.0 4.0 10.0 5.0 14.0 7.0 19.5 8.0 23.0 9.0 26.5
10.0 30.5 10.5 36.0 10.5 41.0 11.0 45.8 11.2 52.0 11.3 60.0 12.0 63.8 14.0 67.8
16.0 72.5 15.0 73.5 14.0 74.8 12.0 76.8 11.0 78.5 11.0 81.2 11.0 86.0 11.0 96.8
9.0120.0 7.0125.5 6.0128.5 5.0132.3 3.0138.5 2.0141.5 1.0145.3
1.0 3.2 2.0 6.5 4.0 13.0 5.0 15.5 7.0 23.0 9.0 28.5 11.0 34.5 11.0 42.0
11.0 49.5 12.0 59.5 13.0 63.0 15.0 66.0 16.0 68.0 17.0 70.5 14.0 72.0 15.0 72.5
15.0 74.5 14.0 76.5 13.0 77.0 12.0 78.2 11.4 84.5 11.0 91.8 11.0 97.2 9.0103.2
7.0110.0 5.0116.0 3.0123.3 2.0126.0 1.0129.0 0.5 134.0
1.0 4.0 2.0 7.5 4.0 13.5 5.0 17.0 7.0 27.3 8.0 31.7 9.0 35.5 11.0 41.7
13.0 47.0 13.0 53.5 13.0 58.5 14.0 60.5 15.0 62.7 16.0 65.7 15.0 66.9 19.0 69.9
15.0 72.4 16.0 74.0 16.0 77.0 15.0 78.0 12.5 81.0 12.5 83.0 12.5 85.0 12.0 92.5
10.0 99.0 9.0102.5 7.0109.0 6.0113.0 4.0120.0 3.0124.0 2.0127.5 1.0130.3
1.0 2.0 2.0 6.0 3.0 9.0 4.0 12.3 5.0 16.0 7.0 23.0 8.0 27.0 9.0 30.0
10.0 34.0 11.0 38.3 12.0 42.8 13.0 46.0 14.0 55.0 15.0 58.0 15.0 61.0 17.0 64.0
16.0 64.5 15.0 67.8 14.0 68.5 16.0 72.0 14.0 74.0 14.0 82.5 13.0 86.5 12.0 90.0
11.0 93.4 9.0100.5 8.0103.9 7.0107.9 5.0116.0 4.0120.0 3.0124.0 2.0128.0
1.0132.3 0.5 137.0
1.0 3.0 2.0 6.0 3.0 9.5 4.0 12.0 5.0 15.0 6.0 17.8 7.0 20.5 8.0 23.5
9.0 26.0 10.0 28.0 12.0 34.0 14.0 40.0 15.0 43.0 17.0 48.3 20.0 53.0 21.0 54.1
21.0 60.0 21.0 61.0 19.0 62.0 18.0 63.0 17.0 64.0 18.0 66.5 17.0 67.8 15.0 70.8
14.0 74.2 13.0 77.8 12.0 82.0 11.0 85.0 10.0 88.0 8.0 93.0 7.0 96.6 6.0 99.7
5.0102.9 3.0109.3 2.0112.3 1.0116.5 0.5 129.0

```

## PLOT 6.2(1)

8223 6 3

22 27 29 23 26 28 32 36

-90.0 -81.19 -74.0 -70.32 -44.25 -39.21 -37.10 -31.35

1.2737 1.4490 1.417 1.4626 1.2587 1.3485 1.3628 1.209

10.0 3.0 11.0 5.0 12.0 10.0 12.0 17.0 13.0 24.0 14.0 30.0 15.0 36.0 16.0 45.0

17.0 51.0 18.0 56.0 19.0 66.0 20.0 62.0 19.0 66.0 18.0 76.0 17.0 79.0 16.0 83.0

15.0 88.0 14.0 92.0 13.0102.0 12.0105.0 11.0115.0 10.0117.0

1.0 1.0 3.0 3.0 5.0 5.0 7.0 7.0 10.0 10.0 11.0 17.0 12.0 26.0 13.0 34.0

14.0 40.0 15.0 48.0 16.0 56.0 17.0 59.0 18.0 63.0 19.0 70.0 20.0 75.0 19.0 78.0

18.0 85.0 17.0 88.0 16.0 92.0 15.0 96.0 14.0102.0 13.0111.0 12.0117.0 11.0125.0

10.0132.0 5.0140.0 1.0144.0

1.0 3.0 3.0 6.0 5.0 9.0 7.0 11.0 9.0 13.0 11.0 15.0 12.0 21.0 13.0 30.0

14.0 38.0 15.0 49.0 16.0 54.0 17.0 57.0 18.0 60.0 19.0 63.0 19.0 72.0 20.0 78.0

19.0 85.0 18.0 92.0 17.0 96.0 16.0100.0 15.0109.0 14.0112.0 13.0125.0 11.0134.0

10.0135.0 7.0139.0 5.0141.0 3.0144.0 1.0147.0

1.0 2.0 4.0 6.0 6.0 9.0 8.0 12.0 10.0 15.0 12.0 17.0 14.0 19.0 14.0 27.0

15.0 38.0 16.0 48.0 17.0 57.0 18.0 59.0 19.0 61.0 20.0 66.0 21.0 76.0 22.0 79.0

21.0 83.0 20.0 86.0 19.0 89.0 18.0100.0 17.0106.0 16.0115.0 15.0122.0

1.0 3.0 3.0 7.0 5.0 11.0 7.0 15.0 9.0 19.0 10.0 21.0 13.0 25.0 16.0 30.0

20.0 33.0 26.0 55.0 29.0 62.0 28.0 70.0 26.0 73.0 24.0 76.0 22.0 84.0 20.0 86.0

18.0 89.0 16.0 92.0 14.0 96.0 12.0 99.0 10.0103.0 8.0106.0 6.0110.0 4.0 13.0

2.0117.0 1.0119.0

2.0 3.0 4.0 8.0 7.0 13.5 9.0 18.0 12.0 24.0 15.0 28.0 17.0 31.0 19.0 35.0

22.0 40.0 24.0 43.5 26.0 53.0 27.0 57.0 27.0 63.0 27.0 68.0 28.0 73.0 28.0 82.0

26.0 87.0 24.0 91.0 20.0 95.0 17.0 98.8 14.0103.0 12.0107.0 10.0110.0 8.0 13.0

6.0117.0 4.0121.0 2.0124.5 1.0127.0

1.0 2.0 2.0 4.0 4.0 9.0 6.0 12.0 8.0 17.0 10.0 21.0 12.0 23.0 14.0 26.0

16.0 30.0 18.0 33.0 20.0 37.0 23.0 40.0 25.0 42.0 27.0 45.0 29.0 40.0 30.0 55.0

32.0 60.0 36.0 65.0 29.0 69.0 31.0 78.0 29.0 80.0 27.0 84.0 25.0 87.0 22.0 91.0

20.0 95.0 17.0 99.0 13.0103.0 10.0108.0 6.0115.0 4.0119.0 2.0123.0 1.0125.0

1.0 2.0 4.0 4.0 5.0 7.0 7.0 10.0 9.0 12.5 11.0 16.0 13.0 19.0 15.0 22.0

18.0 25.0 20.0 27.0 23.0 31.0 25.0 33.5 27.0 36.0 28.0 38.0 30.0 40.0 33.0 43.0

36.0 47.0 37.0 50.0 37.0 56.0 36.0 60.0 35.0 63.0 33.0 65.0 30.0 68.0 28.0 71.0

25.0 75.0 22.0 78.0 20.0 80.0 17.0 83.0 15.0 85.0 14.0 84.0 11.0 89.0 8.0 92.0

5.0 96.0 3.0 99.0 2.0101.0 1.0102.0

## PLOT 6.2(2)

8241 6 3

26 35 32 34 25 27 29 33

-90.0 -81.19 -74.0 -70.32 -44.25 -39.21 -37.10 -31.35

1.2737 1.4490 1.417 1.4626 1.2587 1.3485 1.3628 1.209

1.0 0.5 5.0 1.5 11.0 2.5 12.0 5.0 13.0 15.0 14.0 24.0 16.0 31.0 17.0 43.0

16.0 46.0 15.0 48.0 14.0 54.9 15.0 57.2 16.0 59.0 17.0 61.0 16.0 64.0 15.0 66.0

15.0 69.0 16.0 73.0 17.0 75.0 18.0 81.0 17.0 85.0 16.0 92.2 15.0103.2 14.0116.0

10.0118.3 5.0119.9

1.0 1.0 3.0 2.5 5.0 4.0 8.0 6.9 10.0 7.0 12.0 14.0 13.0 23.0 14.0 29.9

15.0 36.0 16.0 41.0 17.0 50.0 16.0 56.0 15.0 62.0 15.0 69.9 16.0 72.0 17.0 74.0

18.0 76.0 16.0 78.0 15.0 81.0 16.0 89.0 17.0 91.0 18.0 95.0 17.0101.0 16.0108.0

15.0117.0 14.0119.0 15.0121.0 15.0127.0 14.0131.0 14.0134.0 10.0140.0 7.0142.0

5.0143.0 3.0144.5 1.0145.5

1.0 2.0 4.0 6.0 7.0 10.0 10.0 13.0 12.0 14.5 14.0 20.0 15.0 30.0 16.0 38.0

17.0 45.0 18.0 50.0 18.0 53.0 17.0 60.0 16.0 65.0 16.0 72.0 17.0 74.0 18.0 75.0

18.5 77.0 18.0 79.0 17.0 81.0 16.0 83.0 17.0 92.0 18.0 97.0 18.0103.0 17.0111.0

16.6114.0 16.0124.0 12.0135.0 10.0137.0 7.0140.0 5.0142.0 2.0145.0 1.0146.0

1.0 2.0 3.0 7.0 5.0 10.0 8.0 13.0 11.0 16.0 13.0 18.0 15.0 24.5 16.0 31.0

16.5 35.0 17.0 41.0 18.0 47.0 19.0 52.5 19.0 57.0 18.0 60.0 17.0 65.0 16.5 70.0

17.0 74.0 18.0 77.0 19.0 79.0 19.0 81.0 17.0 85.0 17.0 88.0 18.0 95.0 19.0103.0

18.0110.0 16.9114.0 17.0123.0 16.0126.0 12.0133.0 10.0137.0 7.0142.0 5.0146.0

3.0148.0 1.0151.0

1.0 2.0 3.0 6.0 5.0 10.0 7.0 14.0 9.0 18.0 11.0 23.0 15.0 29.0 17.0 32.0

20.0 35.0 22.0 40.0 23.0 50.0 23.0 60.0 25.0 67.0 25.0 73.0 26.0 75.0 25.0 87.0

20.0 91.0 17.0 95.0 15.0 98.0 12.0102.0 10.0105.0 7.0109.0 5.0113.0 3.0117.0

1.0121.0

1.0 1.0 3.0 5.0 5.0 9.0 7.0 12.0 9.0 16.0 11.0 20.0 13.0 24.0 15.0 19.0

18.0 35.0 20.0 39.0 22.0 43.0 23.0 46.0 27.0 58.0 27.0 63.0 26.0 69.0 27.0 72.0

28.0 74.0 27.0 82.0 25.0 84.0 22.0 90.0 17.0100.0 13.0106.0 10.0110.0 8.0103.0

6.0117.0 4.0120.0 2.0124.0

1.0 3.0 3.0 7.0 6.0 12.0 8.0 16.5 12.0 22.0 15.0 28.0 18.0 31.0 20.0 34.0

23.0 38.0 27.0 42.0 30.0 46.0 32.0 54.0 30.0 61.0 29.0 66.0 30.0 69.0 32.0 76.0

30.0 78.0 25.0 86.0 23.0 89.0 22.0 93.0 19.0 97.0 16.0100.0 15.0102.0 12.0106.0

9.0110.0 7.0114.0 5.0117.0 3.0121.0 1.0124.0

1.0 2.0 3.0 5.0 5.0 8.0 7.0 11.0 10.0 15.0 14.0 19.0 17.0 23.0 20.0 26.0

23.0 30.0 27.0 34.0 30.0 37.0 33.0 40.0 35.0 43.0 36.0 46.0 36.0 54.0 34.0 56.0

33.0 58.0 33.0 60.0 33.0 62.0 32.0 64.0 30.0 66.0 25.0 69.0 23.0 72.0 22.5 75.0

20.0 80.0 15.0 85.0 11.0 89.0 9.0 92.0 7.0 94.0 5.0 97.0 3.0100.0 2.0101.0

1.0103.0

## PLOT 6.2(3)

8224 6 3  
 26 23 30 32 28 26 28 31  
 -90.0 -81.19 -74.0 -70.32 -44.25 -39.21 -37.10 -31.35  
 1.2737 1.4490 1.417 1.4626 1.2587 1.3485 1.3628 1.209  
 1.0 0.2 5.0 1.7 10.0 3.0 11.0 4.0 11.2 5.9 11.0 8.0 10.2 17.0 10.0 29.0  
 10.4 39.5 10.9 49.5 10.0 54.9 11.0 57.2 12.0 58.7 13.0 61.0 12.0 62.8 10.0 66.3  
 10.1 68.1 10.6 72.9 10.8 80.0 10.9 86.9 11.0 94.3 11.1103.0 11.3109.0 11.2114.5  
 10.0117.2 4.0119.0  
 11.0 13.5 10.5 21.5 10.6 31.5 10.7 37.0 10.7 44.0 10.8 50.0 10.9 59.0 10.0 68.5  
 11.0 72.0 12.0 73.5 13.0 76.0 13.0 77.0 12.0 78.5 11.0 79.9 10.0 82.0 10.8 89.0  
 10.9 96.9 11.0103.7 11.0118.5 11.2113.3 11.3120.8 11.5127.8 11.8131.7  
 1.0 2.5 3.0 5.0 5.0 7.9 8.0 10.5 10.0 13.0 12.0 14.9 11.9 21.0 11.3 27.9  
 11.6 37.0 11.8 46.8 11.9 55.5 12.0 63.5 11.5 69.9 12.0 73.9 13.0 75.0 14.3 78.0  
 13.0 79.9 11.3 83.0 11.8 89.9 11.9 96.4 12.0102.0 12.1108.5 12.2115.5 12.4123.5  
 12.5126.5 10.0134.5 8.0137.0 5.0140.0 3.0142.2 1.0145.0  
 1.0 1.9 3.0 4.5 5.0 7.9 7.0 11.0 9.0 14.5 11.0 18.2 12.0 26.8 12.0 36.9  
 12.1 45.2 12.2 54.0 12.3 62.6 12.4 67.0 11.8 72.0 12.0 74.0 13.0 77.0 14.0 78.2  
 15.0 80.0 15.0 81.0 14.0 81.5 13.0 83.2 11.6 86.5 12.0 89.0 12.2 92.8 12.4 99.0  
 12.5108.0 12.9116.5 13.0124.5 13.0133.5 5.0142.4 3.0146.5 2.0149.0 1.0151.0  
 1.0 3.2 3.0 8.5 5.0 12.5 7.0 16.5 9.0 21.5 11.0 27.4 13.0 31.5 15.0 34.5  
 18.0 43.0 18.0 50.2 18.0 56.5 19.0 62.0 20.0 65.0 21.0 67.5 22.0 68.5 21.0 69.7  
 20.0 71.2 19.0 73.3 18.0 75.6 18.0 84.6 15.0 90.5 13.0 95.0 11.0 99.0 9.0103.2  
 7.0107.8 5.0112.0 3.0116.5 1.0120.8  
 1.0 1.0 3.0 3.2 5.0 7.2 7.0 11.5 10.0 17.0 12.0 20.5 14.0 24.5 15.5 28.5  
 17.0 33.0 18.0 37.0 20.0 46.5 20.0 56.0 19.5 66.0 19.0 69.4 20.0 71.2 21.0 73.0  
 20.0 85.0 18.0 90.5 15.0 95.9 12.0103.0 10.0107.5 8.0112.0 6.0116.5 4.0120.7  
 2.0125.5 1.0128.0  
 1.0 2.8 3.0 7.5 5.0 10.8 7.0 14.0 9.0 18.0 11.0 22.5 13.0 27.0 15.0 31.5  
 17.0 35.0 19.0 39.0 21.0 43.0 23.0 48.0 23.5 56.0 23.0 61.0 22.5 66.5 25.0 74.9  
 22.0 79.0 20.0 81.0 18.0 86.5 16.0 91.0 14.0 94.5 12.0 99.9 10.0103.8 8.0108.0  
 6.0113.0 4.0117.0 2.0121.5 1.0124.5  
 1.0 1.5 3.0 6.0 5.0 8.5 7.0 11.2 9.0 14.5 11.0 18.0 13.0 21.0 15.0 24.5  
 17.0 27.2 20.0 32.0 22.0 35.0 25.0 40.0 27.0 43.5 29.0 47.3 29.0 55.2 28.0 57.0  
 27.0 58.5 27.0 60.0 28.0 61.8 27.0 63.0 25.0 64.5 21.0 69.0 19.0 72.0 17.0 76.0  
 15.0 80.0 13.0 84.5 10.0 87.8 7.0 91.9 5.0 95.5 3.0 99.0 1.0102.5

## PLOT 6.2(4)

8219 6 3

33 30 30 32 21 26 22 25

-90.0 -81.19 -74.0 -70.32 -44.25 -39.21 -37.10 -31.35

1.2737 1.4490 1.417 1.4626 1.2587 1.3485 1.3628 1.209

1.0 0.5 3.0 1.0 5.0 3.0 6.0 5.0 6.3 7.0 6.0 10.0 6.0 19.0 6.0 27.0

6.0 37.0 6.7 49.5 7.0 56.0 8.0 57.0 9.0 58.0 10.0 59.0 11.0 59.8 13.0 60.5

12.0 61.5 12.0 63.0 11.0 63.5 10.0 65.0 9.0 66.0 7.0 69.0 6.5 74.0 6.7 79.0

6.6 85.0 6.6 97.0 6.6106.5 7.0112.5 7.1114.2 6.0116.0 5.0117.0 4.0118.0

4.0119.0

1.0 1.5 2.0 3.0 3.0 5.0 4.0 7.0 6.0 15.5 6.0 23.0 6.0 33.5 6.1 41.5

6.3 49.0 6.5 60.0 6.3 65.0 7.0 68.0 8.0 70.0 10.0 71.5 12.0 73.5 14.0 75.0

12.0 77.0 12.0 78.0 8.0 81.0 7.0 81.5 6.5 86.0 6.5101.0 6.4108.5 6.4117.0

6.4125.0 6.7132.0 6.0134.5 3.0142.0 2.0143.0 1.0144.5

1.0 1.5 3.0 5.5 4.0 8.0 6.0 11.0 7.0 13.0 7.0 22.5 6.9 30.5 7.0 42.0

7.0 49.0 7.1 59.5 7.2 67.0 8.0 70.0 9.0 71.5 10.0 73.5 12.0 75.5 14.0 77.5

12.0 79.0 12.0 81.0 9.0 82.5 8.0 83.0 7.4 86.0 7.5 97.0 7.5107.0 7.5118.0

7.8125.0 7.5127.5 7.0133.5 5.0136.0 3.0140.5 1.0144.5

1.0 3.0 3.0 7.5 6.0 16.0 7.0 18.0 7.1 26.3 7.1 32.5 7.1 39.0 7.5 48.0

7.6 58.0 7.8 67.0 8.0 70.0 9.0 72.0 9.0 74.0 9.0 76.0 11.0 77.0 13.0 78.0

15.0 80.0 12.0 82.0 11.0 83.0 10.0 84.0 8.0 86.5 7.8 87.5 8.0 91.0 8.0 99.0

8.0105.5 8.0113.5 8.0119.0 8.0125.0 7.0133.0 5.0139.5 3.0145.0 1.0150.0

1.0 3.0 3.0 9.5 4.0 13.0 7.0 23.5 9.0 29.0 10.0 32.0 9.5 41.0 9.5 48.5

9.5 55.0 10.0 59.0 11.0 61.0 18.0 66.0 13.0 72.0 12.0 74.0 11.0 85.0 9.0 91.0

7.0 97.0 5.0105.0 3.0112.0 2.0116.0 1.0119.0

1.0 2.0 3.0 6.0 5.0 10.0 7.0 16.0 8.0 20.0 9.0 23.5 11.0 30.0 12.0 34.0

13.0 40.0 13.4 51.0 13.4 57.0 13.4 62.0 14.0 64.5 15.0 66.5 15.0 69.0 18.0 70.0

20.0 72.0 15.0 80.5 13.0 84.0 11.0 90.0 10.0 93.0 8.0100.0 6.0106.0 4.0113.0

3.0120.0 1.0124.0

1.0 4.0 3.0 10.0 4.0 13.0 5.0 17.0 7.0 24.0 9.0 31.0 11.0 38.0 13.0 45.0

14.0 55.5 14.0 59.0 14.0 63.0 15.0 68.0 20.0 75.0 17.0 77.0 15.0 78.0 12.0 83.0

10.0 90.0 8.0 98.0 6.0104.0 4.0111.0 3.0107.5 1.0121.0

1.0 3.0 3.0 8.0 5.0 13.0 7.0 18.0 9.0 23.0 11.0 29.5 13.0 34.0 15.0 39.0

16.0 43.0 17.0 45.5 17.0 53.5 17.0 57.0 18.0 58.5 22.0 60.5 25.0 62.0 20.0 63.0

17.0 65.0 15.0 66.5 13.0 70.0 11.0 73.5 10.0 76.5 7.0 84.5 5.0 90.0 2.0 98.0

1.0101.0

## PLOT 6.3(1)

10300 6 3  
 24 26 28 28 29 31 34 37 32 31  
 -90.0 -81.9 -74.0 -66.59 -59.10 -51.65 -42.07 -37.10 -31.00 -27.16  
 1.2100 1.3200 1.3500 1.342 1.185 1.279 1.267 1.196 1.223 1.085  
 5.0 1.0 11.0 3.0 10.0 7.0 10.0 12.0 11.0 17.0 12.0 24.0 13.0 33.0 14.0 43.0  
 15.0 52.0 16.0 60.0 17.0 64.0 18.0 68.3 19.0 71.0 20.0 74.0 21.0 83.0 21.0 88.5  
 21.0 95.0 20.0 98.0 19.0102.0 18.0104.0 17.0109.0 16.0112.0 12.0113.0 5.0114.0  
 2.0 1.0 5.0 5.0 8.0 7.0 10.0 11.0 11.0 16.0 12.0 21.0 13.0 28.0 14.0 37.0  
 15.0 52.0 16.0 61.0 17.0 69.0 18.9 76.0 19.0 80.0 20.0 86.0 20.0 90.0 19.0 92.0  
 20.0 96.0 20.0100.0 19.0102.0 19.0105.0 20.0109.0 20.0113.0 19.0117.0 18.0121.0  
 5.0130.0 1.0132.0  
 1.0 1.0 3.0 4.0 5.0 7.0 6.0 9.0 8.0 12.0 10.0 15.0 11.0 24.0 12.0 30.0  
 13.0 37.0 14.0 44.0 15.0 51.0 15.0 58.0 16.0 65.0 17.0 72.0 18.0 75.0 19.0 82.0  
 20.0 86.0 21.0 91.0 20.5 96.0 22.0103.0 21.0110.0 21.0115.0 19.0119.0 13.0126.0  
 10.0130.0 6.0133.0 4.0135.0 1.0137.5  
 1.0 2.0 2.0 4.0 3.0 6.5 6.0 12.0 7.0 15.0 9.0 18.0 11.0 21.0 13.0 26.0  
 13.0 30.0 13.0 34.0 14.0 39.0 15.0 45.0 16.0 54.5 17.0 59.5 18.0 68.0 19.0 74.0  
 20.0 79.5 21.0-83.0 22.0 88.0 22.0 92.0 22.5102.0 21.0105.0 20.0108.0 20.0111.0  
 21.0112.0 19.0122.0 16.0127.0 13.0129.0  
 1.0 2.0 2.0 5.0 4.0 9.0 5.0 11.0 7.0 15.0 9.0 19.0 10.0 20.0 12.0 23.0  
 13.0 25.0 14.0 26.0 16.0 34.0 17.0 39.0 18.0 45.0 19.0 52.0 20.0 58.0 21.0 65.0  
 22.0 70.0 23.0 75.0 23.0 78.0 18.0 98.0 16.0101.0 14.0104.0 12.0107.0 10.0109.0  
 9.0111.0 7.0114.0 5.0117.0 2.0120.0 1.0122.0  
 1.0 2.0 2.0 5.0 3.0 7.0 5.0 12.0 7.0 17.0 9.0 20.0 11.0 23.0 12.0 26.0  
 14.0 30.0 15.0 31.0 17.0 33.0 18.0 34.0 20.0 38.0 21.0 47.0 22.0 59.0 23.0 68.0  
 24.0 76.0 24.0 85.0 23.0 87.0 22.0 97.0 22.0100.0 20.0102.0 18.0106.0 15.0110.0  
 13.0112.0 10.0115.5 8.0118.0 6.0121.0 4.0124.0 2.0127.0 1.0128.5  
 1.0 4.0 3.0 8.0 5.0 13.0 7.0 17.0 10.0 22.0 13.0 26.0 15.0 30.0 17.0 33.0  
 20.0 38.0 22.0 40.0 25.0 43.0 27.0 49.0 28.0 51.0 29.0 55.0 30.0 62.0 31.0 68.0  
 32.0 70.0 31.0 77.0 30.0 80.0 28.0 82.0 26.0 84.0 25.0 86.0 25.0 87.0 24.0 90.0  
 20.0 94.0 18.0 96.0 16.0100.0 14.0102.5 10.0106.0 8.0108.0 7.0110.0 5.0113.0  
 3.0118.0 2.0120.0  
 1.0 4.0 3.0 8.0 4.0 11.0 6.0 15.0 8.0 18.0 10.0 21.0 13.0 24.0 15.0 26.0  
 18.0 30.0 20.0 33.5 22.6 36.0 25.0 40.0 27.0 42.5 28.0 44.0 29.0 49.0 30.0 51.0  
 30.0 55.0 31.0 58.0 33.0 65.0 33.0 67.0 32.0 70.0 29.0 74.0 27.0 77.0 26.0 80.0  
 25.0 82.0 21.0 85.0 20.0 87.0 18.0 89.0 16.0 91.0 15.0 93.0 12.0 95.5 10.0 97.0  
 8.0 99.0 7.0101.0 5.0104.0 3.0108.0 1.0110.0  
 1.0 2.0 3.0 6.0 5.0 10.0 7.0 12.0 9.0 16.0 12.0 20.0 16.0 26.0 19.0 29.0  
 21.0 32.0 25.0 38.0 27.0 40.0 31.0 43.0 33.0 48.0 39.0 56.0 37.0 58.0 36.0 60.0  
 35.0 65.0 33.0 68.0 29.0 73.0 23.0 76.0 21.0 79.0 22.8 83.0 20.0 80.0 18.0 87.0  
 15.0 89.0 13.0 91.0 10.0 93.5 8.0 96.0 5.0100.0 3.0102.0 2.0104.0 1.0105.0  
 1.0 3.0 3.0 6.0 5.0 8.0 9.0 12.0 11.0 15.0 13.0 17.0 15.0 19.0 17.0 21.0  
 20.0 23.0 22.0 25.0 24.0 27.0 26.0 29.0 28.0 31.0 30.0 33.0 33.0 35.0 34.0 37.0  
 34.0 57.0 32.6 60.0 30.0 65.0 27.0 67.0 25.0 70.0 23.0 71.0 20.0 73.5 17.0 76.0  
 15.0 77.5 13.0 80.0 10.0 83.0 7.0 85.0 5.0 86.0 3.0 87.5 1.0 90.0  
 2.0 4.0 4.0 9.0 5.0 12.0 7.0 15.0 9.0 18.0 10.0 21.0 13.0 27.0 15.0 30.0  
 18.0 33.0 20.0 36.0 21.0 37.0 21.0 42.0 22.0 45.0 23.0 48.0 24.0 54.0 25.0 60.0  
 26.0 69.0 27.0 72.0 27.0 76.0 28.0 78.0 29.0 87.0 25.0 91.0 20.0 95.5 17.0 99.0  
 15.0103.0 12.0106.0 10.0108.0 7.0111.0 5.0115.0 3.0117.0 1.0121.0

## PLOT 6.3(2)

```

10284 6 3
24 30 29 27 24 29 37 27 33 24
-90.0 -81.9 -74.0 -66.59 -59.10 -51.65 -42.07 -37.10 -31.00 -27.16
1.2100 1.3200 1.3500 1.342 1.185 1.279 1.267 1.196 1.223 1.085
5.0 1.0 12.0 1.8 13.0 3.0 13.0 8.0 13.0 14.0 14.0 22.0 15.0 35.0 16.0 46.0
17.0 54.0 18.0 60.0 19.0 67.0 19.0 72.0 17.0 76.0 16.0 81.0 18.0 87.0 17.0 90.0
17.0 96.0 18.0 99.0 20.0103.0 19.0107.0 19.0111.0 18.0113.0 13.0114.5 10.0115.5
2.0 1.0 5.0 3.8 7.0 6.0 13.0 10.0 14.0 16.0 14.5 28.0 15.0 37.0 15.5 44.0
16.0 49.0 16.5 54.0 17.0 58.0 17.5 61.0 18.0 66.0 19.0 71.0 19.0 77.0 18.0 80.0
16.5 86.0 16.0 89.0 16.0 95.0 18.0 97.0 18.0100.0 16.5105.0 18.0111.0 19.0115.0
19.5119.0 19.0122.0 10.0129.0 5.0130.5 2.0132.0 1.0133.0
1.0 1.0 3.0 5.0 7.0 9.0 11.0 14.0 14.0 20.0 14.5 28.0 15.0 35.0 16.0 47.0
17.0 58.0 18.0 65.0 19.0 71.0 20.0 79.0 19.0 86.0 17.0 92.0 16.5 96.0 17.0 99.0
19.0101.0 19.8104.0 19.0105.0 18.0106.0 17.5110.0 19.0115.0 19.0119.0 12.0127.0
10.0130.0 7.0132.5 5.0134.0 3.0136.0 1.0138.0
1.0 2.0 3.0 6.0 5.0 10.0 7.0 12.0 9.0 15.0 12.0 19.0 13.5 21.0 15.0 27.0
16.0 38.0 17.0 49.0 18.0 59.0 20.0 71.0 21.0 78.0 20.0 85.0 18.0 90.0 17.8 94.0
18.0 98.0 20.0102.0 20.5104.0 20.0105.0 19.0107.0 19.0111.0 17.0120.0 15.0123.0
14.0126.0 11.0130.0 5.0136.0
1.0 2.0 3.0 7.0 5.0 10.0 7.0 13.0 10.0 18.0 12.0 21.0 15.0 26.0 16.0 32.0
17.0 37.0 18.0 45.0 19.0 52.0 20.0 57.0 22.0 69.0 22.0 78.0 22.0 80.0 20.0 99.0
17.0102.0 15.0106.0 13.0110.0 10.0113.0 8.0115.0 5.0118.5 3.0121.0 1.0124.0
1.0 3.0 3.0 7.5 6.0 14.0 8.0 18.0 10.0 21.0 12.0 25.0 14.0 29.0 15.0 31.0
17.0 34.0 19.0 37.0 20.2 43.0 21.0 60.0 22.0 64.0 23.0 71.0 23.0 78.0 21.0 84.0
21.0 88.0 21.0 96.0 23.0 99.0 20.0102.0 17.0105.0 15.0109.0 13.0113.5 11.0116.0
10.0117.0 7.0120.0 5.0124.0 2.0128.0 1.0130.0
1.0 3.0 3.0 7.0 5.0 11.5 7.0 15.0 9.0 19.0 12.0 23.0 14.0 26.0 16.0 30.0
18.0 34.0 20.0 37.0 23.0 41.0 26.0 48.0 27.0 51.0 28.0 57.0 29.0 61.0 30.0 64.0
31.0 68.0 30.0 70.1 29.0 77.0 27.0 79.0 25.0 81.1 23.0 84.2 22.0 87.3 22.0 90.0
20.0 92.0 18.0 93.7 17.0 94.3 16.0 95.9 15.0 98.0 13.0101.4 11.0106.2 10.0108.0
7.0111.1 5.0114.2 3.0117.1 2.0119.0 1.0120.9
1.0 3.0 3.0 6.7 5.0 10.0 7.0 14.0 9.0 17.1 11.0 20.1 15.0 25.1 17.0 28.0
20.0 32.8 23.0 37.0 27.0 42.0 29.0 44.5 29.0 49.8 32.0 53.0 34.0 58.2 34.0 66.0
31.0 68.9 26.0 74.0 24.0 77.0 22.0 80.2 20.0 84.9 15.0 90.0 13.0 93.8 11.0 97.2
7.0102.2 4.0106.1 2.0108.3
1.0 3.1 3.0 6.3 5.0 9.2 7.0 12.5 9.0 15.4 11.0 18.0 13.0 20.3 15.0 23.0
17.0 25.3 20.0 29.1 23.0 33.0 25.0 36.9 28.0 39.6 30.0 41.3 32.0 43.4 35.0 46.1
37.0 48.0 40.0 55.1 39.0 58.2 35.0 62.0 30.0 66.0 26.0 70.1 24.0 73.9 23.0 76.9
20.0 79.9 16.0 83.2 14.0 87.2 11.0 92.1 8.0 96.0 5.0 99.0 3.0101.2 2.0102.6
1.0104.0
1.0 1.4 3.0 3.9 5.0 6.1 7.0 8.1 9.0 11.0 11.0 14.0 13.0 16.0 15.0 18.2
18.0 21.0 20.0 23.0 23.0 26.0 25.0 27.8 27.0 29.2 29.0 31.0 31.0 33.8 34.0 36.0
34.0 52.0 32.0 54.6 30.0 59.0 28.0 62.0 26.0 65.1 24.0 67.0 22.0 69.0 20.0 71.0
17.0 73.6 15.0 76.1 12.0 80.0 10.0 83.0 8.0 84.0 5.0 85.9 3.0 87.1 1.0 89.0
1.0 2.0 3.0 6.0 5.0 11.0 7.0 14.5 9.0 18.0 12.0 25.0 14.0 28.0 15.0 30.0
17.0 32.0 18.0 34.0 20.0 37.0 22.0 44.0 23.0 48.0 24.0 55.0 25.0 59.0 26.0 65.0
26.0 73.0 25.0 75.0 24.0 79.0 23.0 88.0 22.0 93.0 20.0 94.0 18.0 96.0 16.0 99.0
15.0101.0 13.0105.0 12.0107.0 10.0110.0 7.0113.5 6.0115.0 5.0117.0 4.0118.0
2.0120.5 1.0122.0

```

## PLOT 6.3(3)

10265 6 3

26 26 30 27 22 27 24 28 29 26

-90.0 -81.9 -74.0 -66.59 -59.10 -51.65 -42.07 -37.10 -31.00 -27.16

1.2100 1.3200 1.3500 1.342 1.185 1.279 1.267 1.196 1.223 1.085

5.0 1.0 10.0 2.0 12.0 3.0 12.4 6.0 12.0 16.0 12.0 23.0 12.0 39.0 12.0 51.0

12.0 57.0 12.0 67.0 12.0 77.0 11.6 80.0 12.0 83.0 3.0 84.0 14.0 85.0 13.0 87.0

12.0 88.0 12.0 89.0 12.0 92.0 12.0 96.0 12.2100.0 12.2104.0 12.9109.0 12.0112.0

10.0113.5 5.0114.5

2.0 2.0 4.0 4.0 6.0 6.0 9.0 8.0 12.0 11.0 12.4 14.0 12.2 17.5 12.3 28.0

12.3 39.0 12.4 49.0 12.3 56.0 12.2 66.0 12.2 73.0 12.1 79.0 12.0 90.0 11.7 92.0

12.0 95.0 14.0 97.0 13.0100.0 12.0106.0 12.3114.0 12.5122.0 9.0127.0 5.0129.0

3.0130.5 1.0132.0

1.0 1.0 2.0 2.0 4.0 6.0 6.0 8.0 8.0 11.0 10.0 13.0 13.0 16.5 15.0 23.0

12.5 28.0 13.0 35.0 12.8 44.0 12.8 55.0 12.8 64.0 12.8 75.0 12.8 94.0 12.1 99.0

13.0101.0 14.0102.0 15.0103.0 15.0106.0 14.0107.0 12.0110.0 12.5114.0 13.0119.0

11.0128.0 10.0129.0 8.0131.0 5.0134.0 2.0138.0 1.0140.0

1.0 1.3 3.0 5.3 6.0 10.0 8.0 13.4 11.0 18.0 13.0 21.0 13.5 29.3 13.3 35.0

13.2 46.0 13.2 60.0 13.5 71.5 13.5 84.0 13.5 91.0 13.0 96.0 14.0 99.0 15.0100.0

16.0101.0 16.0103.0 14.0104.0 14.0106.0 13.0111.0 13.0116.0 12.0118.0 11.0121.0

9.0124.0 8.0126.0 7.0128.0

1.0 2.0 3.0 6.0 5.0 10.0 7.0 14.0 9.0 18.0 11.0 21.0 13.0 25.0 15.0 27.0

14.5 34.0 14.5 43.0 14.8 53.0 14.8 64.0 14.9 71.0 14.9 77.0 14.0 96.5 13.0100.0

10.0105.0 8.0109.0 6.0113.0 4.0116.5 2.0120.0 1.0122.0

1.0 2.0 3.0 8.0 5.0 12.0 7.0 16.0 9.0 20.0 11.0 25.0 13.0 30.0 15.0 35.0

17.0 38.0 17.0 43.0 17.0 56.5 17.0 62.0 16.7 70.0 16.5 78.0 16.0 86.0 17.0 95.0

18.0 96.0 18.0 97.0 16.0 99.0 13.0103.0 11.0107.0 9.0111.0 7.0115.0 5.0120.0

3.0124.0 2.0125.0 1.0128.0

1.0 1.5 3.0 6.0 5.0 12.0 7.0 16.0 9.0 20.0 11.0 25.0 14.0 30.5 16.0 35.0

18.0 39.0 20.0 43.0 20.2 50.0 20.0 54.0 20.5 62.0 19.3 67.0 19.0 70.0 18.0 79.0

15.0 83.0 14.0 87.0 14.0 92.0 8.0 98.0 6.0105.0 3.0113.0 2.0117.0 1.0120.0

1.0 4.0 3.0 8.0 5.0 12.0 7.0 15.0 9.0 19.0 11.0 23.0 13.0 26.5 15.0 30.0

17.0 34.0 19.0 38.0 21.0 42.0 22.5 51.0 22.5 55.0 22.0 59.0 22.0 65.0 20.0 69.0

18.0 72.0 15.0 78.0 15.0 82.0 14.0 83.5 12.0 87.5 10.0 91.0 9.0 94.0 7.0 98.0

5.0102.0 3.0106.0 2.0108.0 1.0110.0

1.0 2.0 3.0 6.0 5.0 9.0 7.0 13.0 9.0 16.5 11.0 20.0 13.0 23.0 15.0 27.0

17.0 30.0 19.0 33.2 21.0 36.0 22.0 37.2 23.0 39.0 25.0 43.0 28.0 47.0 28.0 56.0

25.0 61.5 22.0 66.0 20.0 69.0 17.0 72.5 16.0 75.0 15.0 80.0 11.0 84.0 9.0 89.0

7.0103.0 5.0107.0 3.0111.0 2.0112.0 1.0114.0

1.0 2.0 4.0 6.5 7.0 10.0 10.0 14.0 12.0 17.0 15.0 21.0 17.0 23.5 20.0 27.2

22.0 30.0 25.0 34.0 26.0 35.5 29.5 43.2 29.0 51.0 27.0 53.0 25.0 56.0 22.0 60.0

21.0 62.0 21.0 64.0 15.0 69.0 12.0 71.0 10.0 74.0 8.0 77.0 6.0 80.0 4.0 83.0

2.0 85.5 1.0 87.3

1.0 2.0 3.0 6.0 5.0 11.0 7.0 15.0 9.0 20.0 11.0 24.0 13.0 28.8 15.0 32.0

17.0 36.0 18.0 44.0 17.5 49.0 17.2 55.0 17.0 63.0 17.9 72.0 12.6 78.0 17.0 86.0

16.0 89.0 16.0 92.0 13.0 95.0 10.0100.0 9.0103.0 7.0107.0 5.0112.0 3.0117.0

2.0119.0 1.0121.0

## PLOT 6.3(4)

```

10264 6 3
30 31 24 30 23 24 26 24 27 25
-90.0 -81.9 -74.0 -66.59 -59.10 -51.65 -42.07 -37.10 -31.00 -27.16
1.2100 1.3200 1.3500 1.342 1.185 1.279 1.267 1.196 1.223 1.085
5.0 1.0 6.0 2.0 7.0 3.0 7.9 5.0 7.2 11.0 7.3 20.0 7.2 30.0 7.2 38.2
7.2 46.6 7.4 54.3 7.5 60.0 7.8 68.8 7.8 75.2 7.8 78.1 8.0 80.1 10.0 81.6
11.0 83.1 12.0 85.5 14.0 86.8 13.0 87.5 14.0 88.6 10.0 90.6 9.0 91.6 8.0 96.7
8.0106.0 8.1108.1 8.0110.0 7.0111.9 5.0113.8 3.0114.9
1.0 2.0 3.0 4.3 5.0 6.1 8.0 12.3 7.8 16.2 7.8 21.1 7.8 26.6 7.9 34.2
8.0 42.0 8.0 48.9 8.0 56.9 8.0 66.2 8.0 74.5 8.0 82.9 8.0 91.0 9.0 92.3
10.0 94.6 12.0 99.0 13.0101.0 12.0102.0 12.0102.5 11.0103.4 10.0104.0 9.0106.0
8.0110.1 8.0115.8 8.3120.4 8.0123.2 5.0130.1 4.0131.0 2.0132.9
1.0 2.2 2.0 4.9 4.0 8.4 5.0 10.1 6.0 12.0 7.0 14.9 8.0 20.7 7.9 31.1
7.9 38.5 8.0 51.6 8.0 61.0 8.1 68.3 8.2 79.8 8.3 87.9 9.0 94.9 10.0 96.5
10.0 99.3 13.0101.1 15.0102.5 13.0103.9 12.0105.2 10.0108.0 8.0111.0 8.0116.6
1.0 2.4 2.0 5.5 3.0 8.1 4.0 12.0 6.0 17.1 8.0 21.6 8.0 29.8 8.0 35.1
8.1 42.2 8.3 51.8 8.3 57.5 8.7 67.6 8.8 77.5 8.9 85.6 9.0 90.0 10.0 94.0
10.0 98.1 11.0100.0 12.0101.1 13.0104.0 14.0105.6 13.0107.0 11.0109.1 10.0110.6
9.0111.9 8.0120.0 7.0129.9 5.0127.9 3.0133.5 1.0138.9
1.0 3.0 2.0 5.7 3.0 9.0 5.0 15.3 6.0 19.3 7.0 21.3 8.0 24.8 8.0 32.2
8.0 38.1 8.1 43.9 8.2 50.2 8.5 57.0 8.8 63.1 9.0 67.9 9.0 74.3 8.0100.5
7.0104.5 6.0107.0 5.0110.0 4.0113.2 3.0116.0 2.0118.8 1.0121.0
1.0 3.2 2.0 7.0 3.0 10.9 4.0 14.1 6.0 21.5 8.0 29.1 9.0 23.9 10.6 44.1
11.0 57.8 11.0 65.9 11.0 75.5 11.0 85.1 12.0 87.0 13.0 92.6 15.0 94.2 17.0 95.3
15.0 96.9 13.0 99.0 11.0100.8 10.0101.9 8.0106.1 6.0112.4 4.0117.9 2.0124.5
1.0 4.1 2.0 7.1 4.0 15.0 6.0 22.1 7.0 26.0 9.0 33.0 11.0 40.0 12.0 43.0
11.9 52.0 11.9 57.9 11.9 63.9 11.9 69.0 11.0 80.1 11.0 83.1 12.0 87.0 11.0 88.0
13.0 90.0 14.0 91.1 13.0 92.8 10.0 94.3 8.0 97.2 7.0 99.0 5.0106.0 4.0109.5
2.0116.0 1.0119.1
1.0 4.1 3.0 10.2 5.0 17.9 7.0 23.9 9.0 30.2 10.0 34.0 12.0 40.1 13.0 44.3
13.0 51.9 13.0 57.0 13.0 65.0 12.0 68.0 11.0 72.0 12.0 78.0 13.0 79.2 15.0 81.0
14.0 82.1 13.0 83.1 10.0 85.9 7.0 89.2 5.0 96.2 3.0101.5 2.0104.3 1.0108.0
1.0 2.9 3.0 9.2 4.0 12.3 5.0 15.1 7.0 20.1 9.0 26.6 10.0 29.0 12.0 35.0
14.0 40.1 15.0 42.9 17.0 54.3 16.0 58.0 14.0 64.0 14.0 69.0 15.0 70.0 15.0 72.0
15.0 74.0 15.0 76.0 14.0 78.1 11.0 81.0 10.0 82.0 8.0 84.0 7.0 87.0 5.0 92.1
3.0 98.1 2.0100.1 1.0103.0
1.0 3.1 3.0 8.4 4.0 10.8 5.0 13.2 7.0 18.3 9.0 21.9 11.0 25.0 13.0 28.0
14.0 30.1 15.0 33.0 16.0 35.1 17.0 43.0 17.0 45.0 16.0 52.2 15.0 55.2 14.0 58.0
13.0 60.0 11.0 65.1 11.0 67.9 9.0 71.0 7.0 75.0 5.0 79.0 3.0 82.6 2.0 85.1
1.0 88.0
1.0 3.2 2.0 7.1 3.0 10.2 5.0 17.2 6.0 22.0 8.0 28.0 10.0 33.0 11.0 37.2
11.0 47.1 11.0 55.8 11.0 61.2 11.0 65.2 11.0 72.0 11.0 76.2 11.0 85.2 13.0 89.0
15.0 90.6 17.0 91.1 15.0 93.0 12.0 94.3 11.0 95.9 10.0 97.0 8.0100.0 6.0106.1
5.0109.0 3.0115.1 2.0118.0 1.0120.9

```

## PLOT 6.4(1)

8273 6 3

32 37 33 22 32 39 37 41

-90.0 -73.90 -66.6 -59.50 -47.90 -44.15 -34.10 -30.50

1.3579 1.4072 1.285 1.2330 1.1670 1.1680 1.2700 1.160

1.0 0.7 3.0 1.0 6.0 2.0 8.0 3.0 9.0 13.0 10.0 26.5 11.0 41.0 12.0 45.0  
 13.0 48.0 14.0 54.0 15.0 58.0 16.0 64.0 16.0 70.0 17.0 78.0 18.0 82.0 19.0 85.0  
 20.0 90.5 20.0 95.5 20.0101.0 19.0102.0 18.0103.5 17.0105.0 16.0108.5 16.0114.0  
 15.0115.5 14.0117.5 13.0119.0 12.0121.0 11.0123.0 10.0126.0 5.0127.3 1.0128.0  
 1.0 1.0 3.0 4.0 5.0 7.0 7.0 10.0 7.5 12.0 8.0 14.0 8.0 24.5 8.0 34.0  
 9.0 44.0 10.0 48.0 11.0 51.0 12.0 61.0 13.0 66.0 14.0 73.0 15.0 76.0 16.0 79.0  
 17.0 82.5 18.0 85.0 18.0 87.5 19.0 90.0 19.0 91.0 20.0 98.0 20.0104.5 20.0108.0  
 20.0111.0 19.0112.5 18.0114.5 17.0117.0 17.0120.0 16.0125.0 15.0128.0 14.0130.0  
 11.0138.0 8.0141.0 5.0144.0 3.0146.0 1.0148.0  
 1.0 3.0 2.0 5.0 3.0 8.0 5.0 12.0 6.0 13.0 7.0 14.0 9.0 19.0 10.0 25.0  
 11.0 28.0 12.0 32.0 13.0 42.5 14.0 50.0 13.0 56.0 15.0 62.5 16.0 69.0 17.0 73.0  
 18.0 76.0 20.0 80.0 21.0 88.0 20.0 95.0 20.0100.0 19.0102.0 18.0103.3 17.0105.0  
 16.0111.0 14.0118.5 12.0121.0 10.0122.3 8.0124.8 6.0128.0 4.0131.0 2.0133.5  
 1.0134.5  
 1.0 5.0 3.0 9.0 5.0 14.0 7.0 17.5 9.0 20.5 10.0 22.0 12.0 24.0 13.0 25.0  
 15.0 28.0 17.0 38.0 18.0 42.5 19.0 51.0 20.0 55.0 21.0 61.0 22.0 65.0 13.0110.0  
 8.0114.8 6.0117.5 5.0119.0 3.0123.0 2.0125.0 1.0127.0  
 1.0 3.5 3.0 7.8 5.0 13.0 7.0 17.0 9.0 19.0 10.0 21.3 13.0 27.8 15.0 32.5  
 17.0 35.0 18.0 36.5 20.0 39.0 21.0 46.0 23.0 53.0 25.0 60.0 27.0 65.0 28.0 67.5  
 27.0 69.0 26.0 72.0 24.0 75.0 24.0 76.0 23.0 79.5 22.0 84.0 20.0 87.0 17.0 91.0  
 15.0 94.0 10.0100.5 9.0102.0 7.0104.5 5.0108.0 3.0111.0 2.0113.0 1.0115.0  
 1.0 2.3 2.0 4.5 3.0 7.5 5.0 12.0 7.0 15.0 9.0 18.0 11.0 21.0 13.0 23.5  
 15.0 26.5 17.0 29.5 18.0 30.5 19.0 32.0 20.0 33.8 23.0 39.5 25.0 42.5 27.0 45.0  
 28.0 48.5 29.0 52.8 30.0 55.0 30.0 59.5 29.0 63.0 28.0 65.0 30.0 73.0 28.0 76.0  
 26.0 78.5 24.0 80.5 23.0 82.5 20.0 85.0 18.0 87.0 16.0 89.0 14.0 91.0 12.0 94.0  
 10.0 96.0 8.0 98.5 6.0101.5 4.0106.5 3.0107.5 2.0109.5 1.0112.0  
 1.0 2.0 2.0 4.0 4.0 7.5 5.0 9.0 7.0 13.0 9.0 17.0 11.0 19.0 13.0 22.0  
 15.0 25.5 17.0 29.0 19.0 31.5 21.0 33.5 23.0 35.8 25.0 39.0 27.0 41.0 29.0 43.0  
 32.0 46.0 33.0 69.0 33.0 71.5 32.0 74.0 30.0 76.0 28.0 78.0 25.0 81.0 23.0 83.3  
 21.0 85.5 20.0 86.5 19.0 87.5 17.0 90.0 15.0 92.5 13.0 95.0 11.0 96.5 9.0 99.0  
 7.0101.5 5.0104.0 3.0107.5 2.0110.0 1.0112.0  
 1.0 1.5 2.0 3.0 4.0 5.8 5.0 7.0 7.0 9.5 9.0 12.8 11.0 15.5 13.0 17.5  
 15.0 20.0 17.0 22.0 19.0 24.0 21.0 27.0 23.0 30.0 25.0 32.0 27.0 34.0 29.0 36.0  
 30.0 37.0 32.0 40.0 34.0 41.5 36.0 45.5 39.0 56.0 37.0 56.5 35.0 61.5 33.0 63.0  
 31.0 65.5 29.0 57.5 27.0 70.0 25.0 71.5 23.0 73.5 21.0 76.0 19.0 78.0 17.0 80.0  
 15.0 82.0 13.0 84.0 11.0 85.5 19.0 88.0 7.0 90.0 5.0 92.0 3.0 94.5 2.0 96.5  
 1.0 98.5

## PLOT 6.4(2)

8251 6 3  
 31 32 25 37 33 26 27 40  
 -90.0 -73.90 -66.6 -59.50 -47.90 -44.15 -34.10 -30.50  
 1.3579 1.4072 1.285 1.2330 1.1670 1.1680 1.2700 1.160  
 6.0 1.0 8.0 2.0 10.0 3.0 11.0 4.0 12.0 8.0 13.0 19.0 14.0 31.2 15.0 42.8  
 16.0 57.0 17.0 64.0 18.0 70.0 19.0 76.8 19.0 80.5 18.0 82.4 17.0 84.5 16.0 87.3  
 15.0 89.0 14.0 94.0 15.0 97.0 16.0 99.0 16.5100.0 16.0102.0 15.0104.0 14.0106.5  
 13.7109.5 14.0114.4 15.0116.5 16.0119.2 16.0122.2 15.0127.0 14.0128.0  
 1.0 2.0 3.0 4.9 5.0 7.5 8.0 10.5 10.0 12.2 12.0 17.0 13.0 29.9 14.0 43.4  
 15.0 54.5 16.0 64.5 17.0 72.3 18.0 78.0 19.0 83.0 19.0 88.3 18.0 90.0 17.0 91.5  
 16.0 93.0 15.0 96.4 15.0105.0 16.0107.0 16.0110.0 15.0112.0 14.0114.0 13.8117.3  
 14.0121.0 15.0125.0 13.0136.0 9.0139.0 7.0140.8 5.0142.4 3.0144.0 1.0145.5  
 2.0 5.5 4.0 9.0 5.0 11.0 7.0 14.0 10.0 18.0 12.0 21.0 14.0 24.0 16.0 26.5  
 18.0 30.5 18.5 40.0 19.0 45.0 20.0 52.5 20.0 56.0 19.0 60.0 20.0 64.5 18.0 69.5  
 18.0 72.0 17.5 78.0 12.0112.0 10.0115.0 8.0118.0 6.0120.5 4.0124.0 2.0127.0  
 1.0128.5  
 1.0 3.5 2.0 5.7 3.0 7.0 5.0 10.0 7.0 12.8 9.0 15.2 12.0 18.0 13.0 21.0  
 14.0 26.2 15.0 35.0 16.0 44.9 17.0 54.0 18.0 62.0 19.0 67.0 20.0 72.0 21.0 76.7  
 20.0 79.2 19.0 80.5 18.0 82.3 17.0 84.5 16.0 88.8 15.0 93.0 16.0 95.2 17.0 97.3  
 17.5 99.0 17.0100.4 15.0104.0 15.8109.8 15.0119.0 14.0120.4 12.0122.5 10.0124.0  
 8.0127.0 6.0128.5 4.0130.8 2.0133.5 1.0135.0  
 1.0 4.0 3.0 8.0 5.0 11.0 7.0 15.0 9.0 19.0 11.0 22.5 13.0 25.5 14.0 28.0  
 16.0 32.0 18.0 35.0 19.0 36.0 20.0 37.9 21.0 40.0 22.0 45.5 24.0 53.3 26.0 57.5  
 27.0 64.0 26.0 67.0 25.0 69.5 24.0 73.0 23.0 75.5 21.0 83.5 19.0 88.0 17.0 92.0  
 15.0 95.0 13.0 98.0 11.0101.0 9.0104.0 7.0106.7 5.0110.0 3.0113.0 2.0115.0  
 1.0116.0  
 2.0 3.0 4.0 8.0 7.0 12.0 9.0 15.8 12.0 20.0 14.0 24.3 16.0 26.0 19.0 30.0  
 21.0 33.0 23.0 39.5 25.0 44.0 27.0 49.5 28.0 58.0 27.0 61.0 26.0 66.0 25.0 74.5  
 23.0 77.3 20.0 80.7 18.0 84.2 15.0 89.5 13.0 93.0 10.0 98.0 7.0102.0 5.0105.0  
 3.0108.8 1.0112.7  
 1.0 2.0 4.0 6.9 6.0 11.0 9.0 15.5 15.0 23.2 18.0 27.6 20.0 30.0 23.0 24.4  
 26.0 38.0 29.0 41.5 32.0 45.0 32.0 50.0 32.0 54.0 32.0 59.5 30.0 66.0 28.5 69.0  
 27.0 72.7 24.0 77.8 20.0 82.7 18.0 86.9 15.0 90.7 13.0 95.0 10.0 99.0 7.0103.0  
 4.0107.5 2.0111.5 1.0113.0  
 2.0 1.5 4.0 4.5 6.0 7.2 8.0 10.0 11.0 13.0 13.0 15.3 15.0 17.4 17.0 20.0  
 19.0 22.3 20.0 23.5 22.0 25.5 24.0 28.0 26.0 29.5 28.0 31.5 30.0 34.8 33.0 37.0  
 35.0 37.8 38.0 40.0 40.0 41.7 43.0 45.5 39.0 52.0 36.0 55.0 35.0 56.1 34.0 58.0  
 34.0 59.9 33.0 61.3 31.0 63.5 29.0 65.5 27.0 68.0 25.0 70.0 22.0 73.0 20.0 75.0  
 18.0 78.0 15.0 81.5 13.0 84.5 10.0 87.8 8.0 89.8 5.0 93.5 3.0 96.0 1.0 99.5

## PLOT 6.4(3)

8218 6 3

30 26 28 22 26 25 27 34

-90.0 -73.90 -66.6 -59.50 -47.90 -44.15 -34.10 -30.50

1.3579 1.4072 1.285 1.2330 1.1670 1.1680 1.2700 1.160

7.0 2.0 9.0 3.2 10.0 3.5 12.0 6.0 12.0 9.0 12.0 12.0 11.8 18.9 11.8 30.2

11.7 39.4 11.6 52.0 11.4 66.0 11.2 77.0 11.1 85.5 11.0 92.8 10.7 95.5 11.0 96.8

12.0 98.4 13.0 99.9 13.8101.0 13.0102.5 12.0104.4 11.0109.9 11.6116.0 11.7119.9

12.0122.0 12.2124.5 12.0125.5 11.0126.9 5.0128.3 1.0129.2

1.0 2.3 3.0 4.5 5.0 7.0 9.0 11.0 11.0 12.5 11.5 18.2 11.2 28.3 11.2 43.0

11.1 57.0 11.1 66.9 11.2 80.0 11.1 91.0 11.0101.0 10.7103.0 12.0106.0 13.0109.0

13.0110.5 12.0112.5 11.0118.0 11.3123.0 11.5127.3 11.0136.0 8.0140.3 5.0143.0

2.0145.3 1.0148.0

1.0 2.0 2.0 3.2 4.0 6.4 7.0 10.4 9.0 13.0 11.0 17.0 13.0 25.0 12.8 36.0

12.7 46.0 12.8 54.5 12.8 62.0 12.8 72.0 12.7 79.0 12.6 87.5 12.0 91.7 13.0 94.0

14.0 96.5 14.0100.0 13.0102.0 12.3107.0 12.9111.0 13.0117.0 11.0119.9 10.0121.0

7.0125.0 5.0128.0 3.0130.0 1.0132.5

1.0 4.0 3.0 7.8 5.0 11.7 7.0 14.5 9.0 18.0 12.0 23.0 14.0 26.5 14.7 35.0

14.6 43.4 14.6 53.0 14.5 63.0 14.4 70.5 14.0 78.0 15.0103.2 14.0105.5 13.0108.0

11.0112.0 9.0115.0 7.0119.0 5.0122.0 3.0125.0 1.0129.2

1.0 3.5 3.0 7.8 5.0 11.0 7.0 14.5 9.0 19.5 13.0 27.5 15.0 22.5 17.0 35.5

19.0 39.0 20.8 46.0 20.8 50.0 20.8 57.0 21.0 63.0 21.0 67.7 21.0 73.0 20.0 79.0

19.0 83.0 17.0 85.5 15.0 89.0 13.0 93.0 10.0 99.2 8.0103.0 4.0107.2 4.0110.5

2.0114.0 1.0116.0

1.0 1.2 2.0 2.2 3.0 4.5 5.0 8.5 7.0 12.0 9.0 16.0 11.0 20.4 14.0 26.0

15.0 28.0 19.0 21.0 20.0 22.2 22.8 43.5 22.8 51.0 22.9 57.0 22.9 64.0 22.0 72.5

18.0 78.1 14.0 84.0 12.0 90.0 10.0 94.2 8.0 98.6 6.0102.5 4.0106.9 2.0110.2

1.0112.2

1.0 4.0 2.0 6.0 3.0 8.2 5.0 11.0 9.0 17.0 11.0 20.3 14.0 25.5 16.0 29.0

18.0 33.0 22.0 39.0 25.0 43.0 26.0 48.0 26.3 55.0 26.3 60.0 26.0 69.0 25.0 75.0

23.0 76.5 20.0 78.5 20.0 80.1 19.0 81.0 17.0 84.0 15.0 88.5 11.0 96.9 7.0114.5

5.0109.5 2.0114.0 1.0116.2

1.0 1.0 3.0 4.0 5.0 10.0 9.0 12.9 11.0 15.5 13.0 18.4 15.0 21.0 17.0 23.0

19.0 26.9 21.0 30.0 23.0 34.0 24.0 36.5 26.0 39.5 28.0 42.5 30.0 45.5 30.0 53.0

29.0 54.9 28.0 56.9 27.0 58.0 26.0 59.9 26.0 61.5 25.0 63.0 23.0 65.5 21.0 68.0

18.0 71.8 16.0 74.5 15.0 77.0 13.0 80.3 11.0 83.9 9.0 87.0 7.0 90.0 5.0 92.3

3.0 96.5 1.0 99.5

## PLOT 6.4(4)

8204 6 3  
 30 33 28 20 22 21 21 29  
 -90.0 -73.90 -66.6 -59.50 -47.90 -44.15 -34.10 -30.50  
 1.3579 1.4072 1.285 1.2330 1.1670 1.1680 1.2700 1.160  
 4.0 1.1 6.0 3.0 7.0 4.0 7.8 7.1 7.4 12.0 7.4 18.0 7.6 29.0 7.8 38.0  
 7.7 45.6 7.8 61.2 7.8 68.9 7.8 76.3 7.2 88.3 7.1 92.8 8.0 94.0 15.0 96.0  
 11.0 98.0 10.0 99.9 11.0101.0-10.0102.0 12.0105.0 11.0106.2 10.0108.0 9.0109.2  
 8.0110.7 7.3114.5 8.0122.8 7.0126.0 5.0127.5 1.0128.8  
 1.0 2.0 2.0 4.1 4.0 7.9 6.0 11.2 7.5 19.3 7.3 25.8 7.2 34.0 7.2 43.4  
 7.2 53.8 7.2 60.5 7.3 69.0 7.4 75.0 7.5 83.9 7.5 93.4 7.5100.1 8.0102.9  
 10.0104.5 11.0107.0 12.0108.3 13.0110.4 11.0112.3 11.0114.9 10.0116.0 9.0119.0  
 8.0121.8 7.2123.2 7.8127.3 7.5130.5 7.0137.0 5.0140.0 4.0141.7 2.0145.2  
 1.0146.3  
 1.0 2.2 2.0 4.3 3.0 7.4 5.0 12.0 6.0 15.0 8.0 19.0 8.2 30.1 8.3 39.9  
 8.5 47.0 8.6 57.0 8.7 66.1 8.8 81.0 9.0 91.0 11.0 93.0 13.0 95.2 15.0 98.1  
 14.0100.4 12.0103.8 11.0105.2 10.0107.9 9.0109.5 8.0116.0 7.0121.0 5.0124.5  
 4.0127.2 2.0131.0 1.0133.2 13.0101.5  
 1.0 3.2 2.0 6.2 4.0 12.0 5.0 15.1 7.0 21.0 9.0 27.0 9.7 39.0 9.6 46.5  
 9.6 55.0 9.8 62.6 9.7 71.0 9.5 79.8 10.0100.9 8.0105.9 7.0109.2 6.0112.3  
 4.0118.0 3.0120.0 2.0123.0 1.0126.0  
 1.0 5.0 2.0 9.8 4.0 16.4 5.0 19.0 6.0 23.0 8.0 28.9 9.0 32.6 11.0 38.1  
 12.0 41.2 12.0 45.2 12.0 50.3 12.0 57.6 12.3 65.8 12.5 74.0 11.0 84.8 10.0 88.5  
 9.0 92.0 7.0 98.2 6.0101.3 4.0108.0 2.0113.2 1.0115.9  
 1.0 3.1 3.0 9.4 5.0 15.2 7.0 21.9 9.0 29.2 11.0 35.4 12.0 37.8 12.0 48.3  
 12.0 55.1 12.2 60.9 12.5 66.6 19.0 74.9 18.0 78.8 12.0 82.1 10.0 88.6 8.0 92.5  
 6.0 99.5 5.0103.0 4.0106.2 2.0112.2 1.0116.4  
 1.0 3.2 3.0 9.9 6.0 18.3 9.0 27.8 12.0 37.6 14.0 44.1 15.8 55.6 16.0 67.8  
 15.0 69.9 17.0 71.8 19.0 72.5 20.0 73.8 21.0 76.1 16.0 79.0 12.0 80.7 11.0 82.0  
 10.0 86.0 6.0 95.8 3.0105.0 2.0108.0 1.0111.9  
 1.0 3.0 2.0 6.1 4.0 10.5 6.0 14.9 8.0 19.1 10.0 23.2 12.0 28.5 14.0 32.5  
 16.0 37.0 18.0 41.1 20.0 46.0 20.0 54.8 19.0 57.1 19.0 61.0 20.0 64.0 21.0 65.5  
 19.0 67.8 15.0 69.4 13.0 70.8 12.0 72.1 11.0 75.0 10.0 76.0 9.0 78.0 8.0 80.5  
 7.0 84.0 5.0 89.0 3.0 93.6 2.0 96.5 1.0 99.3

REFERENCES

- ALWANG, W., CAVANAUGH, L., BURR, R. & HAUER, A. 1970. Optical Techniques for Flow Visualization and Flow Field Measurements in Aircraft Turbomachinery. Item 1, Final Report PWA-3942. Pratt & Whitney Aircraft Co., East Hartford, Connecticut.
- AMERICAN INSTITUTE OF PHYSICS HANDBOOK, GRAY, D.E. 1972. McGraw-Hill, Inc.
- BRANDT, G.B., ROZELLE, P.F. & PATEL, B.R. 1976. Holographic Flow Visualization in Steam Turbine Cascades. The Engineering Uses of Coherent Optics. Editor: ROBERTSON, E.R. Cambridge University Press.
- BRYANSTON-CROSS, P.J., LANG, T., OLDFIELD, M.L.G. & NORTON, R.J.G. 1980. Interferometric Measurements in a Turbine Cascade using Image-Plane Holography. ASME Journal of Engineering for Power. Paper No. 80-GT-91.
- BRYANSTON-CROSS, P.J. 1977. An Investigation into the Airflow over Heated Disruptive Surfaces by Holographic and Mathematical Techniques. Ph.D. Thesis. University of Aston in Birmingham.
- BURANATHANITT, T. 1979. Some Effects of Langmuir Circulation on Suspended Particles in Lakes and Reservoirs. Ph.D. Thesis. University of Leicester.
- CROWTHER, R.A. & KLUG, A. 1974. Three-Dimensional Image Reconstruction on an Extended Field - A Fast, Stable Algorithm. Nature. 251: 490 - 492.
- DENISYUK, Y.N. 1962. Photographic Reconstruction of the Optical Properties of an Object in Its Own Scattered Radiation. Soviet Physics - Doklady. 7: 543 - 545.

- DeVELIS, J.B. & REYNOLDS, G.O. 1967. Theory and Applications of Holography. Addison-Wesley Publishing Co.
- DOBBINS, H.M. & PECK, E.R. 1973. Change of Refractive Index of Water as a Function of Temperature. Journal of the Optical Society of America. 63: 318 - 320.
- DOWD, A. 1981. Temperature Distribution in an Impinging Gas Jet from Interferometric Measurements. Ph.D. Thesis. University of Leicester.
- ECKERT, E.R.G. 1963. Introduction to Heat and Mass Transfer (Translated by GROSS, J.F.) McGraw-Hill.
- EDE, A.J. 1967. An Introduction to Heat Transfer Principles and Calculations. Pergamon Press.
- FRASER, S.M. & KINLOCH, K.A.R. 1974. Large Viewing Angle Holograms. Journal of Physics E: Scientific Instruments. 7: 774 - 776.
- GABOR, D. 1948. A New Microscopic Principle. Nature. 161: 777 - 779; 1949. Microscopy by Reconstructed Wavefronts. Proc. Roy. Soc. A197: 454 - 487; 1951. Microscopy by Reconstructed Wavefronts, II. Proc. Roy. Soc. B64: 449 - 469.
- GATES, G.W.C. 1968. Holography with Scatter Plates. Journal of Physics E: Scientific Instruments. 1: 989 - 994.
- GILBERT, P. 1972. Iterative Methods for the Three-dimensional Reconstruction of an Object from Projections. Journal of Theoretical Biology. 36: 105 - 117.
- GOLUB, G. 1965. Numerical Methods for Solving Least Squares Problems. Numerical Mathematics. 7: 206 - 216.

- GORDON, R., BENDER, R. & HERMAN, G.T. 1970. Algebraic Reconstruction Techniques (ART) for Three-dimensional Electron Microscopy and X-ray Photography. *Journal of Theoretical Biology.* 29: 471 - 481.
- GRAUBE, A. 1974. Advances in Bleaching Methods for Photographically Recorded Holograms. *Applied Optics.* 9:2942 - 2946.
- HERMAN, G.T. 1980. *Image Reconstruction From Projections (The Fundamentals of Computerized Tomography).* Academic Press.
- HERMAN, G.T. 1975. A Relaxation Method for Reconstructing Objects from Noisy X-rays. *Mathematical Programming.* 8: 1 - 19.
- HERMAN, G.T. & LENT, A. 1976. Iterative Reconstruction Algorithms. *Computers in Biology and Medicine.* 6: 273 - 294.
- HERMAN, G.T., LENT, A. & ROWLAND, S.W. 1973. ART: Mathematics and Applications. A Report on the Mathematical Foundations and on the Applicability to Real Data of the Algebraic Reconstruction Techniques. *Journal of Theoretical Biology.* 42: 1 - 32.
- JEONG, T.H. & LODGE, F.E. 1978. *Holography Using a Helium-Neon Laser.* Metrologic Instruments, Inc.
- KACZMARZ, M.S. 1937. An Approximate Solution of the System of Linear Equations (in German). *Bulletin International de l'Académie Polonaise des Science et des Lettres.* A: 355 - 357.
- KUEHN, T.H. & GOLDSTEIN, R.J. 1978. An Experimental Study of Natural Convection Heat Transfer in Concentric and Eccentric (Cylindrical Annuli). *ASME Journal of Heat Transfer.* 100: 635 - 640.

- LEITH, E.N. & UPATNIEKS, J. 1962. Reconstructed Wavefronts and Communication Theory. *J. Opt. Soc. Am.* 52: 1123 - 1130;
1964. Wavefront Reconstruction with Diffused Illumination and Three-Dimensional Objects. *J. Opt. Soc. Am.* 54: 1295 - 1301.
- MATULKA, R.D. & COLLINS, D.J. 1971. Determination of Three-Dimensional Density Fields From Holographic Interferograms. *Journal of Applied Physics.* 42 (3): 1109 - 1119.
- MEGGERS, W.F. & PETERS, C.G. 1918-19. Measurements on the Index of Refraction of Air for Wavelengths from 2218 Å to 9000 Å. *Bulletin of the Bureau of Standards.* 14: 697 - 740.
- MEYER, B.A., MITCHELL, J.W. & EL-WAKIL, M.M. 1979. Natural Convection Heat Transfer in Moderate Aspect Ratio Enclosures. *ASME Journal of Heat Transfer.* 101: 655 - 659.
- OSTROVSKY, Y.I., BUTUSOV, M.M. & OSTROVSKAYA, G.V. 1980. *Interferometry by Holography.* Springer-Verlag Berlin Heidelberg.
- PENNINGTON, K.S. & HARPER, J.S. 1970. Techniques for Producing Low Noise Improved Efficiency Holograms. *Applied Optics.* 9: 1643 - 1650.
- PHILLIPS, N.J. & PORTER, D. 1976. An Advance in the Processing of Holograms. *Journal of Physics E: Scientific Instruments.* 9: 631 - 634.
- RADULOVIC, P.T. 1977. *Holographic Interferometry of Three-Dimensional Temperature or Density Fields.* Ph.D. Dissertation. The University of Michigan.
- SMITHSONIAN PHYSICAL TABLES, FORSYTHE, W.E. 1954. *The Smithsonian Institute.* 9th Edition.

- SWEENEY, D.W. 1972. Interferometric Measurement of Three-Dimensional Temperature Fields. Ph.D. Dissertation. The University of Michigan.
- SWEENEY, D.W. & VEST, C.M. 1973. Reconstruction of Three-Dimensional Refractive Index Fields from Multidirectional Interferometric Data. Applied Optics. 12 (11): 2649 - 2664.
- SWEENEY, D.W. & VEST, C.M. 1974. Measurement of Three-Dimensional Temperature Fields above Heated Surfaces by Holographic Interferometry. International Journal of Heat and Mass Transfer. 17: 1443 - 1454.
- TILTON, L.W. 1935. Standard Conditions for Precise Prism Refractivity. Journal of Research of the National Bureau of Standards. 14: 393 - 418.
- TILTON, L.W. & TAYLOR, J.K. 1938. Refractive Index of Distilled Water for Visible Radiation, at temperatures 0 - 60°C. Journal of Research of the National Bureau of Standards. 20: 419 - 477.
- VEST, C.M. 1979. Holographic Interferometry. John Wiley & Sons, Inc.
- VEST, C.M. & SWEENEY, D.W. 1970. Holographic Interferometry of Transparent Objects with Illumination derived from Phase Gratings. Applied Optics. 9 (10): 2321 - 2325.
- WALKLATE, P.J. 1977. Numerical Reconstruction of Three-Dimensional Refractive Index Fields from Multidirectional Interferometric Data. Department of Engineering Science, Oxford University.
- WALKLATE, P.J. 1980. Private Communication. AERE Harwell, Oxfordshire.
- WELTY, J.R. 1978. Engineering Heat Transfer - SI Version. John Wiley & Sons, Inc.

YOUSEF, W.W. & TARASUK, J.D. 1981. An Interferometric Study of Combined Natural and Forced Convection in a Horizontal Isothermal Tube. ASME Journal of Heat Transfer. 103: 249 - 256.